Dissertation
zur Erlangung des
Doktorgrades der Naturwissenschaften
(Dr. rer. nat.)

Understanding losses in OLEDs: optical device simulation and electrical characterization using impedance spectroscopy

Stefan Nowy

April 2010

Arbeitsgruppe Organische Halbleiter
Lehrstuhl für Experimentalphysik IV
Institut für Physik
Mathematisch - Naturwissenschaftliche Fakultät
Universität Augsburg

Erstgutachter:	Prof. Dr. Wolfgang Brütting
Zweitgutachter:	Prof. Dr. Achim Wixforth
Tag der mündlichen Prüfung:	06.07.2010

“The only time I become discouraged is when I think of all the things I like to do and the little time I have in which to do them.”

— Thomas Alva Edison

Contents

1. Motivation

On the *"1st day of November, A.D. 1879"* the inventor Thomas Alva Edison signed a patent for *"an Improvement in Electric Lamps, and in the method of manufacturing the same"* using *"a carbon filament or strip coiled and connected to electric conductors"* giving light by incandescence[1]. This invention, generally taken to be the birth of long-lasting incandescent light bulbs, revolutionized the possibilities of illumination. Even today, successors of this type of light bulb are still globally in use. However, only about 5 % of the invested electrical power is radiated as visible light, the other part of the power is emitted as heat. Approximately, 112 TWh of electrical power have been consumed in the year 2007 in the European Union for lighting rooms in households[2]. This is about 14 % of the total power consumed in residential households (801 TWh in 2007[3]). With that in mind, a higher usage of more efficient light sources appears to be a reasonable goal — a goal that is already pursued by law in the European Union[2] and other countries including Australia and Cuba. Besides the common light bulb, there are several other types of illumination sources which are more efficient and therefore used in lighting applications, e.g., fluorescent tubes, compact fluorescent lamps (CFLs), and halogen incandescent lamps. The CFLs, which usually are used to replace light bulbs, are also known as 'energy saving lamps'. However, they lack a wide acceptance since, in early days, they only provided white light which was blueish (not a "warm", continuous emission spectrum in contrast to the "traditional" light emitted by incandescent lamps). Today, manufacturers can produce warm-white CFLs, however, their bad reputation could not be reversed in the minds of people. Another drawback of these lamps is their necessity of some time (in the order of minutes) until reaching maximum light output, hence, not being very useful when lighting is required only for a short period of time.

Promising candidates for more efficient, longer-lasting light sources derive from the area of 'solid-state lighting' (SSL), where light is generated by solid-state electroluminescence, i.e., radiative recombination of holes and electrons; in contrast to light generation by heat, as in incandescent light sources. SSL devices are 'light-emitting diodes' (LEDs, using inorganic semiconductors), or 'organic light-emitting diodes' (OLEDs, using organic materials). LEDs already have a vast distribution being used as indicators in everyday objects, e.g., in consumer electronics, traffic lights, cars, and others. They are also used as backlight in computer displays and flat-panel TVs, saving energy and providing almost constant luminance for very long times (half-luminance lifetimes of several 10 000 to 100 000 hours). For the same reasons, saving energy and extremely long-lasting, LEDs are more and more considered for lighting applications, e.g., for cabin illumination in modern day aircraft (e.g., in the Airbus A330/A340 and A380, and the Boeing 777 and 787 airplanes[4]). Due to their advantages, it is almost certain that LEDs will be featured in many lighting applications in the near future.

Figure 1.1.: ‘Early Future’, an OLED table light designed by Ingo Maurer[6].

There is another class of solid-state light sources besides inorganic LEDs: their organic counterparts using thin films of organic compounds — the organic light-emitting diodes. One of their main advantages is that OLEDs are uniform surface light sources (and not point sources as LEDs, or, to some extent, incandescent lamps). This allows entirely new, fascinating lighting possibilities, such as luminescent ceilings or windows which are transparent at daytime and the source of room illumination at night. OLEDs can be fabricated on different substrates, usually on glass, but also on, e.g., thin metal or plastic foils. As a consequence, OLEDs can be flexible and can be adjusted to different surface forms. Also, cheap processing can be achieved using high-volume printing techniques, like roll-to-roll or inkjet-printing.

OLED matrix displays are already available in some consumer products, e.g., car stereos, cell phones, mp3-players, and blood glucose meters. They do not require a backlight and offer a wide viewing angle that is much larger than other commonly used displays. For lighting applications, organic light-emitting diodes are on the edge of emerging markets: OSRAM Opto Semiconductors (OSRAM OS), Regensburg, recently started to sell tiles of warm-white emitting OLEDs with a circular active area of 79 mm diameter[5]. Before, in 2008, renowned light designer Ingo Maurer developed a table light called ‘Early Future’, see fig. 1.1, which was produced in a limited edition, consisting of ten tiles of OLEDs manufactured by OSRAM OS having an area of 132 mm × 33 mm each[6].

To fully tap the potential of organic light-emitting diodes for lighting applications, they need further improvement concerning light-outcoupling, efficiency, and device lifetime. To achieve a fundamental understanding of the involved processes, these topics are addressed in this thesis: simulation based optical optimization, and electrical characterization and device degradation studies using impedance spectroscopy.

2. Introduction to organic light-emitting diodes (OLEDs)

2.1. Organic semiconductors

Exploration of organic semiconductors and their applications started about 50 years ago. The first organic light-emitting diode (OLED) was reported by Williams and Schadt in the late 1960s using an anthracene crystal, structured electrodes and about 100 V as applied bias[7]. It was not until 1987, when the first efficient OLED was reported by Tang and VanSlyke using a bias of only a few volts and evaporated thin films from small molecule materials[8]. Meanwhile Heeger, MacDiarmid, and Shirakawa showed in the years 1977 and 1978 that the electrical conductivity of organic polymers can be increased by doping[9–11]. Eventually, these three scientists received the Nobel prize for chemistry in 2000[12] (interestingly, in the same year Kilby received the prize in physics for the invention of integrated circuits[13], another pioneering step for the electronic world we live in today). The first polymer OLED has been realized by Burroughes, Bradley, and Friend et al. in 1990[14]. In the meantime, also organic photovoltaic cells (OPVCs) have been realized; the first reported with an efficiency of about 1 % again was fabricated by Tang even a year before he published the efficient OLED[15]. Tang's pioneering work started a boom of studies of organic materials and their applications in OLEDs, OPVCs, and organic field effect transistors (OFETs).

But what are these organic small molecule materials and organic polymers? Organic semiconductors are based on π-conjugated electron systems which are formed in hydrocarbons when not only single bonds are present, but also double and triple bonds. Anthracene (fig. 2.1) is one of the simplest molecules with this conjugated π-system: the carbons are sp^2-hybridized and therefore not only bond by a σ-bond but also by a π-bond of the not hybridized p_z-electrons. This π-bond is weaker than the σ-bond and is essential for the semiconducting properties: in unsaturated hydrocarbons the energy gap between the ground state, the bonding π-orbital (designated as highest occupied molecular orbital — HOMO), and the anti-bonding π^*-orbital (lowest unoccupied molecular orbital — LUMO), is considerably smaller than in saturated hydrocarbons. As the energy gap between HOMO and LUMO is of the order $1.5 - 4\,e\mathrm{V}$, excitation with visible or near-UV light is possible (for a schematic representation, please see fig. 2.2). The probability densities for the HOMO and LUMO of anthracene are shown in fig. 2.3. The exact value of the energy gap depends on the size of the conjugated π-system and therefore on the size of the molecule[16]. As other atoms (e.g., N, S, O, or even metals) are introduced in these complex material systems, their electrical and optical properties can be tuned almost arbitrarily. Some

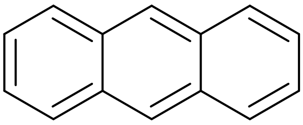

Figure 2.1.: Anthracene ($C_{14}H_{10}$), a prototypical organic semiconductor where the carbons are bonded due to sp^2-hybridization.

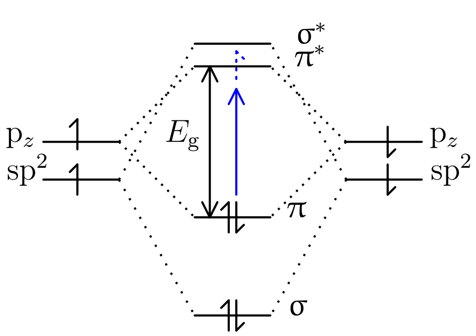

Figure 2.2.: Optical transition (absorption, blue arrow) between the bonding π-orbital (highest occupied molecular orbital, HOMO) and the anti-bonding π*-orbital (lowest unoccupied molecular orbital, LUMO) in a carbon–carbon double bond with energy gap E_g.

examples of small molecule materials and conjugated polymers are shown in fig. 2.4, however, there are literally thousands of different organic materials available.

One of the major differences between inorganic and organic semiconductors is the bonding type between atoms and molecules, respectively. The atoms in inorganic semiconductors form a strong covalent bond, however, the intermolecular forces between molecules of organic semiconductors are of the van-der-Waals type. This bonding type is very weak, resulting in materials with low hardness and low melting points and is also responsible for different electrical and optical properties, which are discussed in the following sections.

2.2. Energy levels in organic semiconductors

If a photon is absorbed by a molecule, a transition from the electronic ground state to an excited state occurs. Both energy levels have a substructure due to vibronic modes. These modes with vibrational quantum number ν are a result of the potential well, described by, e.g., the quantum harmonic oscillator, the Lennard-Jones potential, or the Morse potential. The latter is a better approximation for the vibrational structure of a molecule than the quantum harmonic oscillator as, e.g., it includes the possibility of bond breaking and anharmonicity effects. For a diatomic molecule, where the atoms

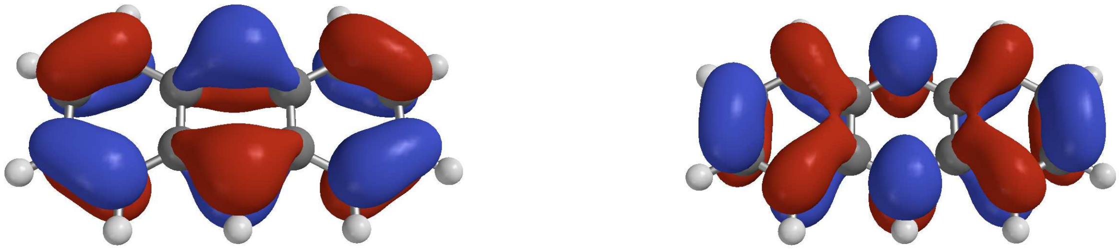

Figure 2.3.: Probability densities of the HOMO (left) and LUMO (right) of anthracene. Dark gray atoms: carbon, light gray atoms: hydrogen. Courtesy of Ben Mills[17].

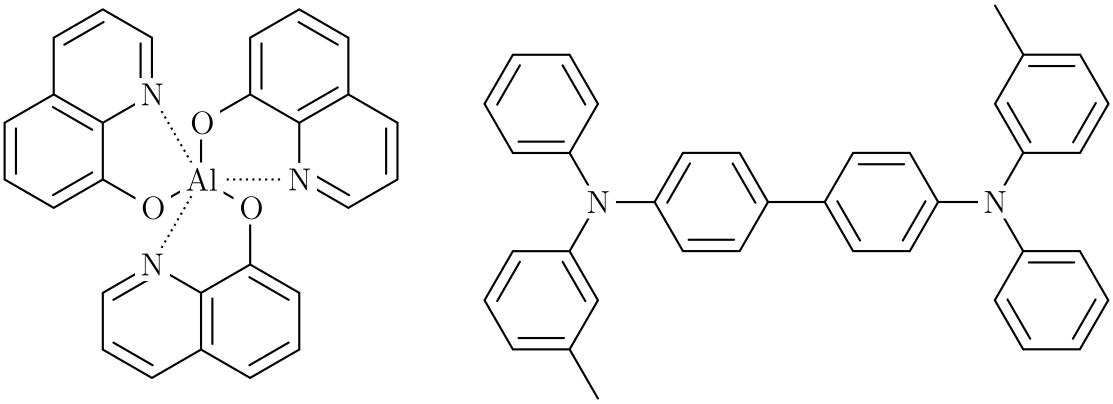

Alq_3 TPD

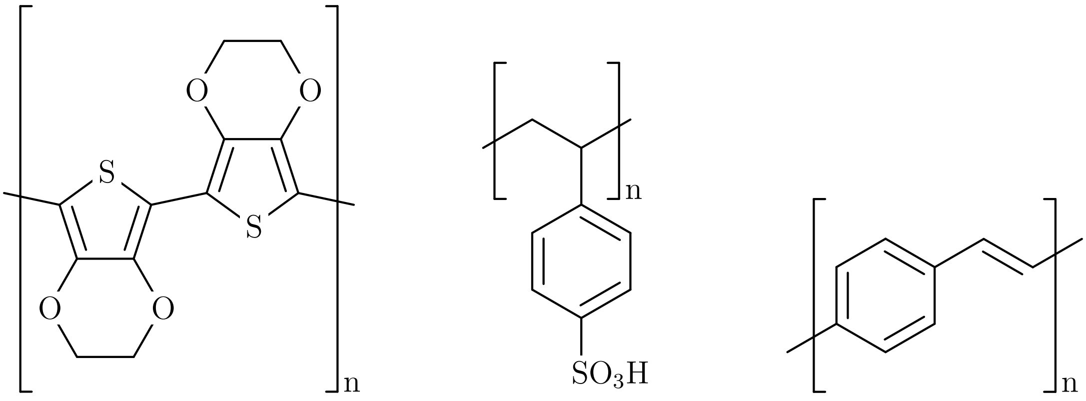

PEDOT PSS PPV

Figure 2.4.: Examples for organic small molecule materials, Alq_3 (tris-(8-hydroxyquinoline) aluminum) and TPD (N,N'-diphenyl-N,N'-bis(3-methylphenyl)-1,1'-biphenyl-4,4-diamine), as well as conjugated polymers, PEDOT (poly(3,4-ethylenedioxythiophene)), PSS (poly(styrene sulfonate)), and PPV (poly(*p*-phenylene vinylene)).

are separated by a distance r the Morse potential is

$$V(r) = D_\mathrm{e} \cdot (1 - \exp\left[-a(r - r_\mathrm{e})\right])^2 \tag{2.1}$$

and the vibronic modes have the eigenvalues

$$E_\nu = \hbar\omega\left(\nu + \frac{1}{2}\right) - \frac{\left[\hbar\omega\left(\nu + \frac{1}{2}\right)\right]^2}{4D_\mathrm{e}}\,, \tag{2.2}$$

where D_e is the depth of the well, a is a parameter associated with the force constant of the bond, r_e is the equilibrium bond distance, and ω is the angular frequency. The reduced Planck constant is indicated with $\hbar$. The Morse potentials for the ground and excited state, respectively, including vibrational energy levels and wave functions, is shown in fig. 2.5.

Absorption can occur from the ground state with vibrational quantum number $\nu = 0$ into excited states with vibrational quantum number ν^*, see fig. 2.6 for a schematic representation. Thereby, the electronic transition is subject of the Franck-Condon principle, which states that the transition is more likely to happen if the two vibrational wave functions of the initial and final state overlap more significantly (for the vibrational wave functions, see fig. 2.5). After non-radiative, vibronic relaxation to $\nu^* = 0$ (Kasha's rule), emission from the excited state to a vibronic level of the ground state occurs radiatively. Eventually, the system relaxes non-radiatively until the vibrational state $\nu = 0$ is reached. As a consequence, the absorption and emission spectra are shifted in energy (or wavelength): higher energies (smaller wavelengths) are required for absorption as compared to what is released by emission (smaller energies/higher wavelengths). This is called Stokes shift. As the potential wells of the ground and excited state are of equal shape and nearly symmetrical, the absorption and emission spectrum are symmetrical in ideal cases (mirror-image rule)[18]. For a diluted gas, symmetrical, narrow lines in the spectra are observed, however, in solids, like thin films of organic semiconductors, inhomogeneous broadening occurs. This is the reason for the broad absorption and emission spectra of organic materials. The absorption and fluorescence emission spectrum of tris-(8-hydroxyquinoline) aluminum ($\mathrm{Alq_3}$) is shown in fig. 2.7 as an example. In contrast to these broad emission spectra of organic materials (width several 100 meV), the emission spectra of inorganic LEDs are very narrow with typical spectral linewidth of $1.8\,k_\mathrm{B}T$ (k_B is Boltzmann's constant, T the temperature)[19], which is approximately 45 meV at room temperature.

There are well defined spin states in organic molecules. The states are designated by the multiplicity $(2S+1)$ which is the number of spatial orientations for the spinvector of two electrons with total spin S. If their spins are anti-parallel, their total spin S is 0 and the multiplicity is 1. This is called a singlet state. $S = 1$ is the total spin for parallel oriented spins of two electrons, having the multiplicity 3, hence called triplet state. The singlet state is having an anti-symmetrical spin state and the triplet state a symmetrical spin state. Due to the multiplicity there is one possible spin combination

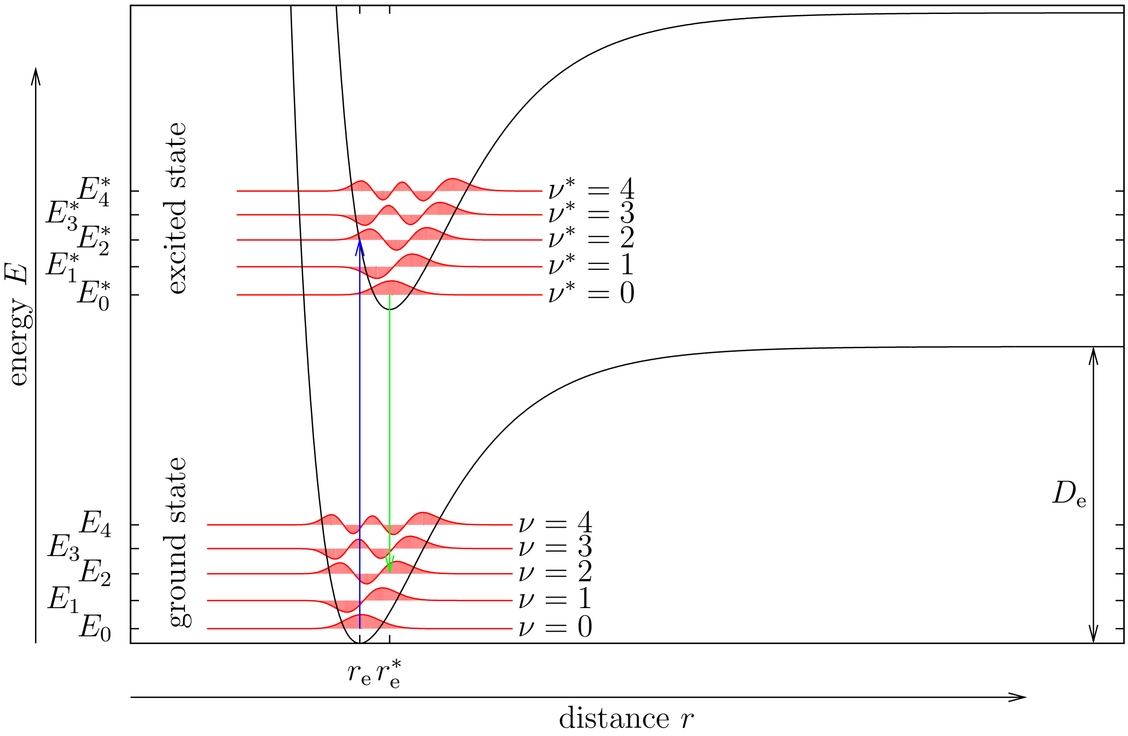

Figure 2.5.: Morse potentials for the ground and excited state, respectively, with corresponding first five vibrational energy levels E_ν and E_ν^* and corresponding vibrational wave functions (red lines). As examples the absorption (blue arrow) from the ground state with vibrational level $\nu = 0$ to the excited states with $\nu^* = 2$ and in analogy (green arrow), the emission from the excited state with $\nu^* = 0$ to the ground state with $\nu = 2$ are shown. If the two vibrational wave functions overlap significantly, the transition is favored (Franck-Condon principle). The depth of the well D_e and its width is chosen in such a way that the wave functions can be depicted.

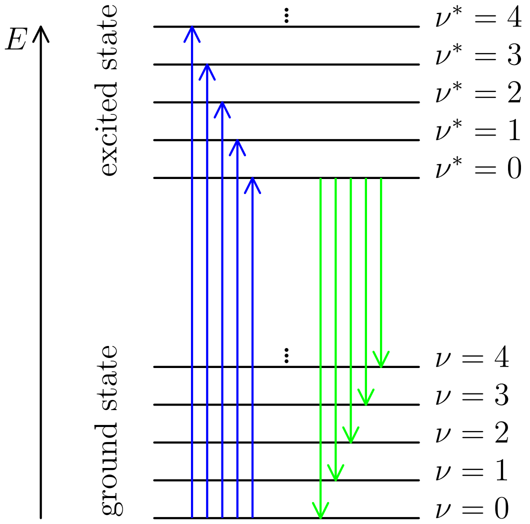

Figure 2.6.: Electronic transitions always start from the vibrational level $\nu = 0$ or $\nu^* = 0$, respectively (Kasha's rule). Absorption from the ground state with $\nu = 0$ to excited states with vibrational level ν^* (blue arrows) and emission (green arrows) from the excited state with vibrational levels $\nu^* = 0$ to ground states with vibrational level ν.

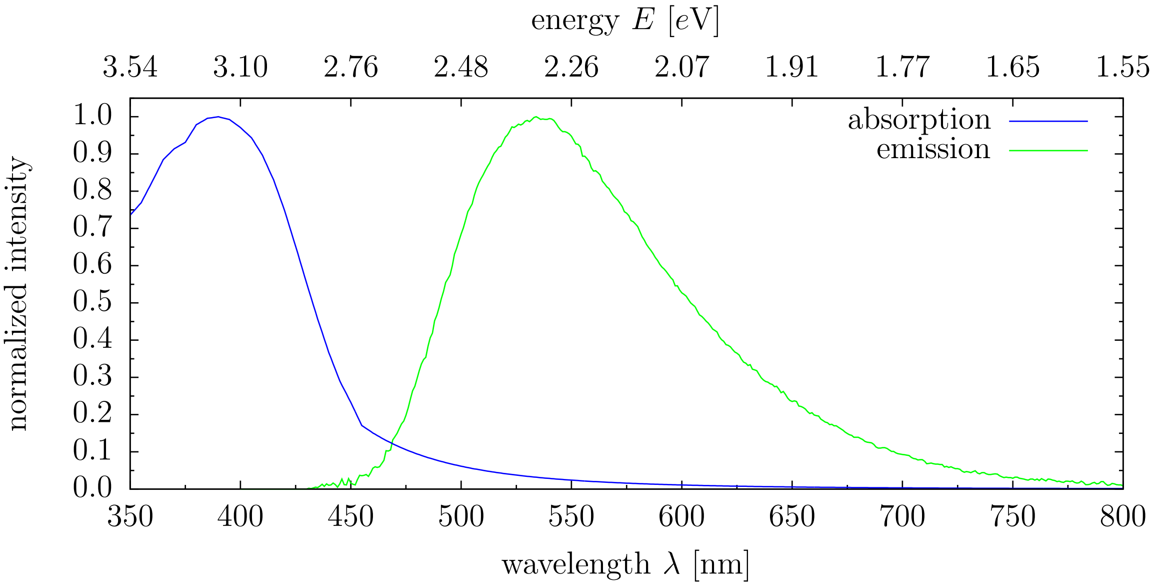

Figure 2.7.: Normalized absorption (blue line) and emission (green line) spectra of the fluorescent green emitter material Alq_3.

for the singlet, however, there are three possible combinations for the triplet:

$$\text{singlet} \qquad \frac{1}{\sqrt{2}}\left(|\upharpoonleft\downharpoonleft> - |\downharpoonleft\upharpoonright>\right) \tag{2.3}$$

$$\text{triplet} \qquad \begin{cases} |\upharpoonleft\upharpoonright> \\ \frac{1}{\sqrt{2}}\left(|\upharpoonleft\downharpoonleft> + |\downharpoonleft\upharpoonright>\right) \\ |\downharpoonleft\downharpoonleft> \end{cases} \tag{2.4}$$

The ground state is a state with spin 0, i.e., the singlet state $\mathrm{S_0}$. The next higher states in energy are the singlet $\mathrm{S_1}$ (spin 0) and the triplet $\mathrm{T_1}$ (spin 1), which, according to Pauli's principle, is energetically lower than the $\mathrm{S_1}$ state, see fig. 2.8 for a simplified (without vibrational levels) energy level diagram. Due to the spins, optical excitation or decay is usually only taking place in the singlet system: absorption from $\mathrm{S_0} \rightarrow \mathrm{S_1}$ is very strong due to the high absorption coefficients, and fluorescent decay from $\mathrm{S_1} \rightarrow \mathrm{S_0}$ is very fast (fluorescence lifetimes $\tau_{\mathrm{r,f}}$: several nanoseconds). As the spins are different, the transition $\mathrm{S_1} \rightarrow \mathrm{T_1}$ through so called inter-system crossing (ISC) is very weak, as it is forbidden. The same is usually true for the phosphorescence $\mathrm{T_1} \rightarrow \mathrm{S_0}$. As a consequence, this process has lifetimes $\tau_{\mathrm{r,p}}$ of the order of milliseconds and is not very effective. However, if heavy ions (e.g., Pt or Ir) are introduced into the organic molecules, mixing of singlet and triplet states occurs and the selection rules are weakened[20], allowing the phosphorescent transition, resulting in lifetimes $\tau_{\mathrm{r,p}}$ of the order of microseconds. There are other decay mechanisms (depending on the energy levels), e.g., the triplet-triplet-annihilation: two triplet states $\mathrm{T_1}$ combined can decay into the singlet ground state $\mathrm{S_0}$ and a higher triplet state $\mathrm{T_n}$, called triplet quenching ($\mathrm{T_1} + \mathrm{T_1} \rightarrow \mathrm{S_0} + \mathrm{T}_n$), or decay into $\mathrm{S_0}$ and a higher singlet state $\mathrm{S_n}$, which eventually relaxes to $\mathrm{S_1}$ and back to $\mathrm{S_0}$ with emission of fluorescent light (delayed fluorescence, $\mathrm{T_1} + \mathrm{T_1} \rightarrow \mathrm{S_0} + \mathrm{S_n}$, $\mathrm{S_n} \rightarrow \mathrm{S_0} + \text{light}$).

2.3. Excitons and generation of light inside an OLED

Organic semiconductors show quite a difference to inorganic semiconductors due to the weak intermolecular van-der-Waals interaction: excited states usually are located on one molecule. On absorption of a photon, an electron e^- from the HOMO is lifted to the LUMO, leaving a hole h^+ in the HOMO behind. This electron-hole-pair is bound by electrostatic interactions and is called an 'exciton', which is a quasi-particle. It is localized on one molecule and its bond is very strong. Therefore, it is also called Frenkel exciton to differentiate it from weakly bound excitons in inorganic semiconductors (Mott-Wannier excitons). Its binding energy can be estimated to about $0.5\,e\mathrm{V}$, using Coulomb attraction for two charge carriers at distance $r = 1\,\mathrm{nm}$ and a relative dielectric constant of $\varepsilon_{\mathrm{r}} = 3$. These excitons are not very mobile, having diffusion lengths of a few nanometers only. As the thermal energy at room temperature is only about $25\,\mathrm{m}e\mathrm{V}$, the excitons are not separated into free holes and

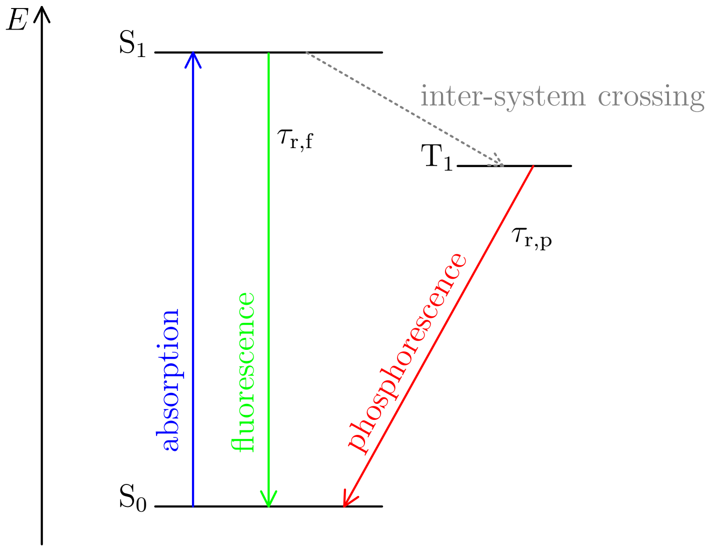

Figure 2.8.: Simplified (without vibrational levels) energy level scheme for transitions within an organic material. Absorption of light (blue arrow): $S_0 \rightarrow S_1$. Fluorescence (green arrow, lifetime $\tau_{\mathrm{r,f}}$ of the excited state S_1): $S_1 \rightarrow S_0$. Inter-system crossing (non-radiative, gray dashed arrow): $S_1 \rightarrow T_1$. Phosphorescence (red arrow, lifetime $\tau_{\mathrm{r,p}}$ of the excited state T_1): $T_1 \rightarrow S_0$.

electrons, respectively, just by absorption of light. A force, e.g., an electric field, has to be applied to move the charges apart until the Coulomb interaction is smaller than the thermal energy (the distance is called Coulomb radius and is of the order of 20 nm in molecular crystals). This separation of the excitons is a major concern in organic photovoltaic cells. Short diffusion lengths and strongly bound excitons are, however, favorable in OLEDs: if a hole and an electron form an exciton, it only can move a few nanometers, as the lifetime of this state is limited to a few nanoseconds. Therefore, the probability that the exciton decays non-radiatively due to defects or impurities in the organic material is pretty low.

In OLEDs excitons are formed from injected holes and electrons, eventually recombining either radiatively or non-radiatively. For fluorescent emitter molecules, electrons and holes form either a singlet state S_n^* that relaxes to S_1 and then to S_0 under emission of light with angular frequency ω_{f}

$$e^- + h^+ \rightarrow S_n^* \rightarrow S_1 \rightarrow S_0 + \hbar\omega_{\mathrm{f}} \,, \tag{2.5}$$

or a triplet state T_n^* that relaxes non-radiatively to S_0, generating heat,

$$e^- + h^+ \rightarrow T_n^* \rightarrow T_1 \rightarrow S_0 + \text{heat} \,. \tag{2.6}$$

The situation is similar for phosphorescent emitters, however, electrons and holes can form a triplet T_n^* that relaxes to T_1 and then to S_0 under emission of light with angular frequency ω_{p}

$$e^- + h^+ \rightarrow T_n^* \rightarrow T_1 \rightarrow S_0 + \hbar\omega_{\mathrm{p}} \,. \tag{2.7}$$

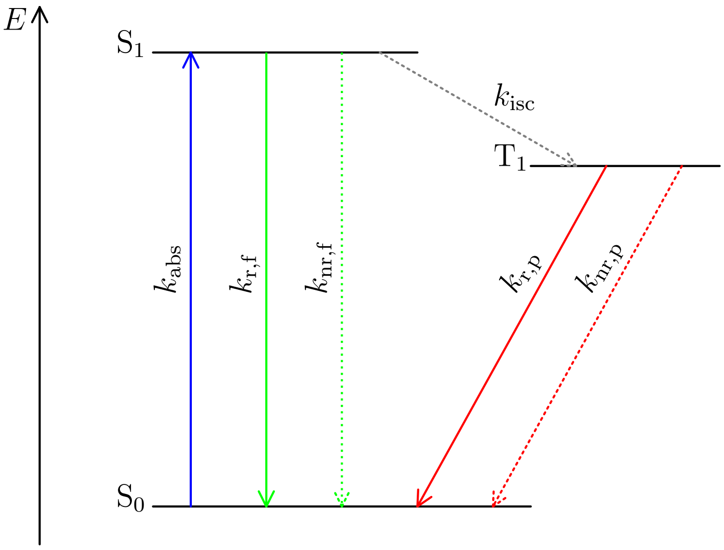

Figure 2.9.: Simplified energy level scheme for radiative (solid arrows) and non-radiative (dashed arrows) processes. Rates indicated with k are the inverse of the lifetimes τ of the different states.

This, however, is only possible if the spin of the triplet is absorbed by, e.g., heavy ions in the organic material. Please note that formation of triplets can also occur by inter-system crossing from a singlet S_1 to a triplet T_1.

There are a lot of competing processes, also being non-radiative, e.g., generation of heat. Several deactivation processes have been shown in the previous section. Evidently, non-radiative processes lower the efficiency of OLEDs and in turn require careful tuning of the materials' energy levels and possible energy transfer routes to overcome this issue. A simplified energy level scheme for the singlet and triplet states is again shown in fig. 2.9, where radiative (solid arrows) and non-radiative rates (dashed arrows) are indicated with the letter k (rates are the inverse of the lifetimes τ).

The ratio of radiative rates k_r to all rates, radiative and non-radiative, defines the radiative quantum efficiency (QE) q of the emitter material:

$$q = \frac{k_\mathrm{r}}{k_\mathrm{r} + \sum k_\mathrm{nr}} \,, \tag{2.8}$$

where $\sum k_\mathrm{nr}$ denotes the sum of all competing non-radiative processes. This means that if an exciton is generated, it has the probability q to decay under the emission of a photon. For the fluorescent green emitter $\mathrm{Alq_3}$, q is approximately 20 % in the solid state[21,22]. However, the radiative rate k_r is not a constant as it is influenced by the surroundings of the emitter material. This will be discussed extensively in chapter 4.

2.4. Injection of charge carriers and charge transport in organic semiconductors

Based on drift-diffusion-models, the current density j through an organic material depends on the density of charge carriers n and their drift velocity ν, which itself depends on the mobility μ and the electric field F:

$$j = en\nu = en\mu F\,, \tag{2.9}$$

where e is the electric charge. The intrinsic density of charge carriers in a semiconductor is $n_\mathrm{i} = N_0 \exp(-E_\mathrm{g}/2k_\mathrm{B}T)$ with N_0 being the density of molecules for organic semiconductors, E_g is the energy gap, k_B Boltzmann's constant and T the temperature. With typical values of $N_0 = 10^{21}$ – $10^{22}\,\mathrm{cm}^{-3}$ and $E_\mathrm{g} \approx 2.5\,e\mathrm{V}$ we do have an insulating material unusable for electrical circuits, as this corresponds to about one electric charge per cubic-centimeter, $n_\mathrm{i} \approx 1\,\mathrm{cm}^{-3}$ at $T = 300\,\mathrm{K}$ (for comparison: for Si with $E_\mathrm{g} = 1.12\,e\mathrm{V}$ and $N_0 = 10^{19}\,\mathrm{cm}^{-3}$ it is $n_\mathrm{i} \approx 4 \cdot 10^{9}\,\mathrm{cm}^{-3}$). Therefore, it is necessary to create a high enough charge carrier density in the organic material: either by injection from electrodes (OLEDs), or by photogeneration (absorption of light in OPVCs), or by the field effect (OFETs). In the last few years also (electro)chemical doping of injection layers has been introduced[23], which is more and more becoming a standard technique to tailor injection properties.

2.4.1. Charge carrier injection

A schematic energy level diagram for an organic material is shown in fig. 2.10. Similar to inorganic semiconductors, the energy difference between HOMO (valance band in inorganic semiconductors) and vacuum level defines the ionization potential IP, i.e., the energy required to remove an electron. The difference between LUMO (conduction band in inorganic semiconductors) and vacuum level is called the electron affinity χ and between the Fermi level E_F and vacuum level the work function $\varPhi$. The energy gap E_g is defined by the positions of HOMO and LUMO. If the organic material comes into contact with a metal, which corresponds to the Mott-Schottky case for inorganic semiconductors, one assumes vacuum level alignment and band bending in the space charge layer to achieve Fermi level alignment (fig. 2.11). However, it has been shown that vacuum level alignment is often not achieved in organic/metal interfaces due to the formation of interface dipoles[24,25], which induce a vacuum level shift Δ that can be as high as $1\,e\mathrm{V}$ (see right side of fig. 2.11)[26]. There are several possible origins of these dipoles, e.g., charge transfer across the interface, redistribution of the probability density of the electrons, interfacial chemical reactions, and other types of rearrangement of electronic charge[24].

The hole and electron injection barriers (HIB and EIB), $\varPhi_\mathrm{h}$ and $\varPhi_\mathrm{e}$, respectively, are then defined as follows:

$$\varPhi_\mathrm{h} = \mathrm{HOMO} - \varPhi_\mathrm{a} - \Delta_\mathrm{a} \tag{2.10}$$

$$\varPhi_\mathrm{e} = \varPhi_\mathrm{c} + \Delta_\mathrm{c} - \mathrm{LUMO}\,, \tag{2.11}$$

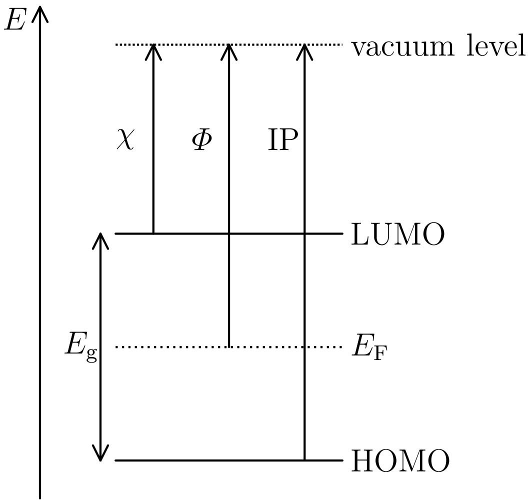

Figure 2.10.: Energy level diagram showing the HOMO and LUMO of an organic semiconductor, the corresponding band gap E_g, the electron affinity χ, the work function $\varPhi$, and the ionization potential IP.

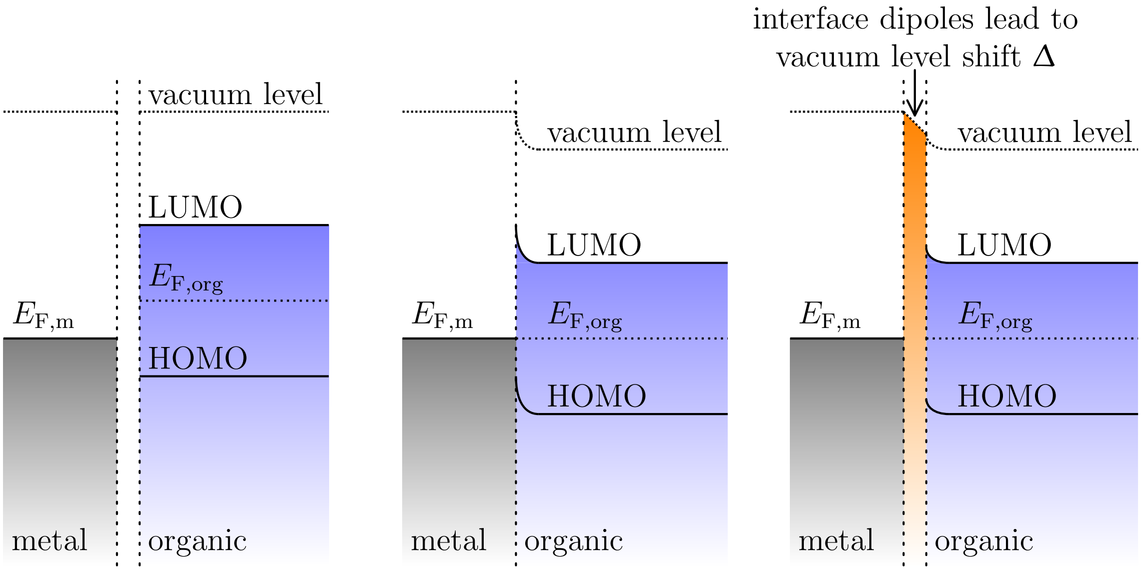

Figure 2.11.: Left: energy levels in a metal and organic semiconductor before contact. Middle: metal and organic semiconductor in contact: vacuum level alignment and band bending to achieve Fermi level alignment. Right: vacuum level shift Δ due to interface dipoles.

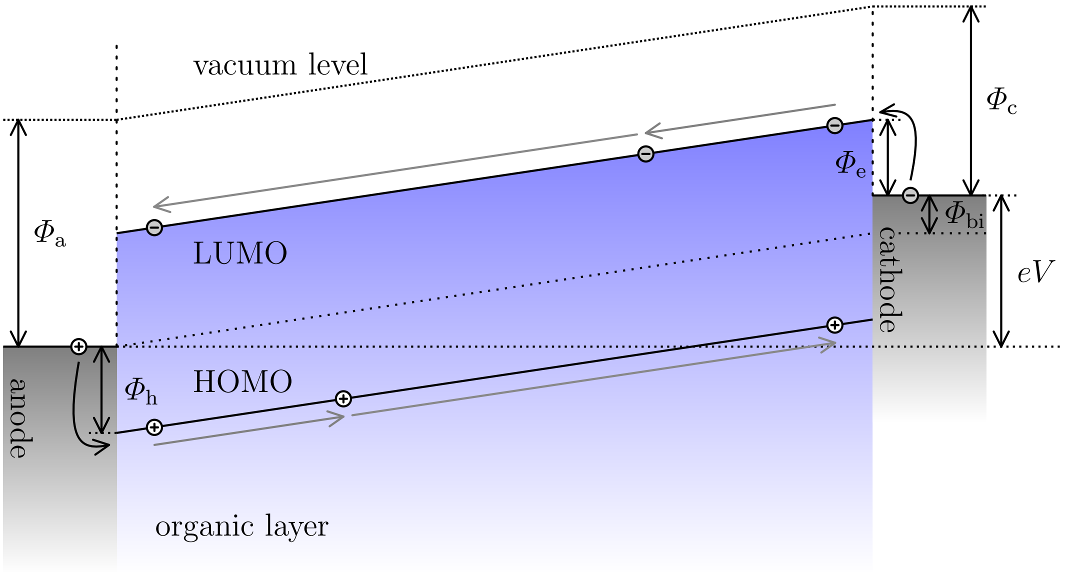

Figure 2.12.: Simplified energy level diagram: injection of excess charge carriers from electrodes into an organic material at an applied bias voltage V with hole and electron injection barriers Φ_h and Φ_e, respectively (for better visibility, the barriers are set rather large for these kind of schematic diagrams and do not represent the real energetic situation inside the device). The energy barriers are determined by the difference of the work function of the electrodes (Φ_a and Φ_c, respectively), the energy levels of the corresponding molecular orbitals (HOMO and LUMO) and a shift in vacuum level Δ due to dipole layer formation at the interfaces (not plotted here), respectively. The difference in the work functions of the electrodes defines the built-in potential $\Phi_{bi} = \Phi_a - \Phi_c = eV_{bi}$. To inject charge carriers, the external bias V must be greater than the built-in voltage V_{bi}, i.e., $V > V_{bi}$.

where Φ_a and Φ_c are the work functions of the anode and cathode, respectively, and Δ_a and Δ_c the corresponding vacuum level shifts. Conventionally, a positive value Δ denotes a rise in vacuum level. To minimize the HIB and EIB, the injection of excess charge carriers into OLEDs requires electrode materials with a work function similar to the HOMO (hole injection) or LUMO (electron injection) of the organic material, respectively. Charge carrier injection into an organic thin film from two electrodes with external bias voltage V is depicted in a simplified energy level diagram in fig. 2.12.

An important quantity for charge carrier injection and transport is the built-in potential Φ_{bi}, or its equivalent, the built-in voltage $V_{bi} = \Phi_{bi}/e$. It is a consequence of the different work functions of the electrodes, Φ_a and Φ_c, respectively, and vacuum and Fermi level alignment:

$$\Phi_{bi} = \Phi_a - \Phi_c \,. \tag{2.12}$$

For non-vanishing built-in potential, e.g., $\Phi_a > \Phi_c$ the HOMO and LUMO are in the reverse bias condition, i.e., holes (electrons) are not transported from the anode (cathode) to the cathode (anode). An external bias voltage $V = V_{bi}$ has to be applied to compensate the reverse band-bending. For charge transport, HOMO and LUMO have to be bent in the opposite direction (see fig. 2.12), which requires $V > V_{\mathrm{bi}}$.

2.4.2. Charge transport and its temperature dependence

For a current of one charge carrier species (unipolar current) and for vanishing injection barriers, the current density in an organic solid is space charge limited (SCLC, space charge limited current) and follows the equation of Mott-Gurney[16]:

$$j = \frac{9}{8} \varepsilon_{\mathrm{r}} \varepsilon_0 \mu \frac{V_{\mathrm{org}}^2}{d^3} , \tag{2.13}$$

where ε_{r} is the relative dielectric constant of the organic material, ε_0 is the permittivity of free space, μ as before the mobility, $V_{\mathrm{org}} = V - V_{\mathrm{bi}}$ the voltage drop at the organic layer, and d its thickness. For typical values used in OLEDs, $j = 10\,\mathrm{mA/cm}^2$, $\varepsilon_{\mathrm{r}} = 3.5$, $V_{\mathrm{org}} = 5\,\mathrm{V}$, and $d = 100\,\mathrm{nm}$, one calculates a necessary mobility of the order of $\mu \approx 10^{-6}\,\mathrm{cm}^2/\mathrm{Vs}$. This is a pretty low value compared to inorganic semiconductors like silicon (amorphous: $\mu \approx 1\,\mathrm{cm}^2/\mathrm{Vs}$, polycrystalline: $\mu \approx 10^2\,\mathrm{cm}^2/\mathrm{Vs}$, crystalline: $\mu \approx 10^3\,\mathrm{cm}^2/\mathrm{Vs}$) and even for organic materials. The mobility in organic materials also depends on the degree of ordering; amorphous layers yield $\mu \approx 10^{-5}\,\mathrm{cm}^2/\mathrm{Vs}$, polycrystalline films are of the order $\mu \approx 0.1 - 1\,\mathrm{cm}^2/\mathrm{Vs}$ and molecular crystals can be grown with mobilities of the order of $10\,\mathrm{cm}^2/\mathrm{Vs}$. For OLEDs, however, charge carrier mobilities of amorphous layers are already sufficient (and are even necessary for high quantum efficiencies).

In organic crystals, band transport is the dominating transport mechanism for charge carriers, however, the conduction and valance band are only broadened a few $100\,\mathrm{m}e\mathrm{V}$ (and not several $e\mathrm{V}$ like in inorganic semiconductors) due to the weak intermolecular van-der-Waals interaction. In these crystals, it has been shown that the mobility for electrons and holes, respectively, is dependent on temperature[27]:

$$\mu \propto T^{-n} , \tag{2.14}$$

with $n = 1..3$. Later on, this dependence has also been shown in OFET devices[28].

However, the relevant transport mechanism for OLEDs is different: in the amorphous organic layers incoherent hopping transport of the charge carriers is responsible for the current, i.e., the charge carriers hop independently from one molecule or one polymer chain, respectively, to another. This hopping is thermally activated and the mobility is also depending on the electric field F, as the energy barrier in direction of the field is lowered:

$$\mu \propto \exp\left(-\frac{E_{\mathrm{a}}}{k_{\mathrm{B}}T}\right) \cdot \exp\left(\beta\sqrt{F}\right) , \tag{2.15}$$

with E_{a} being the activation energy, typically $0.3 - 0.5\,e\mathrm{V}$, and β being the field-enhancement factor. Using a disorder model with Gaussian density of states and a disorder parameter σ, which is the variance of the Gaussian distribution, it has been shown by Monte Carlo simulations that both, E_{a} and β, can be modeled with $\sigma \approx 0.1\,e\mathrm{V}$, see Bässler for details[29]. This model is usually valid for OLEDs, however, mobility studies in diodes and FETs showed that μ also depends on the charge carrier density n, especially at high densities[30]. At very low charge carrier densities, the majority of charge carriers are localized and the effective mobility is low. Increasing n fills more and more localized states and the Fermi energy moves closer to the transport energy, hence the effective mobility increases. This also can be described by a disorder model[31]. Short summaries of the hopping transport are given by Hertel and Bässler[32], and Brütting and Rieß[33].

2.5. OLED stacks, fabrication, sample structure, and basic characterization

In the previous sections the charge transport and generation of light in an OLED has been discussed. Now, this knowledge has to be used to build devices. Even though the simplest OLED consists of an emitter material embedded between two electrodes it is evident that this is not an efficient design, see fig. 2.13: holes and electrons are injected and transported through the organic material under a forward bias voltage V, where they can form an exciton and hopefully recombine radiatively. However, they can also just pass through the device without generation of light but with heat dissipation. Tang's OLED was already a two-layer-design, consisting of a diamine layer and an Alq_3 layer[8]. The respective qualitative energy level diagram is shown in fig. 2.14. As the position of the HOMO is very close to the work function of the anode, holes can be injected into the diamine, which as a consequence acts as hole transporting layer (HTL). The LUMO of Alq_3 is close to the work function of the cathode enabling injection and transport of electrons: Alq_3 acts as electron transporting material (ETL). Holes and electrons are transported to the diamine/Alq_3 interface. As the HOMO and LUMO of both materials are different, holes and electrons are blocked at the interface, increasing the probability of forming a radiative exciton. In this case, Alq_3 is also the emission layer (EML), however, the generation of light takes place at the HTL/ETL interface and very few nanometers into the Alq_3.

This already shows that for highly efficient OLEDs the organic materials have to be chosen wisely with respect to their HOMO and LUMO energy levels. Recent high efficiency OLEDs consist of several different organic layers, each especially suited for a particular purpose. Such an OLED could be composed like this: anode, hole injection layer (HIL), hole transporting layer (HTL), electron blocking layer (EBL), emission layer (EML, usually a dye as dopant in a supporting matrix), hole blocking layer (HBL), electron transporting layer (ETL), electron injection layer (EIL), and finally a cathode (fig. 2.15). The purpose of these layer combinations is to inject the charge carriers easily, transport them to the EML and then confine the generation of excitons and with that the recombination to the EML. The blocking layers are used for the confinement of excitons and for low leakage currents, which otherwise can decrease the OLED's efficiency. The use of doped injection layers reduces the injection barriers for charge carrier injection from the electrodes into the organic layers and gains more and more importance for efficient OLED designs. Usually, fewer materials are used in the OLED stack, as some materials serve two or more purposes. Alq_3, for example,

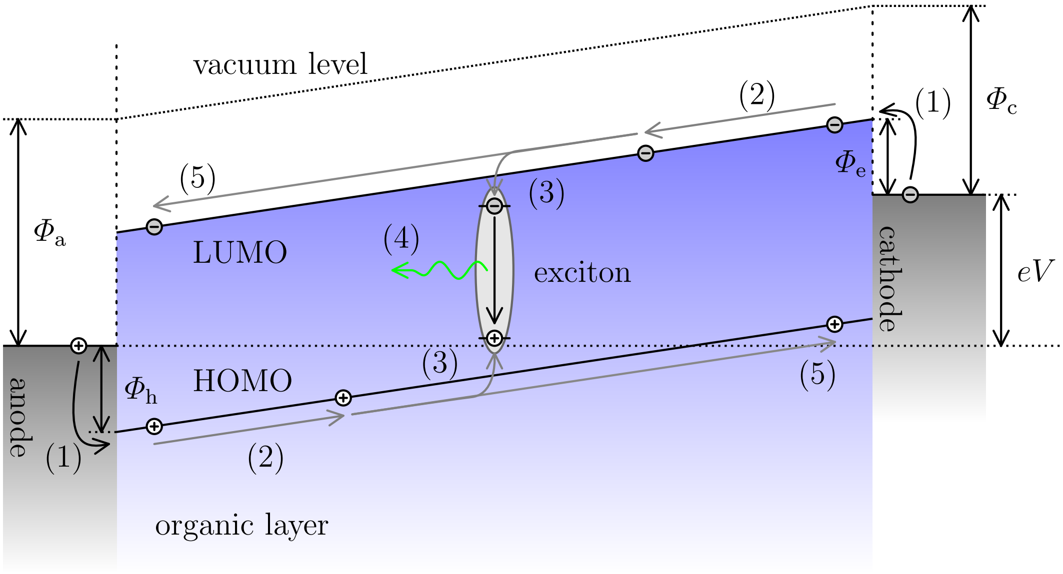

Figure 2.13.: Simplified energy level diagram for an OLED consisting of only one organic layer. (1) charge carrier injection, (2) charge carrier transport, (3) exciton formation, (4) exciton decay / radiative recombination, (5) leakage current.

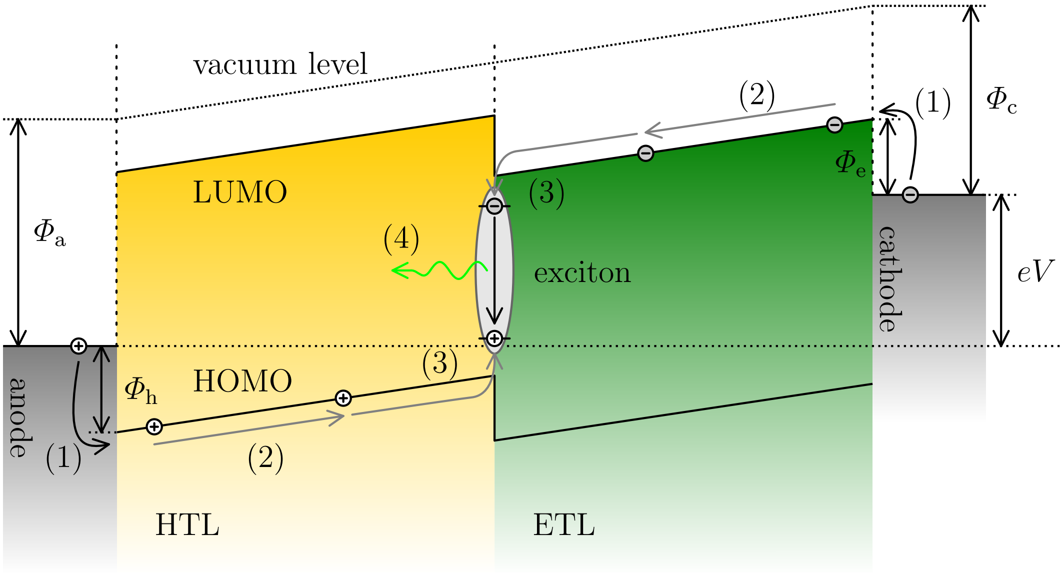

Figure 2.14.: Simplified energy level diagram for an OLED consisting of two organic layers, e.g., a diamine as hole transporting layer (HTL) and Alq_3 as electron transporting layer (ETL) as in reported by Tang et al.[8]. (1) charge carrier injection, (2) charge carrier transport, (3) exciton formation, (4) exciton decay / radiative recombination. Charge carriers are blocked at the HTL/ETL interface due to barriers as a result of differences in the HOMOs (for holes) and LUMOs (for electrons).

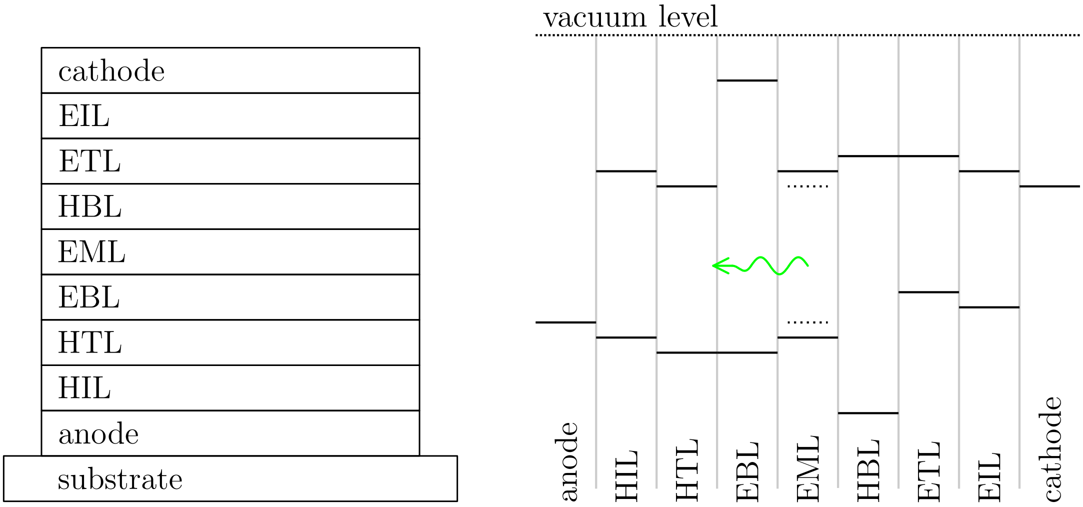

Figure 2.15.: Left: High efficient OLED stack composed of various layers, each having its specific purpose: hole injection layer (HIL), hole transporting layer (HTL), electron blocking layer (EBL), emission layer (EML, usually a dye as dopant in a matrix), hole blocking layer (HBL), electron transporting layer (ETL), electron injection layer (EIL). Right: Schematic HOMO and LUMO energy levels. Energy levels of the dye in the EML indicated with dashed lines.

can serve as electron transporting material and emission material as in Tang et al.[8]. On the other hand, there can even be more layers, e.g., in OLEDs which have more than one emission layer. So called ‘stacked’ OLEDs are in principle several OLEDs on top of each other. They can either be monochrome, increasing the current efficiency: at the same driving current density the luminance (and the necessary driving voltage) roughly scales with the number of stacked OLEDs until a trade off is reached[34]; or can be used for color mixing (red, green, and blue emitter materials) and therefore for efficient white light emitting OLEDs[35].

As cathodes usually metals like calcium, aluminum, and silver, or mixtures of Mg:Ag are used, as these have a low work function and are, therefore, suited for electron injection. For hole injection, materials with high work function, like gold or certain oxides, have to be used. Usually, as the light generated inside an OLED has to be coupled out through one of the electrodes, ITO (indium tin oxide) is used as transparent, conductive oxide, having a high work function. This is usually used in the so called ‘bottom-emitting OLED’ (fig. 2.16), consisting of a transparent substrate, usually glass, ITO, organic layers, and a reflecting metal cathode: the generated light leaves the device through ITO and the substrate on the ‘bottom’ side. ‘Top-emitting OLEDs’ (fig. 2.17) are not so common as a transparent, yet conductive layer has to be deposited on top of the organic layers. This can be achieved by thin metal films or the use of ITO, however, the latter is deposited using sputtering techniques, damaging the organic layers. However, the substrate in this case is rather arbitrary. Both OLED types can be designed as ‘microcavity OLEDs’, i.e., both electrodes consist of metals (one actually being thin enough to be semi-transparent). This leads to different optical behavior as will be shown later.

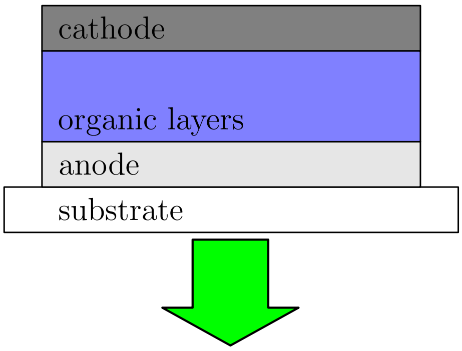

Figure 2.16.: Bottom-emitting OLED with transparent anode and opaque cathode.

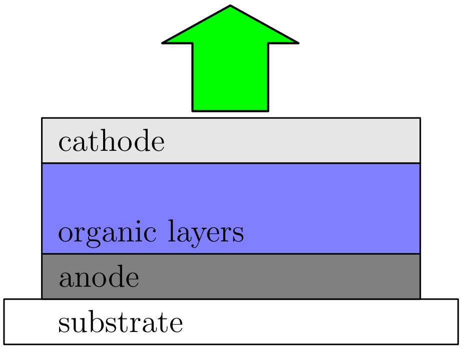

Figure 2.17.: Top-emitting OLED with opaque anode and semi-transparent cathode.

The way of how OLEDs are fabricated depends on the materials which are used. In principle, two deposition techniques can be used: evaporation in high vacuum, and deposition from solution, either by spin-coating techniques, printing, or doctor-blading. Using solutions, usually with polymer materials, can only be used for simpler OLED structures (meaning only few organic layers) as they require orthogonal solvents, i.e., spin-coating one layer on another requires a solvent which does not dissolve the already deposited layer. However, these techniques can be very cheap and fast as no high vacuum systems are needed. As high efficiency OLEDs are in the focus of research and require the use of several layers (fig. 2.15), usually small molecule materials are used, as these are suited for evaporation. All of the OLEDs shown in this work are fabricated by evaporation.

The bottom-emitting OLED stack shown in fig. 2.18 serves as a reference design throughout this thesis. It is similar to Tang's stack[8] and contains materials which have been studied intensively. Its fabrication process is explained in the following as an example. Glass covered with 140 nm ITO is used as a substrate, where the ITO is structured by standard photolithography processes and subsequent etching in HCl. After thorough cleaning in acetone and isopropyl alcohol ultrasonication baths, the samples are dried with a nitrogen stream. All lithography and cleaning processes are carried out in a cleanroom. Oxygen plasma treatment is used to further clean the substrates, enhance the work function of ITO, and thus improve the OLED efficiency[36,37]. A 30 nm thin layer of poly(3,4)-ethylendioxythiophene doped with poly(styrene sulfonate) (PEDOT:PSS) is spincast onto the substrate as HIL and dried on a hot plate in the cleanroom. All following organic and metal layers are deposited through shadow masks in a high vacuum chamber (base pressure $< 3 \cdot 10^{-7}$ mbar) without breaking the vacuum. Organic materials are deposited using effusion cells; metals by resistive heating using boats or baskets. As HTL N,N'-diphenyl-N,N'-bis(3-methylphenyl)-1,1'-biphenyl-4,4-diamine (TPD) with a thickness of 80 nm is used. The ETL and EML is Alq_3 with a thickness of 80 nm. As cathode aluminum on top of calcium is used.

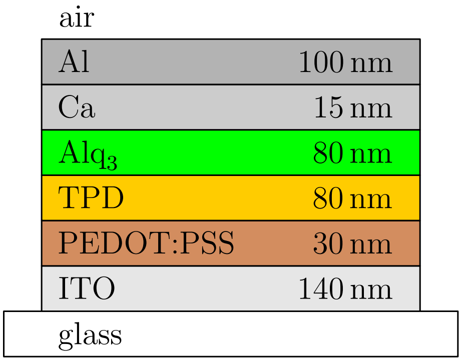

Figure 2.18.: Bottom-emitting OLED stack used as reference device. ITO with PEDOT:PSS (HIL) as anode, TPD as HTL, Alq_3 as ETL and EML, and Ca/Al as cathode.

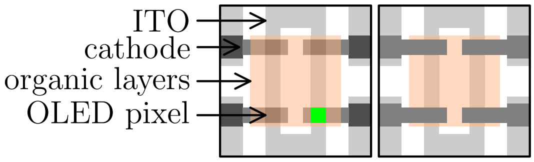

Figure 2.19.: Sample structure for the devices prepared in Augsburg. Left: view through the bottom-side (substrate). Right: view from the top-side. Glass substrate with 20 mm × 20 mm. OLED pixel defined by overlap of ITO and cathode, 2 mm × 2 mm, one pixel illustrated to emit green light.

A representation of the sample structure is shown in fig. 2.19. Please note that the organic materials are evaporated on a large area, however, the actual OLED pixel is just defined by the area where ITO and the metal cathode overlap (separated by the organic materials). The active OLED pixels for the samples prepared in Augsburg are square-sized with an area of $A = 2\,\mathrm{mm} \times 2\,\mathrm{mm}$.

The evaporation system used for the samples prepared in Augsburg contains six effusion cells for organic materials and three places for thermal evaporation of metals. After modification of the vacuum chamber by the author of the present thesis (installation of several quartz microbalances for evaporation rate controlling and development of a Labview monitoring program) it is possible to evaporate two organic materials simultaneously for the purpose of doping: the evaporation rates for both materials are monitored independently by using separate quartz microbalances.

A very basic and yet very simple measurement for OLEDs are current density – voltage ($j - V$) characteristics as it directly shows if the device is working properly and gives a first impression on its quality. A bias voltage sweep is applied to the device and its current response is recorded. Furthermore, the intensity of the generated light can be recorded simultaneously, e.g., by means of a photodiode. Using, e.g., a suitable, calibrated photodiode, which mimics the eye's wavelength dependent sensitivity, the light intensity correlates to the luminance L (please see the next chapter for details). The corresponding measurement is called current density – voltage – luminance ($j - V - L$) characteristics. Usually, the OLEDs prepared in Augsburg are characterized in a light-tight measurement box inside the glovebox system (no encapsulation of the devices is required) with a Keithley 2612 dual-source-measurement-unit. For the purpose of these $j - V - L$ measurements, a Labview program has been implemented for automatic recording of all relevant data, including the temperature inside the measurement box. Typically, the voltage is varied from reverse bias condition, e.g., $V_{\mathrm{min,typ}} = -4\,\mathrm{V}$, to a positive bias above the built-in voltage, e.g., $V_{\mathrm{max,typ}} = 8\,\mathrm{V}$. The step size in voltage (ΔV) should be small ($\Delta V_{\mathrm{typ}} = 0.1\,\mathrm{V}$) and a delay between change in voltage and measurement of the current should be applied ($\Delta t_{\mathrm{typ}} = 2\,\mathrm{s}$): charging or discharging effects of the capacitive organic layers would otherwise yield a too high current. In other words, one should wait for quasi-static conditions in the current before measuring the current. To protect the devices from harmful currents, which lead to Joule heating and degradation effects, a current limit can be set within this program. A measurement cycle typically involves a sweep from negative to positive bias and back, however, for some OLEDs it can be useful to start at positive bias and/ or neglect the negative bias regime.

A typical current density – voltage – luminance measurement for the reference OLED stack is shown in fig. 2.20. The current in the bias regime below the built-in voltage V_{bi} is relatively small as no charge carrier injection is anticipated. Therefore, this kind of current is also called ‘leakage current’, which is almost symmetrical for negative and positive bias (approximately ohmic behavior). However, for increasing bias, starting at $V_{\mathrm{bi}} \approx 2.3\,\mathrm{V}$ (dashed line in fig. 2.20), the current density strongly increases. Concurrently, the OLED starts to emit light which is registered by the photodiode (above a certain threshold given by its dark current). Thus, the increase in current and luminance shows that at bias voltages above V_{bi} both, holes and electrons, are injected into the device. This device characterization measurement indicates the quality of the OLEDs and their fabrication process: the leakage current should be as low as possible, the built-in potential should be low (however, it is determined by the choice of electrode materials), and the rise in current and luminance should preferably be very steep.

2.6. Perception of light

For the design of OLEDs, it is beneficial to have some knowledge on how we humans perceive light and interpret its ‘color’. An extensive treatment can be found in the book of Wyszecki and Stiles[38], or to some extent in the book of Schubert[19].

Generally, there are two categories of photophysical units: radiometric (physical properties) and photometric (as perceived by the eye). Radiometric units are, e.g., the number of photons, photon energy, and radiant flux (optical power). A photometric quantity is the ‘luminous intensity’, which represents the light intensity of a light source as perceived by the human eye. It is measured in candela (cd), a base unit in the SI system, defined as follows[19]: *a monochromatic light source emitting an optical power of* (1/683) W *at* 555 nm *into the solid angle of* 1 sr *has a luminous intensity of* 1 cd.

The ‘luminous flux’, light power as perceived by the eye, is measured in lumen (lm) and defined as[19]: *a monochromatic light source emitting an optical power of* (1/683) W *at* 555 nm *has a luminous flux of* 1 lm. This means that 1 cd equals 1 lm/sr. An isotropic emitter with a luminous intensity of 1 cd thus has a luminous flux of 4π lm.

The ‘illuminance’ is the luminous flux incident per unit area, measured in lux, i.e.,

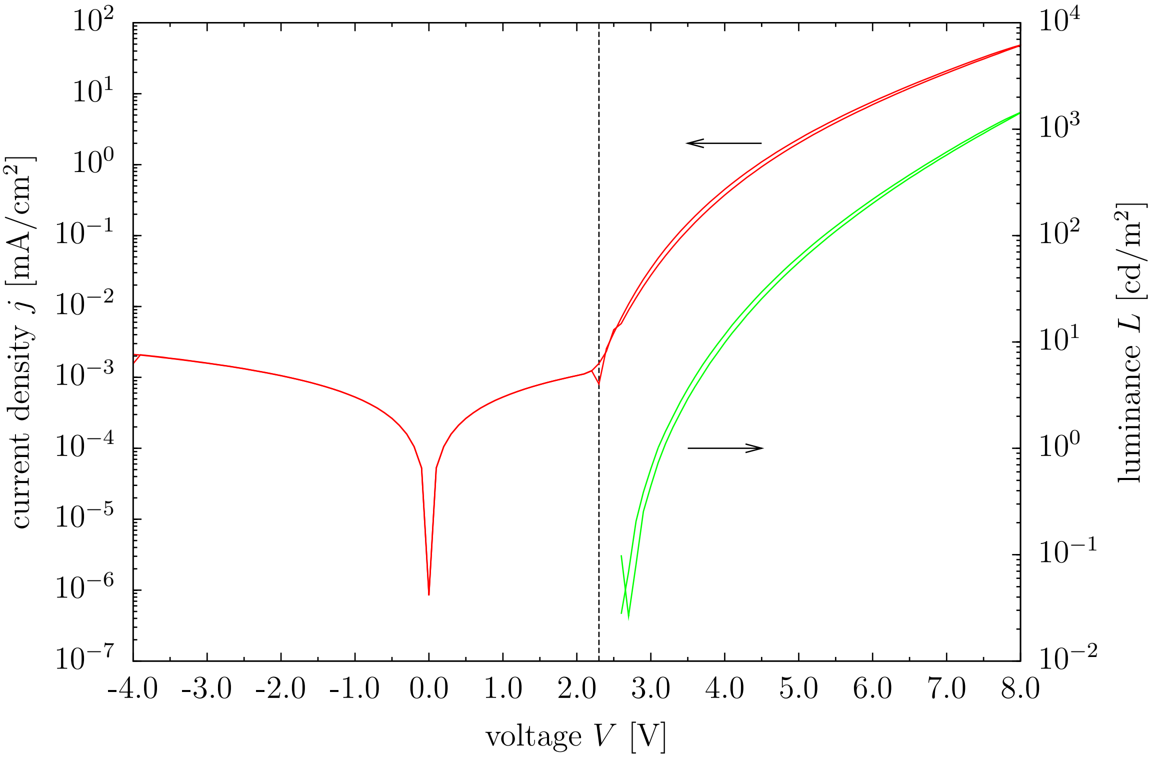

Figure 2.20.: Current density – voltage – luminance ($j - V - L$) characteristic of the reference OLED (fig. 2.18). Below $V_{\mathrm{bi}} \approx 2.3\,\mathrm{V}$ (dashed line): almost symmetrical leakage current. Above V_{bi}: strong increase in current density; the OLED starts to emit light.

$1\,\text{lux} = 1\,\text{lm/m}^2$.

The 'luminance' of a surface source (e.g., an OLED) is the ratio of the luminous intensity in a certain direction (under the angle θ measured against the normal vector of the surface) divided by the projected surface area in that direction ($A \cdot \cos\theta$). Thus, the unit is $1\,\text{cd/m}^2$, which often is called 1 nit. An example for current density – voltage – luminance characteristics of an OLED has already been shown in fig. 2.20. For display applications, a luminance of $300 - 500\,\text{cd/m}^2$ is fairly sufficient, however, for lighting applications higher values are needed. Often $L = 1000\,\text{cd/m}^2$ is used in benchmarks.

A summary of radiometric and photometric units can be found in table 2.1. The conversion between them is given by the eye sensitivity function $V(\lambda)$ (or luminous efficiency function). The eye's sensitivity has a maximum at $\lambda = 555\,\text{nm}$ (in photopic vision, i.e., at ambient light levels) and falls off to both sides, showing the observable wavelength range to be about $380\,\text{nm} \leqslant \lambda \leqslant 780\,\text{nm}$, see fig. 2.21. This figure shows two sensitivity curves*, the 'CIE 1931 $V(\lambda)$ function', which is used as standard, and the 'CIE 1978 $V(\lambda)$ function', which is more accurate, however, not the standard[19]. CIE is the 'Commission Internationale de l'Eclairage', managing standardization in color science. Also shown is the 'luminous efficacy (of optical radiation)' (or 'luminosity function'), which is the luminous flux $\varPhi_{\text{lum}}$ divided by the optical power P of the light source:

$$\text{luminous efficacy} = \frac{\varPhi_{\text{lum}}}{P}\,. \tag{2.16}$$

Thereby, the luminous flux is

$$\varPhi_{\text{lum}} = 683\,\frac{\text{lm}}{\text{W}} \cdot \int_\lambda V(\lambda)P(\lambda)\mathrm{d}\lambda\,, \tag{2.17}$$

where $P(\lambda)$ is the light power emitted per unit wavelength, which defines the optical power

$$P = \int_\lambda P(\lambda)\mathrm{d}\lambda\,. \tag{2.18}$$

The luminous efficacy is also shown in fig. 2.21 for a strictly monochromatic light source ($\Delta\lambda \to 0$).

As the sensation of 'color' is, to some extent, a subjective quantity, there exist standardized measurements of color by means of color-matching functions and the chromaticity diagram. The human eye uses three different types of cones, red, green, and blue, to differentiate color. Therefore, three color-matching functions, $\overline{x}$, $\overline{y}$, and $\overline{z}$, are needed. They reflect that color vision possesses trichromacy, i.e., any color can be described by three variables. There are different versions of the color-matching functions, the ones shown in fig. 2.22 are the CIE 1931 functions for the standard 2° observer, as these are used as standard[19].

---

[*] The data for all sensitivities and stimulus values shown in this thesis are tabulated in the books of Wyszecki and Stiles, and Schubert[19,38], or can be found on a detailed website[39].

radiometric unit	**dimension**	**photometric unit**	**dimension**
radiant flux (optical power)	W	luminous flux	lm
radiant intensity	$\frac{\mathrm{W}}{\mathrm{sr}}$	luminous intensity	$\frac{\mathrm{lm}}{\mathrm{sr}} = \mathrm{cd}$
irradiance (power density)	$\frac{\mathrm{W}}{\mathrm{m}^2}$	illuminance	$\frac{\mathrm{lm}}{\mathrm{m}^2} = \mathrm{lux}$
radiance	$\frac{\mathrm{W}}{\mathrm{sr} \cdot \mathrm{m}^2}$	luminance	$\frac{\mathrm{lm}}{\mathrm{sr} \cdot \mathrm{m}^2} = \frac{\mathrm{cd}}{\mathrm{m}^2}$

Table 2.1.: Radiometric (physical properties) and corresponding photometric units (as perceived by the eye).

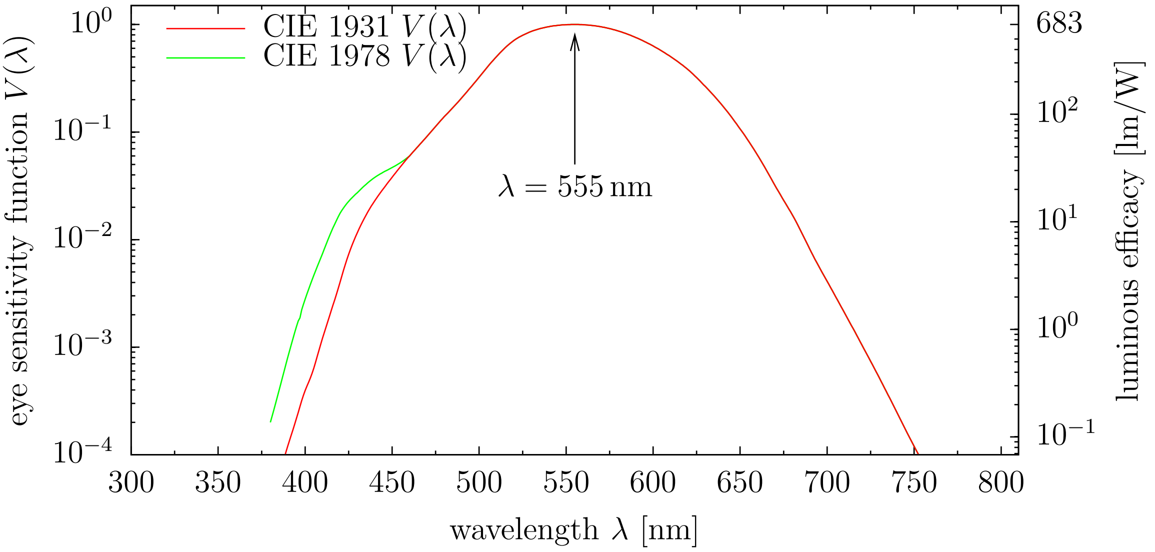

Figure 2.21.: Sensitivity $V(\lambda)$ of the human eye (photopic vision, standard 2° observer) after CIE 1931 (red line, used as standard) and CIE 1978 (green line). Maximum sensitivity at $\lambda = 555\,\mathrm{nm}$ is defined as 1. Right axis: luminous efficacy for a strictly monochromatic source ($\Delta\lambda \to 0$), see eq. (2.16) – (2.18).

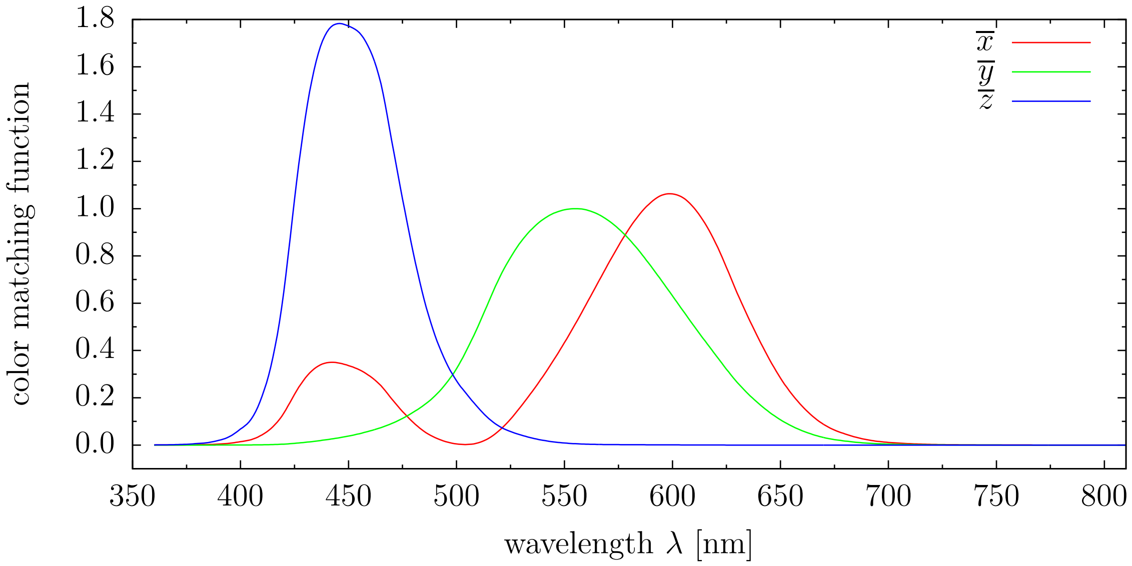

Figure 2.22.: CIE 1931 color-matching functions $\overline{x}$ (red), $\overline{y}$ (green), and $\overline{z}$ (blue) for the standard 2° observer.

With the color-matching functions the 'tristimulus values' X, Y, and Z can be calculated:

$$X = \int_\lambda \overline{x}(\lambda)P(\lambda)\mathrm{d}\lambda\,, \tag{2.19}$$

$$Y = \int_\lambda \overline{y}(\lambda)P(\lambda)\mathrm{d}\lambda\,, \tag{2.20}$$

$$Z = \int_\lambda \overline{z}(\lambda)P(\lambda)\mathrm{d}\lambda\,. \tag{2.21}$$

They give the power (stimulation) of each of the primary red, green, and blue lights needed to match the color of the given power-spectral density $P(\lambda)$[19]. Usually they are given dimensionless. With these, the 'chromaticity coordinates' x, y, and z are given as

$$x = \frac{X}{X+Y+Z}\,, \tag{2.22}$$

$$y = \frac{Y}{X+Y+Z}\,, \tag{2.23}$$

$$z = \frac{Z}{X+Y+Z} = 1 - x - y\,. \tag{2.24}$$

Thus, it is sufficient to describe the color of a light source with the two chromaticity values x and y. As the CIE XYZ color space is designed in such a way that Y is the measure of luminance of a color, the derived color space is also known as 'CIE xyY color space'[40].

The chromaticity coordinates are usually pictured in the chromaticity diagram, see fig. 2.23. The outline, the 'spectral locus', is described by monochromatic light

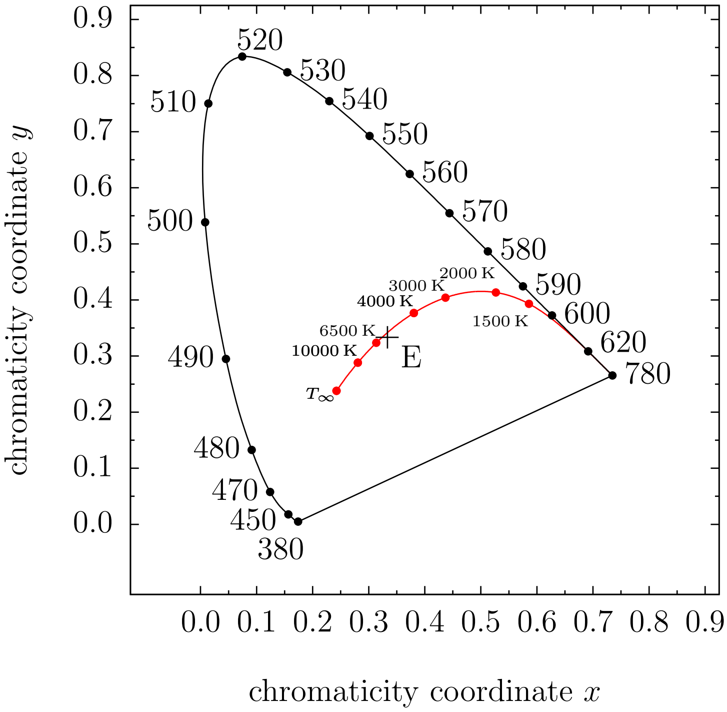

Figure 2.23.: CIE 1931 chromaticity diagram (standard 2° observer). Monochromatic colors are at the outline ('spectral locus', numbers are wavelength λ in [nm]); white light around the equal energy point E at $(x\,,\,y) = (1/3\,,\,1/3)$. All possible colors are within this 'horseshoe'. Additionally, the Planckian locus for ideal black body radiators at different temperatures T is shown as a red line.

sources. All colors are within this so-called 'horseshoe'. The equal-energy point E at $(x\,,\,y\,,\,z) = (1/3\,,\,1/3\,,\,1/3)$ in the center of the chromaticity diagram corresponds to an optical spectrum with constant spectral distribution, which is pure white light. White light with its nuances (cool-white, warm-white, etc.) is thus located close to this value.

2.7. Characterization of OLEDs

In the last chapter the photometric units have been introduced. With these, different OLED efficiencies and benchmarks can be derived. In fig. 2.20 the $j-V-L$ characteristics of the reference OLED was already shown. The luminance L was measured using a calibrated photodiode with a filter to compensate for the sensitivity $V(\lambda)$ of the human eye. Another possibility would be to use a spotphotometer.

From the $j-V-L$ data, a benchmark value for OLEDs can be derived: the current efficiency, which is the luminance L divided by the current density j. It is obvious that its value should preferably be as high as possible. For the reference OLED the current efficiency is shown in fig. 2.24. It reaches almost 3 cd/A which is comparable

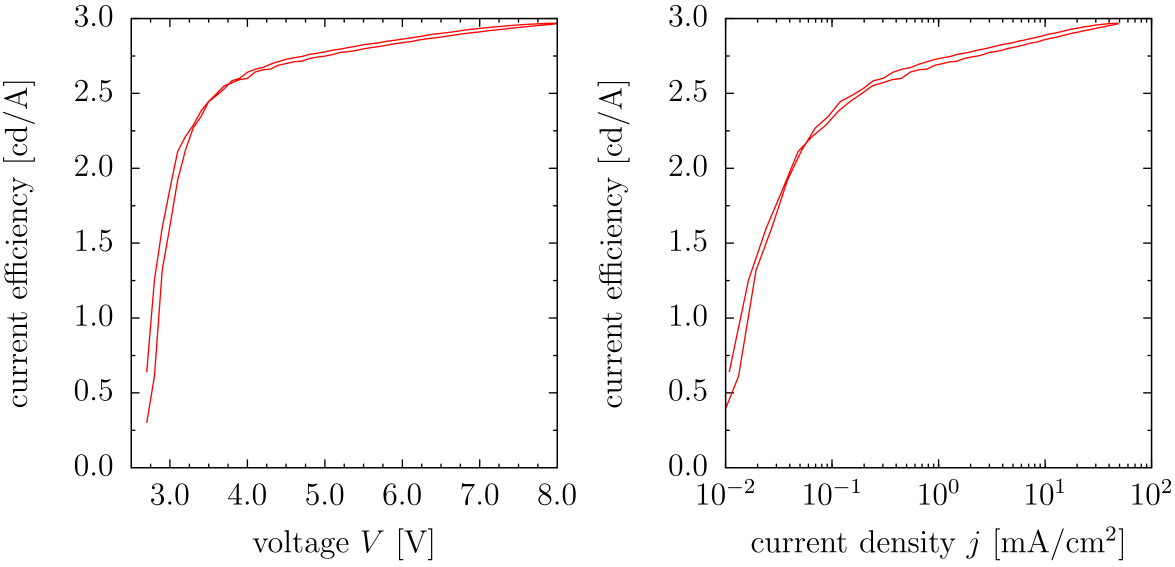

Figure 2.24.: Current efficiency of the reference OLED (stack see fig. 2.18) calculated from the $j-V-L$ characteristics (fig. 2.20). Left: versus applied voltage V. Right: versus current density j.

to values published in literature for a similar OLED stack[41]. However, this value is usually only of interest for display applications, as it uses the forward luminance (the luminance normal to the substrate).

For lighting applications, integral values like the luminous flux are more important. This is measured in integrating spheres: the OLEDs are placed inside a sphere with (preferably perfect) diffuse reflecting surface. An optical fiber which leads to a calibrated spectrometer is connected to this sphere. After calibration with a light source with known spectral intensity, e.g., a halogen lamp, which emits over the entire visible wavelength range (being an almost perfect black body radiator), the radiant and luminous flux can be measured. With this, the 'wall-plug (luminous) efficacy' can be derived, which is the ratio of luminous flux Φ_{lum} and the electrical power P_{el} consumed by the light source. It is also given in lm/W and must not be mistaken for the luminous efficacy which relates luminous flux and the optical power (radiant flux). Detailed instructions on the measurement procedures and what numbers to report in order to obtain comparable values in different labs can be found in a white paper of the OLLA project[42]. The ratio of optical power P and electrical power P_{el} needed to produce this optical power directly yields the efficiency of the device in converting electricity to light.

Photoluminescence quantum efficiencies of dyes are also measured in integrating spheres. Hereby, the dye usually is excited with a laser beam or a LED, preferably with a wavelength which matches the absorption maximum of the dye. For accurate determination of PL quantum efficiencies, three measurements are needed: one to obtain the intensity of the light source, one to obtain the absorption and emission of the sample, and one to correct the absorption and emission as light reflected at the

Figure 2.25.: Setup for recording angular emission spectra of OLEDs, optionally with distinction of s- and p-polarization. OLED is placed on computer controlled rotary stage. Light emitted under angle θ passes the optional polarizer and is collimated to an optical fiber leading to a calibrated spectrometer.

sphere is also absorbed and re-emitted by the sample. The measurement procedure is described in detail by de Mello et al.[43].

The integral measurements are useful when describing efficacies and efficiencies of OLEDs. However, the OLEDs' angular characteristics are also important, as the luminance and color impression usually is different when looking at the OLEDs' surfaces at different angles. Therefore, angular emission spectra are recorded: an OLED is placed on a computer controlled rotary stage. If additionally outcoupling structures are attached to the OLED's substrate, the substrate modes can be investigated. Light emitted from the OLED at a given angle passes an optional polarizer (allowing the distinction between s- and p-polarization), then it is focused by a collimator lens and coupled into an optical fiber, which leads to a calibrated CCD spectrometer (fig. 2.25). The spectrum is recorded for this angle, then the computer program automatically moves the rotary stage forward to the next angle and so on. Building the angular emission spectra setup and the corresponding Labview program was also one task of the author of the present thesis.

3. Interaction of light with matter

3.1. Electromagnetic waves

In previous chapters, absorption and emission of light in an organic semiconductor has been discussed. Here, a short introduction to the physical background of ‘light’, which is electromagnetic waves, shall be given. Maxwell’s equations relate electric and magnetic fields to their sources. Assuming there is no current or electric charge, the Maxwell equations in an isotropic, non-conducting material in their differential form are:

$$\vec{\nabla} \cdot \varepsilon \vec{E} = 0\,, \tag{3.1}$$

$$\vec{\nabla} \cdot \vec{B} = 0\,, \tag{3.2}$$

$$\vec{\nabla} \times \vec{E} = -\frac{\partial \vec{B}}{\partial t}\,, \tag{3.3}$$

$$\vec{\nabla} \times \vec{B} = \mu\varepsilon \frac{\partial \vec{E}}{\partial t}\,. \tag{3.4}$$

Herby, $\vec{E}$ is the electric and $\vec{B}$ the magnetic field, respectively. The permeability $\mu = \mu_r \mu_0$ depends on the material, where μ_r is the relative permeability and μ_0 the permeability of free space. The same is true for the permittivity $\varepsilon = \varepsilon_r \varepsilon_0$, with ε_r being the relative permittivity and ε_0 the permittivity of free space. Permeability and permittivity of free space, respectively, are associated with the speed of light

$$c = \frac{1}{\sqrt{\mu_0 \varepsilon_0}}\,. \tag{3.5}$$

Using the vector identity

$$\vec{\nabla} \times \left(\vec{\nabla} \times \vec{A}\right) = \vec{\nabla}\left(\vec{\nabla} \cdot \vec{A}\right) - \left(\vec{\nabla} \cdot \vec{\nabla}\right)\vec{A}, \tag{3.6}$$

two wave equations follow from the four Maxwell equations:

$$\left(\vec{\nabla} \cdot \vec{\nabla}\right)\vec{E} = \mu\varepsilon \frac{\partial^2 \vec{E}}{\partial t^2}\,, \tag{3.7}$$

$$\left(\vec{\nabla} \cdot \vec{\nabla}\right)\vec{B} = \mu\varepsilon \frac{\partial^2 \vec{B}}{\partial t^2}\,. \tag{3.8}$$

A set of solutions are of the form of sinusoidal plane waves. These solutions can be written in the form of

$$\vec{E}(\vec{r}, t) = \mathrm{Re}\left(\hat{E}_0 \cdot \exp\left[\mathrm{i} \cdot \left(\omega t - \vec{k} \cdot \vec{r}\right)\right]\right)\,, \tag{3.9}$$

$$\vec{B}(\vec{r}, t) = \mathrm{Re}\left(\hat{B}_0 \cdot \exp\left[\mathrm{i} \cdot \left(\omega t - \vec{k} \cdot \vec{r}\right)\right]\right)\,, \tag{3.10}$$

where $\hat{E}_0$ and $\hat{B}_0$ are the complex amplitude vectors of the electric and magnetic field, respectively, $\vec{k}$ is the wave vector giving the traveling direction of the electromagnetic wave and ω its angular frequency. These equations describe monochromatic plane waves. Monochromatic as they include only one frequency ω and plane as they only depend in one direction (the one of $\vec{k}$) of the space^{44}. To satisfy Maxwell's equations, it is required that the angular frequency is

$$\omega = \frac{1}{\sqrt{\mu\varepsilon}} \cdot |\vec{k}| = \frac{c}{\sqrt{\mu_r \varepsilon_r}} \cdot k \,. \tag{3.11}$$

For the case of non-magnetic, i.e., $\mu_r = 1$, and non-absorbing materials, this can also be expressed in terms of the refractive index n of the material:

$$\omega = \frac{c}{n} \cdot k \,. \tag{3.12}$$

Please note that the angular frequency ω can also be expressed in terms of the wavelength λ:

$$\omega = \frac{2\pi c}{\lambda} \,. \tag{3.13}$$

Inserting eq. (3.9) into eq. (3.1) and eq. (3.10) into eq. (3.2), respectively, it follows that $\vec{k} \cdot \vec{E} = 0$ and $\vec{k} \cdot \vec{B} = 0$: the electric and magnetic field are orthogonal to the traveling direction $\vec{k}$ of the wave:

$$\vec{k} \perp \vec{E} \,, \tag{3.14}$$

$$\vec{k} \perp \vec{B} \,, \tag{3.15}$$

as schematically illustrated in fig. 3.1. From the remaining equations it is additionally followed that

$$\vec{E} \perp \vec{B} \,, \tag{3.16}$$

$$|\vec{E}| = c \cdot |\vec{B}| \,. \tag{3.17}$$

Knowing these identities, it is sufficient to describe an electromagnetic plane wave with one equation, e.g.,

$$\vec{E}(\vec{r}, t) = \hat{E}_0 \cdot \exp\left[\mathrm{i} \cdot \left(\omega t - \vec{k} \cdot \vec{r}\right)\right] \,, \tag{3.18}$$

without implicitly noting the use of the real part, as it is evident that $\vec{E}$ and $\vec{B}$ have to be real.

The energy flux of an electromagnetic field is represented by Poynting's vector:

$$\vec{S} = \frac{1}{\mu_0} \cdot \vec{E} \times \vec{B} \,. \tag{3.19}$$

Using the above derived identities for plane waves, it is obvious that $\vec{S}$ and $\vec{k}$ point in the same direction, $\vec{S} \parallel \vec{k}$. Therefore, $\vec{S}$ is also orthogonal to the electric and magnetic

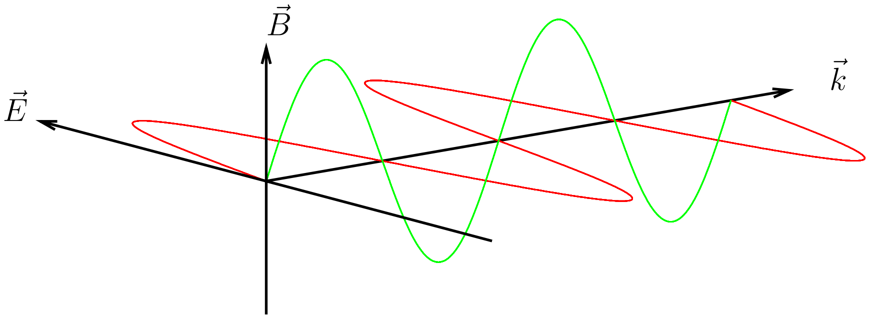

Figure 3.1.: Monochromatic electromagnetic plane wave traveling in direction $\vec{k}$. $\vec{k} \perp \vec{E}$, $\vec{k} \perp \vec{B}$, $\vec{k} \parallel \vec{S}$ as $\vec{S} = \frac{1}{\mu_0} \cdot \vec{E} \times \vec{B}$.

field, respectively. The time-averaged magnitude of Poynting's vector, $\langle\vec{S}\rangle$, also called irradiance or intensity I, can be calculated as

$$\langle\vec{S}\rangle = \frac{\varepsilon_0 c}{2} \cdot |\vec{E}|^2 \,. \tag{3.20}$$

Another important conclusion that can be drawn from Maxwell's equations are the boundary conditions for electromagnetic radiation at an interface between two media, characterized by $\mu_{1,2}$ and $\varepsilon_{1,2}$, respectively. These properties may change abruptly, however, continuity conditions for some components of the field vectors apply, which are derived by using Gauss' theorem

$$\int_V \left(\vec{\nabla} \cdot \vec{F}\right) \mathrm{d}V = \oint_A \vec{F} \cdot \vec{n} \mathrm{d}A \tag{3.21}$$

and Stokes' theorem

$$\int_A \left(\vec{\nabla} \times \vec{F}\right) \cdot \vec{n} \mathrm{d}A = \oint_C \vec{F} \cdot \mathrm{d}\vec{l} \tag{3.22}$$

on Maxwell's equations without currents and charges (eq. (3.1) – (3.4)). Fig. 3.2 is a schematic representation of these mathematical identities; $\vec{n}$ being a normal and $\vec{t}$ being a tangential vector to the interface.

Inserting eq. (3.1) and (3.2) into eq. (3.21), respectively, it is evidently followed that

$$\vec{n} \cdot \left(\varepsilon_2 \vec{E}_2 - \varepsilon_1 \vec{E}_1\right) = 0 \,, \tag{3.23}$$

$$\vec{n} \cdot \left(\vec{B}_2 - \vec{B}_1\right) = 0 \,, \tag{3.24}$$

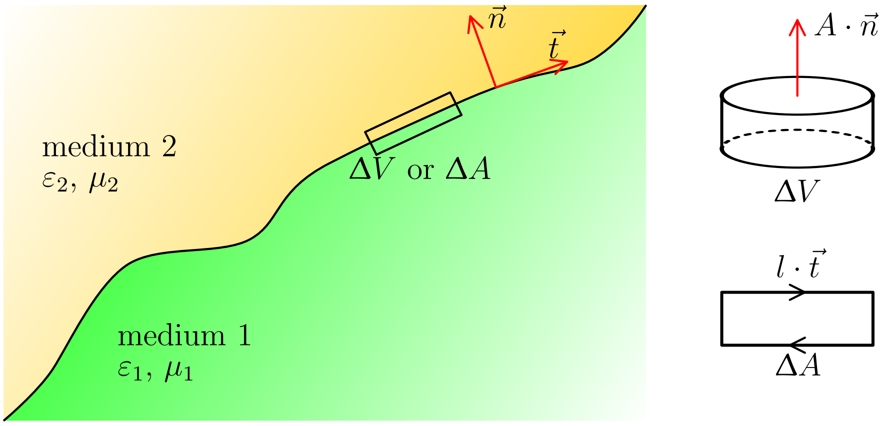

Figure 3.2.: Boundary conditions for the electromagnetic fields at an interface between medium 1 and 2 can be calculated using Gauss' and Stokes' theorem, respectively. Picture adapted from Fließbach[44].

with $\vec{E}_{1,2}$ and $\vec{B}_{1,2}$ being the electric and magnetic field in medium 1 and 2, respectively. Applying Stokes' theorem to eq. (3.3) yields

$$\int_A \left(-\frac{\partial \vec{B}}{\partial t}\right) \cdot \vec{n} \mathrm{d}A = l \cdot \vec{t} \cdot \left(\vec{E}_2 - \vec{E}_1\right) \,. \tag{3.25}$$

As the quantity $\partial \vec{B} / \partial t$ is assumed to be finite at the interface, its contribution is 0 for small ΔA like $\mathrm{d}A$[44]. As there are two independent tangential vectors $\vec{t}$ there are two conditions to be fulfilled, which can be summarized to

$$\vec{n} \times \left(\vec{E}_2 - \vec{E}_1\right) = 0 \,. \tag{3.26}$$

In an analogous way, one derives

$$\vec{n} \times \left(\frac{1}{\mu_2}\vec{B}_2 - \frac{1}{\mu_1}\vec{B}_1\right) = 0 \,. \tag{3.27}$$

In other words, the boundary conditions for electromagnetic waves at an interface between medium 1 and 2 yield that

- the normal component of the electric field is modified, $\vec{E}_{2,n} = \frac{\varepsilon_1}{\varepsilon_2} \cdot \vec{E}_{1,n}$,
- the normal component of the magnetic field is constant, $\vec{B}_{2,n} = \vec{B}_{1,n}$,
- the tangential component of the electric field is constant, $\vec{E}_{2,t} = \vec{E}_{1,t}$,
- the tangential component of the magnetic field is modified, $\vec{B}_{2,t} = \frac{\mu_2}{\mu_1} \cdot \vec{B}_{1,t}$.

3.2. The complex refractive index

The electric field $\vec{E}$ of an optical wave is felt by the electrons of the atoms in a solid and contributes to an induced dipole moment $\vec{p}$ (classical electron model[45]). This can be used to derive the atomic polarizability α, as $\vec{p} = \alpha\vec{E}$. For a non-magnetic medium, i.e., $\mu_\mathrm{r} = 1$, the complex index of refraction $\hat{N}$ is given by

$$\hat{N}^2 = 1 + \frac{N_\mathrm{a}\alpha}{\varepsilon_0}\,, \tag{3.28}$$

where N_a is the number of atoms per unit volume and ε_0 the permeability of vacuum. Using the derived atomic polarizability one obtains[45]:

$$\hat{N}^2 = 1 + \frac{N_\mathrm{a}e^2}{\varepsilon_0 m\left(\omega_0^2 - \omega^2 + \mathrm{i}\gamma\omega\right)}\,, \tag{3.29}$$

with ω_0 being the resonant angular frequency of the electron motion and γ is a damping term. If the second term is small compared to 1, the complex refractive index can be approximated to

$$\hat{N} = 1 + \frac{N_\mathrm{a}e^2}{2\varepsilon_0 m\left(\omega_0^2 - \omega^2 + \mathrm{i}\gamma\omega\right)}\,. \tag{3.30}$$

The complex refractive index $\hat{N}$ can be divided into its real and imaginary part

$$\hat{N} = n - \mathrm{i}\kappa\,, \tag{3.31}$$

where n is the refractive index and κ the extinction coefficient. Using eq. (3.30) and (3.31) this yields

$$n = 1 + \frac{N_\mathrm{a}e^2\left(\omega_0^2 - \omega\right)}{2\varepsilon_0 m\left[\left(\omega_0^2 - \omega^2\right)^2 + \gamma^2\omega^2\right]}\,, \tag{3.32}$$

$$\kappa = \frac{N_\mathrm{a}e^2\gamma\omega}{2\varepsilon_0 m\left[\left(\omega_0^2 - \omega^2\right)^2 + \gamma^2\omega^2\right]}\,. \tag{3.33}$$

If ω rises and gets closer to ω_0 the refractive index n also increases. This means n is higher for blue light than for red light. The phenomenon is called normal dispersion, $n(\omega)$, and is true for almost all transparent materials in the visible spectral range[45].

3.3. Absorption of electromagnetic waves

In eq. (3.33) the extinction coefficient κ was introduced. This represents the absorption of an electromagnetic wave. Considering a monochromatic plane wave with wavelength λ in a medium with $\hat{N} = n - \mathrm{i}\kappa$ traveling in direction z with amplitude $\vec{E}_0$, the electric field of this wave can be written as

$$\vec{E}(z) = \vec{E}_0 \cdot \exp\left[\mathrm{i}\left(\omega t - \hat{k}\cdot z\right)\right]\,, \tag{3.34}$$

where $\hat{k}$ denotes the complex wave number

$$\hat{k} = \omega \cdot \frac{\hat{N}}{c} = \frac{2\pi}{\lambda} \cdot \hat{N} \,. \tag{3.35}$$

Therefore, $\vec{E}$ yields

$$\vec{E}(z) = \vec{E}_0 \cdot \exp\left[\mathrm{i}\left(\omega t - \frac{2\pi n}{\lambda} z\right)\right] \cdot \exp\left(-\frac{2\pi\kappa}{\lambda} z\right) \,. \tag{3.36}$$

The last term is an attenuation term for the electromagnetic wave. It is referred to as absorption and is directly associated with the imaginary part of the complex refractive index $\hat{N}$. With I being the intensity of the electromagnetic wave, an absorption coefficient α can be defined as

$$\alpha = \frac{1}{I} \cdot \frac{\mathrm{d}I}{\mathrm{d}z} \,. \tag{3.37}$$

The intensity $I(z)$ at a traveled distance z is proportional to $|\vec{E}(z)|^2$ (see eq. (3.20)), which leads to the Lambert-Beer law

$$I(z) = |\vec{E}(z)|^2 = I_0 \cdot \exp\left(-\alpha z\right) \,. \tag{3.38}$$

Hereby, I_0 is the intensity at the starting point $z = 0$. Comparing this relation to eq. (3.36), it follows that the absorption coefficient is

$$\alpha = \frac{4\pi}{\lambda} \cdot \kappa \,. \tag{3.39}$$

3.4. Reflection and transmission at interfaces — the Fresnel equations

If an electromagnetic wave is incident on an interface, it will, in general, partially be reflected, and transmitted into the second medium, respectively. The existence of these two waves is a direct consequence of the boundary conditions of the field vectors. It is assumed that the incident wave is propagating with wave vector $\vec{k}_\mathrm{i}$ in medium 1 with refractive index n_1 under the angle θ_i and reaches the interface to medium 2 at $z = 0$. Part of the wave is reflected and thus propagates, still in medium 1, with wave vector $\vec{k}_\mathrm{r}$ under the angle θ_r. The transmitted part propagates in medium 2 with refractive index n_2 and wave vector $\vec{k}_\mathrm{t}$ under the angle θ_t, see fig. 3.3. For the sake of simplicity, the two media are assumed to be non-absorbing, i.e., $\kappa_{1,2} = 0$. The treatment of absorbing materials is analogous, however, the complex refractive index $\hat{N}_{1,2}$ has to be used for all calculations.

From the field amplitudes of the plane waves, $\vec{E}_\mathrm{i} \cdot \exp[\mathrm{i} \cdot (\omega t - \vec{k}_\mathrm{i} \cdot \vec{r})]$, $\vec{E}_\mathrm{r} \cdot \exp[\mathrm{i} \cdot (\omega t - \vec{k}_\mathrm{r} \cdot \vec{r})]$, and $\vec{E}_\mathrm{t} \cdot \exp[\mathrm{i} \cdot (\omega t - \vec{k}_\mathrm{t} \cdot \vec{r})]$ and the requirement that the spatial and temporal variation of all fields have to be the same at any point on the boundary $z = 0$, the following condition has always to be fulfilled[45]:

$$\left(\vec{k}_\mathrm{i} \cdot \vec{r}\right)_{z=0} = \left(\vec{k}_\mathrm{r} \cdot \vec{r}\right)_{z=0} = \left(\vec{k}_\mathrm{t} \cdot \vec{r}\right)_{z=0} \,. \tag{3.40}$$

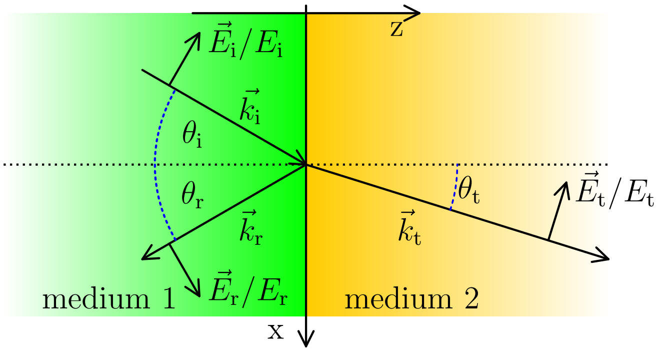

Figure 3.3.: An incident electromagnetic wave in medium 1 with wave vector $\vec{k}_\mathrm{i}$ is reflected ($\vec{k}_\mathrm{r}$) and transmitted/refracted ($\vec{k}_\mathrm{t}$) at an interface to medium 2. The normalized amplitude vectors $\vec{E}_\mathrm{i,r,t}/E_\mathrm{i,r,t}$ correspond to the p-polarized case.

It follows that $\vec{k}_\mathrm{i}$, $\vec{k}_\mathrm{r}$, and $\vec{k}_\mathrm{t}$ are all in one plane, called plane of incidence. Their magnitudes are

$$|\vec{k}_\mathrm{i}| = k_\mathrm{i} = |\vec{k}_\mathrm{r}| = k_\mathrm{r} = \frac{2\pi}{\lambda} n_1 \,, \tag{3.41}$$

$$|\vec{k}_\mathrm{t}| = k_\mathrm{t} = \frac{2\pi}{\lambda} n_2 \,. \tag{3.42}$$

As the tangential components of the wave vectors have to be the same it follows that

$$n_1 \cdot \sin\theta_\mathrm{i} = n_1 \cdot \sin\theta_\mathrm{r} = n_2 \cdot \sin\theta_\mathrm{t} \,. \tag{3.43}$$

This yields the law of reflection $\theta_\mathrm{r} = \theta_\mathrm{i}$, and Snell's law of refraction

$$\frac{\sin\theta_\mathrm{i}}{\sin\theta_\mathrm{t}} = \frac{n_2}{n_1} \,. \tag{3.44}$$

Upon incidence of an electromagnetic field, it is convenient to differentiate between s- and p-polarization, i.e., the oscillating electric field vector $\vec{E}$ perpendicular or parallel to the plane of incidence. Therefore, s-polarization (subscript s) is also called transverse electric (TE) and p-polarization (subscript p) transverse magnetic (TM). Using the continuity conditions, it is possible to calculate the attenuation of the amplitude of the electric field vector for both polarizations. Using only non-absorbing materials with $\varepsilon_{1,2} = n_{1,2}^2$ (the treatment is similar for materials with complex refractive indices, however, for the sake of simplicity, this is not shown here), the continuity equations for the problem depicted in fig. 3.3 are

$$\left(n_1^2\left(\vec{E}_\mathrm{i} + \vec{E}_\mathrm{r}\right) - n_2^2\vec{E}_\mathrm{t}\right) \cdot \vec{e}_\mathrm{z} = 0 \,, \tag{3.45}$$

$$\left(\vec{k}_\mathrm{i} \times \vec{E}_\mathrm{i} + \vec{k}_\mathrm{r} \times \vec{E}_\mathrm{r} - \vec{k}_\mathrm{t} \times \vec{E}_\mathrm{t}\right) \cdot \vec{e}_\mathrm{z} = 0 \,, \tag{3.46}$$

$$\left(\vec{E}_\mathrm{i} + \vec{E}_\mathrm{r} - \vec{E}_\mathrm{t}\right) \times \vec{e}_\mathrm{z} = 0 \,, \tag{3.47}$$

$$\left(\vec{k}_\mathrm{i} \times \vec{E}_\mathrm{i} + \vec{k}_\mathrm{r} \times \vec{E}_\mathrm{r} - \vec{k}_\mathrm{t} \times \vec{E}_\mathrm{t}\right) \times \vec{e}_\mathrm{z} = 0 \,, \tag{3.48}$$

with $\vec{e}_\mathrm{z}$ being the unit vector in z-direction perpendicular to the interface. For the case of p-polarization the amplitudes of the electric field are in the (xz)-plane and perpendicular to the corresponding wave vectors:

$$\vec{e}_\mathrm{y} \cdot \vec{E}_\mathrm{i} = \vec{e}_\mathrm{y} \cdot \vec{E}_\mathrm{r} = \vec{e}_\mathrm{y} \cdot \vec{E}_\mathrm{t} = 0\,, \tag{3.49}$$

$$\vec{k}_\mathrm{i} \cdot \vec{E}_\mathrm{i} = \vec{k}_\mathrm{r} \cdot \vec{E}_\mathrm{r} = \vec{k}_\mathrm{t} \cdot \vec{E}_\mathrm{t} = 0\,, \tag{3.50}$$

with $\vec{e}_\mathrm{y}$ being the unit vector in y-direction. Eq. (3.46) is already fulfilled as the results of the vector products are parallel to $\vec{e}_\mathrm{y}$. The remaining equations (3.45), (3.47), and (3.48) in combination with eq. (3.49) and (3.50) yield

$$n_1^2 \cdot (E_\mathrm{i} + E_\mathrm{r}) \cdot \sin\theta_\mathrm{i} - n_2^2 \cdot E_\mathrm{t} \cdot \sin\theta_\mathrm{t} = 0\,, \tag{3.51}$$

$$(E_\mathrm{i} - E_\mathrm{r}) \cdot \cos\theta_\mathrm{i} - E_\mathrm{t} \cdot \cos\theta_\mathrm{t} = 0\,, \tag{3.52}$$

$$n_1 \cdot (E_\mathrm{i} + E_\mathrm{r}) - n_2 \cdot E_\mathrm{t} = 0\,. \tag{3.53}$$

The amplitudes are $E_\mathrm{i,r,t} = \sqrt{\vec{E}^2_\mathrm{i,r,t}}$. Due to the law of refraction (eq. (3.44)), eq. (3.51) and (3.53) are equivalent. With the remaining two equations the ratio of the amplitudes can be calculated:

$$\left(\frac{E_\mathrm{r}}{E_\mathrm{i}}\right)_p = \frac{n_1 \cdot \cos\theta_\mathrm{t} - n_2 \cdot \cos\theta_\mathrm{i}}{n_1 \cdot \cos\theta_\mathrm{t} + n_2 \cdot \cos\theta_\mathrm{i}}\,, \tag{3.54}$$

$$\left(\frac{E_\mathrm{t}}{E_\mathrm{i}}\right)_p = \frac{2n_1 \cdot \cos\theta_\mathrm{i}}{n_1 \cdot \cos\theta_\mathrm{t} + n_2 \cdot \cos\theta_\mathrm{i}}\,. \tag{3.55}$$

Similar to this derivation, the case for the s-polarization can be calculated. In summary, these are the 'Fresnel equations' for the reflected waves

$$r_s = \left(\frac{E_\mathrm{r}}{E_\mathrm{i}}\right)_s = \frac{n_1 \cdot \cos\theta_\mathrm{i} - n_2 \cdot \cos\theta_\mathrm{t}}{n_1 \cdot \cos\theta_\mathrm{i} + n_2 \cdot \cos\theta_\mathrm{t}}\,, \tag{3.56}$$

$$r_p = \left(\frac{E_\mathrm{r}}{E_\mathrm{i}}\right)_p = \frac{n_1 \cdot \cos\theta_\mathrm{t} - n_2 \cdot \cos\theta_\mathrm{i}}{n_1 \cdot \cos\theta_\mathrm{t} + n_2 \cdot \cos\theta_\mathrm{i}}\,, \tag{3.57}$$

and for the transmitted waves

$$t_s = \left(\frac{E_\mathrm{t}}{E_\mathrm{i}}\right)_s = \frac{2n_1 \cdot \cos\theta_\mathrm{i}}{n_1 \cdot \cos\theta_\mathrm{i} + n_2 \cdot \cos\theta_\mathrm{t}}\,, \tag{3.58}$$

$$t_p = \left(\frac{E_\mathrm{t}}{E_\mathrm{i}}\right)_p = \frac{2n_1 \cdot \cos\theta_\mathrm{i}}{n_1 \cdot \cos\theta_\mathrm{t} + n_2 \cdot \cos\theta_\mathrm{i}}\,. \tag{3.59}$$

The coefficients, r_s, r_p, t_s, and t_p are called the 'Fresnel coefficients'. It is evident from these formulas that upon perpendicular incidence of light, i.e., $\theta_\mathrm{i} = \theta_\mathrm{t} = 0°$, a distinction between s- and p-polarization is not possible, as $r_s = r_p$ and $t_s = t_p$, respectively.

The Fresnel equations give the ratio of the amplitudes of the reflected and transmitted waves to the incident wave, respectively. The amount of energy reflected or transmitted perpendicular to the interface is determined by the reflectance $R_{s/p}$ and transmittance $T_{s/p}$, which can be calculated using the normal component of the time-averaged Poynting's vector[45] $\vec{S}$:

$$R_s = \left| \frac{\vec{e}_\mathrm{z} \cdot \vec{S}_{s,\mathrm{r}}}{\vec{e}_\mathrm{z} \cdot \vec{S}_{s,\mathrm{i}}} \right| , \tag{3.60}$$

$$R_p = \left| \frac{\vec{e}_\mathrm{z} \cdot \vec{S}_{p,\mathrm{r}}}{\vec{e}_\mathrm{z} \cdot \vec{S}_{p,\mathrm{i}}} \right| , \tag{3.61}$$

$$T_s = \left| \frac{\vec{e}_\mathrm{z} \cdot \vec{S}_{s,\mathrm{t}}}{\vec{e}_\mathrm{z} \cdot \vec{S}_{s,\mathrm{i}}} \right| , \tag{3.62}$$

$$T_p = \left| \frac{\vec{e}_\mathrm{z} \cdot \vec{S}_{p,\mathrm{t}}}{\vec{e}_\mathrm{z} \cdot \vec{S}_{p,\mathrm{i}}} \right| . \tag{3.63}$$

For a plane wave with real wave vector $\vec{k}$,

$$\vec{S} = \frac{\vec{k}}{2\omega\mu_0} \cdot |\vec{E}|^2 , \tag{3.64}$$

and the reflectance $R_{s,p}$ and $T_{s,p}$ can be expressed by the Fresnel coefficients:

$$R_s = |r_s|^2 , \tag{3.65}$$

$$R_p = |r_p|^2 , \tag{3.66}$$

$$T_s = \frac{n_2 \cdot \cos\theta_\mathrm{t} \cdot |t_s|^2}{n_1 \cdot \cos\theta_\mathrm{i}} , \tag{3.67}$$

$$T_p = \frac{n_2 \cdot \cos\theta_\mathrm{t} \cdot |t_p|^2}{n_1 \cdot \cos\theta_\mathrm{i}} . \tag{3.68}$$

For $n_1 = 1$ (e.g., air) and $n_2 = 1.5$ (e.g., glass) the reflectance as a function of the angle of incidence θ_i is shown in fig. 3.4a. Due to energy conservation, in case of non-absorbing materials, $R_{s/p} + T_{s/p} = 1$ and the transmittance can easily be depicted from the plotted reflectance curves.

If the incident wave is propagating in a medium with higher refractive index than the adjacent medium, $n_1 > n_2$, the reflectance and transmittance curves show an interesting behavior at the so called critical angle θ_c: the reflectance approaches $R = 1$. This is shown for $n_1 = 1.5$ (e.g., glass) and $n_2 = 1$ (e.g., air) in fig. 3.4b. This phenomenon is called 'total internal reflection', see fig. 3.5. The reason can be found in Snell's equation (eq. (3.44)): $0° \leq \theta_\mathrm{t} \leq 90°$ requires $0° \leq \theta_\mathrm{i} \leq \theta_\mathrm{c}$, with

$$\theta_\mathrm{c} = \arcsin \frac{n_2}{n_1} . \tag{3.69}$$

For an incident angle $\theta_\mathrm{i} = \theta_\mathrm{c}$, the refracted wave propagates parallel to the interface. If $\theta_\mathrm{i} > \theta_\mathrm{c}$, the angle θ_t is a complex angle (loosing its physical interpretation as an

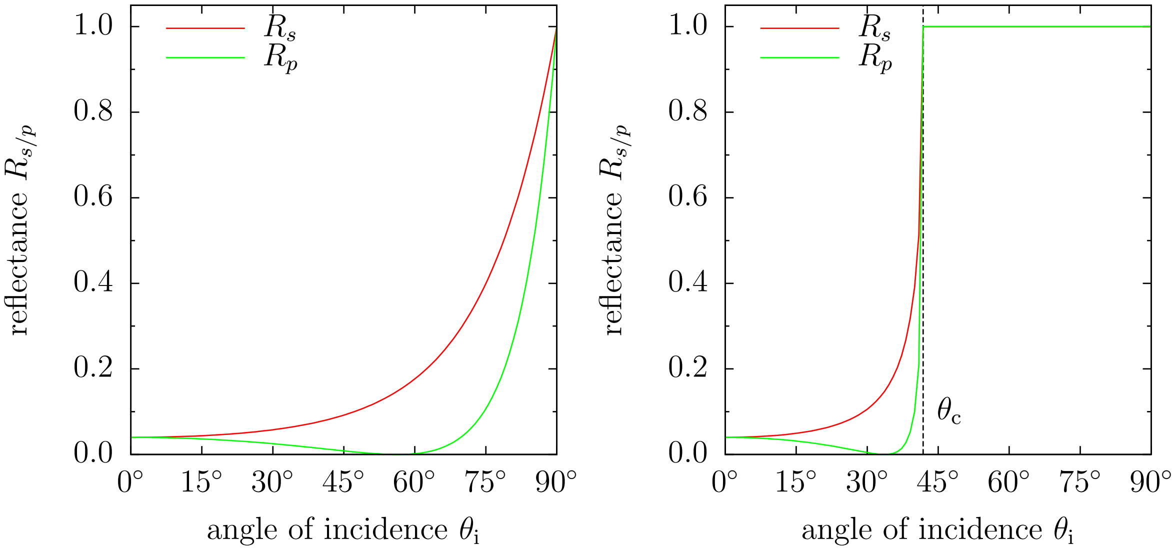

(a) *Adjacent medium is optically denser than incident medium, $n_1 < n_2$. Calculation for $n_1 = 1$ (e.g., air) and $n_2 = 1.5$ (e.g., glass).*

(b) *Incident medium is optically denser than adjacent medium, $n_1 > n_2$. Dashed line: critical angle θ_c. Calculation for $n_1 = 1.5$ (e.g., glass) and $n_2 = 1$ (e.g., air), yielding $\theta_\mathrm{c} \approx 41.8°$.*

Figure 3.4.: Reflectance $R_{s/p}$ with distinction of s- and p-polarization as a function of the angle of incidence θ_i (fig. 3.3).

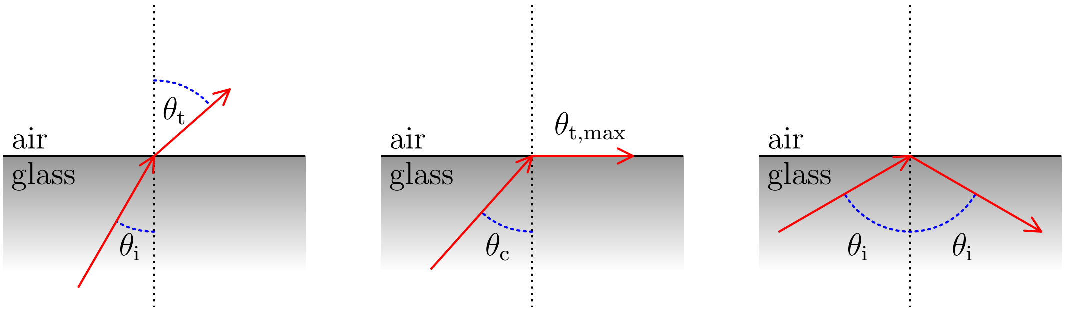

Figure 3.5.: Total internal reflection at a glass/air interface: $n_\mathrm{glass} > n_\mathrm{air}$ ($n_\mathrm{glass} = 1.5$, $n_\mathrm{air} = 1$). Left: normal refraction, $\theta_\mathrm{i} < \theta_\mathrm{c}$ and $\theta_\mathrm{i} < \theta_\mathrm{t}$. Middle: $\theta_\mathrm{t,max} = 90°$ for critical angle $\theta_\mathrm{i} = \theta_\mathrm{c}$, here $\theta_\mathrm{c} \approx 41.8°$. Right: total internal reflection, $\theta_\mathrm{i} > \theta_\mathrm{c}$.

angle, but still allows the description of the wave vector components parallel and perpendicular to the interface):

$$\cos\theta_\mathrm{t} = -\mathrm{i}\cdot\sqrt{\left(\frac{\sin\theta_\mathrm{i}}{\sin\theta_\mathrm{c}}\right)^2 - 1}\,. \tag{3.70}$$

This means that the transmitted wave has an exponential decay perpendicular to the interface for increasing z. Thus, the reflection coefficients can be expressed as

$$r_s = \frac{n_1\cdot\cos\theta_\mathrm{i} + \mathrm{i}\cdot n_2\cdot|\cos\theta_\mathrm{t}|}{n_1\cdot\cos\theta_\mathrm{i} - \mathrm{i}\cdot n_2\cdot|\cos\theta_\mathrm{t}|}\,, \tag{3.71}$$

$$r_p = \frac{-\mathrm{i}\cdot n_1\cdot|\cos\theta_\mathrm{t}| - n_2\cdot\cos\theta_\mathrm{i}}{-\mathrm{i}\cdot n_1\cdot|\cos\theta_\mathrm{t}| + n_2\cdot\cos\theta_\mathrm{i}}\,, \tag{3.72}$$

which yield $R_s = R_p = 1$, meaning that all energy is reflected at the interface. This can be easily understood with some mathematical transformations*, shown for $|r_s|^2 = R_s$ as an example:

$$|r_s|^2 = \left|\frac{n_1\cdot\cos\theta_\mathrm{i} + \mathrm{i}\cdot n_2\cdot\sqrt{\left(\frac{\sin\theta_\mathrm{i}}{\sin\theta_\mathrm{c}}\right)^2 - 1}}{n_1\cdot\cos\theta_\mathrm{i} - \mathrm{i}\cdot n_2\cdot\sqrt{\left(\frac{\sin\theta_\mathrm{i}}{\sin\theta_\mathrm{c}}\right)^2 - 1}}\right|^2 \tag{3.73}$$

$$= |\exp(\mathrm{i}\cdot 2\varPhi_s)|^2 \tag{3.74}$$

$$= |\cos 2\varPhi_s + \mathrm{i}\cdot\sin 2\varPhi_s|^2 = 1\,. \tag{3.75}$$

The amplitudes of incident and reflected field differ by a phase shift $2\varPhi_{s,p}$, being different for s- and p-polarization. The phase factors are calculated as

$$\varPhi_s = \arctan\left(\frac{n_2}{n_1}\cdot\frac{\sqrt{\left(\frac{\sin\theta_\mathrm{i}}{\sin\theta_\mathrm{c}}\right)^2 - 1}}{\cos\theta_\mathrm{i}}\right), \tag{3.76}$$

$$\varPhi_p = \arctan\left(\frac{n_1}{n_2}\cdot\frac{\sqrt{\left(\frac{\sin\theta_\mathrm{i}}{\sin\theta_\mathrm{c}}\right)^2 - 1}}{\cos\theta_\mathrm{i}}\right). \tag{3.77}$$

A similar way to obtain these identities can be found in the book of Fouckhardt[47]. For a glass/air interface ($n_1 = 1.5$, $n_2 = 1$) the phase shifts with distinction of s- and p-polarization are shown in fig. 3.6.

---

[*] $\hat{Z} = a \pm \mathrm{i}b = |\hat{Z}|\cdot\exp(\pm\mathrm{i}\varPhi)$ with $\varPhi = \arctan(b/a)$. Furthermore, $\exp(\pm\mathrm{i}\varPhi) = \cos\varPhi \pm \mathrm{i}\cdot\sin\varPhi$. See, e.g., Bronstein et al.[46].

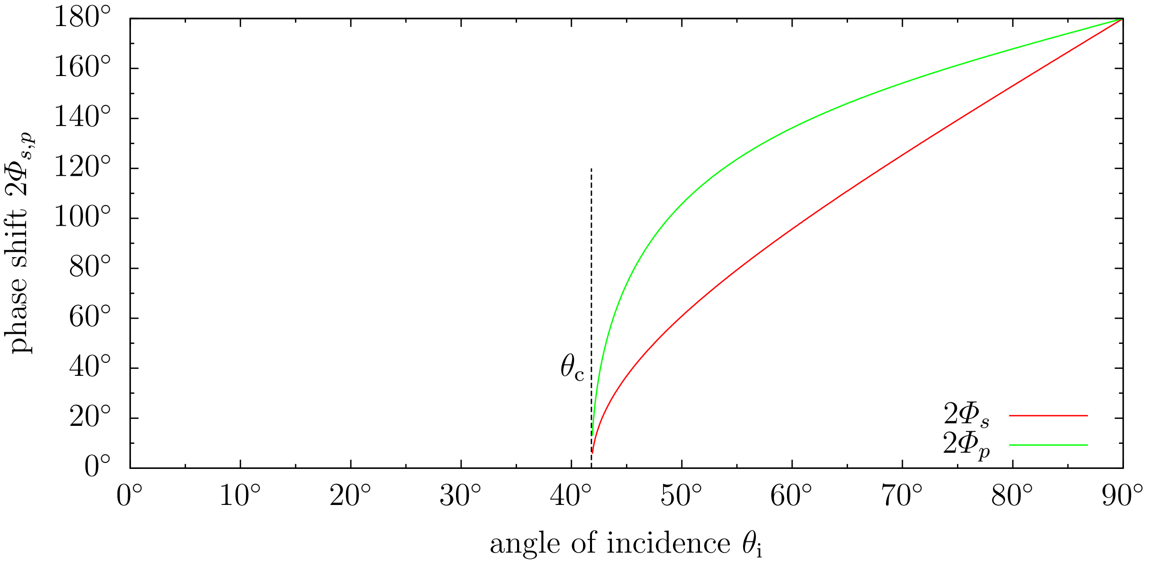

Figure 3.6.: Phase shift $2\varPhi_{s,p}$ for total internal reflection at a glass/air interface, $n_1 = 1.5$, $n_2 = 1$.

If the angle of incidence θ_i is greater than the critical angle θ_c, it has been shown that the reflectance $R_{s,p}$ is equal to unity. However, the Fresnel coefficients for transmission do not vanish ($t_{s,p} \neq 0$) for $\theta_\mathrm{i} > \theta_\mathrm{c}$. This means that upon total internal reflection and despite total reflection of the energy a damped electric field penetrates into the second medium. Zero transmission of energy, in fact, means that the normal component of Poynting's vector is zero. However, there is a power flow parallel to the interface. The electric field of the transmitted wave is proportional to

$$\exp\left[\mathrm{i}\left(\omega t - k_\mathrm{i} x \cdot \sin\theta_\mathrm{i}\right)\right] \cdot \exp\left(-u \cdot z\right) \, , \tag{3.78}$$

where

$$u = k_\mathrm{t} \cdot \sqrt{\left(\frac{\sin\theta_\mathrm{i}}{\sin\theta_\mathrm{c}}\right)^2 - 1} \tag{3.79}$$

is a positive and real number[45]. The electric field therefore decreases exponentially with increasing distance z to the interface. It is propagating parallel to this interface and is called 'evanescent wave'. Its attenuation length, described by $1/u$, is only a few wavelengths (except for θ_i near the critical angle).

3.5. Transfer-matrix formulation

The Fresnel equations (ch. 3.4) can be easily calculated for a single interface, however, in OLED stacks many thin films are used, leading to several interfaces. In addition, multiple reflection and interference effects are possible. It is evident that the analysis is complicated due to the large number of equations to be solved. However, the problem can be simplified by introducing a transfer-matrix method. The book of Yeh offers a good introduction into this topic[45]; therefore, only a short discussion shall be given here.

Consider a multilayer stack with $N + 1$ isotropic media, see fig. 3.7. A layer i has the thickness d_i (layers 0 and N are taken to be semi-infinite) and the complex refractive index $\hat{N}_i = n_i - \mathrm{i}\kappa_i$. A wave propagating in this layer i to the right side has the amplitude A_i, the wave propagating to the left has the amplitude B_i. Between two layers, layer $i - 1$ and layer i, the following equation shows the relation of the amplitudes in both layers:

$$\begin{pmatrix} A_{i-1} \\ B_{i-1} \end{pmatrix} = D_{i-1,i} \cdot \begin{pmatrix} A_i \\ B_i \end{pmatrix} . \tag{3.80}$$

$D_{i-1,i}$ is the transmission matrix containing the Fresnel coefficients r and t:

$$D_{i-1,i} = \frac{1}{t_{i-1,i}} \begin{pmatrix} 1 & r_{i-1,i} \\ r_{i-1,i} & 1 \end{pmatrix} . \tag{3.81}$$

Another matrix is needed, P_i which is called propagation matrix as it accounts for the propagation in the bulk of layer i:

$$P_i = \begin{pmatrix} \exp\left(\mathrm{i}\mathit{\Phi}_i\right) & 0 \\ 0 & \exp\left(-\mathrm{i}\mathit{\Phi}_i\right) \end{pmatrix} , \tag{3.82}$$

with $\mathit{\Phi}_i = \hat{k}_i d_i \cdot \cos\theta_i$. Herein, $\hat{k}_i = \frac{2\pi}{\lambda} \cdot \hat{N}_i$ is the (complex) wave vector and $\cos\theta_i$ is the angle of propagation within layer i. The transfer-matrix M for the entire stack can be written as

$$M = \left[\prod_{i=1}^{N-1} D_{i-1,i} \cdot P_i \right] D_{N-1,N} , \tag{3.83}$$

which gives the relation of the amplitudes of layers 0 and N as:

$$\begin{pmatrix} A_0 \\ B_0 \end{pmatrix} = M \begin{pmatrix} A_N \\ B_N \end{pmatrix} . \tag{3.84}$$

The coefficients of this (2×2)-transfer-matrix

$$M = \begin{pmatrix} M_{11} & M_{12} \\ M_{21} & M_{22} \end{pmatrix} \tag{3.85}$$

define the reflection and transmission coefficients for the whole stack, r and t, respectively,

$$r = \frac{M_{21}}{M_{11}} , \tag{3.86}$$

$$t = \frac{1}{M_{11}} , \tag{3.87}$$

as well as the reflectance (if medium $i = 0$ is lossless, i.e., $\kappa_0 = 0$)

$$R(\theta_0) = |r|^2 = \left| \frac{M_{21}}{M_{11}} \right|^2 , \tag{3.88}$$

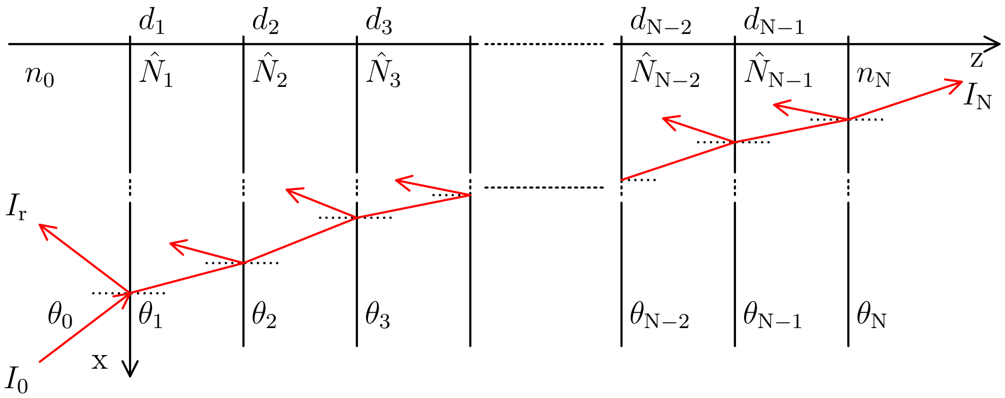

Figure 3.7.: Multilayer stack used by the transfer-matrix method. Incident light with intensity I_0 under angle θ_0, reflected and transmitted light of the total stack with intensities I_r and I_N, respectively. d_i, $\hat{N}_i$, and θ_i are the thickness, complex refractive index, and angle of layer i, respectively.

and transmittance (if medium $i = 0$ and $i = N$ are pure dielectrics and $\hat{N}_0$ and $\hat{N}_N$ are real numbers)

$$T(\theta_0) = \frac{n_N \cdot \cos\theta_N}{n_0 \cdot \cos\theta_0} |t|^2 = \frac{n_N \cdot \cos\theta_N}{n_0 \cdot \cos\theta_0} \left| \frac{1}{M_{11}} \right|^2 . \tag{3.89}$$

The absorption $A(\theta_0)$ of the stack can be calculated by using the energy conservation principle as

$$A(\theta_0) = 1 - (R(\theta_0) + T(\theta_0)) . \tag{3.90}$$

If only dielectrics without absorption are calculated, it can be shown that $R(\theta_0) + T(\theta_0) = 1$, as required by the energy conservation principle.

3.6. Waveguides

In waveguide structures the effect of total internal reflection (discussed in ch. 3.4) is used to guide light in a medium without loss due to imperfect reflections. The simplest waveguide is the classic three-layer waveguide. Light guided in a medium being infinite in two dimensions, having a thickness d in the third direction with refractive index n_{wg} is sandwiched between two materials, a substrate and a cladding material with refractive indices n_{s} and n_{c}, respectively (see fig. 3.8). Again, for the sake of simplicity non-absorbing materials are assumed. For total internal reflection, it is required that $n_{\mathrm{wg}} > n_{\mathrm{s}}, n_{\mathrm{c}}$ and that the angle of incidence θ_{wg} is higher than both critical angles $\theta_{\mathrm{c,s}}$ and $\theta_{\mathrm{c,c}}$, respectively:

$$\theta_{\mathrm{wg}} \geq \theta_{\mathrm{c,s}} = \arcsin \frac{n_{\mathrm{s}}}{n_{\mathrm{wg}}} , \tag{3.91}$$

$$\theta_{\mathrm{wg}} \geq \theta_{\mathrm{c,c}} = \arcsin \frac{n_{\mathrm{c}}}{n_{\mathrm{wg}}} . \tag{3.92}$$

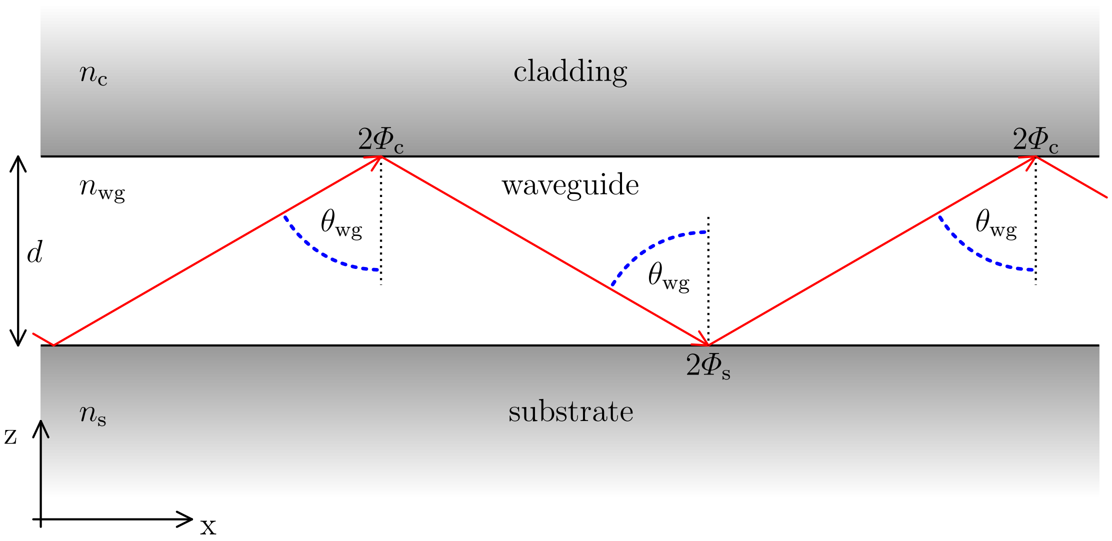

Figure 3.8.: Classical three-layer waveguide structure. It is required that $n_{wg} > n_s$, n_c, and that $\theta_{wg} > \theta_{c,s}$, $\theta_{c,c}$.

Upon reflection, the electromagnetic wave is shifted in its phase, $2\Phi_s$ on reflection at the substrate and $2\Phi_c$ on reflection at the cladding layer, respectively. For constructive interference, it is required that the difference in phase is an integer multiple of 2π:

$$2dkn_{wg}\cos\theta_{wg} - 2\Phi_c - 2\Phi_s = 2\pi \cdot m\,, \tag{3.93}$$

with $m = 0, 1, 2, \ldots$. Please note that as the phase shifts are different for s- and p-polarization, see eq. (3.76) and (3.77), this condition also depends on the polarization. In literature, it is often called ‘transverse resonance condition’ (TRC). Only if light is satisfying this equation, waveguiding is possible and the use of the term ‘waveguided mode’ is permitted.

Similar to the calculation of the Fresnel coefficients for an actual OLED stack with various layers, a transfer-matrix method has to be used to calculate the waveguided modes, including the use of complex refractive indices $\hat{N}$. An extensive treatment of this topic is given by Kogelnik in the book of Tamir[48].

3.7. Surface plasmon polaritons

Surface plasmons polaritons (SPPs, further on designated as ‘plasmons’) are fluctuations of electron charges at the interface of conductive and dielectric layers. These are longitudinal electromagnetic waves in the plane of the interface with angular frequency ω, having a dispersion relation which can be written as

$$\hat{k}_x = \frac{\omega}{c} \cdot \sqrt{\frac{\hat{\varepsilon}_1\hat{\varepsilon}_2}{\hat{\varepsilon}_1 + \hat{\varepsilon}_2}}\,, \tag{3.94}$$

with $\hat{k}_x$ being the complex in-plane (tangential to the interface) wave vector component of the complex wave vector $\hat{k}$, c the speed of light, and with $\hat{\varepsilon}_1$ and $\hat{\varepsilon}_2$ being the complex

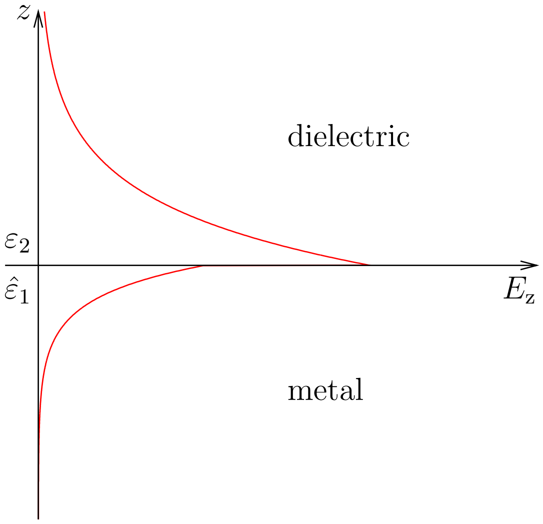

Figure 3.9.: Exponential decay of the electric field of a surface plasmon polariton (SPP) on both sides of the interface.

dielectric functions of medium 1 and 2, respectively[49]. As these waves are in the plane of the interface, the plasmons have TM (or p-) polarization. Such waves are excited if the conditions for total internal reflection apply, $\theta_\mathrm{i} \geq \theta_\mathrm{c}$. In this case, according to eq. (3.78), the surface plasmons' electric field E_z perpendicular to the interface drops exponentially on both sides, see fig. 3.9.

The complex dielectric function $\hat{\varepsilon}$ is associated with the complex refractive index $\hat{N}$:

$$\hat{\varepsilon} = \varepsilon' + \mathrm{i}\varepsilon'' \equiv \hat{N}^2 = (n - \mathrm{i}\kappa)^2 \,. \tag{3.95}$$

If medium 2 is a dielectric material with only a real part, $\hat{\varepsilon}_2 = \varepsilon_2$, the real part of the in-plane wave vector $\hat{k}_\mathrm{x} = k'_\mathrm{x} + \mathrm{i}k''_\mathrm{x}$ is

$$k'_\mathrm{x} = \frac{\omega}{c} \cdot \sqrt{\frac{\varepsilon'_1 \varepsilon_2}{\varepsilon'_1 + \varepsilon_2}} \,. \tag{3.96}$$

This requires $\varepsilon'_1 < 0$ and $-\varepsilon'_1 > \varepsilon_2$, which is fulfilled for metals or doped semiconductors near their plasma frequency[49]. The imaginary part k''_x determines the attenuation of the plasmonic mode upon propagation. In the following k_x designates the real part k'_x.

For a metal, e.g., silver, the dielectric function can be expressed as a function of its plasma frequency ω_p according to the free electron model:

$$\varepsilon_1 = 1 - \frac{\omega_\mathrm{p}^2}{\omega^2} \,, \tag{3.97}$$

however, its validity is limited to near-infrared frequencies[50]. A schematic dispersion relation for a metal after eq. (3.96) and (3.97) is shown in fig. 3.10 for a metal/air and a metal/organic interface. A plasma frequency of $\omega_\mathrm{p} = 1.12 \cdot 10^{16}\,\mathrm{Hz}$ is assumed. The refractive indices are $n_\mathrm{air} = 1$ and $n_\mathrm{organic} = 1.8$. Additionally, the plasmon dispersion was calculated from the experimental complex refractive index of Ag for these interfaces (points in fig. 3.10). It is already evident from this figure that plasmons in the frequency range of visible light ($2.36 \cdot 10^{15}\,\mathrm{Hz} \lesssim \omega \lesssim 4.71 \cdot 10^{15}\,\mathrm{Hz}$) require large values of k_x to fulfill the dispersion relation. For very high values of k_x the plasmon dispersion relation approaches a limit in ω, indicated with dashed lines in fig. 3.10,

$$\lim_{k_\mathrm{x} \to \infty} \omega = \frac{\omega_\mathrm{p}}{\sqrt{1 + \varepsilon_2}}\,, \tag{3.98}$$

which can be calculated by using eq. (3.96) and (3.97).

Excitation of plasmons with an external light source is not possible, as the light line

$$\omega = c \cdot \frac{k}{\sin \theta_\mathrm{i}} = c \cdot k_\mathrm{x}\,, \tag{3.99}$$

corresponding to light with frequency ω under incident angle θ_i in air, is always, even for $\theta_\mathrm{i} = 90°$, left of the dispersion relation of the plasmon and thus never crosses it. The physical interpretation is that energy ($\hbar\omega$) and momentum ($\hbar k_\mathrm{x}$) conservation can not be fulfilled at the same time. However, excitation of surface plasmons is possible through near-field coupling of an emitting dipole sitting close enough to the metal interface (fig. 3.9, $z <$ decay length). As plasmons are longitudinal modes in the plane of the interface, only the p-polarized part of light can excite the plasmon.

Other possibilities to excite SPPs is either to use the Kretschmann configuration, or electron beams[49]. However, both are not relevant for this thesis. Nevertheless, analyzing the Kretschmann configuration provides insight into the excitation of plasmons. Thus, it can be found in the appendix (A.2).

As will be shown in detail later, the excitation of surface plasmons is one major loss channel for OLED efficiency and their excitation should either be prevented or at least minimized.

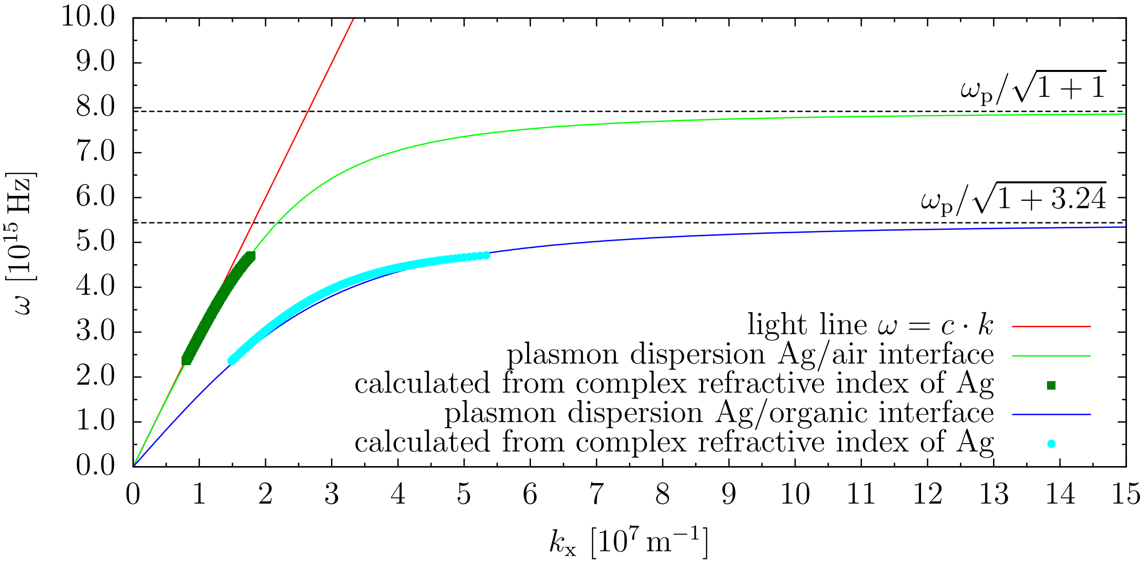

Figure 3.10.: Dispersion relations for a plasmon at a metal/air interface (green line) and at a metal/organic interface (blue line) calculated according to eq. (3.97) with $\omega_\mathrm{p} = 1.12 \cdot 10^{16}\,\mathrm{Hz}$, $n_\mathrm{air} = 1$, and $n_\mathrm{organic} = 1.8$, respectively. For the limit in ω for large k_x, please see eq. (3.98). Additionally, the plasmon dispersion calculated from the complex refractive index of Ag is shown, again for the metal/air (dark green points) and metal/organic (cyan points) interface, respectively. The light line (red line), $\omega = c \cdot k$ for $\theta_\mathrm{i} = 90°$, has no intersection with the dispersion relations.

4. Optimization of OLEDs via optical device simulation

4.1. Introduction

To compete with established lighting technologies, OLEDs need to be improved further, e.g., concerning the efficiency of converting electrical power into emitted photons. Traditionally, the external quantum efficiency η_{EQE} (or EQE), i.e., the number of photons emitted from the OLED per charge carriers injected into the device, is given by the product of four factors[51],

$$\eta_{\mathrm{EQE}} = \gamma \cdot \eta_{\mathrm{s/t}} \cdot q \cdot \eta_{\mathrm{out}} \, . \tag{4.1}$$

Therein, γ is the charge balance factor, $\eta_{\mathrm{s/t}}$ is the singlet/triplet ratio, q is the radiative quantum efficiency (QE) of the emitter material (eq. (2.8)), and η_{out} is the outcoupling factor. These factors shall be explained in the following.

Holes and electrons are usually injected in different amounts from the anode and cathode, respectively. However, the device performance is best if the ratio of holes and electrons is 1 : 1 and all of them recombine to form an exciton that can, in principle, decay radiatively. An excess of one or the other charge carrier species can not be used to generate light, and thus reduces the external quantum efficiency. The value of the charge balance factor is defined as $0 \leqslant \gamma \leqslant 1$, where $\gamma = 1$ is the optimal case for equal hole and electron amounts. It was already demonstrated in the pioneering work of Tang and VanSlyke[8] that γ can be brought close to one in heterolayer structures. As $\gamma = 1$ is achieved by choosing the right layer combinations for the OLED stack, in particular using HBLs and EBLs, this factor is not a bottleneck for the development of highly efficient OLEDs.

The singlet/triplet ratio is given by quantum mechanics. If excitons are formed in the OLED, they either occupy a singlet state (S_1) or one of three triplet states (T_1), see ch. 2.2. Statistically, as only the excited singlet state is able to generate light under relaxation to the ground singlet state (S_0), only one of four generated excitons are radiative, therefore $\eta_{\mathrm{s/t}} = 1/4$ for fluorescent emitters. However, an important step in increasing OLED performance was the introduction of phosphorescent emitters by Baldo et al.[20]. Due to the introduction of heavy metals in the emitter material also the triplet states can decay radiatively (see ch. 2.3), therefore $\eta_{\mathrm{s/t}} = 1$ for phosphorescent emitters.

The product $\gamma \cdot \eta_{\mathrm{s/t}}$ thus gives the fraction of injected carriers forming excitons that are able to generate radiation inside an OLED. Their fate is determined by the remaining two factors in eq. (4.1), $q \cdot \eta_{\mathrm{out}}$. Usually, the QE q is taken to be the photoluminescence (PL) quantum efficiency of the emitter material in an unbounded medium, which is the ratio of emitted to absorbed photons (see also ch. 2.2). The extraction efficiency η_{out} is a measure of how many of the generated photons are actually leaving the device to the outside world. As the organic layers of the OLED stack usually have a higher refractive index ($n_{\mathrm{organic}} \approx 1.8$) than the glass substrate ($n_{\mathrm{glass}} \approx 1.5$) and air ($n_{\mathrm{air}} = 1$), total internal reflection occurs (fig. 3.5), reducing the amount of outcoupled photons. As a crude approximation from geometric optics, η_{out} can be estimated as $1/2n^2$ for isotropic emitters, where n is the refractive index of the emitting organic layer[52]. For a typical organic emitter ($n_{\mathrm{organic}} \approx 1.8$), the maximum external quantum efficiency can be estimated in this way to be

$$\eta_{\mathrm{EQE,fluorescent}} \leqslant 1 \cdot 0.25 \cdot 1 \cdot 0.15 \approx 4\,\%\,, \tag{4.2}$$

$$\eta_{\mathrm{EQE,phosphorescent}} \leqslant 1 \cdot 1 \cdot 1 \cdot 0.15 \approx 15\,\%\,, \tag{4.3}$$

for fluorescent (singlet) and phosphorescent (triplet) emitters, respectively, if an ideal charge balance factor γ and ideal radiative quantum efficiency q are assumed. This shows that unfortunately only a small amount of the injected charge carriers is generating light which is emitted from the OLED.

However, in detail, both q and η_{out} depend on the composition of the OLED stack as well as the position and the orientation of the emitting molecules inside the structure[53,54] and therefore can be higher than the approximated values. It also has been realized by various authors that the radiative decay rates of fluorescent dyes close to a metal electrode or embedded in the microcavity of an OLED can be significantly different as compared to the free-space values[55–59], meaning that q is also altered due to the OLED stack itself. Consequently, for optical device optimizations $q \cdot \eta_{\mathrm{out}}$ has to be maximized, however, as both factors are influenced by the OLED structure their determination is not straightforward. In the following section the so called 'dipole model' is introduced, which allows the determination of the quantum efficiency of the emitter material inside the OLED stack, as well as the extraction efficiency η_{out}. It will furthermore be used to evaluate different techniques to increase the external quantum efficiency η_{EQE}.

4.2. Dipole model

4.2.1. Theory

The dipole model is a traditional approach for optical simulations of OLEDs. There are, however, several other possibilities to simulate the emission spectra of OLEDs, but these do not grant access to the non-radiative modes and often are limited to specific stack types such as microcavity OLEDs[60–62]. The basis for the dipole model can be found in an early paper by Sommerfeld[63], where the propagation of radiowaves above the Earth's conducting surface was investigated. Chance, Prock, and Silbey (CPS)[56,57] adapted Sommerfeld's model for molecular fluorescence and energy transfer near interfaces. The model of CPS was extended to the near-field optics of OLEDs by various authors[53,54,64–66], where an exciton within the OLED is modeled as a point dipole driven by the reflected electromagnetic waves inside a microcavity.

The optical simulations presented in this work are also based on the traditional CPS approach of emissive dipoles. The dipoles, embedded in the multilayer stack of an OLED, are treated as forced damped harmonic oscillators[54]:

$$\frac{\mathrm{d}^2 p\,(t)}{\mathrm{d}t^2} + \omega_0^2 p\,(t) = \frac{e^2}{m} E_\mathrm{r}\,(t) - k_\mathrm{r} \frac{\mathrm{d}p\,(t)}{\mathrm{d}t} \,. \tag{4.4}$$

Here, p is the electric dipole moment, ω_0 is the resonant angular frequency in the absence of damping, m is the effective mass, e is the electric charge, E_r is the reflected electric field at the dipole position, and k_r is the radiative decay rate (or damping constant) in the absence of any interfaces. Both the dipole and the reflected field oscillate with the same complex frequency $\hat{\Omega} = \omega - \mathrm{i}k_\mathrm{r}^*/2$, as

$$p\,(t) = p_0 \exp\left(-\mathrm{i}\hat{\Omega}t\right) \,, \tag{4.5}$$

$$E_\mathrm{r}\,(t) = E_0 \exp\left(-\mathrm{i}\hat{\Omega}t\right) \,, \tag{4.6}$$

where ω and k_r^* are the frequency and decay rate in the presence of the interface, p_0 and E_0 are the amplitude of the dipole moment and reflected electric field, respectively. Inserting eq. (4.5) and (4.6) in eq. (4.4) yields

$$\hat{\Omega} = -\mathrm{i} \cdot \frac{k_\mathrm{r}}{2} + \omega_0 \sqrt{\left(1 - \frac{k_\mathrm{r}^2}{4\omega_0^2} - \frac{e^2}{p_0 m \omega_0^2} E_0\right)} \,, \tag{4.7}$$

which can be approximated to

$$\hat{\Omega} = -\mathrm{i} \cdot \frac{k_\mathrm{r}}{2} + \omega_0 \left(1 - \frac{k_\mathrm{r}^2}{8\omega_0^2} - \frac{e^2}{2p_0 m \omega_0^2} E_0\right) \,, \tag{4.8}$$

as $k_\mathrm{r}^2 \ll \omega_0^2$ and $\frac{e^2}{2p_0 m} E_0 \ll \omega_0^2$. Dividing eq. (4.8) into real and imaginary part and keeping in mind that $\hat{\Omega} = \omega - \mathrm{i}k_\mathrm{r}^*/2$, the modified decay rate k_r^* is obtained as

$$k_\mathrm{r}^* = k_\mathrm{r} + \frac{e^2}{p_0 m \omega_0} \mathrm{Im}\left(E_0\right) \,, \tag{4.9}$$

and the frequency shift as

$$\Delta\omega \equiv \omega_0 - \omega = \frac{k_\mathrm{r}^2}{8\omega_0} + \frac{e^2}{2p_0^2 m \omega_0} \mathrm{Re}\left(E_0\right) \,. \tag{4.10}$$

In general the shift is negligible and not considered further. From eq. (4.9) we see that the change due to the OLED cavity in the radiative decay rate is due to the magnitude of the reflected electric field at the position of the emitting dipole.

Calculating the reflected field has been the focus of many reports; therefore, this thesis does not follow through the development that leads to the electric field. In principle, it is calculated using the Hertz vector and solving the Helmholtz equation by an expansion of the field in plane waves (for details, see, e.g., Lukosz and Kunz[67]). Thereby, all layers in this multilayer stack are treated as infinite in two dimensions, having a certain thickness in the third direction. The interface between two layers is assumed sharp and without roughness. Using a transfer-matrix method the Fresnel coefficients are calculated (see ch. 3.5) by taking the optical constants and thicknesses of the different layers of the OLED stack into account, as well as the position of the dipoles within the OLED, which is assumed to be sharp as well. The orientation of the emitting dipoles usually is taken to be isotropic. The modified decay rate for an isotropic emitter $k^*_{\mathrm{r,iso}}$ is a 2 : 1 combination of the modified parallel and perpendicular decay rates, $k^*_{\mathrm{r},\parallel}$ (dipoles oriented parallel to the interfaces) and $k^*_{\mathrm{r},\perp}$ (dipoles oriented perpendicular to the interfaces), respectively:

$$k^*_{\mathrm{r,iso}} = \frac{2}{3} k^*_{\mathrm{r},\parallel} + \frac{1}{3} k^*_{\mathrm{r},\perp} \,. \tag{4.11}$$

However, any arbitrary dipole orientation can be considered as it is a combination of perpendicular and parallel dipoles. The decay rates are calculated numerically by integrating over all in-plane wave vector magnitudes $|\vec{k}_{\mathrm{x}}|$ from 0 to ∞ using the Fresnel coefficients for s- and p-polarized light (for details, see CPS[57] or Barnes[54])[*].

The term in-plane wave vector $\vec{k}_{\mathrm{x}}$ needs explaining here. Consider light inside a layer of the OLED traveling with wave vector $\vec{k}$, having the magnitude $k(\lambda) = \frac{2\pi}{\lambda} \cdot n(\lambda)$. Here, λ is the vacuum wavelength of the light and $n(\lambda)$ is the refractive index of the actual layer at this wavelength. The in-plane wave vector $\vec{k}_{\mathrm{x}}$ is the projection of $\vec{k}$ on the interface of the layer (see fig. 4.1). Light with wavelength λ traveling under a certain angle therefore can be fully described by the magnitude $k_{\mathrm{x}} = |\vec{k}_{\mathrm{x}}|$. The in-plane wave vector is a very useful way to describe light traveling inside the OLED, as k_{x} is constant for light crossing from one layer to another (which is a result of the boundary conditions for Maxwell's equations, see eq. (3.26))[†]. It is also used to distinguish light which is coupled out of the OLED, trapped in the substrate, or coupled to waveguided modes or plasmons. This, however, will be addressed in detail later.

As a result of the simulation, calculated with the above described methods, the power radiated from dipoles inside the OLED stack at wavelength λ and in-plane wave vector k_{x} is obtained. However, this has to be weighed with the spectrum of the organic emitter, resulting in the so-called power dissipation spectrum, which shows the power radiated from a dipole at a certain wavelength of the emitter material and in-plane wave vector for the particular OLED stack. Knowing the power dissipation spectrum, it is one more step to calculate the amount of light which is extracted to air or the substrate. The simulation routine is summarized in a flow chart, fig. 4.2.

As the organic emitters have a broad spectral width it is intuitive that the simulations should be carried out at multiple frequencies (wavelengths). In this work, the

---

[*] For technical reasons, the upper integration limit is set to a certain value $|\vec{k}_{\mathrm{x,max}}|$ and not infinity in the simulation program, please see the appendix (A.4) for details.

[†] Please note that despite using the term in-plane wave "vector" for k_{x} further on, its magnitude is meant.

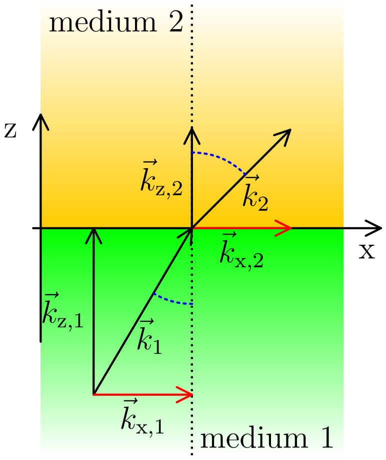

Figure 4.1.: Light traveling in medium 1 with wave vector $\vec{k}_1$ is having an in-plane wave vector $\vec{k}_{x,1}$, which is its projection on the interface of the layer. Additionally, for medium 2, the in-plane wave vector is identical due to the boundary conditions: $\vec{k}_{x,1} = \vec{k}_{x,2}$.

wavelength range usually is taken to be $400\,\mathrm{nm} \leqslant \lambda \leqslant 800\,\mathrm{nm}$. This requires that the optical constants for each layer of the OLED are also known in this spectral range. The simulation method has been implemented in a MAPLE program called "PDCalc" by Nils Reinke as part of his PhD work[68] and our collaboration with OSRAM OS, Regensburg, within the project "OPAL2008" funded by the German Federal Ministry of Education and Research (BMBF). The author of the present thesis fixed some bugs, adapted the program for batch mode processing (e.g., for layer thickness variations) and variable wavelength ranges/steps, implemented a code to identify and distinguish between waveguided modes and plasmons (which will be discussed later) and did intensive testing of the program and its parameters. The technical difficulties encountered (e.g., the right choice of the step size Δk_x or the runtime of one simulation) and their solution are subject of a chapter in the appendix (A.4) as this is not that interesting from a scientific point of view, however, a lot of man and machine time has been invested.

4.2.2. Application to a well-known OLED stack as an example

To explain the outcome of the simulation with the dipole model in detail, a well-known OLED stack, already introduced as reference design in this thesis, is chosen as a first example, as it shows all possible channels into which the generated light is emitted. The device structure is shown again in fig. 4.3. As the emission zone is known to be located at the TPD/Alq_3 interface, the location of the dipoles is set between those layers, with isotropic dipole orientation. However, in detail, the emission zone extends a few nanometers into the Alq_3 layer, but this is, for the sake of simplicity, neglected here and the location of the dipoles is assumed to be a δ-distribution. As stated

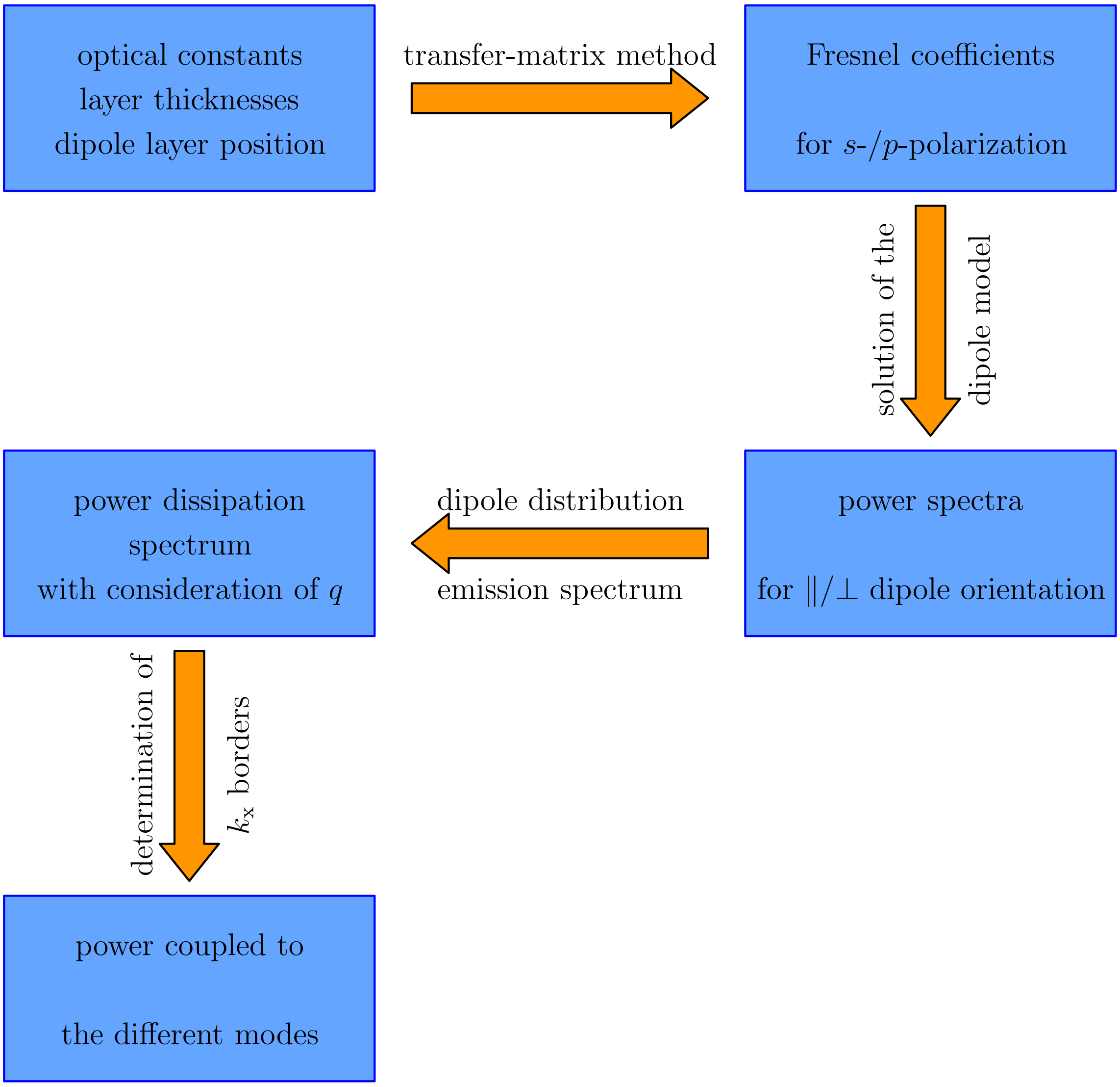

Figure 4.2.: Flow chart of the simulation routine “PDCalc” using the dipole model.

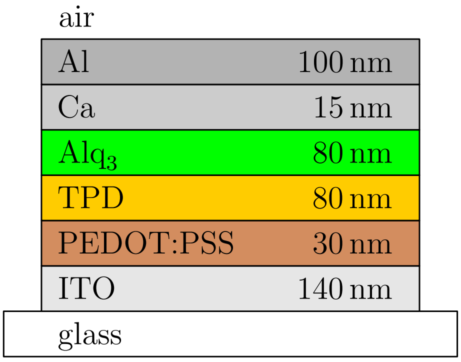

Figure 4.3.: Bottom-emitting OLED stack used as reference device.

earlier, the simulation is using the full wavelength range from 400 to 800 nm. The corresponding refractive indices for all layers can be found in the appendix (A.3) and have been obtained by ellipsometry measurements.

First, the power spectrum, i.e., the power radiated from the dipoles, is shown in fig. 4.4 as a function of the in-plane wave vector k_x and the wavelength λ. However, as the dipoles are not white emitters (meaning emitting at constant intensity for all wavelengths), this spectrum has to be weighed with the emission spectrum of the Alq$_3$ emitter (fig. 4.5), leading to the power dissipation spectrum shown in fig. 4.6. Additionally, a corresponding cross section at $\lambda = 525\,\mathrm{nm}$ (approximately peak wavelength of Alq$_3$) is also shown. As already indicated in these figures, there are four different regions, which are dependent on k_x and λ.

These regions need explaining: as stated in the previous section the in-plane wave vector k_x is constant for all layers. We first consider light which is coupled out from the OLED through the substrate into air: the wave vector magnitude is $k_\mathrm{air}(\lambda) = \frac{2\pi}{\lambda} \cdot n_\mathrm{air}$. Therefore the in-plane wave vector k_x can range between 0 (angle of emission $\theta = 0°$, perpendicular to the substrate) and its maximum value for emission to air $k_\mathrm{x,max,air} = k_\mathrm{air} = \frac{2\pi}{\lambda} \cdot n_\mathrm{air}$ (angle of emission $\theta = 90°$, parallel to the substrate). In other words, this means that light with an in-plane wave vector $k_\mathrm{x} \leqslant \frac{2\pi}{\lambda} \cdot n_\mathrm{air}$ can leave the device, which is region 1 in fig. 4.6. The depicted border itself corresponds to the emission angle $\theta = 90°$ in air.

The same arguments now can be used for light which is trapped in the glass substrate, region 2: $k_\mathrm{glass}(\lambda) = \frac{2\pi}{\lambda} \cdot n_\mathrm{glass}(\lambda)$ leading to $k_\mathrm{x,max,glass} = \frac{2\pi}{\lambda} \cdot n_\mathrm{glass}(\lambda)$. The power dissipation spectrum already shows that a large fraction of the generated light is trapped inside the substrate ($\frac{2\pi}{\lambda} \cdot n_\mathrm{air} \leqslant k_\mathrm{x} \leqslant \frac{2\pi}{\lambda} \cdot n_\mathrm{glass}(\lambda)$) due to total internal reflection at the glass/air interface. However, this fraction can be coupled out to air if outcoupling structures such as lenses, prisms, corrugated surfaces, or light-scattering foils are used to overcome the total internal reflection (indicated in fig. 4.7). For examples of different outcoupling techniques see Meerholz and Müller[69].

Region 3 shows two sharp modes. These are waveguided modes: the light is generated in and surrounded by organic layers with high refractive index ($n > 1.5$). The refractive indices of the OLED's boundaries (glass substrate and metal) are lower, leading to a waveguide structure. Based on the classical three-layer waveguide, a

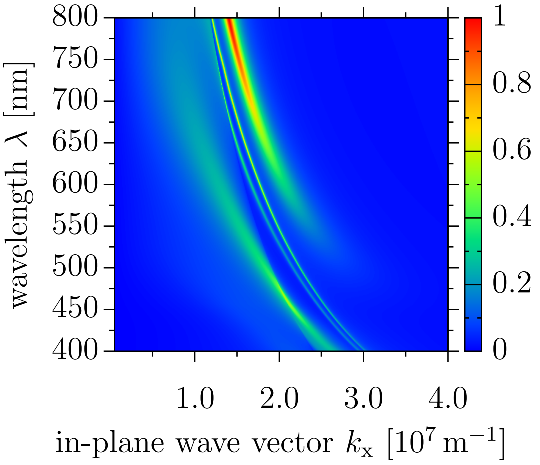

Figure 4.4.: Power spectrum of the OLED presented in fig. 4.3. Emitting dipoles as white emitters and isotropically distributed. (Step size for simulation: $\Delta k_x = 5 \cdot 10^4\,\mathrm{m}^{-1}$)

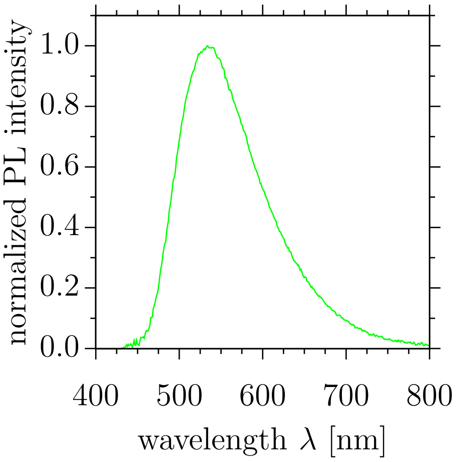

Figure 4.5.: Photoluminescence spectrum of the green emitter material $\mathrm{Alq_3}$.

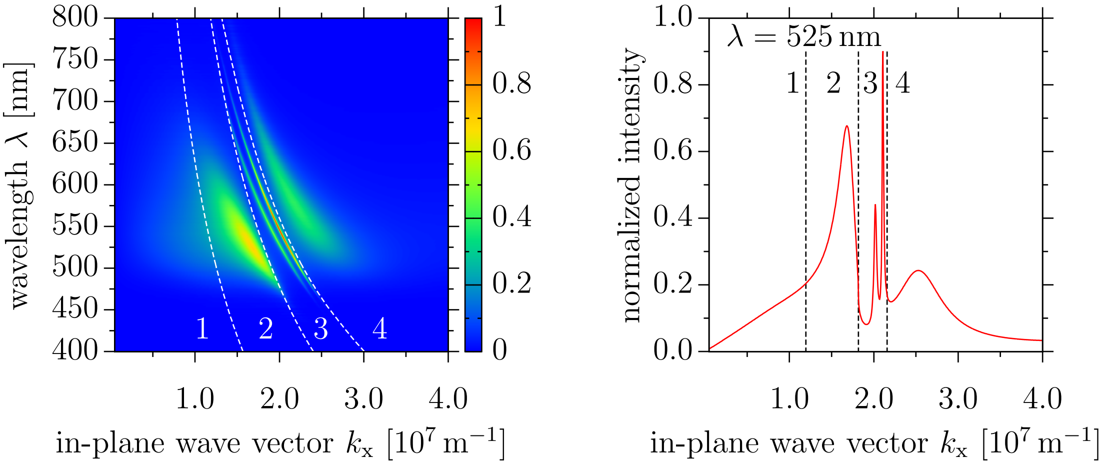

Figure 4.6.: Power dissipation spectrum of the OLED presented in fig. 4.3: power spectrum (fig. 4.4) weighed with $\mathrm{Alq_3}$ spectrum (fig. 4.5). Left: power dissipation spectrum for the full wavelength range. Right: cross section of the power dissipation spectrum at wavelength $\lambda = 525\,\mathrm{nm}$. Isotropic dipole distribution. (1) light emitted directly from the OLED, (2) light trapped inside substrate, (3) two sharp waveguided modes, and (4) plasmons. ($\Delta k_x = 5 \cdot 10^4\,\mathrm{m}^{-1}$)

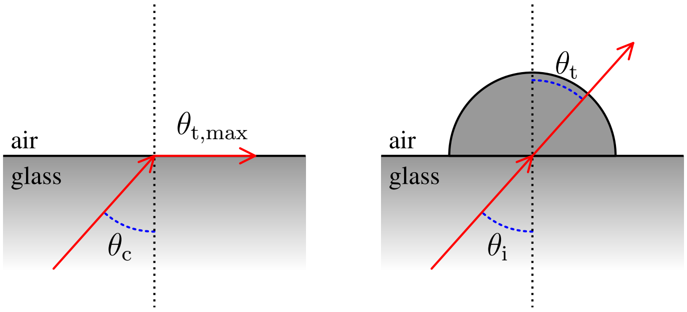

Figure 4.7.: Left: glass/air interface without outcoupling structure. Right: light outcoupling of substrate modes with the use of a hemisphere as outcoupling structure. Other possible outcoupling structures are, e.g., prisms, lenses, or light-scattering foils.

transfer-matrix method[48] was implemented to identify these modes, also using the wavelength dependent complex refractive indices and layer thicknesses of all layers involved. As the transverse resonance condition (eq. (3.93)) is different for the different polarizations, the program distinguishes between TE (transverse electric or *s*-polarized) and TM (transverse magnetic or *p*-polarized) modes, see fig. 4.8. The two sharp modes can be identified as a TM and a TE waveguided mode (the latter having higher k_{x} values) in the organic and adjacent ITO electrode. As the program is not limited to the waveguided regime (value of k_{x}), it also shows that the light trapped in the substrate (region 2) is mainly *s*-polarized and that the broad feature in region 4 is *p*-polarized.

This broad feature in region 4 is a surface plasmon polariton. Plasmons always have TM polarization and therefore are successfully identified by the above described program. A requirement for the plasmon is a high value in k_{x}. However, drawing the border between waveguiding and plasmons is not intuitive at once. At first glance, one could suggest that the excitation of plasmons is possible for in-plane wave vectors $k_{\mathrm{x}} > \frac{2\pi}{\lambda} \cdot n_{\mathrm{Alq_3}}(\lambda)$ (this is the maximum wave vector for light generated in the Alq$_3$ layer). However, in the case of the OLED we must consider the use of thin films. We can do this by calculating an effective refractive index $n_{\mathrm{ITO+organic}}(\lambda)$ of the ITO and organic layers taken together. It is calculated from the complex dielectric functions $\hat{\varepsilon}$ of these layers, similar to calculating the capacitance of a plate capacitor with several dielectric media (effective medium approach):

$$\hat{\varepsilon}_{\mathrm{ITO+organic}} = \frac{\sum\limits_i d_i}{\sum\limits_i \frac{d_i}{\hat{\varepsilon}_i}} . \tag{4.12}$$

Here d_i and $\hat{\varepsilon}_i$ are the thickness and complex dielectric function of layer i, respectively. Therefore, $\sum\limits_i d_i$ is the total thickness $d_{\mathrm{ITO+organic}}$ of the layers contributing to waveguided modes. As

$$\hat{\varepsilon} = \varepsilon_1 + \mathrm{i} \cdot \varepsilon_2 \equiv \hat{N}^2 = (n - \mathrm{i}\kappa)^2 , \tag{4.13}$$

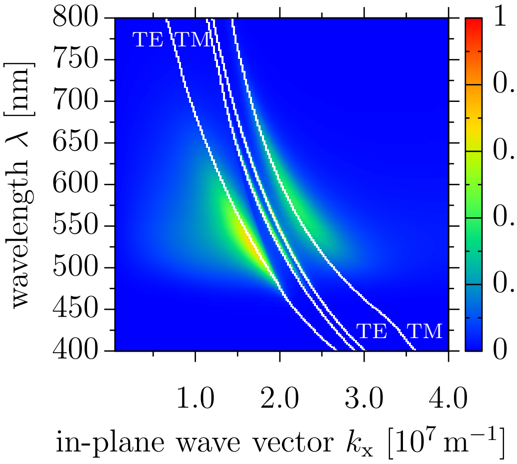

Figure 4.8.: Identification of TE (transverse electric or *s*-polarized) and TM (transverse magnetic or *p*-polarized) modes. Same power dissipation spectrum as fig. 4.6.

where $\varepsilon_1 = \mathrm{Re}\,(\hat{\varepsilon})$, $\varepsilon_2 = \mathrm{Im}\,(\hat{\varepsilon})$, $\hat{N}$ being the complex refractive index (assuming non-magnetic materials with $\mu = 1$), n the refractive index and κ the extinction coefficient, it follows that

$$n = \sqrt{\frac{\sqrt{\varepsilon_1^2 + \varepsilon_2^2} + \varepsilon_1}{2}} \tag{4.14}$$

$$\kappa = \sqrt{\frac{\sqrt{\varepsilon_1^2 + \varepsilon_2^2} - \varepsilon_1}{2}}\,. \tag{4.15}$$

Using eq. (4.12) and (4.14) the effective refractive index $n_{\mathrm{ITO+organic}}\,(\lambda)$ has been calculated and the border between waveguided modes and plasmons thus can be determined. For $k_x > \frac{2\pi}{\lambda} \cdot n_{\mathrm{ITO+organic}}\,(\lambda)$ the dipoles couple to the plasmons traveling at the organic/metal interface.

The four different regions and their limits are summarized in table 4.1. Integrating over the different regions in the polychromatic power dissipation spectrum (fig. 4.6) leads to the amount of power coupled into the different modes. For the OLED presented in fig. 4.3, having $\mathrm{Alq_3}$ as emitter with radiative QE $q = 0.2$, we obtain: light emitted directly: 4.2 %, light emitted to the substrate: 6.3 %, waveguided modes: 3.0 %, plasmons: 9.5 %, absorption: 3.3 %, and all other (intrinsic non-radiative) losses 73.7 % (for a graphic representation please see fig. 4.9). Keeping in mind that $\mathrm{Alq_3}$ is a singlet emitter, the numbers have to be multiplied by a factor of $\eta_{\mathrm{s/t}} = 1/4$ in order to obtain the external quantum efficiency (eq. (4.1)) of about 1 % (only direct emission) for this OLED, which is in good agreement with published results[8,70]. The value of the intrinsic non-radiative losses of 73.7 % also deserves some comment. Starting with a QE of 20 %, one would expect this value to be exactly 80 %; however, as will be

	k_x limits	**description**
region 1	$0 < k_\text{x} < \frac{2\pi}{\lambda}$	direct emission
region 2	$\frac{2\pi}{\lambda} < k_\text{x} < \frac{2\pi}{\lambda} \cdot n_\text{glass}$	emission to substrate
region 3	$\frac{2\pi}{\lambda} \cdot n_\text{glass} < k_\text{x} < \frac{2\pi}{\lambda} \cdot n_\text{ITO+organic}$	waveguided modes
region 4	$k_\text{x} > \frac{2\pi}{\lambda} \cdot n_\text{ITO+organic}$	plasmons

Table 4.1.: Limits of the in-plane wave vector k_x and description of the four different regions shown in the power dissipation spectrum (fig. 4.6).

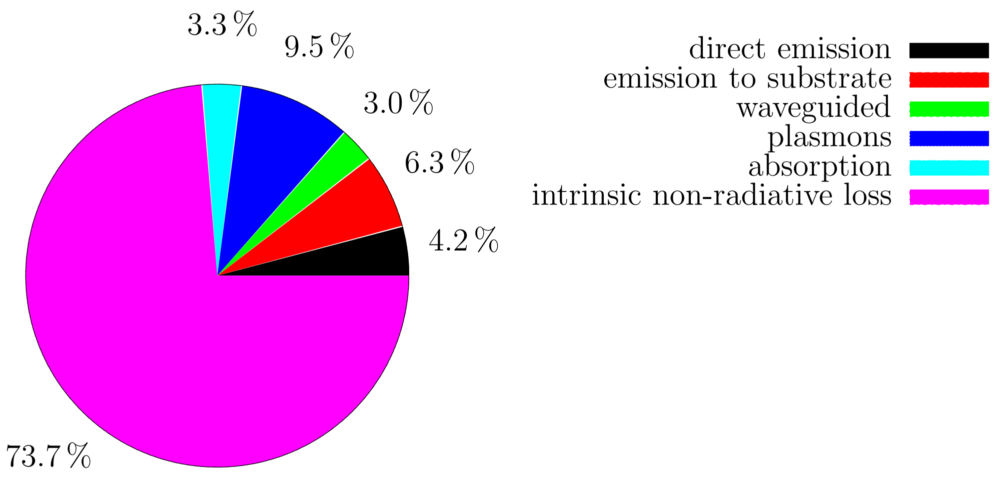

Figure 4.9.: Amount of power coupled into the different channels for the OLED presented in fig. 4.3. QE of Alq_3: $q = 0.2$.

discussed in detail later, the presence of microcavity effects in an OLED modifies the radiative rates of the emitting molecules, thus modifying the QE.

4.2.3. Verification of the dipole model

As stated in the previous chapter, the dipole model is able to predict the experimental EQE of the reference OLED. However, to justify the use of the dipole model and verify “PDCalc” it is beneficial to compare its results both to other experimental data and calculations from literature.

Angular emission spectra

First, the simulation results for the reference OLED (fig. 4.3) are compared to the experimental angular dependent emission spectra which are recorded with a calibrated spectrometer (see ch. 2.7). Usually, the angular emission spectra of the plain OLED substrate are recorded. Furthermore, a semicircle prism can be attached as outcoupling structure to the OLED's glass substrate by applying an optical gel. Compared to the spectrum without the prism, this additionally allows the study of the substrate modes (fig. 4.7).

As the simulation results have discrete k_x steps as independent variable and not emission angles, the external angle of emission θ has to be calculated from a given in-plane wave vector component k_x and a corresponding wave vector $k\left(n\left(\lambda\right),\lambda\right)$:

$$\theta(k_\mathrm{x},\lambda) = \arcsin\left(\frac{k_\mathrm{x}}{k\left(n\left(\lambda\right),\lambda\right)}\right) = \arcsin\left(\frac{k_\mathrm{x}}{2\pi n(\lambda)}\cdot\lambda\right) . \tag{4.16}$$

The refractive index $n(\lambda)$ is either the refractive index of air n_air (for emission to air) or of the glass substrate n_glass (for light originally trapped inside the substrate). As the power dissipation spectrum represents the power emitted to a hemisphere, the data has to be divided by $\sin\theta$ as the angular emission spectrum is a cross section of the hemisphere (see fig. 4.10). Furthermore, a multiplication with $\cos\theta$ is necessary to account for the change in visible area A_eff of the device while rotating, $A_\mathrm{eff} = A\cdot\cos\theta$, A being the area visible at $\theta = 0°$. In summary, a given value of k_x from the power dissipation spectrum results in an angle θ (eq. (4.16)) and the data at this angle is obtained as:

$$\begin{aligned}\mathrm{data}(\theta,\lambda) &= \frac{\mathrm{data}(k_\mathrm{x},\lambda)}{\sin\theta}\cdot\cos\theta\\ &= \frac{\mathrm{data}(k_\mathrm{x},\lambda)\cdot 2\pi n(\lambda)}{k_\mathrm{x}\cdot\lambda}\cdot\cos\left(\arcsin\left(\frac{k_\mathrm{x}}{2\pi n\left(\lambda\right)}\cdot\lambda\right)\right) .\end{aligned} \tag{4.17}$$

With eq. (4.16) and (4.17) the angular emission spectra are calculated from the simulated data and compared to the experimental data. This is shown, with distinction of s- and p-polarization, in fig. 4.11 for the direct emission and in fig. 4.12 for the substrate modes.

The experimental and simulated spectra for the direct emission (fig. 4.11) are in very good agreement concerning the angular characteristics, see also fig. 4.13a for a single wavelength, $\lambda = 525\,\mathrm{nm}$. The spectral pattern is slightly broadened at longer wavelengths in the simulation; the reason might be a too broad PL spectrum of Alq_3 used in the simulations. Both, simulation and experiment, show the maximum emission perpendicular to the substrate ($\theta = 0°$). The decrease in the emission intensity at higher angles θ nearly follows Lambert's cosine law (fig. 4.13a). Since the emission pattern is changing very little with the angle θ, the device's color stability is very good, see fig. 4.14a for the chromaticity coordinates. Light emitted from this reference device is mainly unpolarized, since the s-polarized and p-polarized spectra differ only very little.

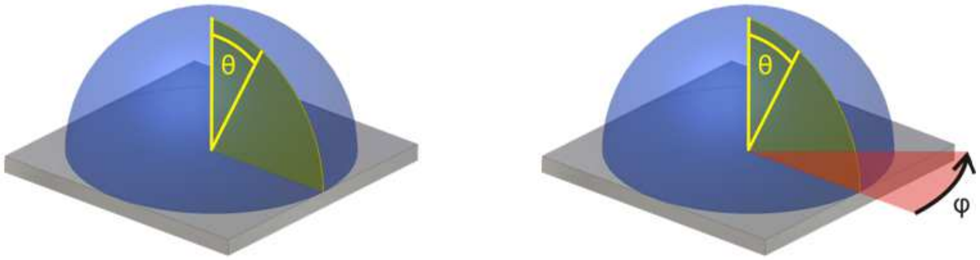

Figure 4.10.: The angular emission $I_{\text{angular}}(\theta)$ is a cross section of the emission to a hemisphere (left). The total power I_{integral} is the integration of $I_{\text{angular}}(\theta)$ over the element area $\mathrm{d}A = \sin\theta \; \mathrm{d}\varphi \, \mathrm{d}\theta$ (right): $I_{\text{integral}} = \int_0^{\pi/2} \int_0^{2\pi} I_{\text{angular}}(\theta) \cdot \sin\theta \; \mathrm{d}\varphi \, \mathrm{d}\theta = 2\pi \cdot \int_0^{\pi/2} I_{\text{angular}}(\theta) \cdot \sin\theta \; \mathrm{d}\theta$. In terms of the power dissipation spectrum for angle θ, $I_{\text{pd}}(\theta)$, the total power is $I_{\text{integral}} = 2\pi \cdot \int_0^{\pi/2} I_{\text{pd}}(\theta) \; \mathrm{d}\theta$. A comparison yields that the factor $\sin\theta$ has to be accounted when calculating the angular emission spectra from the power dissipation spectra.

With attached semicircle prism to the glass substrate, the simulated spectra are again in good agreement with the experiment (fig. 4.12 and fig. 4.13b for $\lambda = 525\,\text{nm}$). Comparison of these results to the OLED with planar substrate (fig. 4.11) shows that in the latter a considerable amount of radiation is trapped inside the glass substrate. As the intensity of light emitted perpendicular to the substrate is the same for both cases (with and without prism), there is actually a big portion of light emitted at large angles; the peak intensity at about $\theta \approx 65°$ is almost two times higher than the peak intensity of the perpendicular emission ($\theta = 0°$). Please note that the figures 4.11 and 4.12 are normalized with respect to the highest intensity obtained in each of them except that corresponding *s*- and *p*-polarized spectra are normalized with the same factor. The difference in *s*- and *p*-polarized emission shows that the substrate-guided light is *s*-polarized, which is consistent with the simulation and the identification of modes in fig. 4.8. So after attaching an outcoupling structure to the OLED substrate, an *s*-polarized leaky mode is emitted, having a slight dispersion in the wavelength. Hence the color at different viewing angles θ is not stable, see fig. 4.14b for the corresponding chromaticity coordinates.

The dipole model is also suited to simulate microcavity OLEDs. Based on the reference OLED (fig. 4.3), a device with a thin (i.e., semi-transparent) Ag anode (substituting ITO and PEDOT:PSS) and slightly different cathode, see fig. 4.15, is analyzed. The corresponding power dissipation spectrum is shown in fig. 4.16, the experimental and simulated angular emission spectra in fig. 4.17. The features of the angular emission of the microcavity OLED are again well represented by the simulation. In contrast to the reference ITO-OLED, the emission spectrum of this microcavity device is now strongly dependent on the emission angle θ and mainly *s*-polarized. Also the angular emission spectra are changing drastically over a wide wavelength range. This is even more pronounced if the semicircle prism is attached to the microcavity device (not shown here). For the chromaticity coordinates, please see fig. 4.18. The simulations have also been verified with experimental data for other

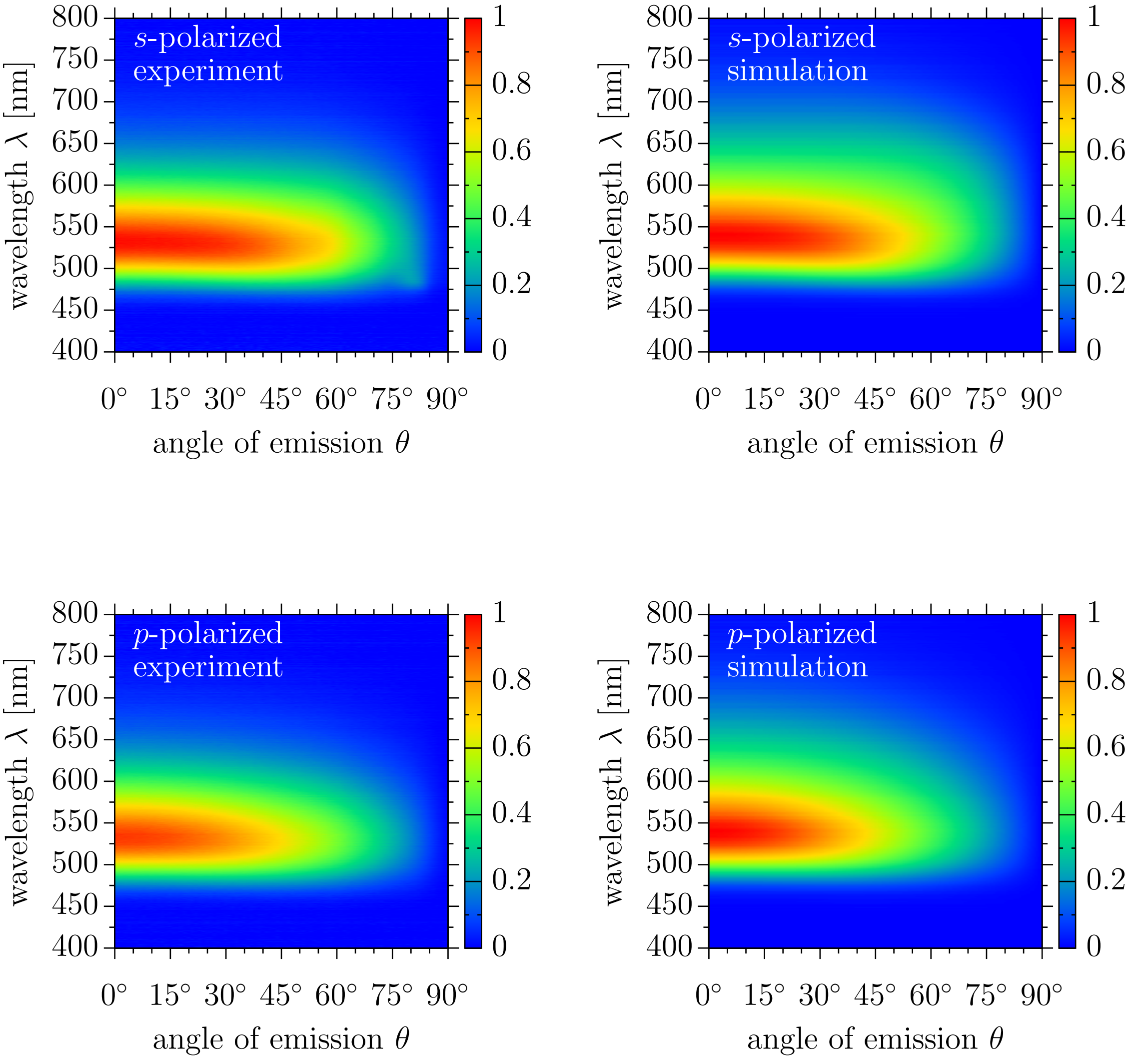

Figure 4.11.: Angular emission spectrum of the reference OLED (fig. 4.3) with distinction of s- and p-polarization. Left: experiment. Right: simulation. For a cross section at wavelength $\lambda = 525\,\text{nm}$, please see fig. 4.13a.

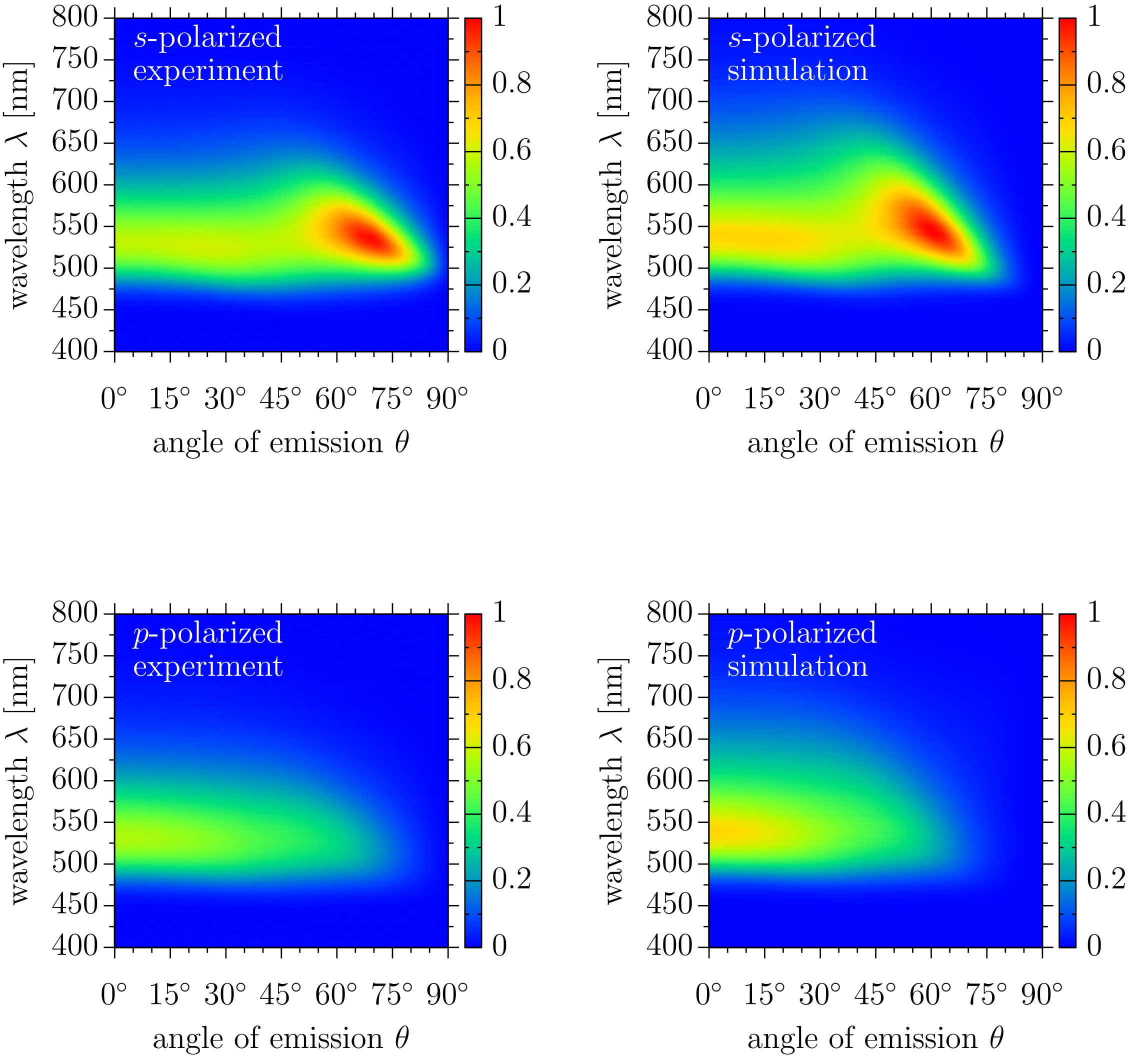

Figure 4.12.: Angular emission spectrum of the reference OLED (fig. 4.3) with attached semi-circle prism (no total internal reflection at the glass/air interface, fig. 4.7) with distinction of s- and p-polarization. Left: experiment. Right: simulation. For a cross section at wavelength $\lambda = 525\,\mathrm{nm}$, please see fig. 4.13b.

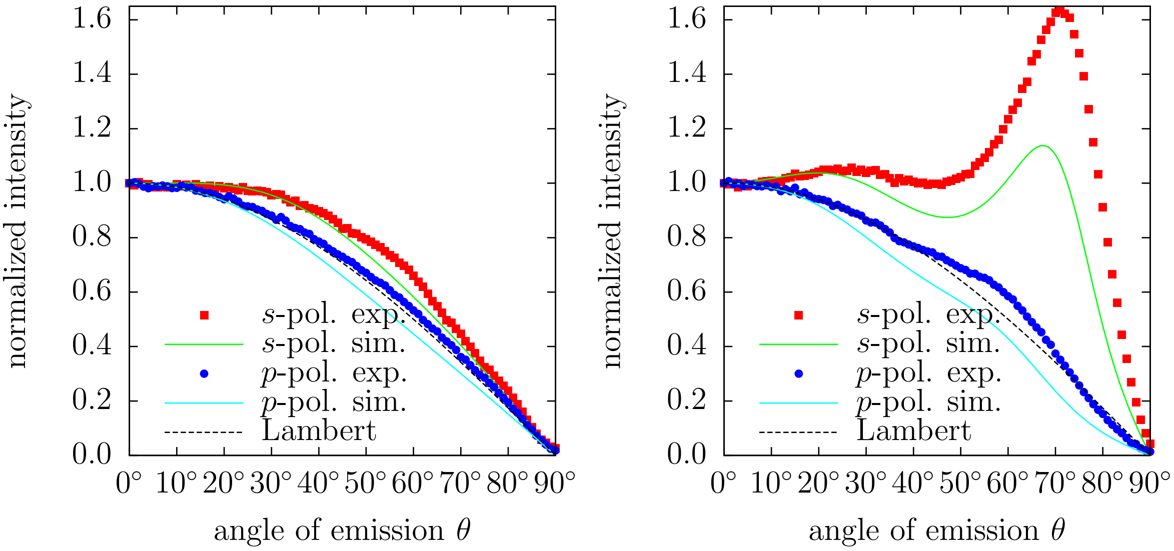

(a) *Direct emission.*

(b) *Emission with substrate modes (attached semi-circle prism).*

Figure 4.13.: Angular emission spectrum for wavelength $\lambda = 525\,\text{nm}$. Additionally, Lambert's cosine law is shown (black dashed line). Only very small variations in experimental and simulated data for light emitted directly. Slightly lower values in the simulation of substrate modes, however, similar curve progression. Simulation data compensated for the refractive index of the fused silica semi-circle prism.

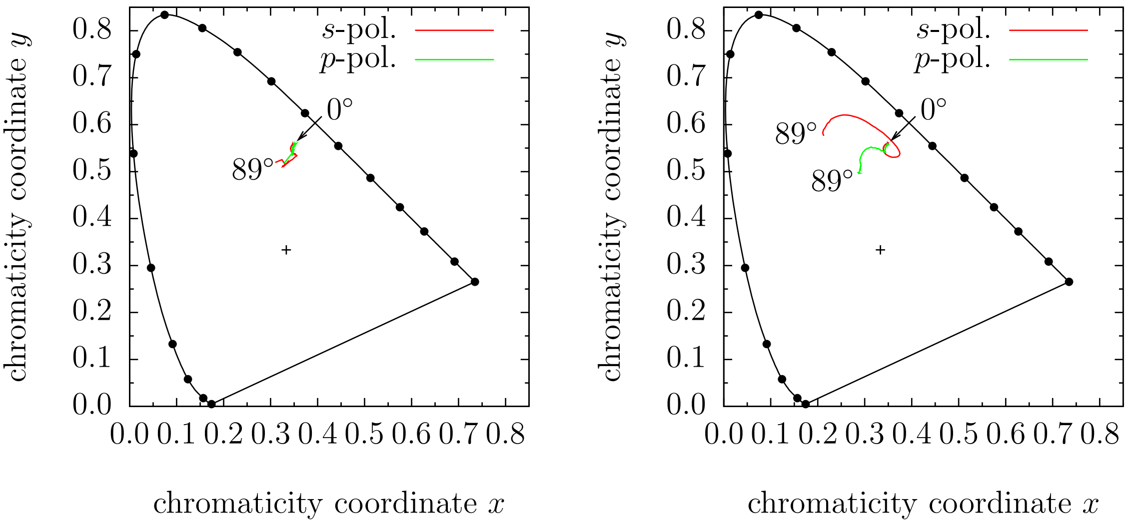

(a) *Direct emission.*

(b) *Emission with substrate modes (attached semi-circle prism).*

Figure 4.14.: Chromaticity coordinates for light emitted from the reference OLED under different angles θ calculated from the experimental values shown in fig. 4.11 and 4.12. Direct emission: good color stability. Emission with substrate modes: color is changing with viewing angle (dispersion in wavelength).

microcavity OLEDs with different anode metals, but these are not shown here.

Comparison to data from literature

Simulations using "PDCalc" have also been compared to data from literature. Two examples shall be shown here; however, further examples will follow in the next chapters. First, calculations of a famous paper by Adachi et al. are presented, as this was the first report of an OLED stack with a phosphorescent emitter with nearly 100 % internal quantum efficiency[71]. The stack comprises a glass substrate covered with 160 nm ITO, 60 nm HTL (HMTPD), 25 nm EML (12 % of $(ppy)_2Ir(acac)$ doped into a TAZ host), 50 nm ETL (Alq_3), and 150 nm Mg:Ag (10 : 1) as cathode covered with 20 nm Ag as capping layer, see fig. 4.19. The chemical names of the materials can be found in the appendix (A.1). To simplify their simulation, Adachi et al. model the OLED as a four layer device (fig. 4.20): glass ($n_{\text{glass}} = 1.5$), 160 nm ITO ($\hat{N}_{\text{ITO}} = 1.9 - 0.01\text{i}$), 125 nm organic layer ($n_{\text{organic}} = 1.7$), and semi-infinite Mg:Ag ($\hat{N}_{\text{Mg:Ag}} = 0.25 - 4.36\text{i}$). Glass and the organic layer are considered to be non-absorbing. The distance of the emitting dipoles from the cathode is varied within the limits of the organic layer. Please note that there is an inconsistency in the original paper[71] for the thickness of all organic layers (135 nm) and the thickness (125 nm) used in the simplified structure. From their calculations, see fig. 4.21a, the authors come to the conclusion that for maximum light outcoupling (direct emission) the dipoles should be located 75 nm

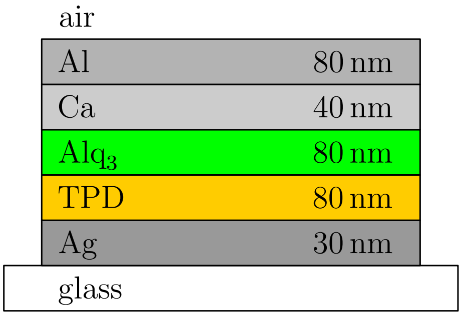

Figure 4.15.: Microcavity OLED stack based on the reference device (fig. 4.3) with a thin silver anode instead of ITO/PEDOT:PSS and slightly different cathode thickness.

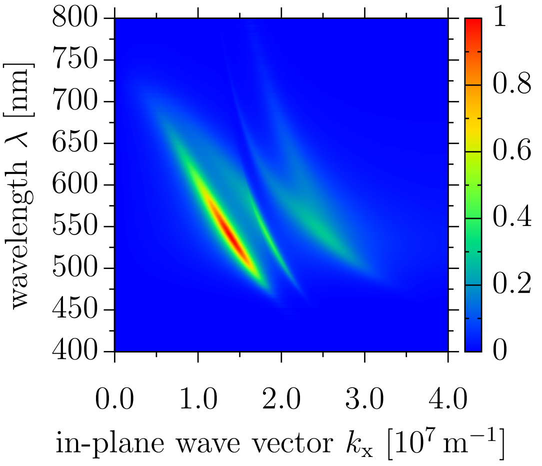

Figure 4.16.: Power dissipation spectrum of the microcavity OLED with thin Ag anode (fig. 4.15). ($\Delta k_x = 5 \cdot 10^4\,m^{-1}$)

from the cathode, resulting in the above described OLED stack. The simplified OLED stack is now investigated with “PDCalc” using the same refractive indices. As, unfortunately, the emission spectrum of (ppy)$_2$Ir(acac) was not available two cases have been simulated: a monochromatic calculation at wavelength $\lambda = 520\,nm$ (peak wavelength of the emitter[71]) and a calculation assuming a white emission spectrum. The results for the direct emission and an emitter quantum efficiency of $q = 1$ are shown in fig. 4.21b. Both results from “PDCalc” are quite similar to the results from Adachi et al. Differences for small distances of the dipoles to the cathode ($d < 20\,nm$) or anode ($d > 105\,nm$) are due to slightly different simulation routines and are not of further interest at this point. The monochromatic calculation yields a maximum outcoupling efficiency of 19.9 % at a dipole distance of 70 nm to the cathode and the white emission calculation yields 21.6 % at 76 nm. For more accurate results the emission spectrum of (ppy)$_2$Ir(acac) would be needed. But still, these numbers are in good agreement with the data from the original paper: (22 ± 2) % at 75 nm.

The main result of the paper also deserves some comment: the external quantum efficiency was measured to be $\eta_{EQE} = (19.0 \pm 0.5)\,\%$ and thus, after eq. (4.1), they claim nearly 100 % internal quantum efficiency for the emitter, however, calculated it to be (87 ± 7) %. This represents the usual way found in literature: perform the simulation for a quantum efficiency $q = 1$, calculate the outcoupling efficiency, compare the simulation with the experimental EQE value and adjust the quantum efficiency accordingly. However, as will be shown in the following chapter, the quantum efficiency of an emitter is influenced by its surroundings (the OLED stack) and the above method is not quite correct. The simulation has to be performed with the actual

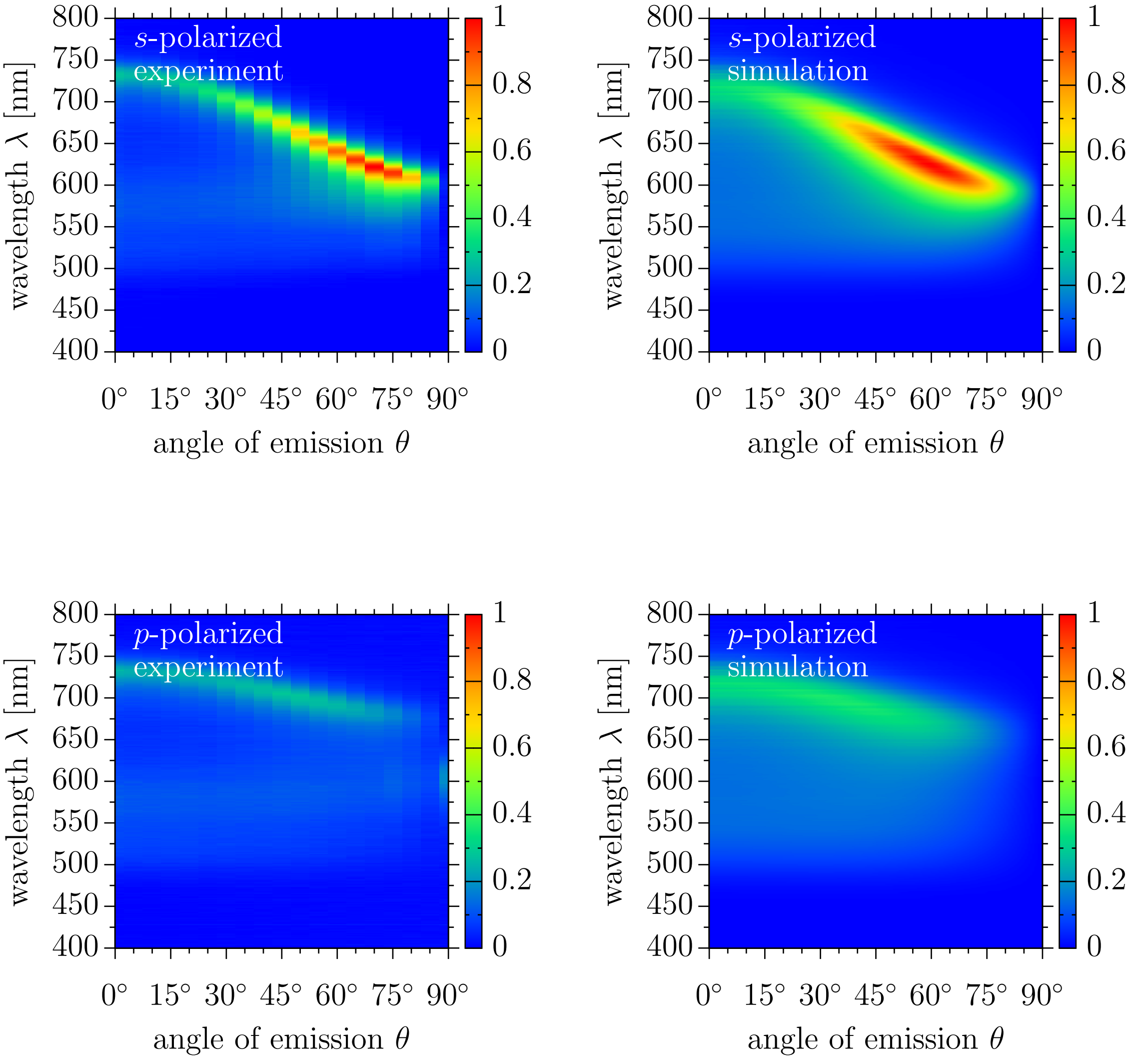

Figure 4.17.: Angular emission spectrum of the microcavity OLED (fig. 4.15) with distinction of *s*- and *p*-polarization. Left: experiment (unfortunately using a primitive setup). Right: simulation.

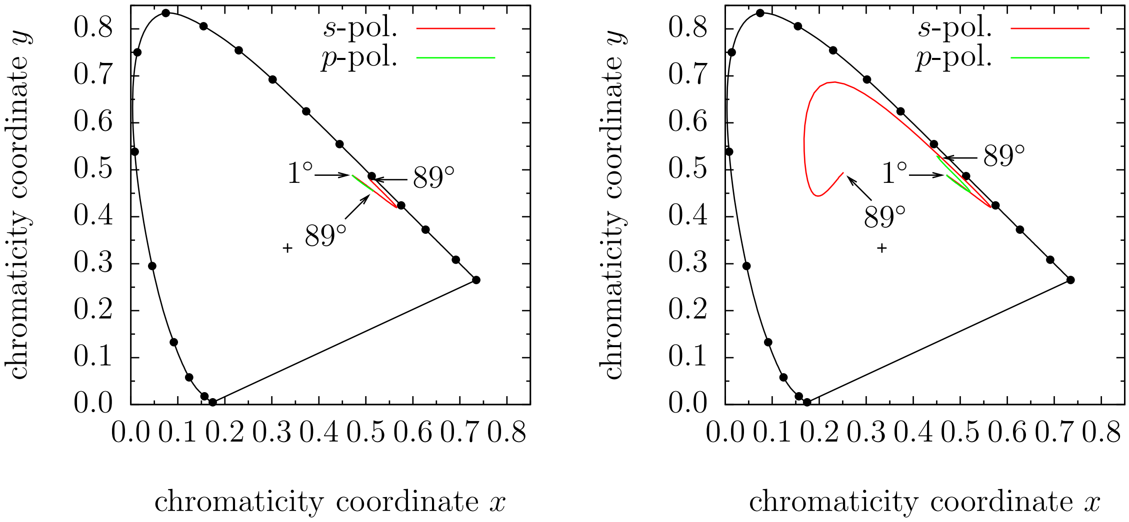

(a) *Direct emission.*

(b) *Emission with substrate modes.*

Figure 4.18.: Chromaticity coordinates for light emitted from the microcavity OLED (fig. 4.15) under different angles θ calculated from the simulated values. Color is changing with viewing angle in both cases, however, even more drastically when using outcoupling structures.

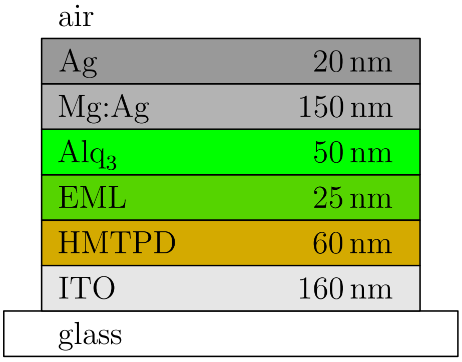

Figure 4.19.: OLED stack used by Adachi et al.[71]. Emission layer: TAZ:$(ppy)_2Ir(acac)$. Dipole layer located at the HMTPD/TAZ:$(ppy)_2Ir(acac)$ interface.

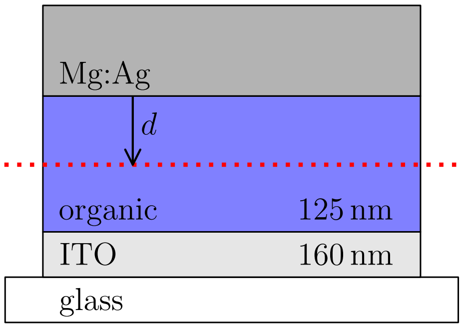

Figure 4.20.: Simplified OLED stack used for calculation by Adachi et al.[71]. Refractive indices used: $n_{\mathrm{glass}} = 1.5$, $\hat{N}_{\mathrm{ITO}} = 1.9 - 0.01\mathrm{i}$, $n_{\mathrm{organic}} = 1.7$, and $\hat{N}_{\mathrm{Mg:Ag}} = 0.25 - 4.36\mathrm{i}$. Distance d of the dipole layer to the cathode subject of variation. Mg:Ag cathode semi-infinite.

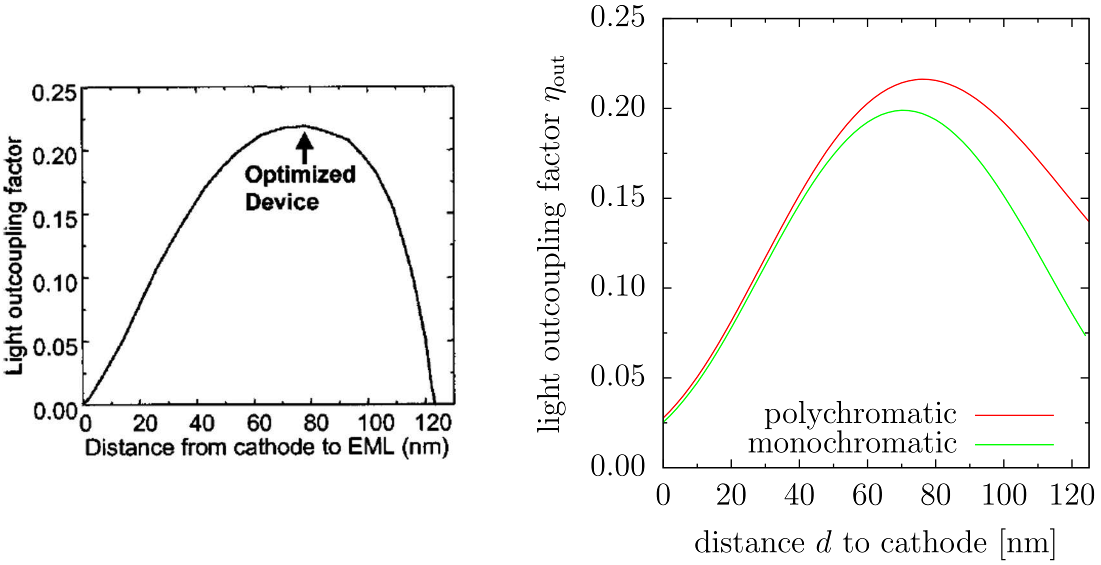

(a) *Picture taken from Adachi et al.*[71]. ***(b)*** *Calculated using "PDCalc".*

Figure 4.21.: Calculated outcoupling efficiency for directly emitted light for the simplified stack shown in fig. 4.20. Variation of the distance d of the emitting dipoles to the cathode. Left: calculation by Adachi et al.[71]. Right: calculated using "PDCalc". Green curve: monochromatic calculation ($\Delta k_x = 1 \cdot 10^3\,\mathrm{m}^{-1}$), $\lambda = 520\,\mathrm{nm}$. Red curve: polychromatic calculation, using a white emitter ($\Delta k_x = 2 \cdot 10^5\,\mathrm{m}^{-1}$). For both calculations $q = 1$, $\Delta d = 2\,\mathrm{nm}$.

quantum efficiency of the emitter, resulting in an effective quantum efficiency q_{eff} for the particular OLED stack, differing from the free-space value. If one assumes $q = 0.87$ in "PDCalc" as calculated by Adachi et al., the calculated EQE at 76 nm distance is 19.6 % (not 21.6 % as before) with an effective quantum efficiency of $q_{\mathrm{eff}} = 0.91$ (calculation for the white emission spectrum).

The second example is a report by Lin et al.[72], showing an inverted bottom-emitting OLED with doped injection layers. The device consists of a glass substrate, 120 nm ITO, 20 nm EIL (BPhen:Cs, 5 wt %), 20 nm ETL (BPhen), 20 nm EML (Alq_3:C545T, 1 wt %), 40 nm HTL (α-NPD), a HIL (m-MTDATA:F_4-TCNQ, 1.5 wt %) with variable thickness d, and 100 nm Ag, see fig. 4.22. Again, the chemical names can be found in the appendix (A.1). The refractive indices (shown in the appendix (A.3)) and the emission spectrum of the fluorescent dye C545T (fig. 4.23) have been provided by Sami Hamwi, TU Braunschweig. Unfortunately, the complex refractive index of m-MTDATA has not been available; as a substitute the refractive indices of α-NPD have been used in the calculations, as they should not differ too much. The calculated outcoupling factor by Lin et al. for a thickness variation of the HIL m-MTDATA:F_4-TCNQ is shown in fig. 4.24a along with the external quantum efficiency of four devices. The resemblance between calculated and experimental efficiency is quite good, however, a detailed analysis would require more experimental data points. Comparing the numbers of the outcoupling efficiency and the EQE requires a quantum efficiency of

$q = 1$ for the fluorescent emitter C545T (after eq. (4.1)), which seems unlikely. Again, more experimental data would be needed for a thorough investigation. Comparing the calculated results to the calculations with "PDCalc", fig. 4.24b, for $q = 1$, again shows the same tendencies. To complete the comparison of this OLED stack the amount of power coupled into the different modes calculated by Lin et al. and "PDCalc" are shown in fig. 4.25 and fig. 4.26, respectively. Again, these results are a comforting assurance for the reliability of "PDCalc". The different trends of the amount of power coupled into the different modes is not discussed at this point; beforehand, several other, simpler, stacks have to be discussed (see the following chapters).

4.3. Microcavity effects on the internal quantum efficiency

The radiative quantum efficiency q, which is defined as the efficiency of radiative decay of the emitter material in an unbounded space filled by the dye and its matrix, is a crucial factor in the simulation, as it handles any non-radiative decay of the emitting dipoles,

$$q = \frac{k_\mathrm{r}}{k_\mathrm{r} + \sum k_\mathrm{nr}} \,, \tag{4.18}$$

where k_r is the radiative decay rate and $\sum k_\mathrm{nr}$ denotes the sum of the decay rates of all competing processes. In the work of Smith et al.[65], effects of a quantum efficiency smaller than 100 % have been discussed; however, the impact on the simulation and device optimization of OLEDs has not been investigated in detail.

The effect of the radiative quantum efficiency q on the external quantum efficiency η_EQE of the OLED can be described by the following equation:

$$\eta_\mathrm{EQE} = \gamma \cdot \eta_\mathrm{s/t} \cdot q_\mathrm{eff} \cdot \eta_\mathrm{out} \,, \tag{4.19}$$

where, as before (eq. (4.1)), γ is the charge balance factor, $\eta_\mathrm{s/t}$ is the singlet/triplet ratio (for fluorescent emitters it is assumed that $\eta_\mathrm{s/t} = 1/4$ and for phosphorescent emitters $\eta_\mathrm{s/t} = 1$), and η_out is the outcoupling factor. The presence of a cavity, for example, due to the electrodes in an OLED, influences the lifetime of the radiative dipoles[56,57,59]. This means that the radiative decay channel of the dipoles can be attenuated or enhanced due to the surrounding material of the dipole or the presence of interfaces, in particular to metals, due to changes in the reflected electric field E_r (eq. (4.4)). As a consequence the radiative quantum efficiency q (defined for an emitter in an unbounded medium) has to be replaced by an effective quantum efficiency q_eff (depending on q), which has the consequence that for a given (experimentally determined) value of the external quantum efficiency the outcoupling factor η_out will change, too. Therefore, we define q_eff as the radiative quantum efficiency of an excited molecule due to the presence of the cavity,

$$q_\mathrm{eff} = \frac{k_\mathrm{r}^*}{k_\mathrm{r}^* + \sum k_\mathrm{nr}} \,, \tag{4.20}$$

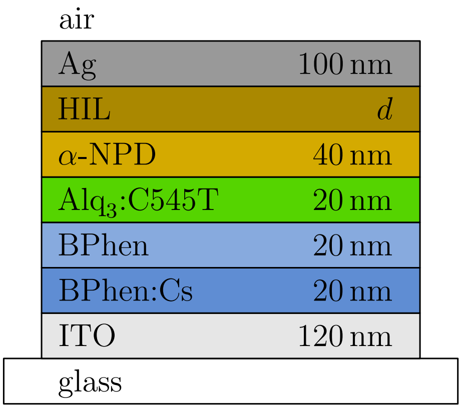

Figure 4.22.: Inverted OLED stack used by Lin et al.[72]. HIL: m-MTDATA:F_4-TCNQ. Dipole layer located at the α-NPD/Alq_3:C545T interface.

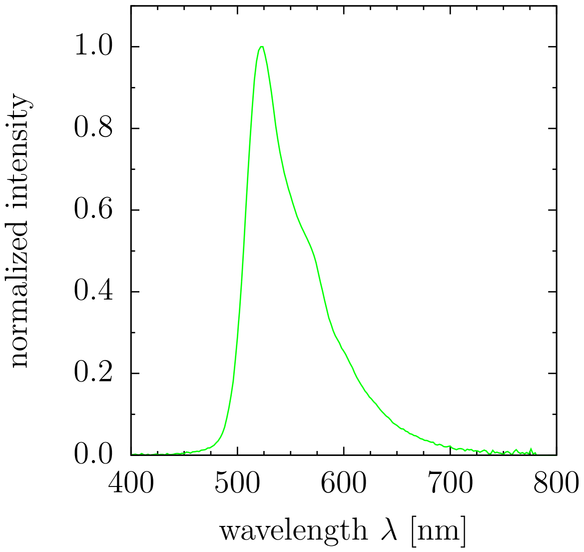

Figure 4.23.: Emission spectrum of the dye C545T. Courtesy of Sami Hamwi, TU Braunschweig.

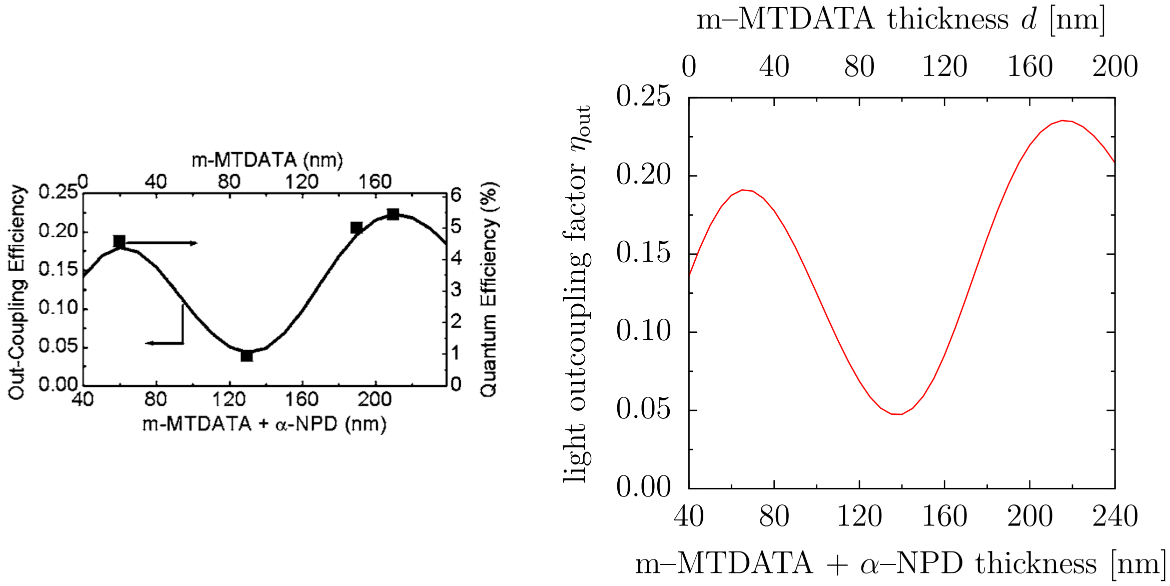

(a) *Picture taken from Lin et al.*[72]*.*

(b) *Calculated using "PDCalc".*

Figure 4.24.: Calculated outcoupling efficiency depending on the m-MTDATA thickness d for the stack shown in fig. 4.22. Left: calculation by Lin et al.[72], additionally showing the external quantum efficiency of four devices. Right: calculated by "PDCalc". m-MTDATA simulated as α-NPD. ($q = 1$, $\Delta k_{\mathrm{x}} = 2{\cdot}10^5\,\mathrm{m}^{-1}$, $\Delta d = 5\,\mathrm{nm}$, $400\,\mathrm{nm} \leqslant \lambda \leqslant 780\,\mathrm{nm}$)

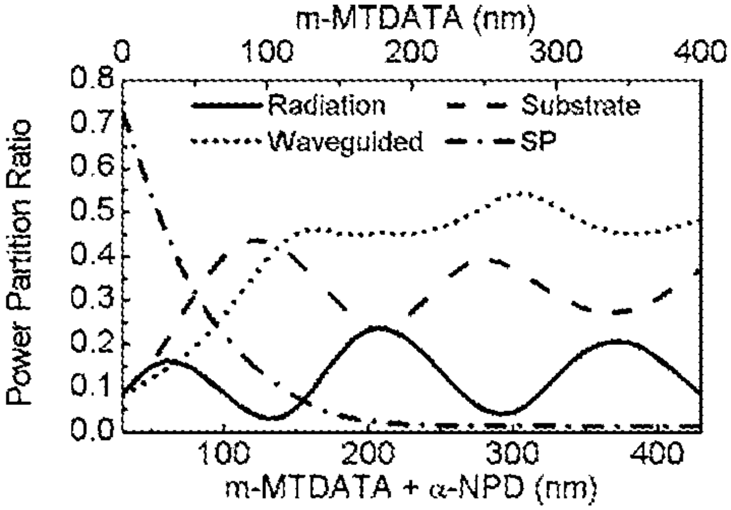

Figure 4.25.: Amount of power coupled into the different modes as determined by Lin et al. for the stack shown in fig. 4.22 with different m-MTDATA thickness[72]. Radiation: direct emission. Substrate: emission to substrate. SP: plasmons.

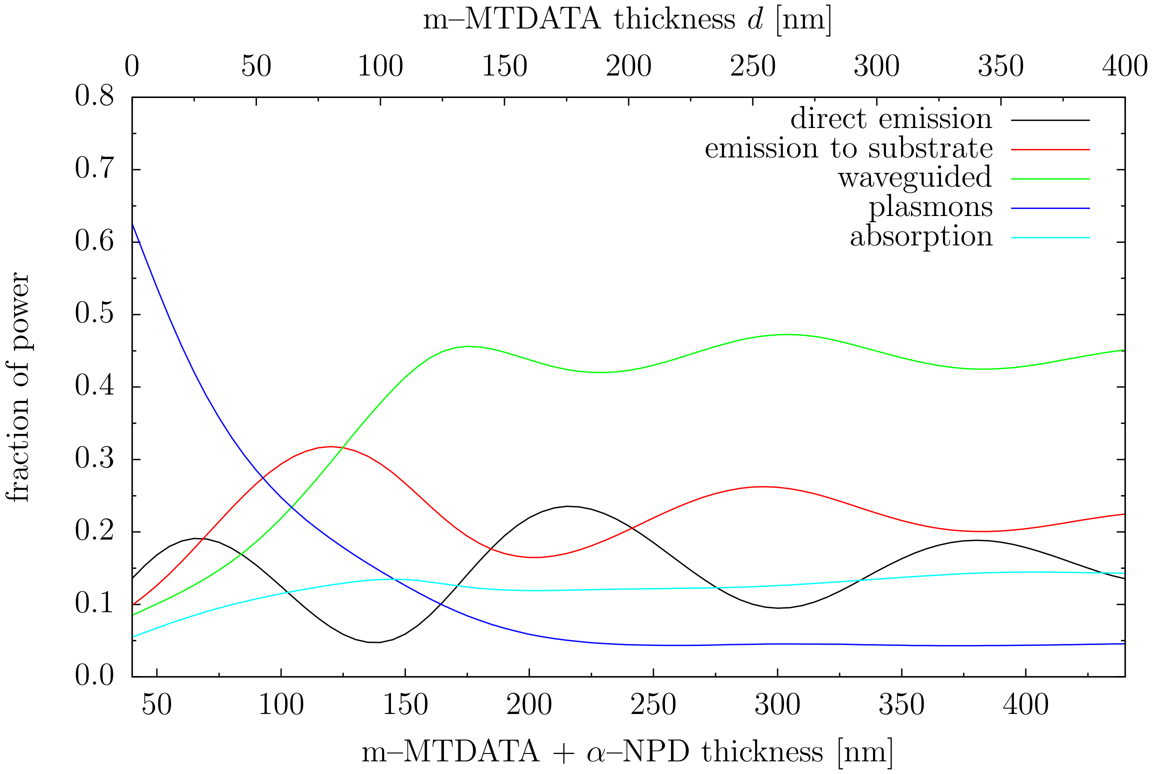

Figure 4.26.: Amount of power coupled into the different modes as determined by "PDCalc" for the OLED stack shown in fig. 4.25. ($q = 1$, $\Delta k_x = 2 \cdot 10^5\,\mathrm{m}^{-1}$, $\Delta d = 5\,\mathrm{nm}$, $400\,\mathrm{nm} \leqslant \lambda \leqslant 780\,\mathrm{nm}$)

where k_r^* is the radiative decay rate determined by the boundary conditions of the electromagnetic field in the optical cavity. Please note that q_eff is specific for a given stack structure, its layer thicknesses, and the distance of the dipoles to interfaces.

To demonstrate the effect of the cavity on q_eff, simulations on some simple model structures have been performed (fig. 4.27), comprising $\mathrm{Alq_3}$ as the emitter material and different electrodes (Ag, ITO, and Ca/Al). Furthermore, the “bulk value” of the radiative quantum efficiency of $\mathrm{Alq_3}$ is taken to be $q = 0.20$, i.e., equal to the PL quantum efficiency determined independently by earlier measurements[21,22]. Please note that higher values have been reported in literature[73,74]; however, this is not essential in the context of this discussion. The different fractions of radiation for the different channels are listed together with the values for q_eff, $1 - q_\mathrm{eff}$ (effective non-radiative losses), and η_out in table 4.2. Values of q_eff larger than the assumed quantum efficiency $q = 0.20$ indicate that due to the presence of the cavity the emission of the dipoles is accelerated. η_out is calculated as the fraction of the total emission (sum of direct emission and emission to substrate, equal to the use of outcoupling structures) and q_eff.

As $\mathrm{Alq_3}$ is set to be non-absorbing, device 1 (corresponding to dipoles embedded in an infinitely thick $\mathrm{Alq_3}$ layer) shows no absorption at all and obviously no waveguide modes and surface plasmons can be excited. Since there is no cavity, the dipole does not get accelerated and the effective quantum efficiency is equal to the radiative quantum efficiency $q_\mathrm{eff} = q = 0.20$, as expected. This is the simplest consistency test of the correct implementation of “PDCalc”. Device 2 corresponds to a thin film of $\mathrm{Alq_3}$ (now and further on absorption is considered) in air. As expected, a huge amount of power is coupled to waveguided modes. The excitation of plasmons is not expected; however, the border between waveguided modes and plasmons is not as sharp as assumed for the calculation, please see fig. 4.28 for cross sections of the power dissipation spectra at $\lambda = 525\,\mathrm{nm}$ for some of the model devices. Therefore, the values of waveguided modes and plasmons might slightly tend to one or the other, but the value in summation is the same. The dipole in device 2 is slightly damped, $q_\mathrm{eff} = 0.17$, which means that $1 - q_\mathrm{eff} = 83\,\%$ of the energy is lost. Next, Ag as a metal with very good reflectivity is introduced in device 3. As expected, coupling to plasmons occurs. The dipole is accelerated, $q_\mathrm{eff} = 0.24 > q$ due to the reflected electric field. 3.7 % of the generated light would be radiated to air with an outcoupling efficiency of 15.5 %.

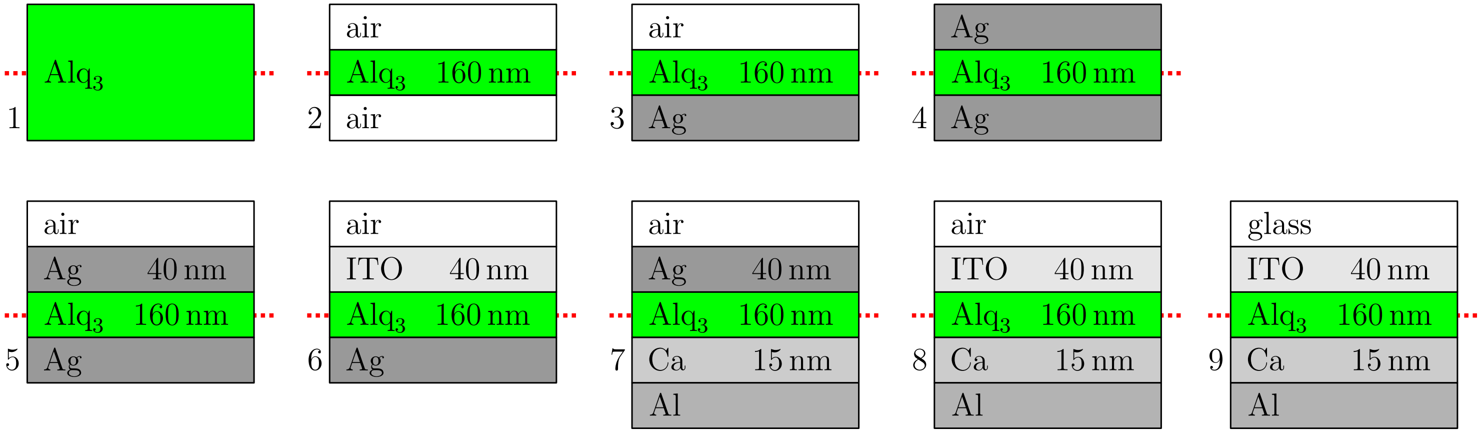

Figure 4.27.: Sample stacks for the illustration of q_{eff}. Layers without thickness specification are assumed to be semi-infinite. The emissive dipoles are located in the middle of the Alq_3 layer (indicated with a red dashed line) as a δ-distribution. Only for device 1, Alq_3 is assumed to be non-absorbing.

device	**total emission** [%]	**waveguided** [%]	**plasmons** [%]	**absorption** [%]	q_{eff}	$1 - q_{\text{eff}}$	η_{out} [%]
1	20.0	0.0	0.0	0.0	0.20	0.80	100
2	2.5	14.5	0.2	0.0	0.17	0.83	14.6
3	3.7	10.6	9.7	0.1	0.24	0.76	15.5
4	0.0	15.3	10.4	7.9	0.34	0.66	0.0
5	1.8	15.0	10.4	6.0	0.33	0.67	5.2
6	5.8	9.7	9.6	0.3	0.25	0.75	22.6
7	0.7	14.3	11.3	6.4	0.33	0.67	2.2
8	5.2	10.7	8.4	0.7	0.25	0.75	20.7
9	11.3	4.5	8.4	1.4	0.26	0.74	44.1

Table 4.2.: Calculation of q_{eff} for the model stacks in fig. 4.27. Radiative quantum efficiency $q = 0.20$. If $q_{\text{eff}} > q$, then the emission of the dipole is amplified. Only for device 1, Alq_3 is assumed to be non-absorbing. ($\Delta k_{\text{x}} = 5 \cdot 10^4\,\text{m}^{-1}$)

All devices discussed until now are simple model stacks, however, OLEDs need two electrodes as electric contacts. Therefore, simplified OLED stacks are investigated in the following. Device 4 represents a very strong cavity: the Alq_3 layer is embedded between two Ag mirrors. As these are semi-infinite it is obvious that no light can leave the device. Huge amounts of energy are coupled to waveguided modes and plasmons[‡]. In this cavity the dipoles are accelerated considerably, $q_{\text{eff}} = 0.34$. However, as the OLED shall be able to emit light, at least one electrode has to be transparent at least for some part of the generated light. One possibility is to use a thin layer of Ag, e.g., 40 nm as used in device 5. Now 1.8 % of the generated light can be emitted from the device. Interestingly, the thin Ag layer is still very efficient on the effective quantum efficiency, $q_{\text{eff}} = 0.33$, which is almost as high as in device 4. ITO is used instead of the thin Ag layer in device 6, also with a thickness of 40 nm. It is not surprising, that the amount of outcoupled light is increased with this transparent electrode and reaches 5.8 %. The effective QE is not as high as in the previous device due to the lower reflectivity of ITO, as it shows a weaker microcavity effect as compared to a Ag electrode, however, the outcoupling factor η_{out} is quite high. Devices 7 and 8 are the counterparts of devices 5 and 6, respectively, where the semi-infinite Ag has been substituted by a Ca/Al electrode. The calculated values are similar, meaning that the Ca/Al electrode is only slightly less effective in optical terms and could be used for some material systems, where it might be a better solution for the charge carrier injection compared to a Ag electrode. Device 9 corresponds to a simplified OLED with glass substrate, where the substrate modes are also emitted from the device. Hence, an outcoupling factor $\eta_{\text{out}} = 44.1\,\%$ is achieved.

At this point it should be noted that the relation between the radiative quantum efficiency q and the effective quantum efficiency q_{eff} is not just a linear one ($q_{\text{eff}} \neq q \cdot \text{const.}$). This is illustrated in fig. 4.29, which shows the relation between q (which is an input parameter for the simulation) and q_{eff} (which is determined by the simulation) for device 9 (left axis). The right axis in fig. 4.29 shows the fraction of the total emitted power versus q. To guide the eye, a linear relation between q_{eff} and q is included in the figure. What can be seen clearly is a non-linear enhancement being largest (in absolute values) at $q \approx 0.46$. As mentioned before, q_{eff} is specific for a given stack type, its layer thicknesses, and the dipole position within it. The strong dependence of q_{eff} on the distance of the dipoles to a silver surface (fig. 4.30) is shown in fig. 4.31. The dipoles reside in Alq_3, the radiative quantum efficiency is again set to $q = 0.20$. What can be seen is that q_{eff} oscillates around the bulk value of q; however, the oscillation is damped and for large distances q_{eff} becomes equal to q. This means that far away from the metal the dipoles are no longer influenced by the presence of the interface. This effect has already been described in the original work of CPS[56,57]. Please note that as the simulation does not distinguish between plasmons and energy transfer from the dipoles to the metal electrodes, the strong increase in q_{eff} for very short distances to the metal ($d \lesssim 25\,\text{nm}$) is mostly due to quenching effects (see also appendix (A.4)).

[‡] Here again, the border between waveguided modes and plamsons is slightly problematic: due to two metal interfaces two plasmonic modes are excited. However, one of them is partially attributed to the waveguided modes, please see fig. 4.28.

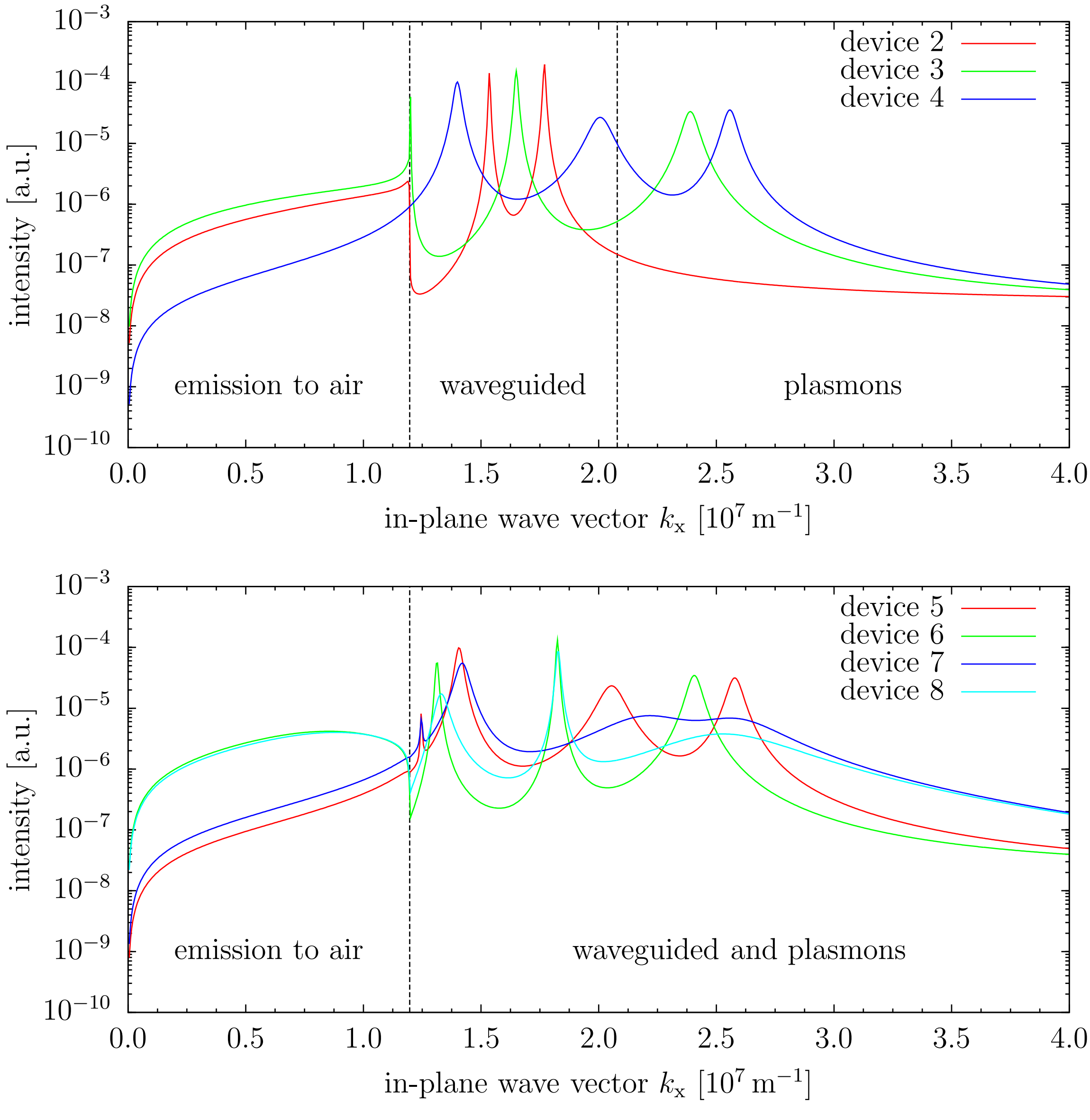

Figure 4.28.: Cross sections at wavelength $\lambda = 525\,\mathrm{nm}$ of the power dissipation spectra for some of the model stacks (fig. 4.27). Please note that this is the device-internal spectrum; the transmission to the outside world is not yet considered.

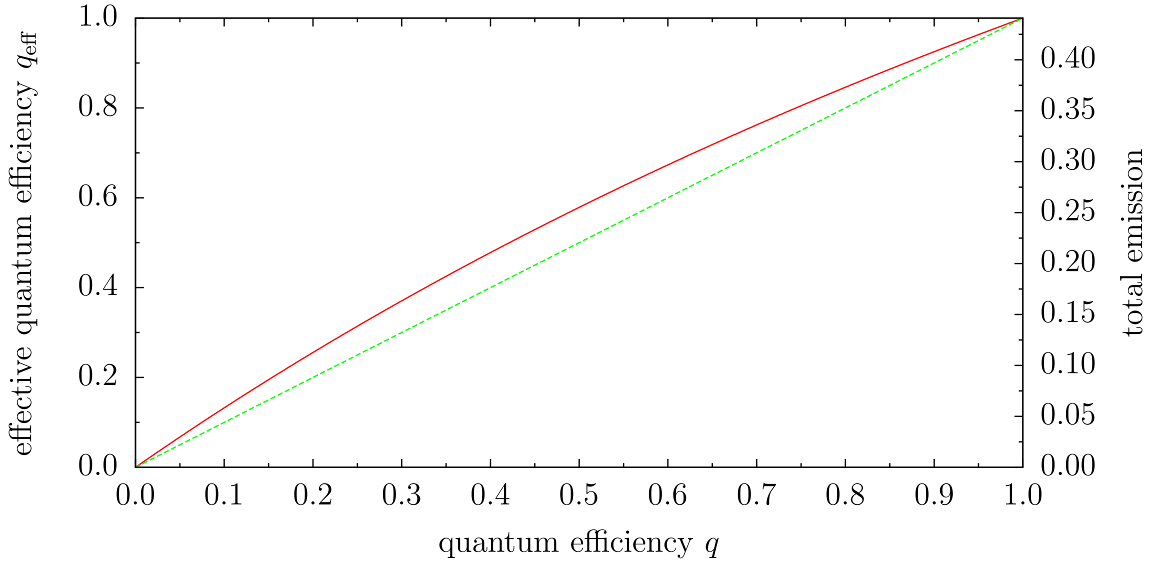

Figure 4.29.: Solid red curve: relation between the radiative quantum efficiency q and the effective quantum efficiency q_{eff} (left axis) for device 9 (fig. 4.27) and simulated fraction of power of the total emission (right axis). Dashed green curve: assumed linear dependence between q and q_{eff} (left axis) and the fraction of power of the total emission (right axis), respectively.

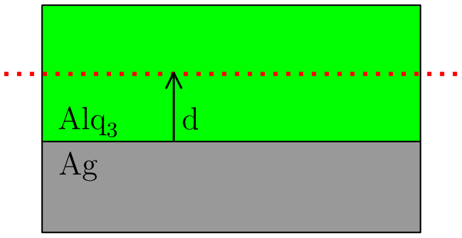

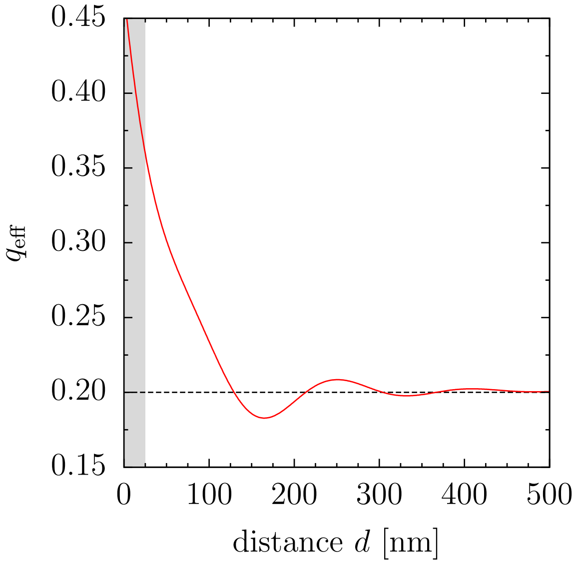

Figure 4.30.: Stack for variation of the distance d of dipoles embedded in semi-infinite Alq$_3$ facing a semi-infinite Ag mirror.

Figure 4.31.: Effective quantum efficiency q_{eff} as a function of the distance d of dipoles facing a Ag mirror (fig. 4.30). Small distances d (gray area): quenching effects. ($q = 0.20$ (dashed line), $\Delta k_{\mathrm{x}} = 2 \cdot 10^5\,\mathrm{m}^{-1}$, $\Delta d = 1\,\mathrm{nm}$)

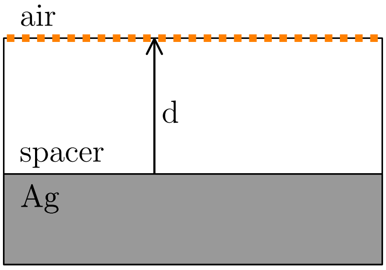

Figure 4.32.: Simple stack used by Drexhage[75] for determining the radiative lifetime of Eu^{3+} emitters (indicated by orange dots) with different distances d to a semi-infinite Ag interface. Refractive indices at the emission wavelength $\lambda = 612\,\text{nm}$, according to CPS[57]: $\hat{N}_{\text{Ag}} = 0.06 - 4.11\text{i}$, $n_{\text{spacer}} = 1.50$. Spacer non-absorbing.

4.4. Radiative lifetime of an emitter in the vicinity of a metal surface

As discussed in the previous chapter, microcavity effects play an important role in OLEDs as the quantum efficiency of the emitter material and therefore the lifetime of the exited state (inverse of the radiative rate) is changed. As already indicated in eq. (4.9), the radiative decay rates of fluorescent dyes close to a metal electrode or embedded in the microcavity of an OLED can be significantly different as compared to the bulk values. This has been realized by various authors[55–59].

To measure radiative lifetimes of a dye usually pulsed lasers (pulse length considerably shorter than the radiative lifetime and with a wavelength preferably in the absorption maximum) are used to excite the dye. Then the photoluminescence intensity of the dye is recorded over time, e.g., by a streak camera system. From the intensity decay, which usually is exponential for fluorescent emitters, the lifetime of the emissive state can be extracted. Experiments on a simple stack have been performed by Drexhage[75] in the years 1966 – 1970. The stack (see fig. 4.32) consists of a Ag substrate, a spacer, and a monolayer of Eu^{3+} containing molecules as emissive layer (emission wavelength $\lambda = 612\,\text{nm}$). As the thickness of the spacer is varied, the lifetime of the emissive state of Eu^{3+}, excited with UV light, is altered significantly, see the symbols fig. 4.33. Later on, Chance et al. used the experimental data and simulated the lifetime dependence[57]. Their best fit (black line in the same figure) of the experimental data revealed an intrinsic lifetime of $\tau_0 = 632\,\mu\text{s}$ and a quantum efficiency of $q = 0.760$. For the simulation of the lifetime dependence with "PDCalc" these parameters have also been used. The results are plotted as an overlay (red line) in fig. 4.33. The excellent agreement between the original experimental data, simulation by CPS, and simulation with "PDCalc" is another encouraging verification of the dipole model and our simulation tool.

The variation of the emissive lifetime of an emitter material depends on its quantum efficiency q. With the help of simulation, one can elucidate its value. Fig. 4.34 shows a similar stack to the one used by Drexhage: semi-infinite Ag as substrate, a spacer of SiO_2, and 10 nm of Alq_3. The dipoles reside in the middle of the Alq_3

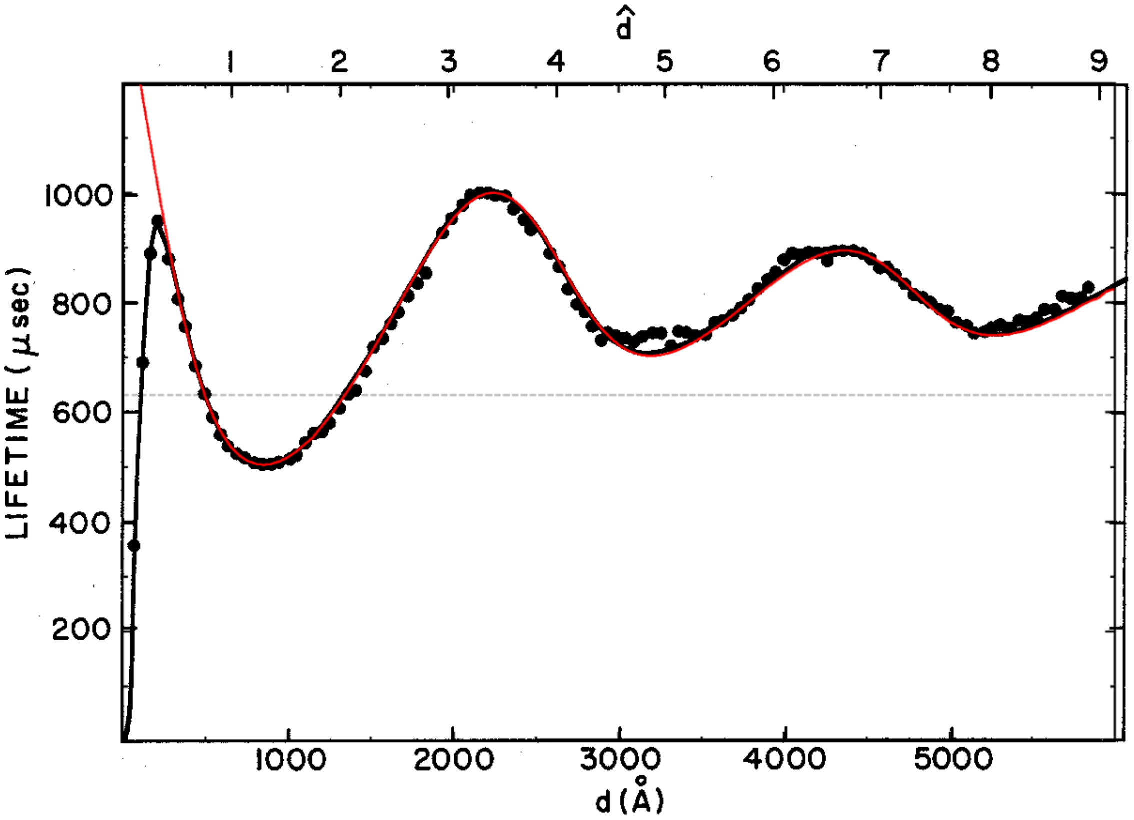

Figure 4.33.: Radiative lifetime of a monolayer of Eu^{3+} molecules with distance d from a Ag mirror (fig. 4.32). Dots: experimental data from Drexhage[75]. Black line: simulation results from CPS, optimal fit for QE $q = 0.760$ and intrinsic lifetime $\tau_0 = 632\,\mu s$ (gray dashed line). Emission wavelength $\lambda = 612\,nm$. Picture taken from CPS[57]. As overlay, red line: radiative lifetime calculated with "PDCalc" (monochromatic calculation at the emission wavelength). Excellent agreement between experimental data from Drexhage, simulation from CPS and simulation with "PDCalc" (for the differences at very small distances to the mirror please see the appendix (A.4)).

layer. The normalized lifetime (referred to the free-space lifetime τ_0) τ/τ_0 for different thicknesses d of SiO_2 is shown for different quantum efficiencies q in fig. 4.35[§]. The curve progressions could be used to fit experimental lifetime data in order to obtain the quantum efficiency of Alq_3.

Unfortunately, the variation in Alq_3 lifetime for the expected quantum efficiency of $q = 0.2$ is less than 10 % over the entire thickness range. Experimental data for this kind of stack is not very conclusive[76]. Other emitter materials with high quantum efficiencies have to be chosen for such measurements, consequently providing large variations in lifetime, as can be seen in fig. 4.35 for different q. A correlation between simulation and experiment would be easier and more precise and the determination of the quantum efficiency would be possible. For this reason, Lumogen yellow or Lumogen orange, dyes from BASF[77] used to color PMMA, can be used as fluorescent emitters with high QE, $q \approx 0.90$ and $q \approx 0.65$, respectively[78]. The dyes have been spincast in a matrix of PMMA on sputtered SiO_2, the latter with variable thickness. Additionally, this kind of experiment was repeated with a soluble phosphorescent emitter deposited by spincasting. However, experimental data and simulations can not be shown here as the experiments have not yet been finished; they will be part of Benjamin Lebsanft's diploma thesis[76].

Nevertheless, using the same method, it is also possible to extract the quantum efficiency of a complete OLED stack (where one layer thickness is varied) using photoluminescence or pulsed electroluminescence lifetime measurements and concurrent simulations. This is shown later in chapter 4.6.2.

4.5. Optimization of the reference OLED stack as an example

In this section, systematic variations of the reference OLED stack (fig. 4.3) are shown to get a general understanding of the complex interactions of the different emission channels. This well-known OLED structure, although not being particularly efficient, still serves as a model system for OLEDs with a single emitting material enclosed by a hole and an electron conducting compartment. This does also include phosphorescent emitters. Evidently, a strong influence on the amount of energy coupled into waveguided modes comes from the thickness of the various layers and the dipole layer position within the OLED stack. For the plasmonic modes, the distance of the dipole layer to metallic electrodes is of great importance, as will be demonstrated below. Within certain limits, these results can be used to define some coarse design rules for efficient OLEDs.

The following simulations use a radiative quantum efficiency of $q = 0.2$ for the Alq_3 emitter (unless otherwise noted) and the full wavelength range ($400\,\mathrm{nm} \leqslant \lambda \leqslant 800\,\mathrm{nm}$). The dipole layer is always assumed to be at the interface between TPD and Alq_3. Please note that the calculations presented here exclusively show the optical

---

[§] The reason for the not so smooth curves especially at large thickness d of the spacer is explained in the appendix (A.4).

Figure 4.34.: Stack for emissive lifetime variations using Alq$_3$ as emitter and a SiO$_2$ spacer with variable thickness d. Dipoles are embedded in the middle of the Alq$_3$ layer.

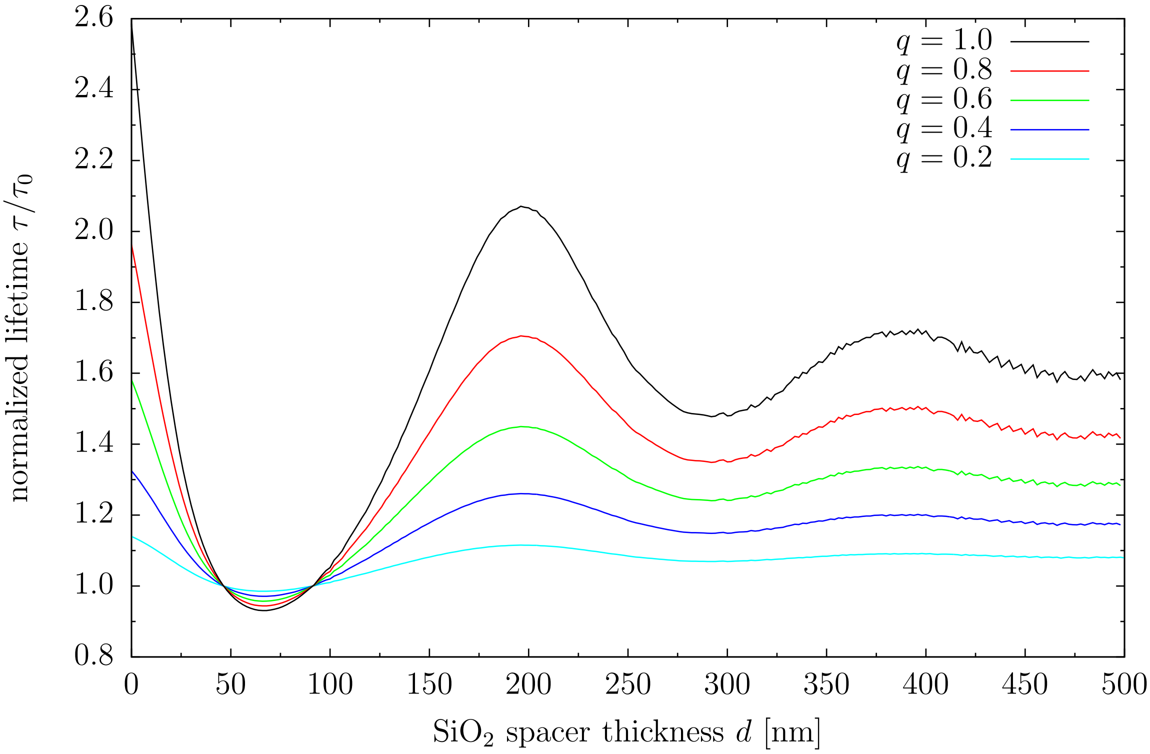

Figure 4.35.: Variation of the emissive lifetime τ, normalized to the free space lifetime τ_0, for the stack presented in fig. 4.34 for different quantum efficiencies q. ($\Delta k_x = 2 \cdot 10^4\,\mathrm{m}^{-1}$, $\Delta d = 2\,\mathrm{nm}$)

performance of the devices. Altering layer thicknesses has an influence on the electrical characteristics, which have to be optimized as well. Optimization of both the optical and electrical performance may require a compromise to be made; however, this is not addressed here. Changing the electrical characteristics can be avoided if doped transport layers are used. Therefore, the variations of the reference OLED stack are only theoretical, however, they give a deep understanding.

4.5.1. Influence of the dipole layer position in an OLED with fixed thickness

In fig. 4.36 the dipole layer position is shifted successively from the cathode (Ca/Al interface) to the anode (PEDOT:PSS interface). This is achieved by fixing the overall thickness of the OLED, varying only the thicknesses of TPD and Alq_3 accordingly. As their refractive indices are almost identical, this variation shows the performance of the OLED if the recombination zone could be positioned arbitrarily within the organic layers (assuming that the electrical performance of the OLED is not affected). The simulation results, i.e., the fractions of power dissipated into the different channels, are shown in fig. 4.37 as accumulated values (which eventually add up to 1). The similar refractive indices result in an almost constant absorption loss regardless of the dipole layer position. Most obvious, the plasmons are affected by the dipole layer position. Starting with the dipole layer position at the cathode a huge amount of power is coupled into plasmons. Moving farther away from the metal interface reduces this amount drastically. Therefore, the values for the direct emission and emission to substrate can increase. The direct emission reaches a maximum at an Alq_3 layer thickness of about 70 nm. A further increase in the Alq_3 thickness decreases this value again, which is caused by the increasing amount of power coupled into waveguided modes. As a consequence of this simulation one can say that the recombination zone should not be placed too close to a metal interface due to the strong coupling to plasmons, although, the intrinsic loss would be extremely small. At larger distances d to the cathode the intrinsic loss increases, while the coupling to the plasmon is decreased.

4.5.2. Variation of the hole transporting layer thickness

Changing the thickness of the hole transporting layer (TPD) at a fixed Alq_3 thickness (fig. 4.38) shows the influence of the waveguided modes on the emission of light, as can be seen in fig. 4.39. The dipole layer has a fixed distance from the metallic cathode, resulting in an almost constant plasmonic contribution. From an optical point of view, the fraction of light coupled out directly has its maximum at small TPD layer thicknesses, whereas the amount of light going to the glass substrate has its maximum at a layer thickness where the waveguided modes have a minimum. This shows that the coupling to waveguided modes can be reduced to the benefit of light, which can leave the device through light-extraction structures; however, the total amount of light (direct emission and emission to the substrate added together) would, from an optical point of view, suggest a preferably thin TPD layer.

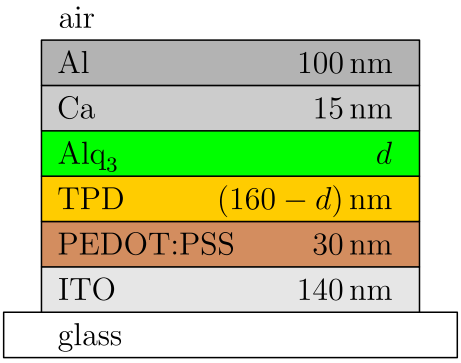

Figure 4.36.: Stack for variation of the dipole layer position. Overall thickness of the OLED is kept constant, thicknesses of TPD and $\mathrm{Alq_3}$ varied accordingly. The dipole layer is located at the TPD/$\mathrm{Alq_3}$ interface and is shifted from the Ca/Al cathode ($d = 0$ nm) to the PEDOT:PSS anode ($d = 160$ nm).

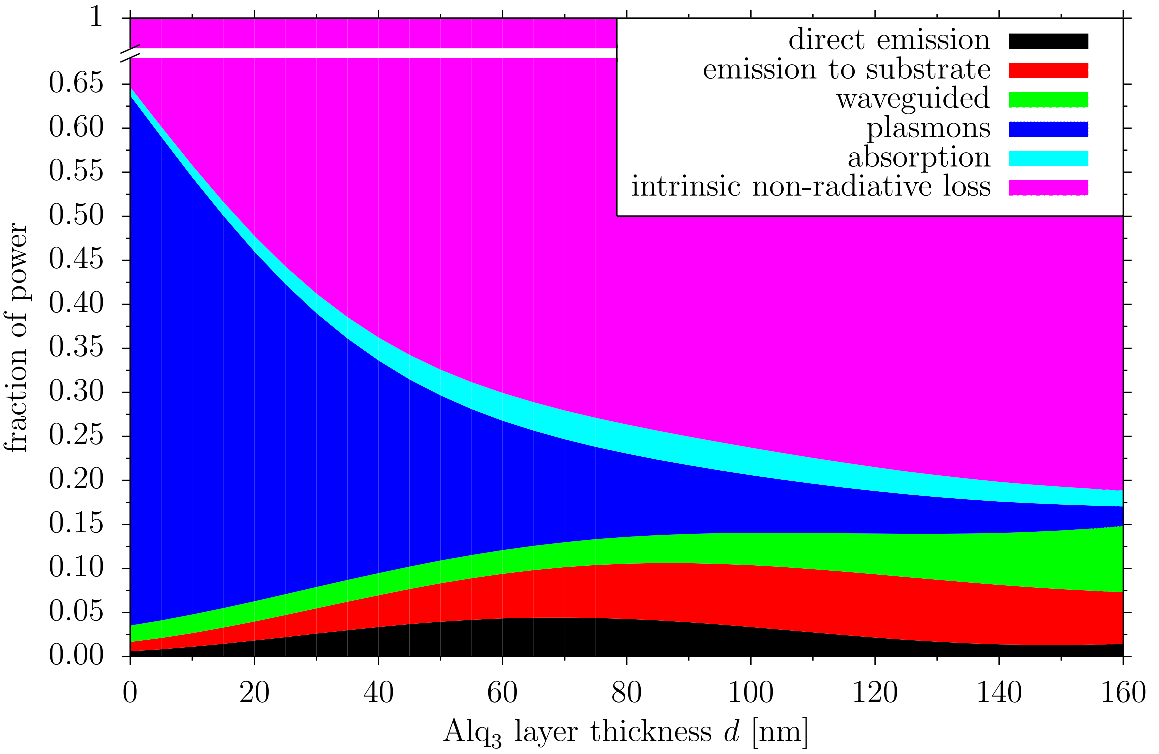

Figure 4.37.: Simulation results for the variation of the distance of the dipole layer to the metallic cathode by changing the $\mathrm{Alq_3}$ layer thickness d and TPD layer thickness $(160\,\mathrm{nm} - d)$ (stack shown in fig. 4.36). ($q = 0.2$, $\Delta k_x = 2 \cdot 10^5\,\mathrm{m}^{-1}$, $\Delta d = 5\,\mathrm{nm}$)

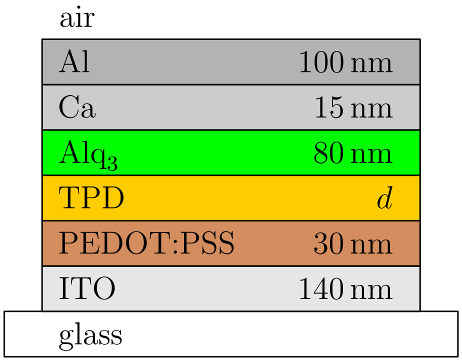

Figure 4.38.: Stack for variation of the TPD layer (HTL) thickness d.

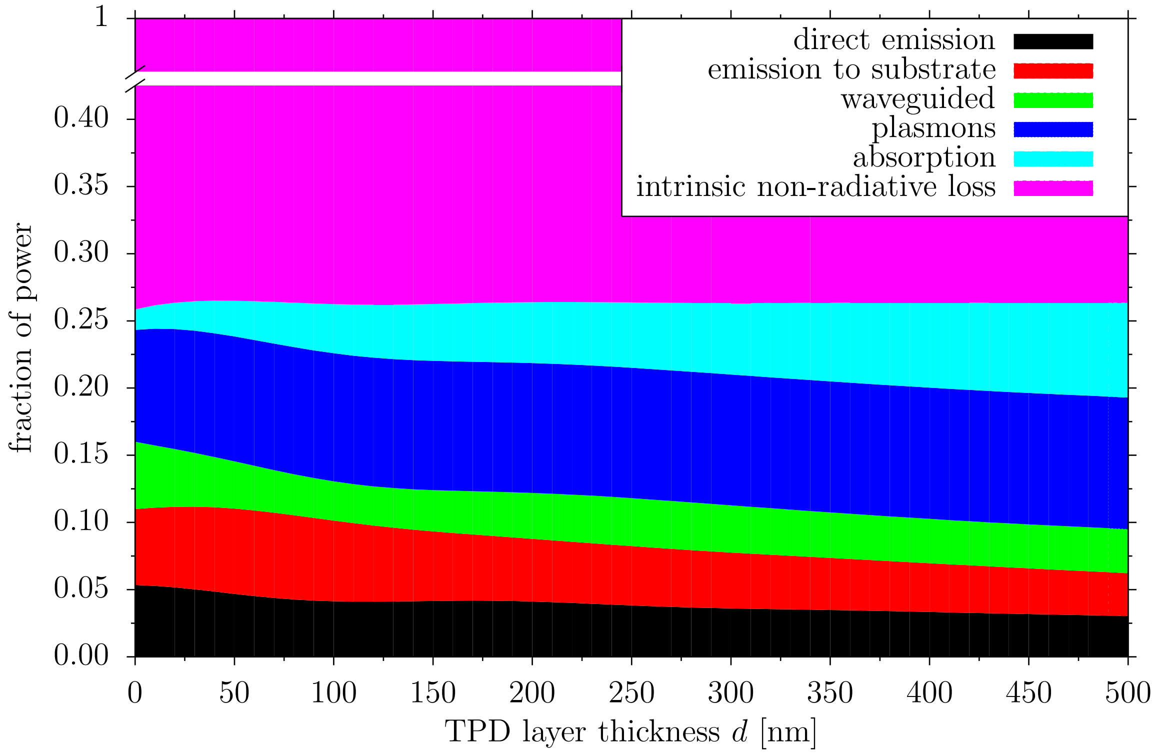

Figure 4.39.: Simulation results for the variation of the TPD layer (HTL) thickness d (stack shown in fig. 4.38). ($q = 0.2$, $\Delta k_x = 2 \cdot 10^5\,\mathrm{m}^{-1}$, $\Delta d = 10\,\mathrm{nm}$)

According to these results one could imagine that either the TPD layer should be avoided for optical reasons or that a shorter distance of the dipole layer to the anode could improve the fraction of light emitted from the OLED. For this reason, changes at the anode side of the OLED stack have been applied: the PEDOT:PSS layer is omitted and the ITO thickness is reduced to 50 nm; the TPD layer thickness is still subject to variation (fig. 4.40). The results (fig. 4.41) show a clear maximum (about 5.2 %) for the direct emission at about 90 nm TPD layer thickness. Together with the previous simulation (fig. 4.39), this leads to the conclusion that the TPD layer alone does not have a negative influence on the optical properties of the Alq_3-OLED stack, but that the distance of the dipole layer to the glass substrate is of importance.

4.5.3. Variation of the distance of the emitting dipoles to the metallic cathode

The next simulations show the variation in the Alq_3 layer (ETL) thickness while keeping the TPD layer (HTL) thickness fixed at 80 nm (fig. 4.42). Here not only the layer thickness is changing, influencing the waveguided modes, but also the dipole position with respect to the cathode, resulting in a variation in the plasmonic contribution. As the dipole layer is moved farther away from the cathode, the coupling to plasmons is reduced drastically, see fig. 4.43. For the direct emission there exist several local maxima and minima as a function of distance. The first maximum at around 60 nm Alq_3 layer thickness shows the highest fraction of outcoupled light (about 4.5 %). This thickness (which at the same time is the distance of the dipole layer to the cathode) and also the value of the maximum external quantum efficiency of 1.1 % (calculated from eq. (4.19) with $\gamma = 1$ and $\eta_{s/t} = 0.25$) are consistent with the optimal thickness of Alq_3 found in the experimental work[79–81]. However, if light-extractors are attached to the OLED's glass substrate, the maximum fraction of totally outcoupled light (about 10.4 %) is achieved with a slightly larger Alq_3 layer thickness of about 80 nm, which is the reference OLED design.

4.5.4. Influence of the emitter quantum efficiency on device optimizations

As the thickness of Alq_3 increases further, a second maximum in the direct emission appears at 230 nm in fig. 4.43, which is slightly lower in value (about 4.0 %) than the first maximum (about 4.5 % at 60 nm). Calculations where the radiative quantum efficiency is assumed to be $q = 1.0$ show that this second maximum can be even higher (about 18.4 % at 230 nm) than the first one (about 16.2 % at 80 nm), see fig. 4.44. This effect has also been reported by Lin et al.[72]; the calculation has already been shown in chapter 4.2.3 without stressing this detail. Therefore, OLED stacks with high quantum efficiency emitters would benefit from an increased layer thickness on the cathode side of the emitter. Now the question arises why for emitters with small quantum efficiency this second maximum is lower than the first maximum for thinner layers. This behavior can be explained by the modification of the effective radiative

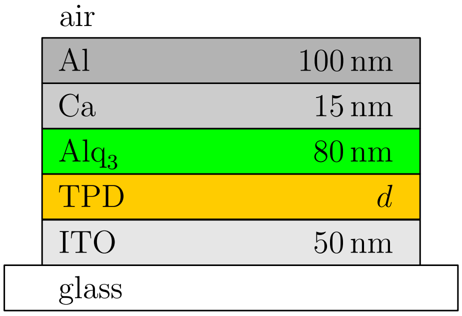

Figure 4.40.: Modified stack for variation of the TPD layer (HTL) thickness d: no PEDOT:PSS interlayer and ITO thickness reduced to 50 nm.

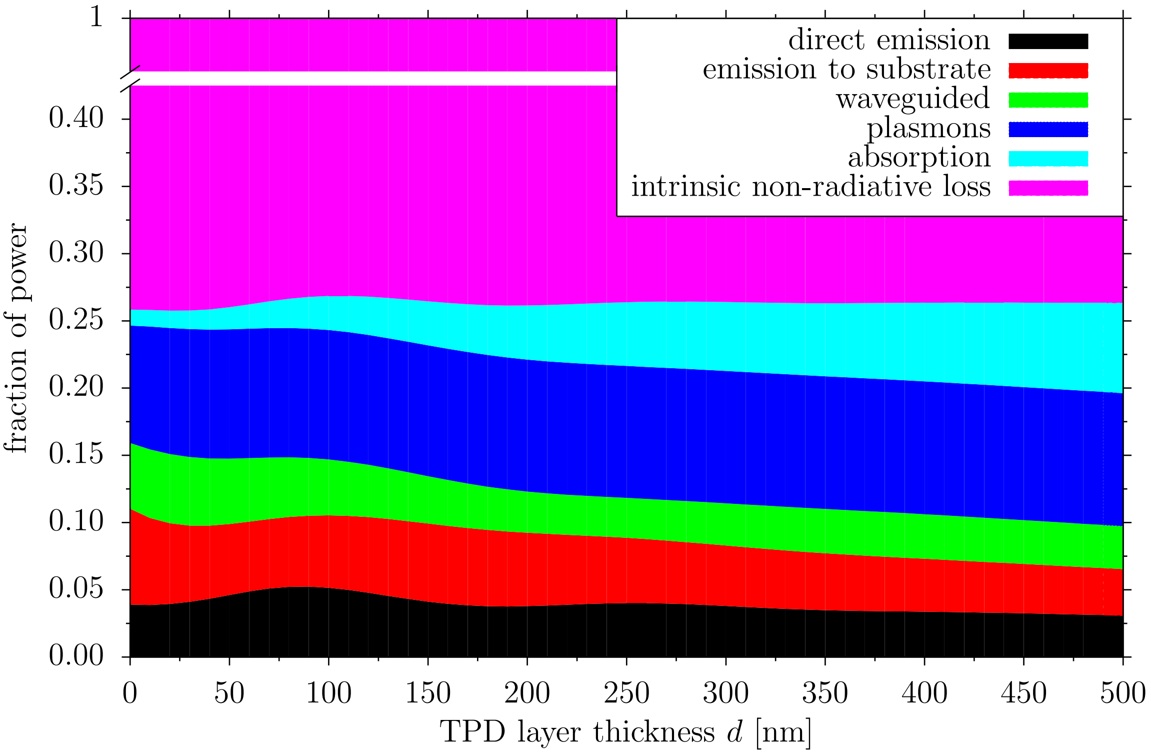

Figure 4.41.: Simulation results for the variation of the TPD layer (HTL) thickness d with modified anode (stack shown in fig. 4.40). ($q = 0.2$, $\Delta k_x = 2 \cdot 10^5\,\mathrm{m}^{-1}$, $\Delta d = 10\,\mathrm{nm}$)

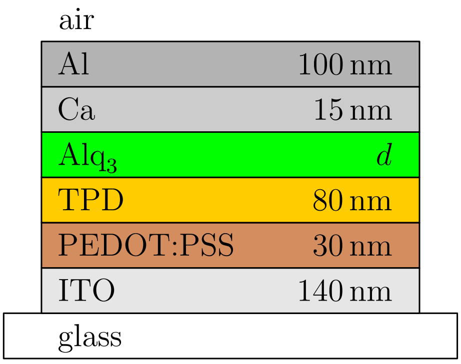

Figure 4.42.: Stack for variation of the dipole distance to the cathode via the Alq_3 layer thickness d.

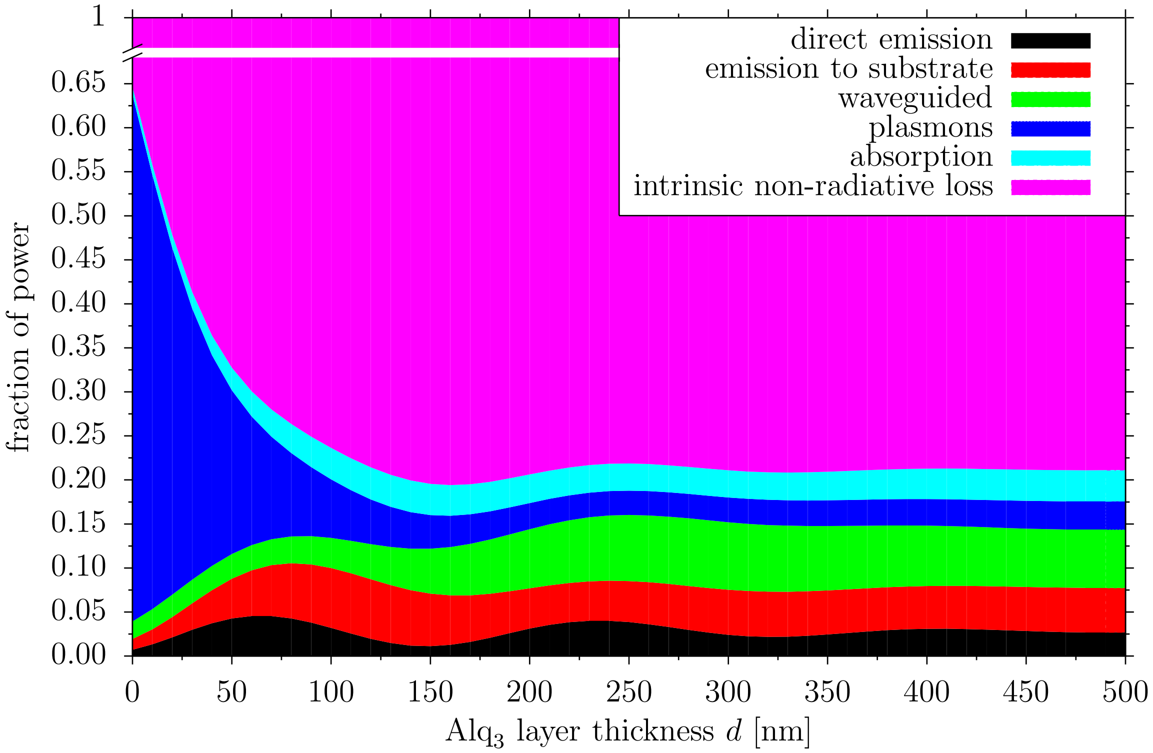

Figure 4.43.: Simulation results for the variation of the dipole distance to the cathode (stack shown in fig. 4.42). ($q = 0.2$, $\Delta k_x = 2 \cdot 10^5\,\mathrm{m}^{-1}$, $\Delta d = 10\,\mathrm{nm}$)

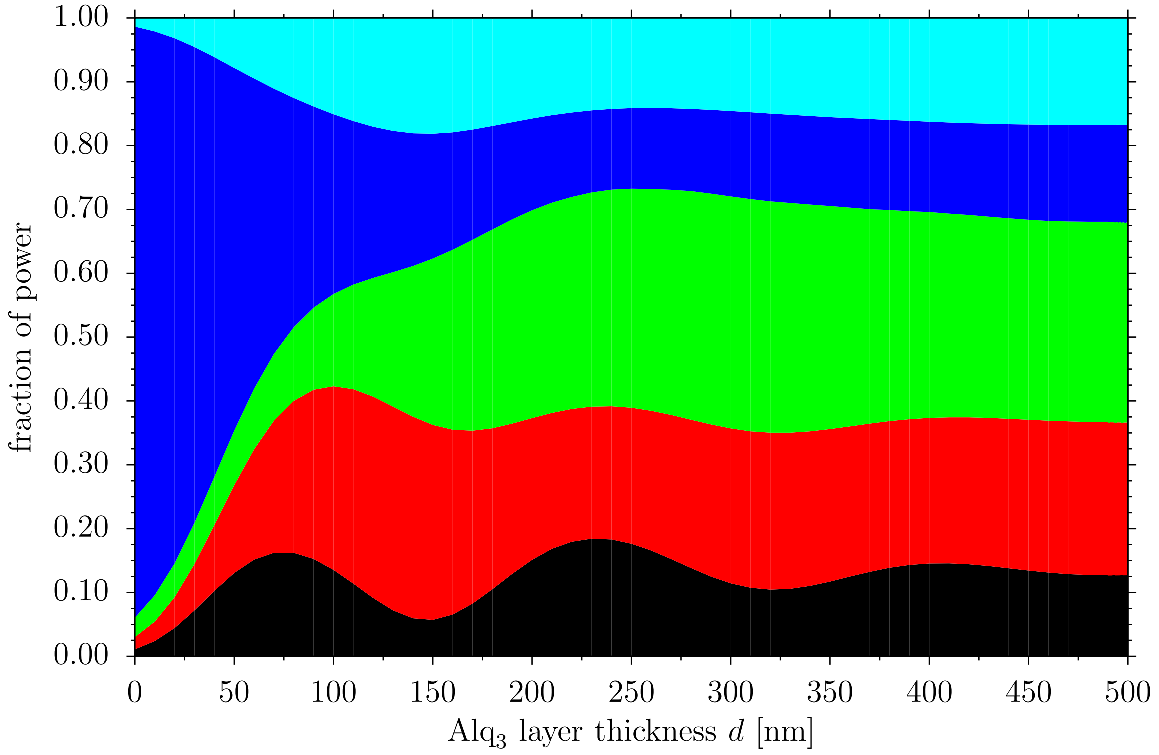

Figure 4.44.: Simulation results for the variation of the dipole distance to the cathode (see fig. 4.42). This time calculated with an emitter quantum efficiency of $q = 1$. Colors for the different loss channels are the same as in fig. 4.43. ($\Delta k_\mathrm{x} = 2 \cdot 10^5\,\mathrm{m}^{-1}$, $\Delta d = 10\,\mathrm{nm}$)

quantum efficiency q_eff by the OLED cavity. As already shown in fig. 4.31 q_eff is enhanced especially at distances of the emitting dipole to the metal electrode below 100 nm. This means that if the dipole is closer to the cathode (approx. 60 nm) it gets amplified more as for larger distance (approx. 230 nm), hence leading to a larger value for the fraction of directly emitted light in the first maximum in fig. 4.43. However, as the direct emission is amplified for small distances, the amount of power coupled into the plasmon also rises.

The simulations with different radiative quantum efficiencies q demonstrate that the value of q not only determines the amount of light that can be coupled out from an OLED but also the optimal layer thicknesses of the device. As a consequence, the radiative quantum efficiency of the emitter in an OLED should be known for accurate device simulations and optimizations. In the next chapter it will be shown that, if q is not known beforehand, simulations can be used to get access to its value by fitting the external quantum efficiency of devices with systematic layer thickness variations.

4.5.5. Summary of the device optimization results

In conclusion, the simulations presented above show that the optical performance of OLEDs depends on several factors. Clearly the layer thicknesses of both the hole and the electron transporting layers have a decisive influence. The dipole layer has to be located at the right position, so that the feedback exerted by the cavity on the emitting molecules is optimal for the fraction of light emitted directly or to the glass substrate and the fraction coupled to waveguided modes or plasmons is minimized. An important point is that the optimal dipole layer position (and thus the device structure) also depends on the radiative quantum efficiency q of the material used as emitter. Therefore, this quantity has to be known for accurate device simulations and optimizations. Last, when optimizing the device it has to be considered if outcoupling structures will be used for the OLED, as the optimal layer thicknesses are slightly different to the ones for a plain OLED. Nevertheless, it is evident from these results that even in an optimized structure (with 100 % radiative quantum efficiency) only some 40 % of the radiation generated inside the OLED can actually be extracted, provided that all of the light guided as substrate modes could be coupled out using suitable techniques. Further enhancement of the external quantum efficiency will therefore require the development of methods to couple out radiation from waveguided modes or even surface plasmons, or other, entirely different, approaches. Some of them will be shown in chapter 4.7.

4.6. Extraction of the emitter quantum efficiency and charge balance factor inside the OLED cavity

4.6.1. Using external quantum efficiency measurements

It has been shown in the previous section that the knowledge of the radiative quantum efficiency q is necessary for accurate device simulations. Neglecting the impact of competing processes on q inevitably leads to erroneous results, not only in terms of the total amount of light extracted from an OLED, but also concerning the optimal device architecture to achieve this. Together with experimental data this is shown in this section for an OLED with a red phosphorescent emitter. Furthermore, it will be shown that even if the radiative quantum efficiency of an emitter material is not known beforehand, it can be extracted by an analysis of experimental data based on optical simulation.

The OLEDs discussed in this section have been fabricated and measured by OSRAM OS, Regensburg, as part of our collaboration within the OPAL project. As the materials used are part of non-disclosure agreements, no chemical names or refractive indices can be cited. Nevertheless, this is not important for the discussion, as the optical properties are the ones that matter. The structure of the bottom-emitting OLEDs (pixel area 4 mm^2) is as follows: glass, 115 nm ITO, 203 nm HTL, 10 nm EBL, 7 nm EML, 10 nm HBL, ETL with variable thickness d, and 200 nm Ag as cathode (fig. 4.45). The spectrum of the red phosphorescent emitter is shown in fig. 4.46. It is important to know that the hole and electron transporting layers are doped by materials improving hole and electron transport, respectively. This ensures that the electrical characteristics are not changing even if the thickness of the ETL is varied. For the devices with the thinnest (48 nm) and thickest ETL (110 nm), respectively, the

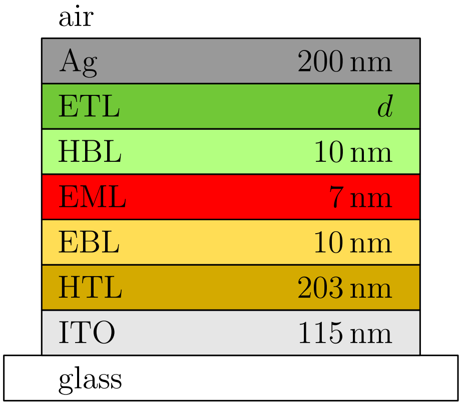

Figure 4.45.: Red phosphorescent OLED stack from OSRAM OS for variations of the ETL thickness d.

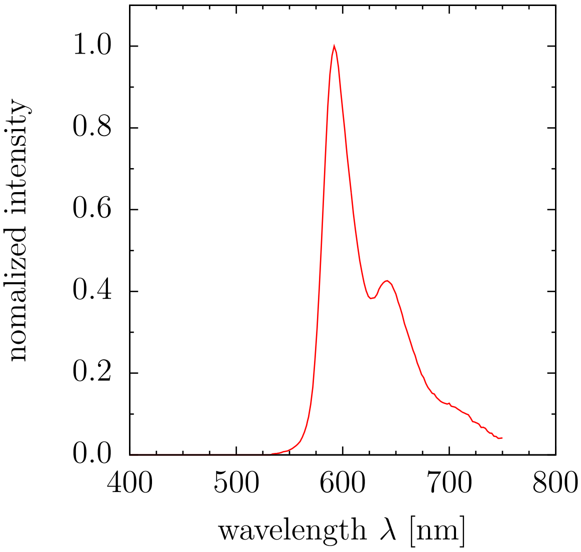

Figure 4.46.: Spectrum of the red emitter used in the OLED stack shown in fig. 4.45.

current density – voltage characteristics are shown in fig. 4.47. Both characteristics do not differ significantly, which can be attributed to appropriate n-doping of the ETL. As will be shown below, the optical properties of the devices are strongly affected by the thickness variation of the n-doped ETL, while there is almost no change in the electrical properties of the diode. However, the CIE chromaticity coordinates (measured in an integrating sphere with a glass hemisphere attached to the device), shown in fig. 4.48, are almost unaffected by the thickness variation, meaning that there is no redistribution of power to other wavelengths.

As a first result from “PDCalc” for the red phosphorescent OLED, the contributions to the different channels are shown in fig. 4.49. As quantum efficiency, $q = 1$ is assumed, and the dipole layer is located at the EML/HBL interface. This can be concluded from the excellent hole transporting properties of the host material used for the EML. The variation of the ETL thickness not only influences the waveguided modes, but the dipole layer position with respect to the cathode as well. This leads to changes in the contribution of the plasmonic losses. The coupling to plasmons is reduced drastically as the dipole layer moves further away from the cathode. At the same time the fraction of ITO/organic waveguided light increases. Furthermore, the total amount of absorbed light increases with increasing ETL thickness. As all other layer thicknesses have been kept constant, this is mostly due to the absorbing n-dopant of the ETL. The direct emission shows a maximum at 75 nm ETL thickness. The amount of light coupled from the active layers into air and substrate has its maximum at 105 nm ETL thickness. This configuration has to be chosen if optimum efficiency based on substrate surface modification is desired. However, as has been shown in the previous chapter, the optimal dipole layer position also depends on the radiative quantum efficiency q. The role of q on the total amount of outcoupled light

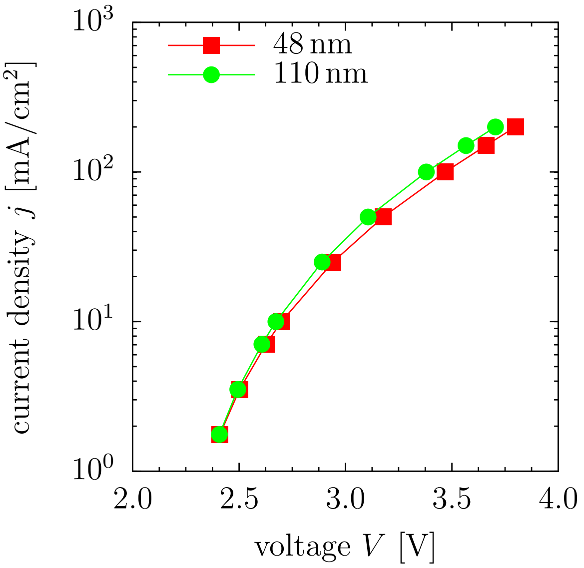

Figure 4.47.: Current density – voltage characteristics of the devices (fig. 4.45) with the thinnest (48 nm) and thickest ETL (110 nm). Almost identical characteristics due to n-doping of the ETL.

ETL thickness d [nm]	x	y
48	0.612	0.387
56	0.612	0.386
64	0.613	0.385
72	0.614	0.384
98	0.616	0.383
110	0.617	0.380

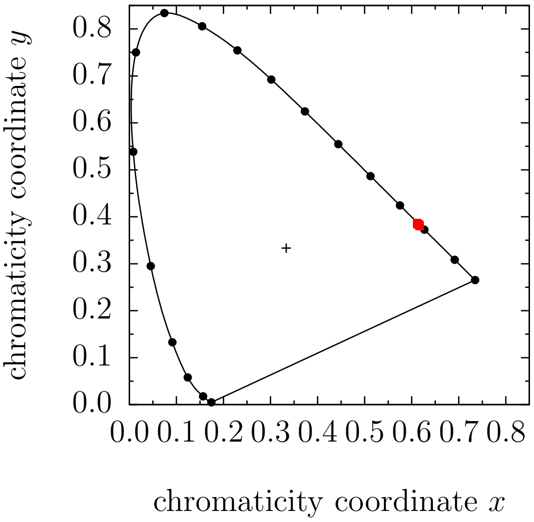

Figure 4.48.: CIE 1931 2° chromaticity coordinates for the red phosphorescent OLED stack (fig. 4.45) measured in integrating sphere with a glass hemisphere attached to the device. Current density $j = 7.5\,\mathrm{mA/cm^2}$.

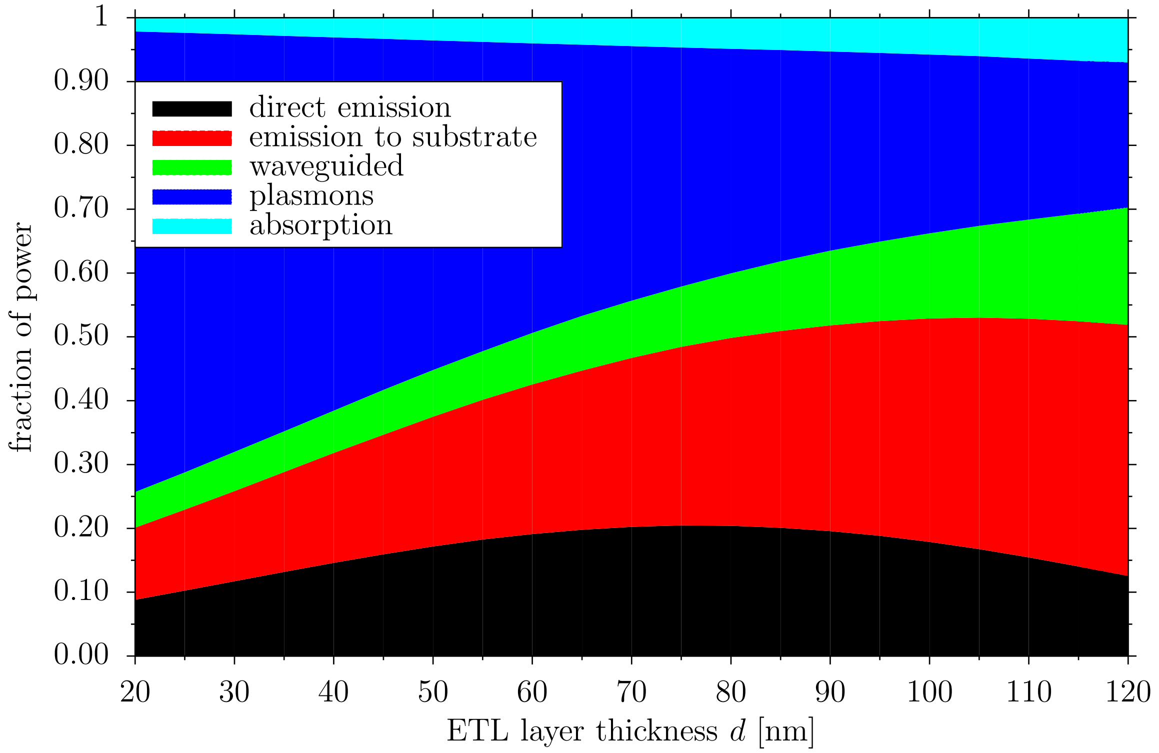

Figure 4.49.: Contributions to the different channels of the red phosphorescent OLED stack with variation of ETL thickness d (fig. 4.45). ($q = 1$, $\Delta d = 5\,\mathrm{nm}$)

is shown in fig. 4.50 and 4.51, where in the latter case the data are normalized to a device with 40 nm ETL thickness, hence giving the improvement on the total amount of outcoupled light in comparison to the reference configuration. It can be seen that both the value of total outcoupled light and the progression of the maxima depend on q. The ETL thickness where the maximum of light is accessible by substrate surface modification increases for higher values of q. For a fixed value of q, the location of this maximum is given by the trade-off between effective radiative rate and plasmon losses, which are both dependent on the distance between the emission zone and the metal cathode. The achievable improvement evidently depends on the radiative quantum efficiency q. Higher improvement can be obtained based on higher values of q, but at the same time the optimum device configuration moves to larger ETL thickness. This, however, implies that neither the optimum ETL thickness nor the achievable efficiency improvement can be predicted based on optical simulation alone if the radiative quantum efficiency q is not known beforehand. Usually, this is the case for new or undisclosed emitter systems.

However, systematic variations of the OLED stack and the comparison of measured external quantum efficiencies to simulation results allow determination of both the radiative quantum efficiency q and the charge recombination factor γ after eq. (4.19). Please remember that q_{eff} is depending on q. The factor $q_{\text{eff}} \cdot \eta_{\text{out}}$ is determined by "PDCalc". The singlet/triplet ratio is set to $\eta_{\text{s/t}} = 1$ as the red dye is phosphorescent. This leaves q and γ as variables, which can be fitted to the experimental EQE data

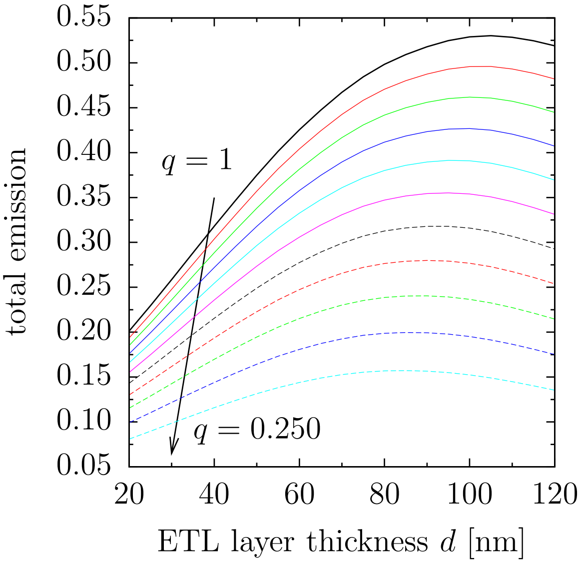

Figure 4.50.: Total amount of outcoupled power for variations of the ETL thickness d and for different emitter quantum efficiencies q of the red phosphorescent OLED (fig. 4.45). ($\Delta d = 5\,\text{nm}$, $\Delta q = 0.075$)

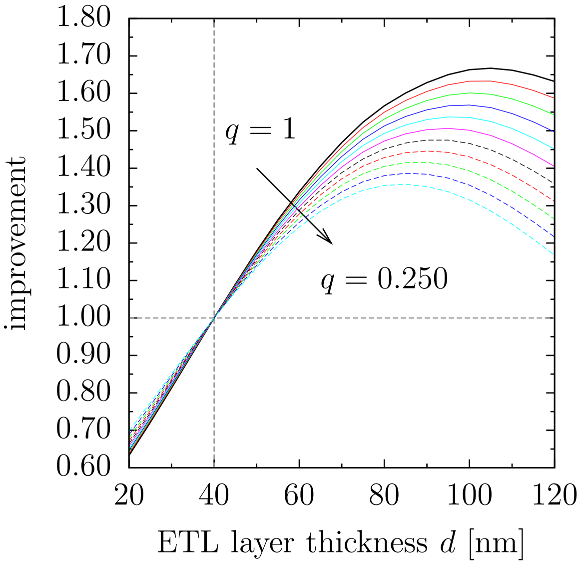

Figure 4.51.: Same data as fig. 4.50, normalized to the device with 40 nm ETL thickness, showing the achievable improvement to the reference design. ($\Delta d = 5\,\text{nm}$, $\Delta q = 0.075$)

obtained in an integrating sphere with attached glass hemisphere. Fig. 4.52a shows the results for different values of q, assuming a fixed charge balance of $\gamma = 1$. As the EQE scales linearly with the charge recombination factor, which can not be higher than one, it is concluded from this figure that the quantum efficiency of the emitter must be at least $q = 0.275$ or higher.

As discussed above (fig. 4.50), q determines the curve progression, i.e., the position of the maximum. Thus, assuming a higher value for q can lead to a better correlation with the experimental data, but requires a charge recombination factor smaller than one (see eq. (4.19)). This is shown in fig. 4.52b for different combinations of q and γ. From this figure one concludes that the quantum efficiency q for this red phosphorescent emitter is about $(33 \pm 5)\,\%$. Even higher values of q result in a mismatch of the curve progression, which can not be scaled by the linear factor γ. The best fit result (green line in fig. 4.52b) is obtained for $q = 0.325$ and $\gamma = 0.87$. For a more precise determination of both q and γ more experimental data points are required. However, this method, combining simulations and experimentally derived EQE, shows that a simultaneous determination of both quantities is possible.

The determined value of the quantum efficiency of the red phosphorescent dye, $(33 \pm 5)\,\%$, also deserves some comment. Usually people assume that if phosphorescent dyes are used the internal quantum efficiency is automatically almost equal to unity. Evidently, this is not the case and requires the determination of the value, e.g., by the above described method. Another possibility to obtain the QE would be photoluminescence (PL) quantum efficiency measurements of the dye without the

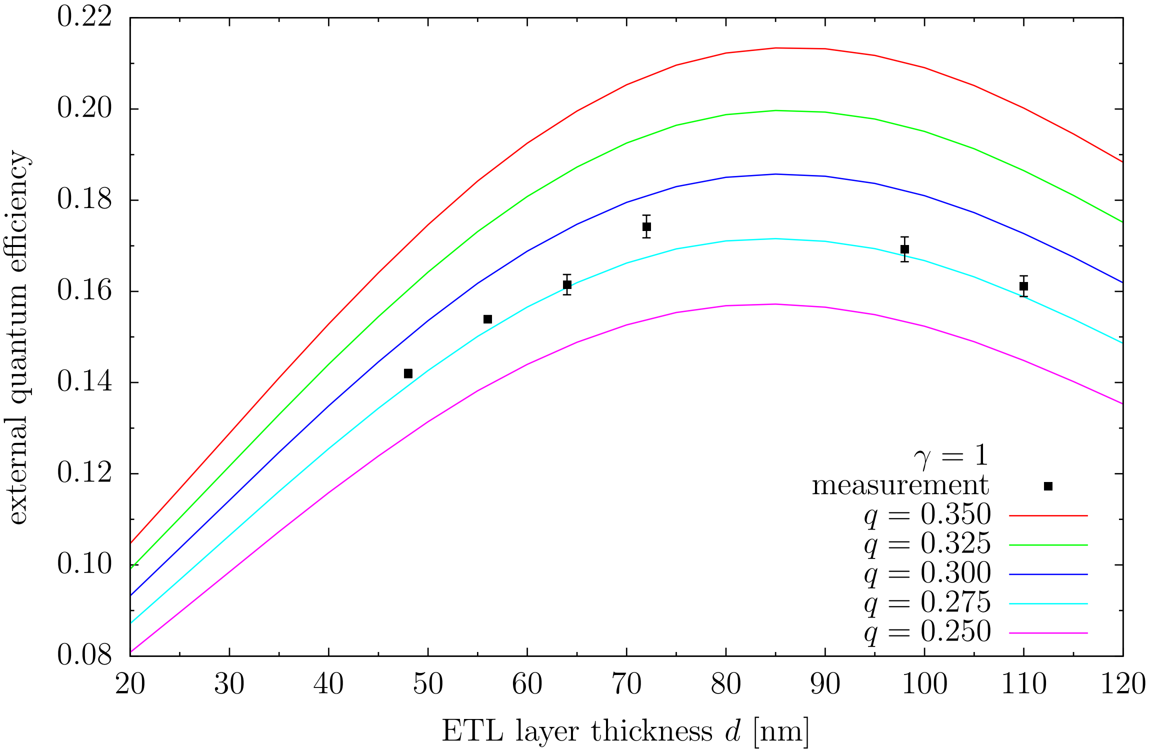

(a) *Fixed charge recombination factor: $\gamma = 1$.*

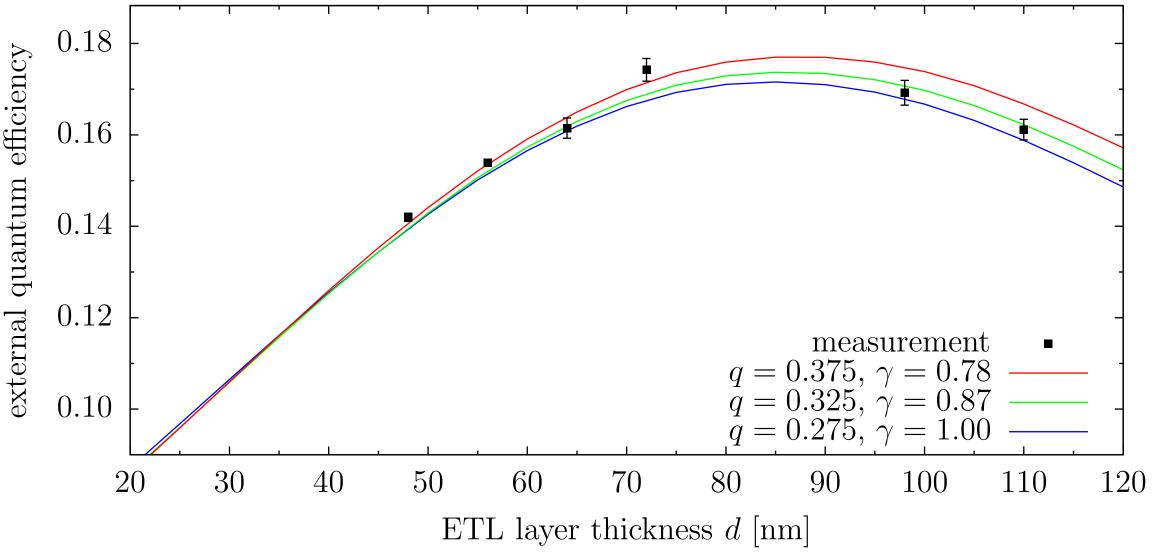

(b) *Charge recombination factor γ as fit parameter using selected values of q.*

Figure 4.52.: Black squares: measured external quantum efficiency of the red OLED (fig. 4.45) as a function of ETL thickness. Current density $j = 7.5\,\mathrm{mA/cm^2}$. Solid lines: corresponding simulations for different quantum efficiencies q and charge balance factors γ. The error bars represent the standard deviation resulting from the measurements of several devices with the same ETL thickness (for the two thinnest devices the error is very small and the error bars are covered by the data point).

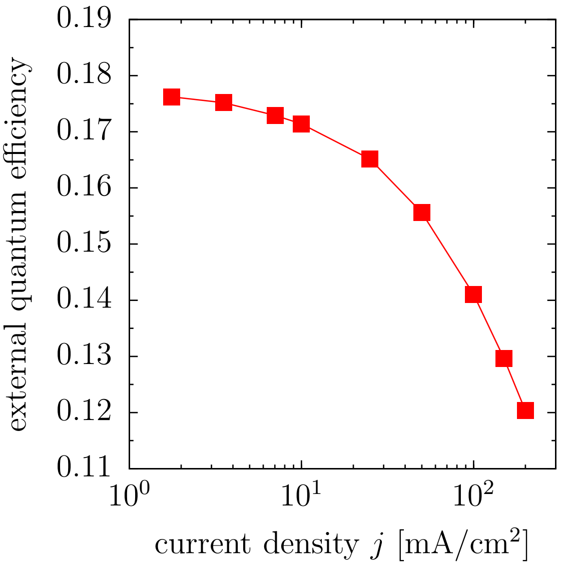

Figure 4.53.: Measured external quantum efficiency as a function of current density for the device presented in fig. 4.45 with an ETL thickness of 72 nm.

surrounding OLED stack. This value, however, might be different to the QE of the dye inside the OLED, especially, as will be shown in the following, at high current densities, but it would at least give an estimate. Unfortunately, such comparing PL QE measurements are not available for the red dye used in this particular OLED stack.

As can be seen in fig. 4.53, device efficiency decreases with increasing current density (shown for the device with 72 nm ETL). This is expected due to the enhancement of triplet-polaron and triplet-triplet annihilation at higher values of current density, i.e., the rate of competing non-radiative processes is enhanced by increasing the operational current density. Fig. 4.54a shows the external quantum efficiency as a function of ETL thickness as derived from the measurements of the devices operated at a high current density of $j = 150\,\mathrm{mA/cm^2}$. The simulation results for $\gamma = 1$ yield a lower limit for q of 0.20. The adaption to the curve progression is shown in fig. 4.54b. The best fit of the experimental data in the case of $j = 150\,\mathrm{mA/cm^2}$ is obtained for $q = 0.25$ and $\gamma = 0.85$ (again the value of γ should be taken only as an estimate, but it is astonishing that it is almost the same as before). Compared to the above case, this lower radiative quantum efficiency reflects the expected enhancement of non-radiative recombination at higher current density, resulting in a lower EQE (fig. 4.53). Altogether, the described method demonstrates the ability to extract the quantum efficiency of an emitter embedded inside an OLED even for different current densities.

4.6.2. Using photoluminescence or pulsed electroluminescence measurements

As mentioned previously, it is also possible to extract the emitter quantum efficiency using photoluminescence measurements from stacks where the distance between the emitter and a reflecting electrode is varied. This has already been shown by CPS for

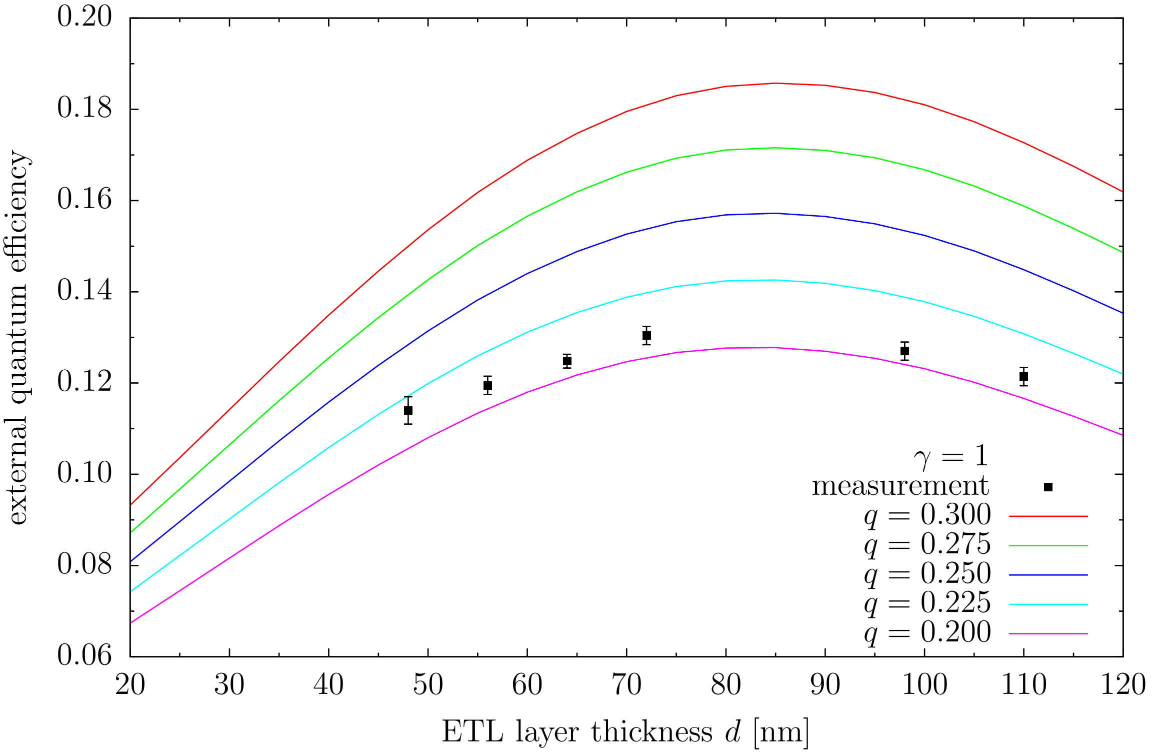

(a) *Fixed charge recombination factor:* $\gamma = 1$.

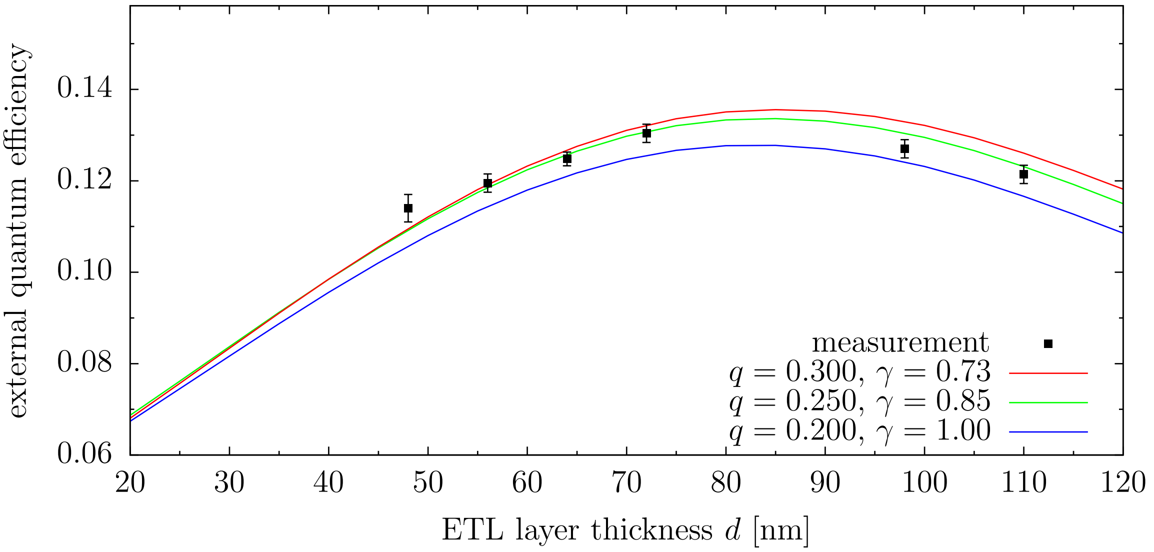

(b) *Charge recombination factor* γ *as fit parameter using selected values of* q.

Figure 4.54.: Black squares: measured external quantum efficiency of the red OLED (fig. 4.45) as a function of ETL thickness. Current density $j = 150\,\mathrm{mA/cm^2}$. Solid lines: corresponding simulations for different quantum efficiency q and charge recombination factors γ.

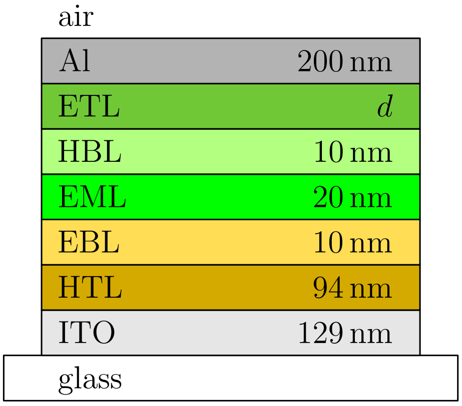

Figure 4.55.: OLED stack from OSRAM OS with Ir(ppy)$_3$ as emitter in an undisclosed matrix. Dipoles assumed to be located in the middle of the EML.

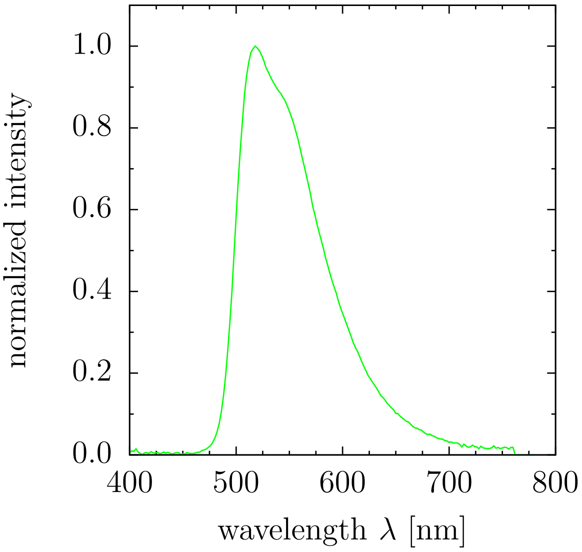

Figure 4.56.: Normalized spectrum of the Ir(ppy)$_3$ emitter used in the devices shown in fig. 4.55.

the experimental data of Drexhage[57]. As will be shown in the following, this method can also be applied to complete OLED stacks.

Again, OLEDs fabricated by OSRAM OS are used and again the thickness of the doped ETL is varied. The OLED stack is shown in fig. 4.55. For this stack, however, Ir(ppy)$_3$ (tris(2-phenylpyridine)) is used as phosphorescent green emitter in an undisclosed matrix (for the spectrum, please see fig. 4.56). All other materials are also undisclosed; but this is not relevant for the discussion. The simulated spectra for perpendicular emission of the devices with different ETL thickness are shown in fig. 4.57. These are in very good agreement with experimental data (not shown here). The different peak heights already indicate that the ETL thickness variation influences the cavity considerably.

As before, the quantum efficiency q of the emitter can be extracted from simulations and measurements of the external quantum efficiency. This is shown in fig. 4.58 for direct emission and in fig. 4.59 for total emission (a hemisphere was used for outcoupling of the substrate modes). The applied current density was $j = 2.58\,\mathrm{mA/cm^2}$. From both figures the quantum efficiency is determined to be in the range of $q \approx 0.6$.

Fig. 4.60 shows the normalized radiative lifetime for different values of the emitter quantum efficiency q as determined by “PDCalc”. All curves intersect at an ETL thickness of $d \approx 111\,\mathrm{nm}$, where the normalized radiative lifetime τ/τ_0 equals 1, hence the dipoles are neither damped nor accelerated. Also shown in the same figure are three different radiative lifetime measurements: two photoluminescence (PL) measurements and a pulsed electroluminescence (EL) measurement. Two excitation wavelengths, $\lambda = 337\,\mathrm{nm}$ and $\lambda = 355\,\mathrm{nm}$, respectively, with different pulse lengths and energy densities have been used in the PL measurements, where a pulsed laser excites the emitter

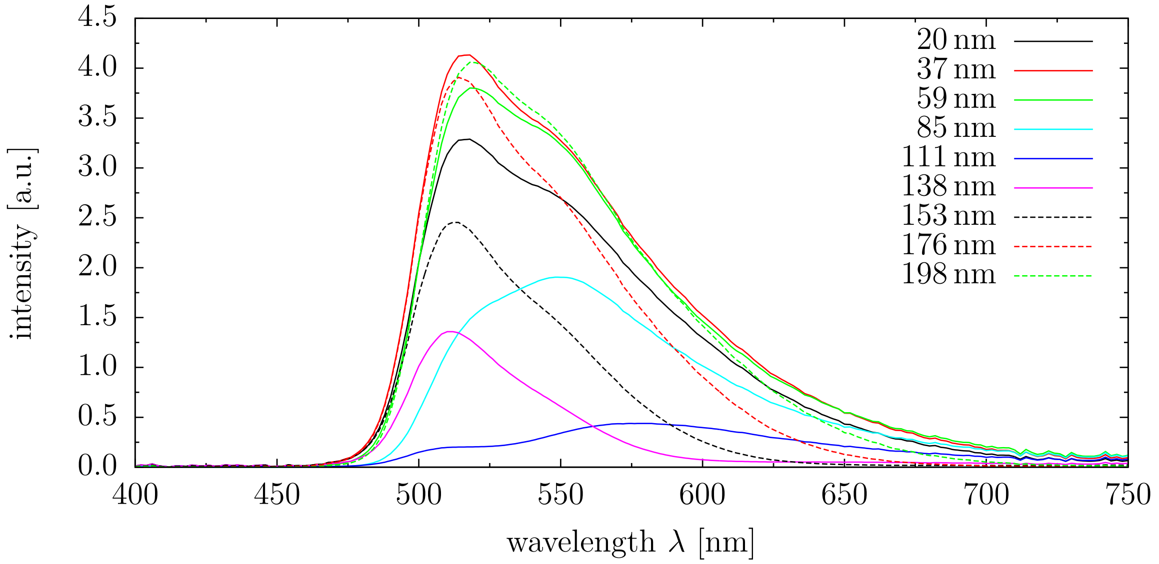

Figure 4.57.: Simulated spectra (perpendicular emission) of the OLEDs shown in fig. 4.55 using different ETL thicknesses d. Very good agreement with experimental data (not shown here).

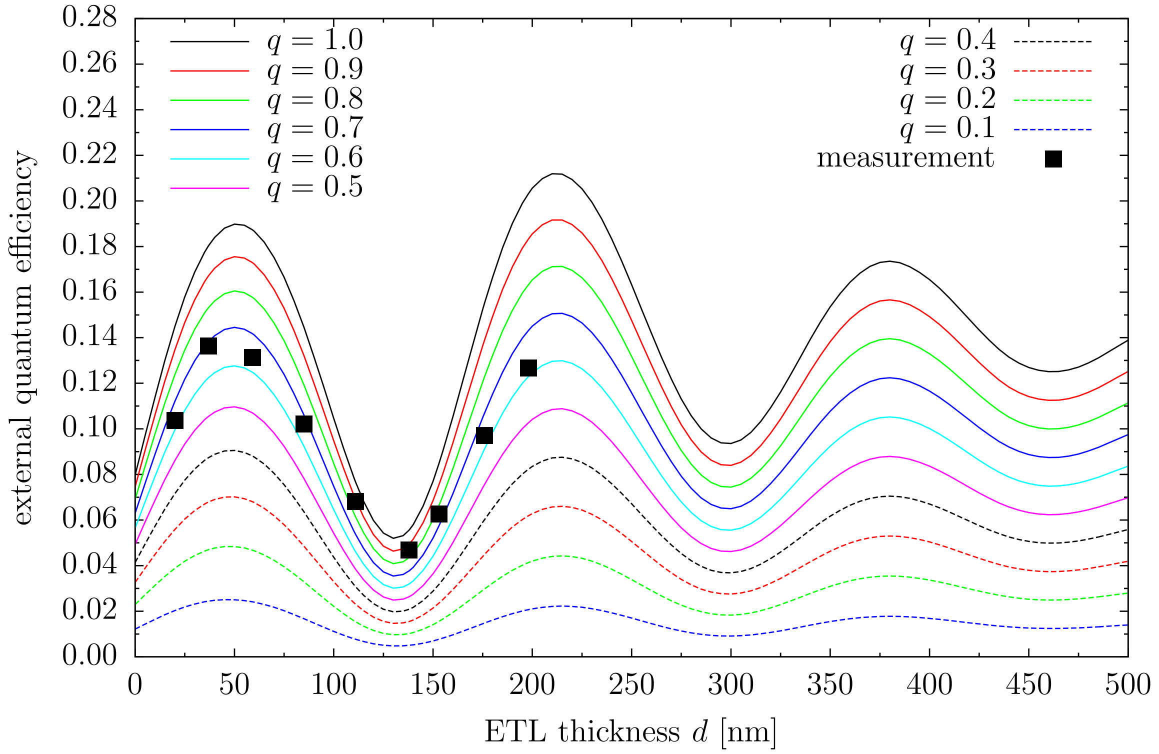

Figure 4.58.: Simulated external quantum efficiencies (direct emission) for the OLED stack shown in fig. 4.55 (lines). Experimental data shown as symbols. ($j = 2.58\,\mathrm{mA/cm^2}$, $\Delta k_\mathrm{x} = 2 \cdot 10^5\,\mathrm{m^{-1}}$, $\Delta d = 5\,\mathrm{nm}$)

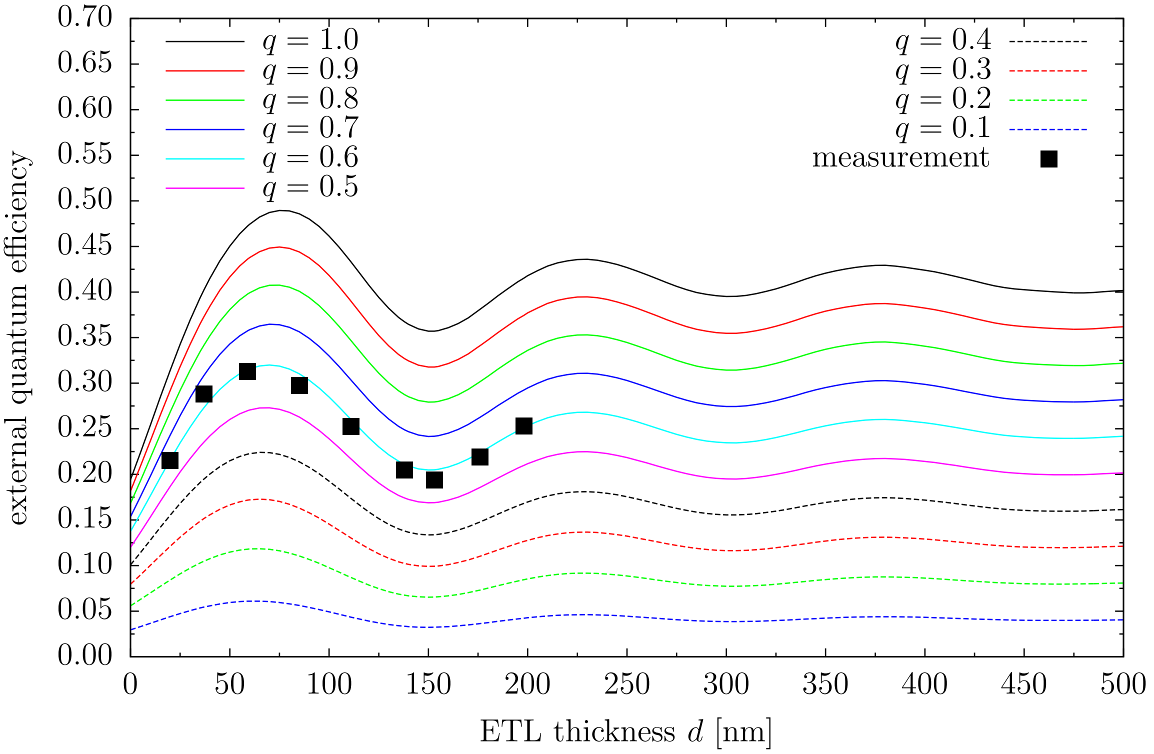

Figure 4.59.: Simulated external quantum efficiencies for the OLED stack shown in fig. 4.55 using a hemisphere for outcoupling of substrate modes (lines). Experimental data shown as symbols. ($j = 2.58\,\mathrm{mA/cm}^2$, $\Delta k_\mathrm{x} = 2 \cdot 10^5\,\mathrm{m}^{-1}$, $\Delta d = 5\,\mathrm{nm}$)

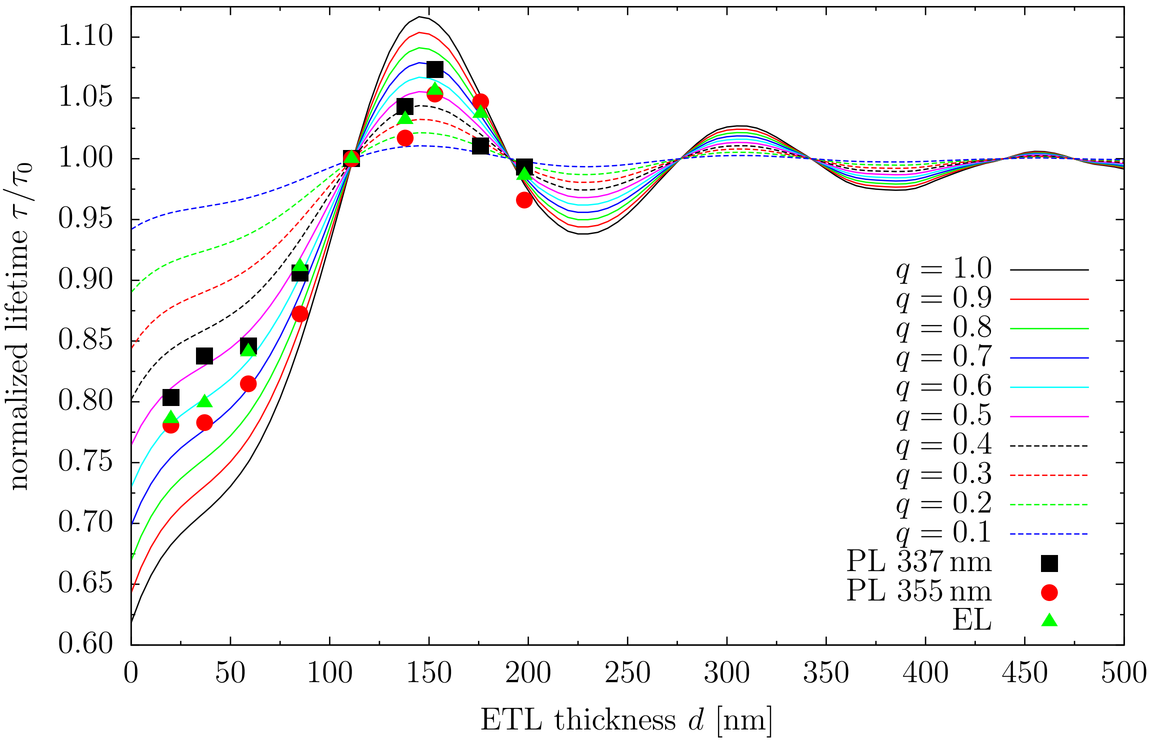

Figure 4.60.: Simulated radiative lifetime of the OLEDs shown in fig. 4.55 using different ETL thicknesses d and quantum efficiencies q (lines). Experimental data obtained with photoluminescence and pulsed electroluminescence measurements (normalized to the device with $d = 111\,\text{nm}$ as here $\tau/\tau_0 = 1$ for all q as determined by the simulation) is shown as symbols. It can be concluded that the emitter quantum efficiency is $q \approx (0.6 \pm 0.1)$.

molecules. For the EL measurements, the emission from the OLEDs is stimulated with a square wave voltage. In both types of measurements, the time-dependent emission spectra are recorded with a streak camera system. Afterward, the lifetimes of the emissive states are calculated. The measurements shown here are by courtesy of my colleague Tobias Schmidt, who will discuss the measurement methods in more detail in his PhD thesis[82]. The obtained lifetimes, shown as symbols in fig. 4.60, are all normalized to the OLED stack with an ETL thickness of $d = 111\,\text{nm}$, as here $\tau/\tau_0 = 1$ independently of q. From the curves progressions the quantum efficiency is determined to be in the range of $q \approx (0.6 \pm 0.1)$ which is in perfect agreement with the value obtained from the external quantum efficiency measurements. However, it should be noted that more experimental data points, especially at larger ETL thickness, would be beneficial for a more accurate determination of the quantum efficiency q.

4.7. Exploring other approaches for device efficiency enhancement

In the previous chapters it has been shown that even in optimized and ideal devices with charge balance factor $\gamma = 1$, singlet/triplet ratio $\eta_{\mathrm{s/t}} = 1$, and quantum efficiency $q = 1$ only about 40 % of the injected charge carriers are radiated from the OLED as photons. To improve efficiency novel approaches have to be considered to uplift this number. Some ideas shall be explored in the following.

4.7.1. Recycling of plasmons

Usually, a metal is used in OLEDs as electric contact, most commonly as cathode. Unfortunately, this allows the excitation of plasmons: light which is lost inside the OLED stack. As discussed earlier, one possible way out is moving the emission layer farther away from the metal electrode, however, this might change the electrical characteristics of the device and the amount of energy coupled to waveguided modes and may not be favorable. However, if the energy coupled into the plasmons can be "recycled" and re-emitted as light, the efficiency of the OLED could be increased. Andrew and Barnes showed a simple experiment (fig. 4.61)[83], where light from a green dye (Alq_3 in PMMA) excites a surface plasmon at the interface to a thin Ag film. Its evanescent wave extends through the thin film to the other interface. The magnitude of the wave is attenuated, however, it still complies to the dispersion relation of a plasmon at a PMMA/Ag interface. This plasmon in turn excites a red dye (rhodamine 6G (R6G) in PMMA) on the other side of the metal. With a combination of control experiments and thickness variations of the silver layer, the authors could show that an increased R6G emission is due to an efficient energy transfer from Alq_3 to R6G, which is mediated through a plasmon. For this kind of energy transfer, it is required that the acceptor (R6G) is absorbing in the emission region of the donor (Alq_3). Furthermore, the use of the same matrix (here: PMMA), or more precise materials with almost identical refractive indices, is required to fulfill the plasmon dispersion relation on both sides of the Ag film. Benedikt Arndt has performed similar experiments, investigating the influence of the Ag layer thickness on the energy transfer; please see his bachelor's thesis for details[84].

With this configuration it is possible to release energy originally trapped in the excited plasmon. If this configuration is transferred to an OLED, this would mean that more light can be emitted from the OLED, practically at no cost. One could even think of designing the OLED in such a way that the plasmon is specifically pumped to maximize the energy transfer. Such an OLED could be very thin: automatically more energy is coupled to the plasmon and, if the device is thin enough, could even be without waveguided light. If the energy transfer is efficient, one could also build a microcavity OLED with two metal electrodes where the plasmon energy excites dyes on the outside. These techniques awake special interest for signage applications, e.g., signs for emergency exits (emitting on both sides) or street numbers, as the desired light emitting area could easily be defined by using printing techniques for the dye.

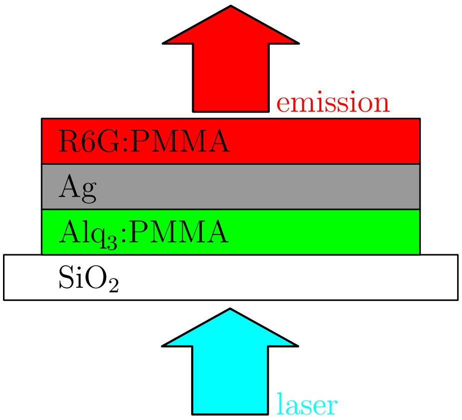

Figure 4.61.: Stack used by Andrew and Barnes to demonstrate transfer of energy through a metal film from a green dye (Alq_3 in PMMA) to a red dye (rhodamine 6G (R6G) in PMMA) mediated by plasmon energy transfer[83].

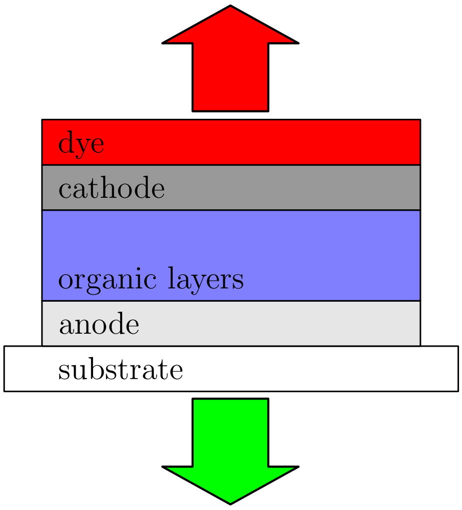

Figure 4.62.: OLED emitting on two sides: Lambertian emission to the bottom, emission to top from an excited dye (plasmon mediated energy transfer).

It could also be used to build an OLED which emits Lambertian light on one side of the stack and shows a logo of a company through the excited dye on the other side (fig. 4.62). These ideas have been filed in a patent application[85] and are currently under investigation by my colleagues Jörg Frischeisen and Bert Scholz and will be part of their PhD and diploma theses, respectively[86,87]. In a proof-of-concept experiment (fig. 4.63), the energy transfer has been visualized: a thin film of Alq_3 (20 nm) is excited with a laser beam and therefore excites plasmons at the adjacent Ag interface. As the glass substrate on the other side of the silver film (50 nm) has higher effective medium refractive index than a thin Alq_3 film, the evanescent wave is coupled to a plasmon, which eventually re-emits light coupled out through a glass prism. This configuration is shown from above in a photograph, fig. 4.64[86]. The outcoupled plasmon shows different color (dispersion in the wavelength) at different angles of emission θ. The simulation result of “PDCalc” for the outcoupled light is shown in fig. 4.65, showing the dispersion relation visible in the photograph (fig. 4.64).

4.7.2. Using substrates with high refractive index

As the refractive indices of the organic layers and ITO ($n \approx 1.8$) are larger than the refractive index of the substrate ($n \approx 1.5$) waveguided modes are excited inside the OLED cavity (see ch. 4.2.2). However, if the refractive index of the substrate is higher, there would be no total internal reflection at the ITO/substrate interface and more light can be coupled into the substrate. With suitable outcoupling techniques this light is accessible, leading to higher outcoupling efficiencies. This has already been

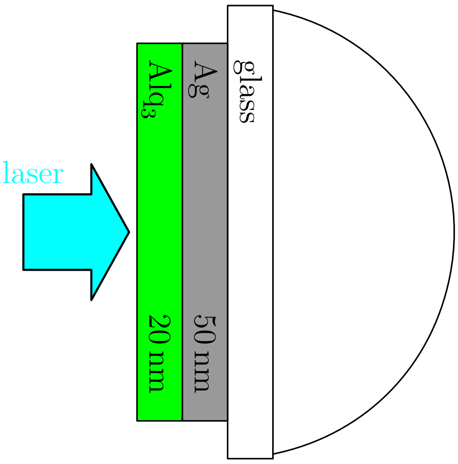

Figure 4.63.: Proof-of-concept experiment of the energy transfer across a Ag film. Excitation of Alq$_3$ with a laser beam.

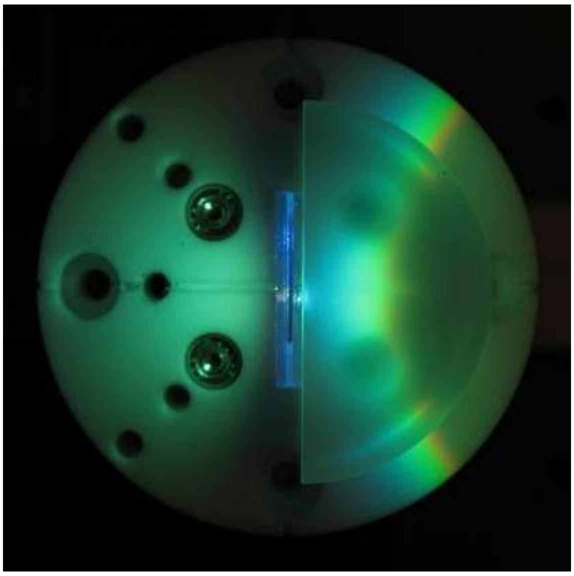

Figure 4.64.: Photograph of the proof-of-concept experiment (fig. 4.63). Courtesy of Jörg Frischeisen[86].

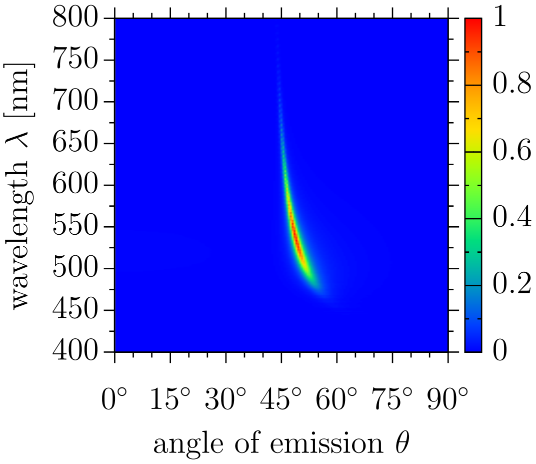

Figure 4.65.: Angular emission spectrum of the proof-of-concept experiment (fig. 4.63) calculated by "PDCalc". $\Delta k_\mathrm{x} = 1 \cdot 10^5\,\mathrm{m}^{-1}$.

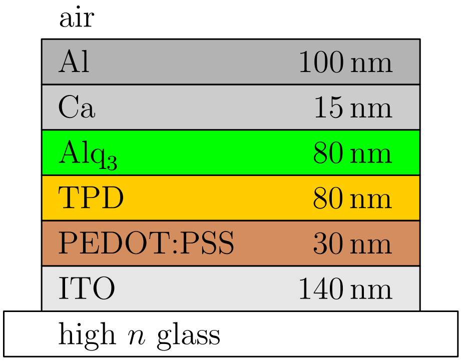

Figure 4.66.: OLED stack with high index glass substrates: $n_{\text{glass}} = 1.8$, 2.0, 2.2, 2.4, 2.6, and 2.8. Dipole layer located at the TPD/Alq_3 interface.

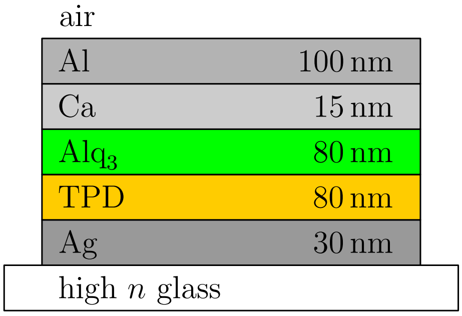

Figure 4.67.: Microcavity OLED stack using a thin Ag anode with high index glass substrates: $n_{\text{glass}} = 1.8$, 2.0, 2.2, 2.4, 2.6, and 2.8. Dipole layer located at the TPD/Alq_3 interface.

shown by Mladenovski et al.[88] and Reineke et al.[35] for different high refractive index substrates ($n \approx 1.8$). However, even more light is accessible, when substrates with even higher refractive index are used.

The OLEDs presented here are again based on the reference design of the Alq_3-OLED, fig. 4.3, using glass substrates with different refractive indices (fig. 4.66): $n_{\text{glass}} = 1.8$, 2.0, 2.2, 2.4, 2.6, and 2.8. Additionally, these variations of the substrate have been applied to a microcavity design, fig. 4.67, which could be used to couple out part of the plasmons excited at the anode as well (see previous chapter). Please note that the stacks should be optimized for using the different substrates, however, this is not undertaken here.

The results for the OLED containing ITO are shown in tab. 4.3. With increasing refractive index the direct emission is increasing, but the value for the emission to the substrate has a maximum, and therefore also the value for the total emission for a refractive index of $n = 2.2$. There are no waveguided modes left, as expected, and the amount of power coupled to plasmons is reduced as well. However, absorption is increasing with increasing refractive index of the substrate. This is attributed to the higher reflectivity of the substrates, as is evident from the Fresnel coefficients (eq. (3.56) – (3.59)).

As has been shown in the previous chapter, plasmons can be coupled out of a thin metal if the adjacent material has high refractive index. This can be the case for the anode in the microcavity design; the corresponding simulation results are shown in tab. 4.4. Again, in agreement with the ITO-OLED, the value for direct emission is increasing with increasing refractive index of the substrate and also the power coupled into the substrate is increasing. At the same time the amount of power coupled to (non-emissive) plasmons is reduced drastically. When comparing the calculated angular emission spectra for the ITO-OLED (fig. 4.68) and the microcavity OLED (fig. 4.69) with refractive index $n = 2.4$, respectively, it is evident that the emitted light is neither Lambertian nor stable in color with respect to the viewing angle,

substrate	direct emission [%]	emission to substrate [%]	wave-guided [%]	plasmons [%]	absorption [%]
BK7 glass	16.2	23.8	11.6	35.9	12.5
$n = 1.8$	16.8	31.7	0.1	35.3	16.1
$n = 2.0$	17.0	33.0	0.0	23.5	26.4
$n = 2.2$	17.3	32.9	0.0	14.2	35.7
$n = 2.4$	17.4	32.6	0.0	9.2	40.8
$n = 2.6$	17.6	32.3	0.0	6.4	43.8
$n = 2.8$	17.7	32.0	0.0	4.5	45.8

Table 4.3.: Fractions of power coupled to the different modes for the OLED stack with substrates having different refractive indices (fig. 4.66). ($q = 1$, $\Delta k_\mathrm{x} = 1 \cdot 10^5\,\mathrm{m}^{-1}$)

substrate	direct emission [%]	emission to substrate [%]	wave-guided [%]	plasmons [%]	absorption [%]
BK7 glass	4.9	7.0	5.8	37.2	45.2
$n = 1.8$	5.5	10.0	0.0	33.6	50.9
$n = 2.0$	5.8	11.9	0.0	25.2	57.1
$n = 2.2$	6.1	13.8	0.0	14.0	66.1
$n = 2.4$	6.4	14.8	0.0	8.2	70.6
$n = 2.6$	6.6	15.3	0.0	5.4	72.8
$n = 2.8$	6.7	15.6	0.0	3.6	74.0

Table 4.4.: Fractions of power coupled to the different modes for the microcavity OLED stack with substrates having different refractive indices (fig. 4.67). ($q = 1$, $\Delta k_\mathrm{x} = 1 \cdot 10^5\,\mathrm{m}^{-1}$)

thus the outcoupled light has to be "processed" further to regain a uniform emission spectrum, if desired.

4.7.3. Metal-free, transparent OLED

In the previous chapter it has been shown how the light coupled into the plasmons can be extracted again as visible light. Another approach for efficiency enhancement could be to avoid the excitation of plasmons at all: a metal-free OLED. Such a stack has been published by our colleagues from the OPAL project from the TU Braunschweig[89]. Meyer et al. use a traditional substrate covered with ITO, several organic layers, then a tungsten oxide buffer layer as protection from a sputtered ITO layer on top (glass substrate, 130 nm ITO, 40 nm BPhen:Li, 5 nm TPBi, 15 nm TPBi : Ir(ppy)$_3$, 40 nm TCTA, WO$_3$ with variable thickness d (20 – 80 nm), and 60 nm of sputtered ITO, see fig. 4.70. Again, the chemical names can be found in the appendix (A.1).). They find

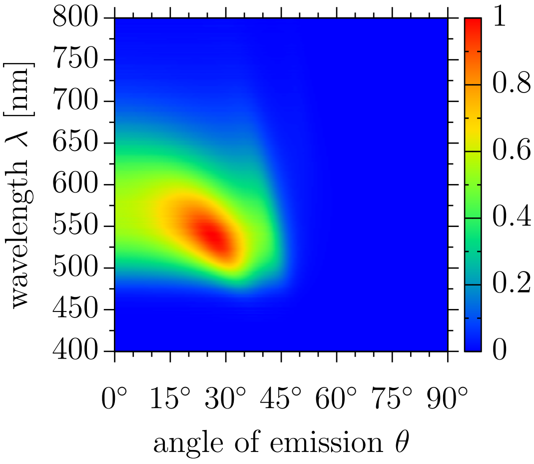

Figure 4.68.: Simulated angular emission spectrum for an OLED (fig. 4.66) with refractive index $n = 2.4$ substrate. ($\Delta k_\mathrm{x} = 1 \cdot 10^5\,\mathrm{m}^{-1}$)

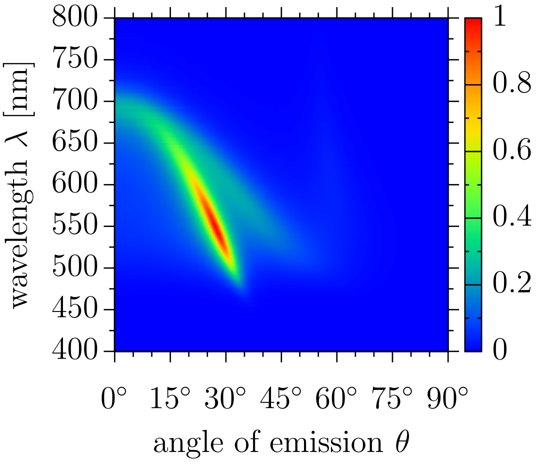

Figure 4.69.: Simulated angular emission spectrum for a microcavity OLED (fig. 4.67) with refractive index $n = 2.4$ substrate. ($\Delta k_\mathrm{x} = 1 \cdot 10^5\,\mathrm{m}^{-1}$)

that the optimal thickness of the buffer layer is around 60 nm in terms of protection, as well as current efficiency and power efficiency.

This stack has the benefit of being metal-free and therefore is transparent in the *off*-state as there are no reflecting electrodes. In the *on*-state the device emits light on both sides. The author's main interest in this paper lies on the WO_3 thickness necessary to provide a good sputter protection layer. As has been shown before, variations of layer thicknesses influence device efficiency. This is investigated again with "PDCalc" and compared to the published results. The refractive indices of the materials used have been provided by Sami Hamwi, TU Braunschweig. As quantum efficiency $q = 1$ is assumed for the $\mathrm{Ir(ppy)_3}$ emitter, however, this value might be lower in reality, which then would change the simulation results slightly, as has been shown for the $\mathrm{TPD/Alq_3}$ OLED.

The emission pattern in bottom (glass side) and top direction is shown in fig. 4.71 for a device with 60 nm WO_3. The two spectra agree well with the data published[89]. Experimentally it was found that nearly 70 % of the total outcoupled light is emitted through the bottom side. "PDCalc" yields a value of 60 % for this 60 nm WO_3 device (fig. 4.72). The difference is that the simulation considers the total half-space into which the OLED emits its light, whereas the measurement is done only in the direction perpendicular to the device.

Now the WO_3 layer thickness is varied and the amount of power coupled into the different modes is analyzed (see fig. 4.73). For light emitted directly there exists a broad maximum at about 46 nm WO_3 thickness of 16.6 %. However, the optimal layer thickness has been reported to be around 60 nm. This might be related to the use of WO_3 as a buffer layer in the ITO sputter process: thin layers (< 60 nm) do

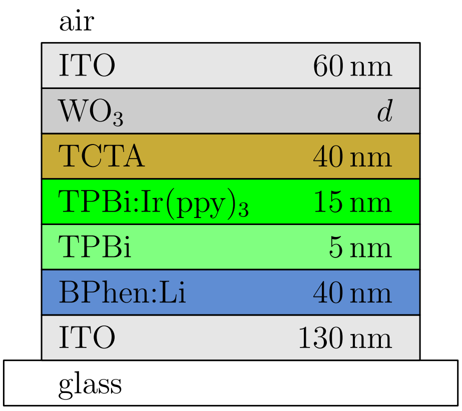

Figure 4.70.: Transparent, metal-free, inverted OLED stack used by Meyer et al.[89] with variable WO$_3$ thickness.

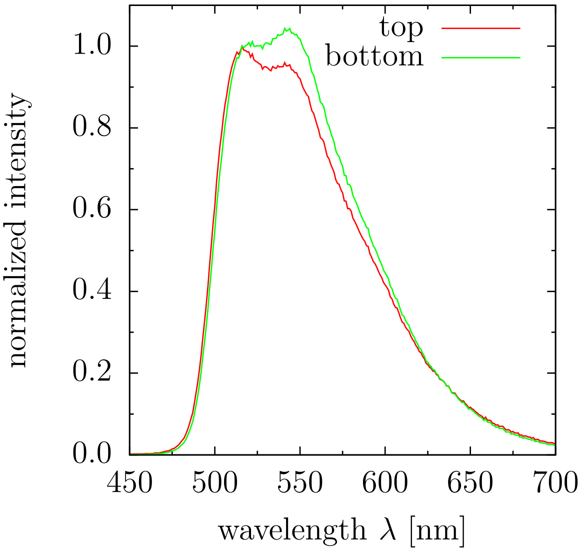

Figure 4.71.: Simulated top (red line) and bottom (green line) emission in forward direction of the OLED presented in fig. 4.70 with 60 nm WO$_3$ layer thickness.

not protect the OLED sufficiently, hence the OLED is damaged and light output is decreased. As the OLED is metal-free one expects that no plasmons are excited. If the emitting dipoles do not couple energy into plasmons, this "free" amount of energy could instead increase light outcoupling. But fig. 4.73 shows that even if an outcoupling structure is used on the glass substrate side only about 35 % of the generated light is emitted from the OLED. This is even less than for the device with conventional metal cathode shown earlier (fig. 4.44). The reason is that a huge amount of power is coupled into waveguided modes[¶]. As the amount of power coupled to total light emission and absorption is similar to the device of fig. 4.44, one concludes that the power distribution is just shifted from the plasmons to the waveguided modes for the transparent OLED. This means that a rise in outcoupled power is not achieved by substituting the metal electrodes with transparent ones per se.

4.7.4. Dipole orientation of the emitter material

In the simulations the isotropic emission of the dipoles is a mixture of three dipole orientations (eq. (4.11)): one dipole perpendicular and two dipoles parallel to the interfaces of the OLED (fig. 4.74). For the reference OLED presented in fig. 4.3, the power dissipation spectra for each dipole orientation is shown in fig. 4.74. The total power dissipation spectrum, already shown in fig. 4.6, is composed of these three

---

[¶] The plasmon contribution in this simulation is not expected due to the metal-free electrodes. Analysis of the power dissipation spectra shows that the waveguided modes "leak" into the k_x region where plasmons are usually excited.

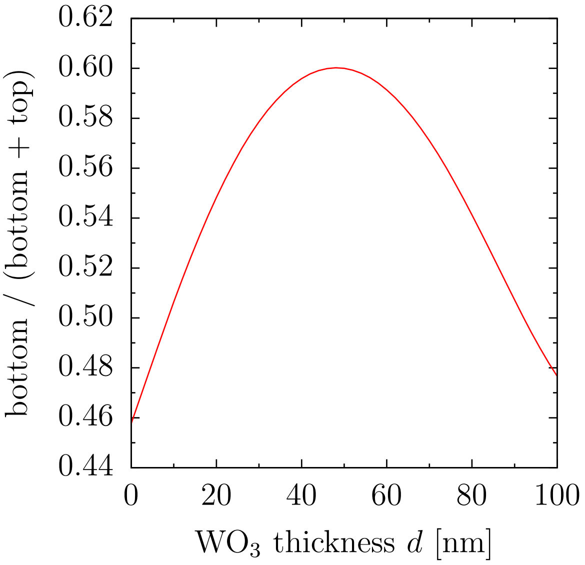

Figure 4.72.: Ratio of the bottom and (bottom + top) light emission without outcoupling structures for different WO_3 layer thickness d (fig. 4.70). ($q = 1$, $\Delta k_x = 2 \cdot 10^5\,\mathrm{m}^{-1}$, $\Delta d = 2\,\mathrm{nm}$, $400\,\mathrm{nm} \leqslant \lambda \leqslant 700\,\mathrm{nm}$)

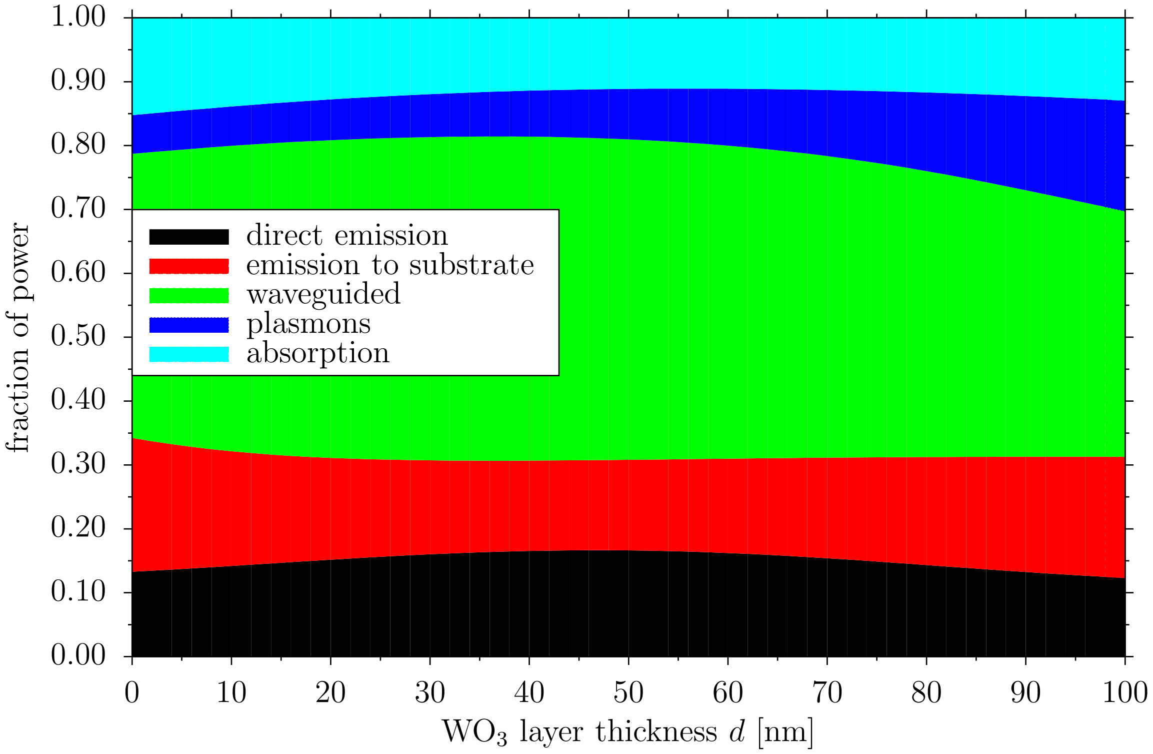

Figure 4.73.: Power coupled into the different modes for different WO_3 layer thickness d (fig. 4.70). ($q = 1$, $\Delta k_x = 2 \cdot 10^5\,\mathrm{m}^{-1}$, $\Delta d = 2\,\mathrm{nm}$, $400\,\mathrm{nm} \leqslant \lambda \leqslant 700\,\mathrm{nm}$)

contributions. The perpendicular dipole is mainly responsible for the excitation of the plasmon (fig. 4.74). One orientation of the parallel dipoles couples to the TE waveguided mode, to a large fraction of light trapped in the substrate, and to light emitted directly (parallel dipole 1 in fig. 4.74). The other parallel dipole couples to the TM waveguided mode, to light emitted directly or trapped in the substrate, and slightly contributes to the plasmon (parallel dipole 2 in fig. 4.74). As the coupling to the plasmon is undesired for high performance OLEDs, it would be best if the plasmonic mode would not be excited at all. From fig. 4.74 one concludes that if the perpendicular dipole orientation is avoided (and therefore the main contribution to the plasmon), one could reach better outcoupling efficiencies. The simulation where only the parallel dipole orientations are considered shows that the direct emission is increased from 16.2 % to 23.0 % for the reference OLED stack (fig. 4.3) with quantum efficiency $q = 1$ (for the fraction of power for the different modes, please see fig. 4.75a for isotropic dipole orientation and fig. 4.75b for parallel dipole orientation). If outcoupling structures are used, the increase is from 40.0 % to 56.5 %, which is a relative enhancement of about 41 %. The coupling to the plasmons is reduced from 35.9 % to 14.9 %. Further optimizations, e.g., layer thickness variations, might even yield higher outcoupling values. However, controlling the dipole orientation during fabrication of the OLED is a major issue, but it has been shown in literature that ordered dipole moments can be achieved in devices[59,90–92]. Controlling the dipole moment of the emitter therefore seems a promising candidate for high efficiency OLEDs. These promising ideas are under investigation by my colleague Jörg Frischeisen for his PhD thesis[86]. He already showed that it is possible to determine the molecular dipole orientation of dyes by combining photoluminescence measurements and simulations using "PDCalc"[93].

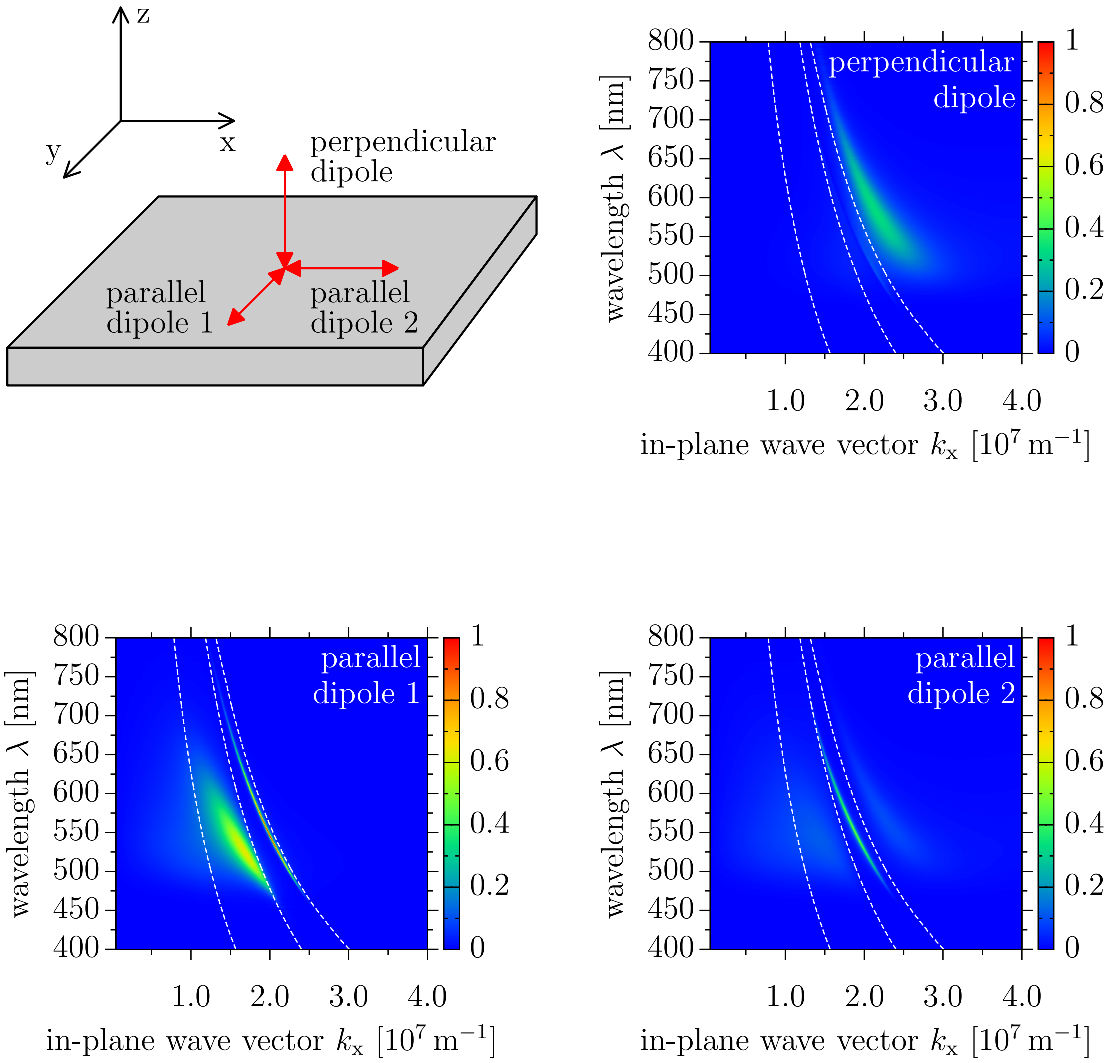

Figure 4.74.: Power dissipation spectra for different dipole orientations of the reference OLED (fig. 4.3). All spectra normalized to the same factor. ($\Delta k_x = 1 \cdot 10^5\,\mathrm{m}^{-1}$)

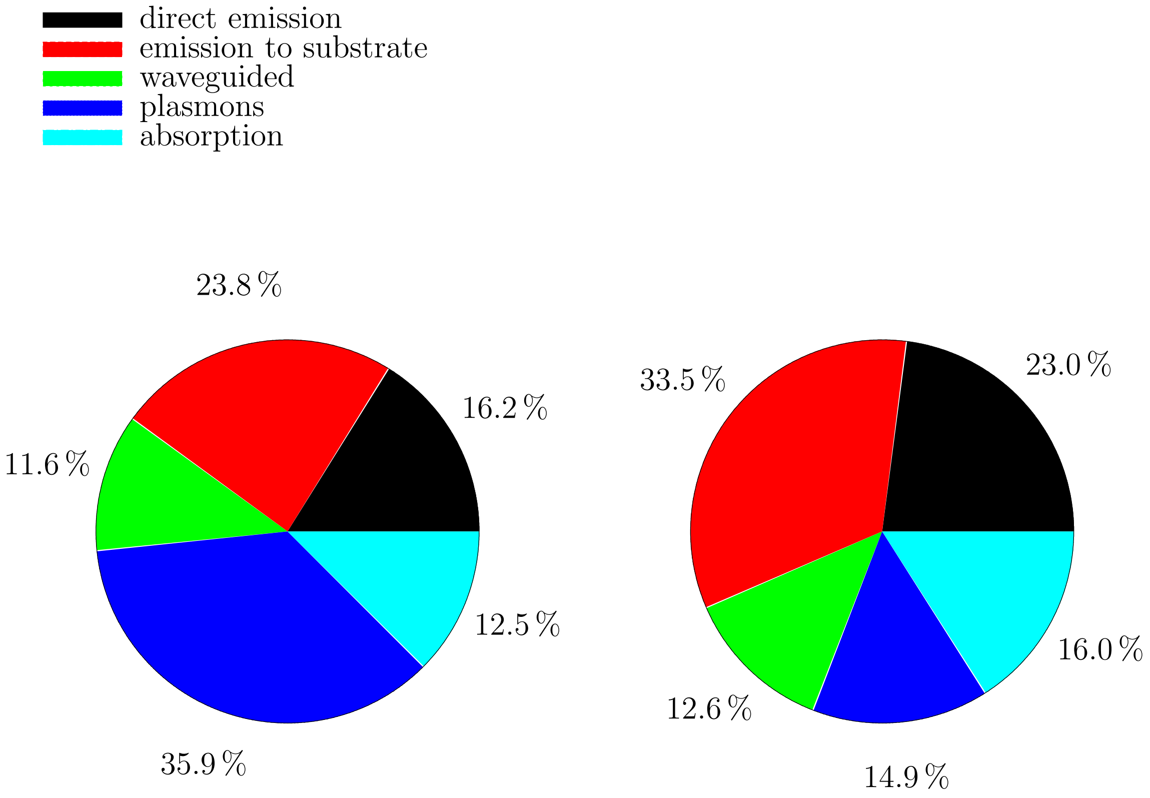

(a) *Isotropic dipole orientation.*

(b) *Only parallel dipole orientation.*

Figure 4.75.: Fraction of power coupled into the different modes for the reference OLED shown in fig. 4.3 for isotropic and parallel dipole orientations. ($q = 1$, $\Delta k_{\mathrm{x}} = 1 \cdot 10^5\,\mathrm{m}^{-1}$)

5. Electrical characterization of OLEDs via impedance spectroscopy

5.1. Introduction

Current density – voltage – luminance ($j-V-L$) measurements have been introduced in chapter 2.5 as a basic characterization method for OLEDs. A typical $j-V-L$ characteristic for an OLED containing F_4-TCNQ as hole injection layer (fig. 5.1) is shown in fig. 5.2. Please note that this hetero-layer OLED stack is a variant of the reference OLED stack, shown again in fig. 5.3, containing a hole-conducting (TPD) and an electron-conducting (Alq_3) compartment.

For reverse bias and even small positive bias the leakage current is below $j = 10^{-5}\,\mathrm{mA/cm^2}$. At a positive bias of approximately $V_{\mathrm{bi}} = 2.2\,\mathrm{V}$ the current density drastically increases and the OLED starts to emit light, as can be seen in the increasing luminance value. This increase in current density is due to injection of holes and electrons into the device. As discussed before, these charge carriers are forming excitons at the TPD/Alq_3 interface, which eventually recombine with a certain probability under emission of light.

However, the quasi-static $j-V$ measurements do not reveal further information about the device behavior under reverse bias conditions, i.e., below the built-in voltage V_{bi}. For this purpose impedance spectroscopy (IS) measurements can be used, which, e.g., yield the capacitance of the device for different applied bias voltages V_{DC}. For the OLED presented above this is shown in fig. 5.4 as an example. A small peak at the built-in voltage V_{bi} indicates the beginning of bipolar charge carrier injection; for even higher bias the capacitance decreases as charge is annihilated (holes and electrons recombine under emission of light). This information (the built-in voltage and light emission at higher bias voltage), however, is also accessible by the $j-V-L$ characteristics. But another feature is of interest as this has no equivalent in $j-V$ measurements: in reverse bias condition a transition from a lower to a higher capacitance occurs at a characteristic voltage. It is called transition voltage V_{t} (for this particular sample: $V_{\mathrm{t}} \approx -0.9\,\mathrm{V}$). Its origin is investigated with impedance spectroscopy measurements in the following chapters. Additionally, IS is used to identify other features relevant for organic devices.

Impedance spectroscopy, now generally speaking, is employed to investigate the dynamics of bound or mobile charge in the bulk or interfacial regions, with the great advantage of being a non-destructive analysis. It is a widely used tool for inorganic

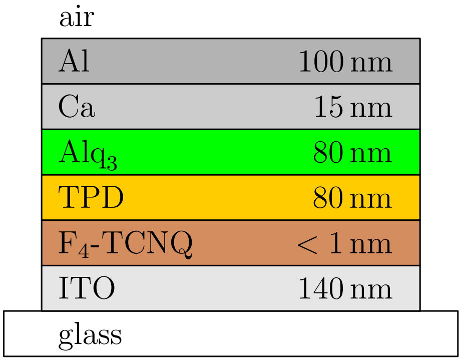

Figure 5.1.: OLED stack based on the reference design (fig. 5.3), however, using F_4-TCNQ as hole injection layer.

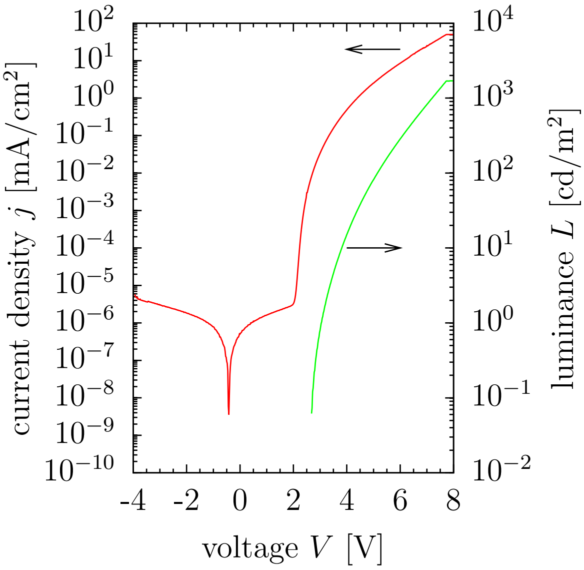

Figure 5.2.: Current density – voltage – luminance characteristic of the OLED with thin F_4-TCNQ interlayer (fig. 5.1).

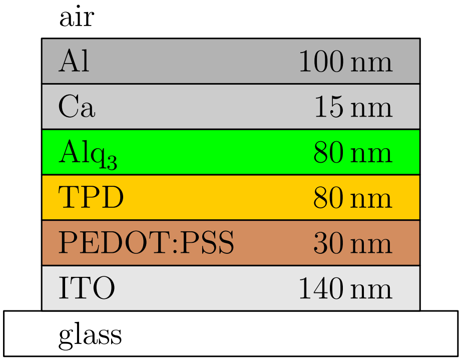

Figure 5.3.: Bottom-emitting OLED stack used as reference device.

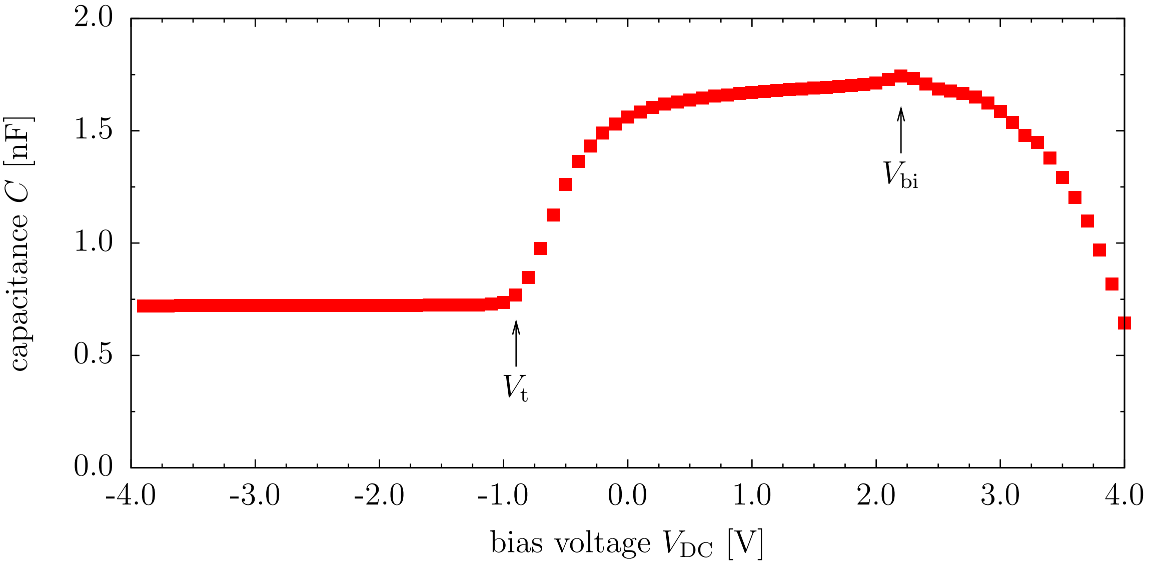

Figure 5.4.: Capacitance – voltage characteristic of the device shown in fig. 5.1. Built-in voltage indicated by small peak, $V_{\mathrm{bi}} \approx 2.2\,\mathrm{V}$. Above V_{bi}: decrease in capacitance due to charge annihilation (recombination of holes and electrons). Change in capacitance at the so-called transition voltage $V_{\mathrm{t}} \approx -0.9\,\mathrm{V}$ is not visible in $j-V$ characteristics (fig. 5.2). $f = 100\,\mathrm{Hz}$.

semiconductors and also for studies of solid/liquid interfaces[94,95]. In literature, IS has also been successfully applied to a variety of issues for organic electronic devices. Capacitance – voltage ($C-V$) measurements were used to extract the acceptor dopant concentration in poly-(p-phenylene-vinylene) (PPV) Schottky diodes[96]. Additionally, the energetic depth and the density of states created by doping of PPV were extracted from temperature dependent investigations[97]. The trap and transport states distributions for hole transport in PPV were determined by transient capacitance measurements[98]. Furthermore, the dynamics of injected charge carriers was investigated under space charge limited current (SCLC) conditions, i.e., under forward bias, for PPV derivatives[99] and $\mathrm{Alq_3}$[100]. More recently, it was shown that $C-V$ analysis in single carrier devices can also yield information about injection barriers and the built-in voltage resulting from different metal contacts[101]. Going to double carrier devices, such as OLEDs or OPVCs, additional features related to the dynamics of electron-hole pairs can be monitored using IS. It was shown, e.g., that charge carrier recombination leads to the appearance of negative capacitance[102].

In the following the concept of impedance spectroscopy is presented. IS is then applied to different OLED stacks to study charge injection and transport, its temperature dependence, and finally degradation processes.

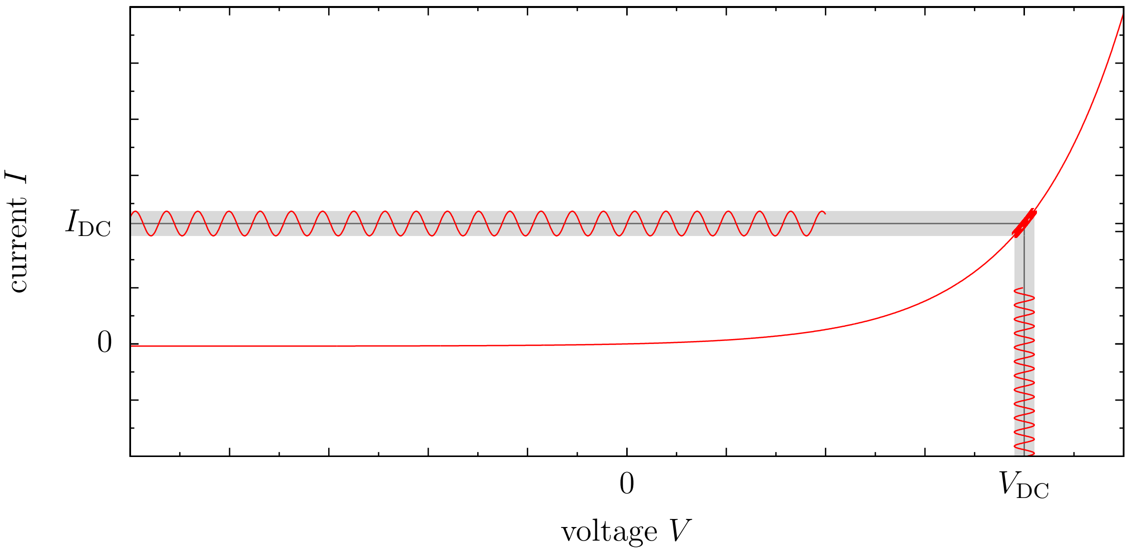

Figure 5.5.: Current – voltage characteristic of an ideal semiconductor diode, $I(V) = I_0 \cdot \left[\exp\left(\frac{eV}{k_B T}\right) - 1\right]$. In an impedance spectroscopy measurement the working point is chosen by a bias voltage V_{DC}. A small alternating voltage signal $V_{\mathrm{AC}}(t)$ is superimposed, resulting in an alternating current $I_{\mathrm{AC}}(t)$.

5.2. Impedance spectroscopy

In an IS experiment, a small, alternating electrical signal $V_{\mathrm{AC}}(t) = V_{\mathrm{AC}} \cdot \cos(2\pi f \cdot t)$ with small amplitude V_{AC} and frequency f is applied to the sample in addition to a constant bias voltage V_{DC}, resulting in a total applied voltage of

$$V(t) = V_{\mathrm{DC}} + V_{\mathrm{AC}}(t) \tag{5.1}$$
$$= V_{\mathrm{DC}} + V_{\mathrm{AC}} \cdot \cos(2\pi f \cdot t)\,. \tag{5.2}$$

The response of the sample, the current $I(t)$, therefore is also a result of a combined DC and AC response, I_{DC} and

$$I_{\mathrm{AC}}(t) = I_{\mathrm{AC}} \cdot \cos(2\pi f \cdot t + \varphi)\,, \tag{5.3}$$

where φ is a phase shift between voltage and current. V_{DC} serves as a handle to change the working point on the current – voltage characteristics of the sample, see fig. 5.5. It is obvious from this figure that the amplitude of the applied alternating voltage has to be small; otherwise the current response is not linear.

The complex impedance $\hat{Z}(f)$ is defined as the ratio of the applied alternating voltage and the current response in complex notation $\hat{V} = V_{\mathrm{AC}} \cdot \exp(\mathrm{i} \cdot 2\pi f \cdot t)$ and $\hat{I} = I_{\mathrm{AC}} \cdot \exp(\mathrm{i} \cdot (2\pi f \cdot t + \varphi))$, respectively, including their mutual phase shift:

$$\hat{Z}(f) = \frac{\hat{V}}{\hat{I}} = \frac{V_{\mathrm{AC}}}{I_{\mathrm{AC}}} \cdot \exp(-\mathrm{i}\varphi) = \mathrm{Re}(\hat{Z}) + \mathrm{i} \cdot \mathrm{Im}(\hat{Z})\,. \tag{5.4}$$

The modulus $|\hat{Z}|$ and the phase shift therefore are given by

$$|\hat{Z}| = \sqrt{\mathrm{Re}^2(\hat{Z}) + \mathrm{Im}^2(\hat{Z})}\,, \tag{5.5}$$

$$\varphi = \arctan\left(\frac{\mathrm{Im}(\hat{Z})}{\mathrm{Re}(\hat{Z})}\right)\,, \tag{5.6}$$

respectively. There are different equivalent representations of the complex impedance, however, the most intuitive one for semiconductor devices is the capacitance C, defined as

$$C(f) = \frac{1}{2\pi f} \cdot \frac{-\mathrm{Im}(\hat{Z})}{\mathrm{Re}^2(\hat{Z}) + \mathrm{Im}^2(\hat{Z})}\,. \tag{5.7}$$

The complementary quantity is the dielectric loss (the conductance G divided by the angular frequency $\omega = 2\pi f$, i.e., energy that goes into heating of the dielectric when varying the electric field):

$$\frac{G(\omega)}{\omega} = \frac{1}{2\pi f} \cdot \frac{\mathrm{Re}(\hat{Z})}{\mathrm{Re}^2(\hat{Z}) + \mathrm{Im}^2(\hat{Z})}\,. \tag{5.8}$$

The data obtained by impedance spectroscopy can be represented in several different forms, each especially suited for the topic of interest. In this thesis plots of capacitance – frequency ($C - f$) and capacitance – voltage ($C - V$) will be used to explain charge injection/transport and an interfacial charge in the OLEDs, respectively. Impedance measurements were performed using a frequency response analyzer (Solartron SI 1260 Impedance/Gain-Phase Analyzer) combined with a dielectric interface (Solartron 1296). This setup allows frequency sweeps covering a range from 10^{-2} to 10^{7} Hz. The AC oscillator level is set to $V_{\mathrm{AC,rms}} = 100\,\mathrm{mV}$ for all measurements.

5.2.1. Capacitance of a double RC circuit

The hetero-layer OLEDs under investigation in the following chapters are derived from the reference OLED design (fig. 5.3), consisting of two undoped organic semiconductor materials as HTL and ETL, respectively. Each of these two layers has a low, but non-vanishing, conductivity and a dielectric constant. Thus, they can be represented by a resistor R and a capacitor C connected as a parallel RC element. To model the OLED stack, two of these RC elements connected in series are considered (fig. 5.6), representing the HTL and the ETL. The combined capacitance of a double RC element is derived in the following.

A resistor with resistance R has the (complex) impedance $\hat{Z}_R = R$, a capacitor with capacitance C has $\hat{Z}_C = 1/(\mathrm{i}\omega C)$. If both are combined in parallel to a RC element, we obtain the impedance

$$\hat{Z}_{RC} = \frac{1}{\dfrac{1}{R} + \mathrm{i}\omega C}\,. \tag{5.9}$$

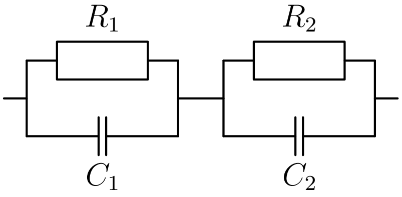

Figure 5.6.: Two RC elements combined in series to a double RC circuit.

Consider now two of these RC elements connected in series, fig. 5.6; the impedance of this circuit is

$$\hat{Z} = \hat{Z}_{R_1C_1} + \hat{Z}_{R_2C_2} \,. \tag{5.10}$$

From eq. (5.7) the total capacitance for the double RC element is calculated as

$$C(f) = \frac{R_1^2C_1 + R_2^2C_2 + 4\pi^2 f^2 R_1^2 R_2^2 \cdot C_1C_2 \cdot (C_1 + C_2)}{(R_1 + R_2)^2 + 4\pi^2 f^2 R_1^2 R_2^2 \cdot (C_1 + C_2)^2} \,. \tag{5.11}$$

If now an alternating voltage according to eq. (5.1) is applied with varying frequency f, we find two plateaus in the capacitance for low and high frequency and a transition region around a characteristic relaxation frequency f_r, see fig. 5.7. According to eq. (5.11) the limiting case for the total capacitance C of the double RC circuit in the high frequency range is

$$\lim_{f\to\infty} C(f) = C_\mathrm{hf} = \frac{C_1C_2}{C_1 + C_2} \,, \tag{5.12}$$

which is just the total capacitance of two capacitors in series. However, the low frequency limit (which corresponds to the DC regime) also depends on the values of the two resistors:

$$\lim_{f\to 0} C(f) = C_\mathrm{lf} = \frac{R_1^2C_1 + R_2^2C_2}{(R_1 + R_2)^2} \,. \tag{5.13}$$

The transition between these two limiting cases happens near the relaxation frequency f_r where the capacitance $C(f_\mathrm{r})$ is just in the middle of the two limiting cases

$$C(f_\mathrm{r}) = C_\mathrm{hf} + \frac{C_\mathrm{lf} - C_\mathrm{hf}}{2} = \frac{1}{2} \cdot \frac{(C_1R_1 + C_2R_2)^2}{(R_1 + R_2)^2 \cdot (C_1 + C_2)} \,. \tag{5.14}$$

Thus the relaxation frequency, which is related to the relaxation time τ_r of the circuit[103], can be calculated:

$$f_\mathrm{r} = \frac{1}{2\pi\tau_\mathrm{r}} = \frac{1}{2\pi} \cdot \frac{R_1 + R_2}{R_1R_2 \cdot (C_1 + C_2)} \,. \tag{5.15}$$

Eq. (5.11) thus can be simplified to

$$C(f) = C_\mathrm{hf} + \frac{C_\mathrm{lf} - C_\mathrm{hf}}{1 + \left(\frac{f}{f_\mathrm{r}}\right)^2} \,. \tag{5.16}$$

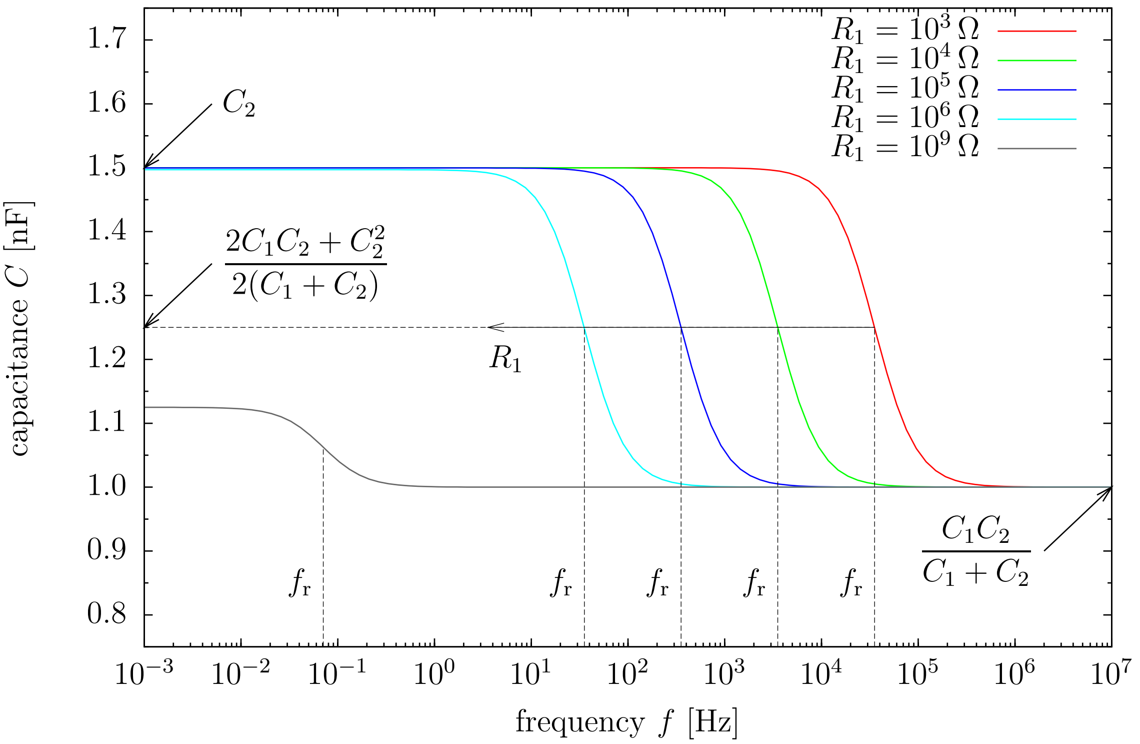

Figure 5.7.: Capacitance of a double RC circuit (see fig. 5.6) with variation of R_1. All other values fixed: $R_2 = 10^9\,\Omega$, $C_1 = 3\,\text{nF}$, and $C_2 = 1.5\,\text{nF}$. Relaxation frequency f_r is shifted to lower frequencies for higher values of R_1. Simplified limiting case for the capacitance at low frequency ($\lim_{f\to 0} C(f) = C_2$): only valid for $R_1 \ll R_2$ (colored lines).

Assuming that one of the two resistors is significantly less resistive, e.g., $R_1 \ll R_2$, eq. (5.13) – (5.15) yield

$$\lim_{f \to 0} C(f) = C_2\,, \tag{5.17}$$

$$f_\mathrm{r} = \frac{1}{2\pi} \cdot \frac{1}{R_1 \cdot (C_1 + C_2)}\,, \tag{5.18}$$

$$C(f_\mathrm{r}) = \frac{C_1 C_2}{C_1 + C_2} + \frac{C_2 - \dfrac{C_1 C_2}{C_1 + C_2}}{2} = \frac{2C_1 C_2 + C_2^2}{2 \cdot (C_1 + C_2)}\,. \tag{5.19}$$

Fig. 5.7 shows the capacitance of a double RC circuit for different values of R_1. All other values are fixed, $R_2 = 10^9\,\Omega$, $C_1 = 3\,\mathrm{nF}$, and $C_2 = 1.5\,\mathrm{nF}$. As long as $R_1 \ll R_2$ both limiting cases for high and low frequency are independent of the values of the resistors according to eq. (5.12) and (5.17). If $R_1 = R_2$ (gray line in fig. 5.7), the low frequency limit is considerably smaller. Still two plateaus are observable as the two capacitances have different values (if they would be equal, a constant capacitance over the entire frequency range would be observed). The most interesting behavior visible in $C - f$ measurements is the transition region: the relaxation frequency f_r is shifted to lower values with increasing R_1, see eq. (5.15). Therefore, f_r can be used as an indicator for the ratio of the resistances in the double RC element.

5.2.2. Influence of the impedance spectroscopy setup on the measured capacitance

In an ideal case, like the above modeled double RC element, the result in capacitance is flawless. However, the IS setup itself influences the obtained experimental data due to, e.g., the resistance, capacitance, and inductance of the lead cables and contact resistances at the electrodes. Equivalent circuits with more elements are needed to model the data; some of these are discussed in the following. The device under test (DUT) is always the double RC element discussed above.

First, the influence of a non-vanishing resistance in the lead cable or a contact resistance R_lead is shown in fig. 5.8; see fig. 5.9 for the corresponding model circuit. Upon increasing R_lead, a roll off at high frequency is visible, which is shifting to lower frequencies. This feature must not be mistaken with the step due to the double RC element at its relaxation frequency ($f_\mathrm{r} \approx 22\,\mathrm{Hz}$). This resistance can account for both, the resistance of the cable and, e.g., the resistance of the anode contact in OLEDs.

Next, the lead cable's inductance L_lead is additionally considered, see fig. 5.10. Usually, RG-58/U coaxial cables with BNC connectors are used in labs. Its inductance is given by[104]

$$L_\mathrm{coax} = \frac{\mu_0 \mu_r}{2\pi} \cdot l \cdot \ln\left(\frac{D}{d}\right)\,. \tag{5.20}$$

Here, l is the length of the cable, D is the inner diameter of the shield/diameter of the dielectric, d the diameter of the inner conductor. For this kind of coaxial cable $D = 2.9\,\mathrm{mm}$, $d = 0.9\,\mathrm{mm}$, and considering $\mu_r = 1$, the inductance per unit length

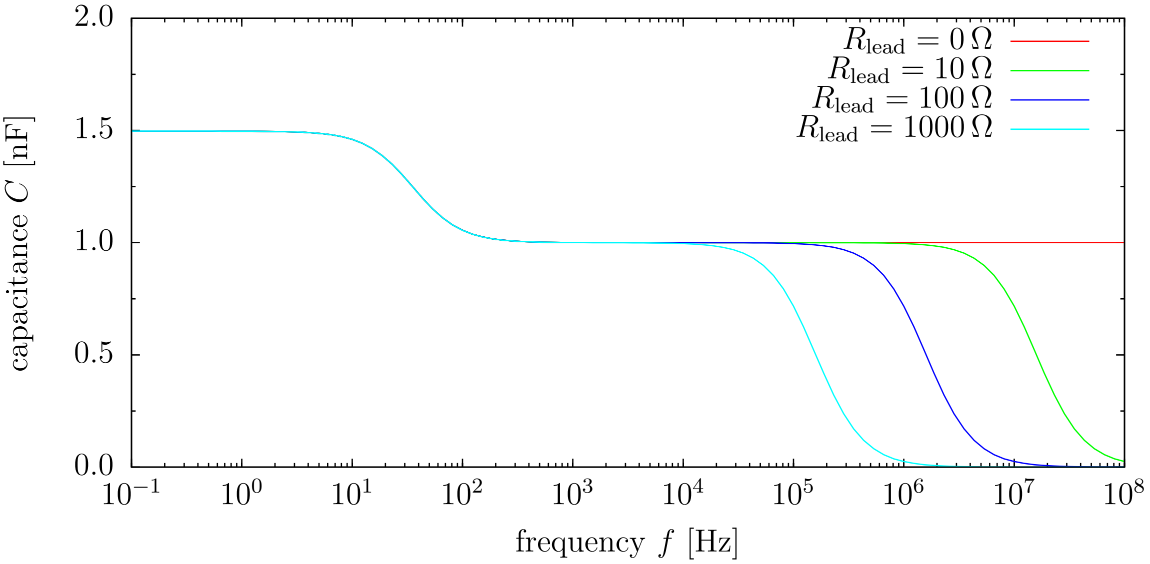

Figure 5.8.: Influence of a lead resistance R_{lead} on the measured capacitance. Equivalent circuit: see fig. 5.9. Device under test (DUT): double RC element ($R_1 = 10^6\,\Omega$, $R_2 = 10^9\,\Omega$, $C_1 = 3\,\text{nF}$, and $C_2 = 1.5\,\text{nF}$). Lead resistance leads to a roll off at high frequency.

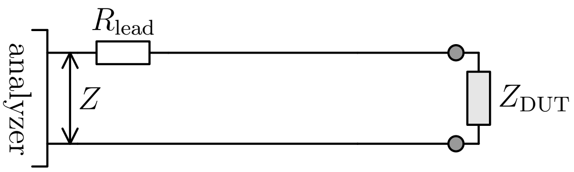

Figure 5.9.: Equivalent circuit with lead resistance R_{lead}.

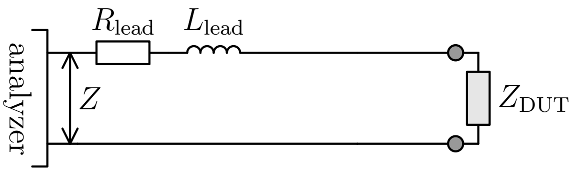

Figure 5.10.: Equivalent circuit with lead resistance R_{lead} and lead inductance L_{lead}.

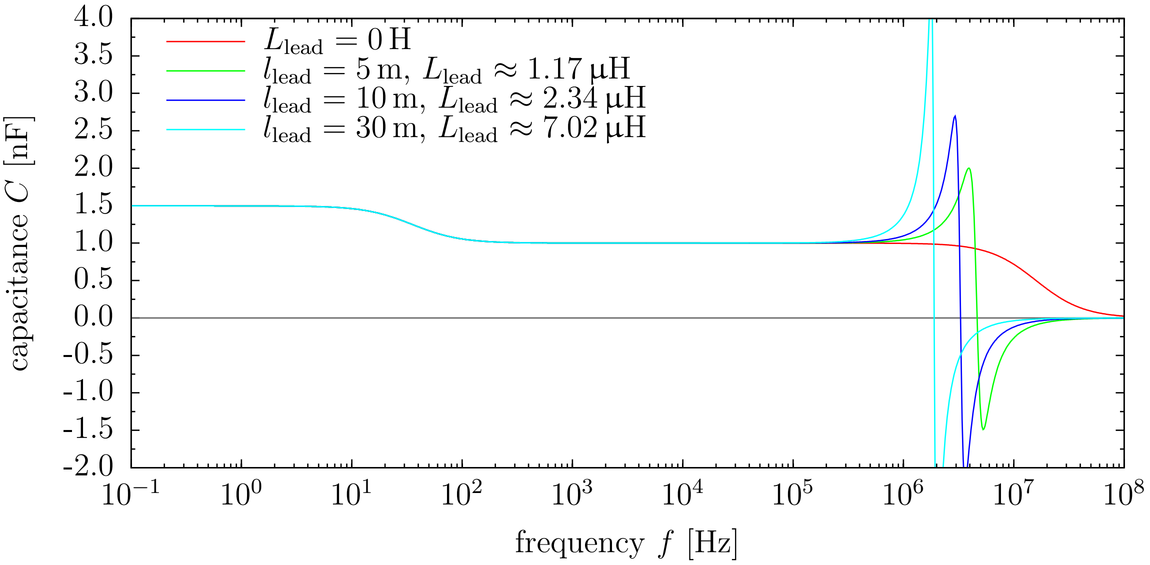

Figure 5.11.: Influence of the lead inductance L_{lead} (cables with different lengths l_{lead}) and lead resistance $R_{\text{lead}} = 10\,\Omega$ on the measured capacitance. Equivalent circuit: see fig. 5.10. DUT: double RC element ($R_1 = 10^6\,\Omega$, $R_2 = 10^9\,\Omega$, $C_1 = 3\,\text{nF}$, $C_2 = 1.5\,\text{nF}$).

is $L_{\text{coax}}/l \approx 2.34 \cdot 10^{-7}\,\text{H/m}$. The simulation in fig. 5.11 shows the influence of the inductance for different lengths l of this cable with a lead resistance* of $R_{\text{lead}} = 10\,\Omega$; the same kind of simulation is shown in fig. 5.12, however, with a lead resistance of $R_{\text{lead}} = 100\,\Omega$. As some of the samples have been studied with very long cables (approximately 15 m for each, anode and cathode connection), such effects have occurred in the measurements, typically the blue curves in fig. 5.11.

Other influences from the coaxial lead cables are a stray capacitance C_{stray} (equivalent circuit see fig. 5.13) and a leakage current through the dielectric (or stray resistance R_{stray}, see fig. 5.14). The leakage current can be considered very small and usually is neglected ($R_{\text{stray}} \to \infty$). The capacitance of the coaxial cable (being a cylindrical capacitor) is given by[105]

$$C_{\text{coax}} = \frac{2\pi\varepsilon_0\varepsilon_r}{\ln\left(\dfrac{D}{d}\right)} \cdot l\,. \tag{5.21}$$

For the RG-58/U cable ($Z = 50\,\Omega$), with $\varepsilon_{\text{r}} \approx 1.97$ the capacitance per meter is $C/l \approx 94\,\text{pF/m}$. This would have a significant influence on the measured capacitance, especially when using long cables. However, for the measurement setup only the inner conductors of two coaxial lead cables are used, therefore the stray capacitance is significantly less, having almost no influence. Nevertheless, the influence of the coaxial capacitance on the double RC element is shown in fig. 5.15 as if the outer conductor (shield) would be used as second connection to the sample.

---

[*] The ohmic resistance of the coaxial cable is almost negligible even for long cables and thus considered to be included in R_{lead}.

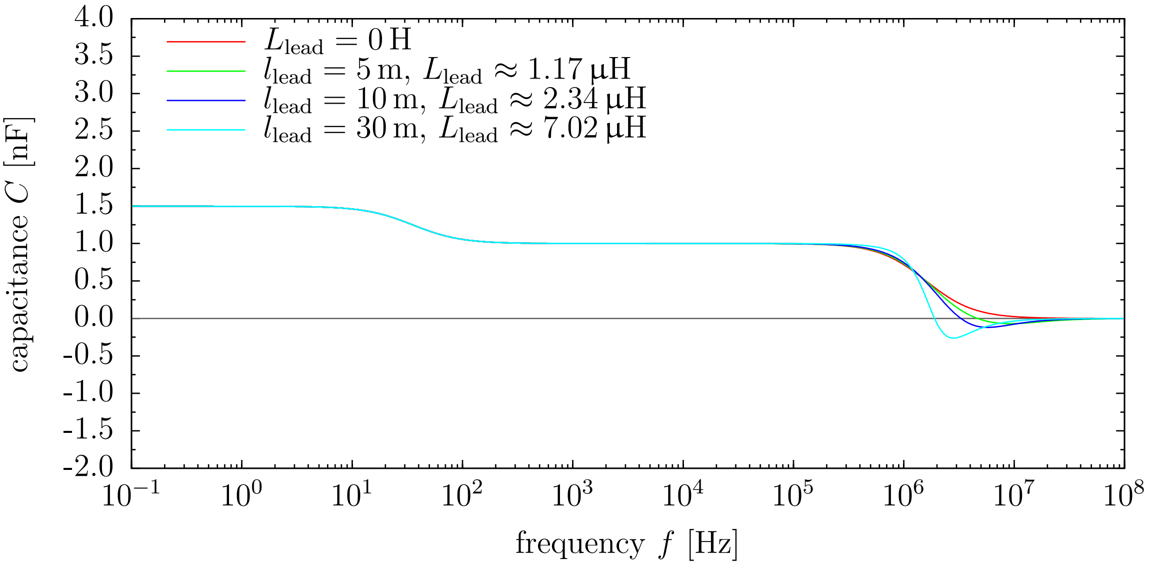

Figure 5.12.: Influence of the lead inductance L_{lead} (cables with different lengths l_{lead}) and lead resistance $R_{\mathrm{lead}} = 100\,\Omega$ on the measured capacitance. Equivalent circuit: see fig. 5.10. DUT: double RC element ($R_1 = 10^6\,\Omega$, $R_2 = 10^9\,\Omega$, $C_1 = 3\,\mathrm{nF}$, $C_2 = 1.5\,\mathrm{nF}$).

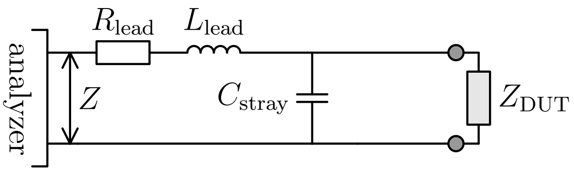

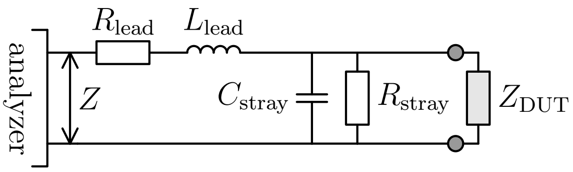

Figure 5.13.: Equivalent circuit with lead resistance R_{lead}, lead inductance L_{lead}, and stray capacitance C_{stray}.

Figure 5.14.: Equivalent circuit with lead resistance R_{lead}, lead inductance L_{lead}, stray capacitance C_{stray}, and stray resistance R_{stray}.

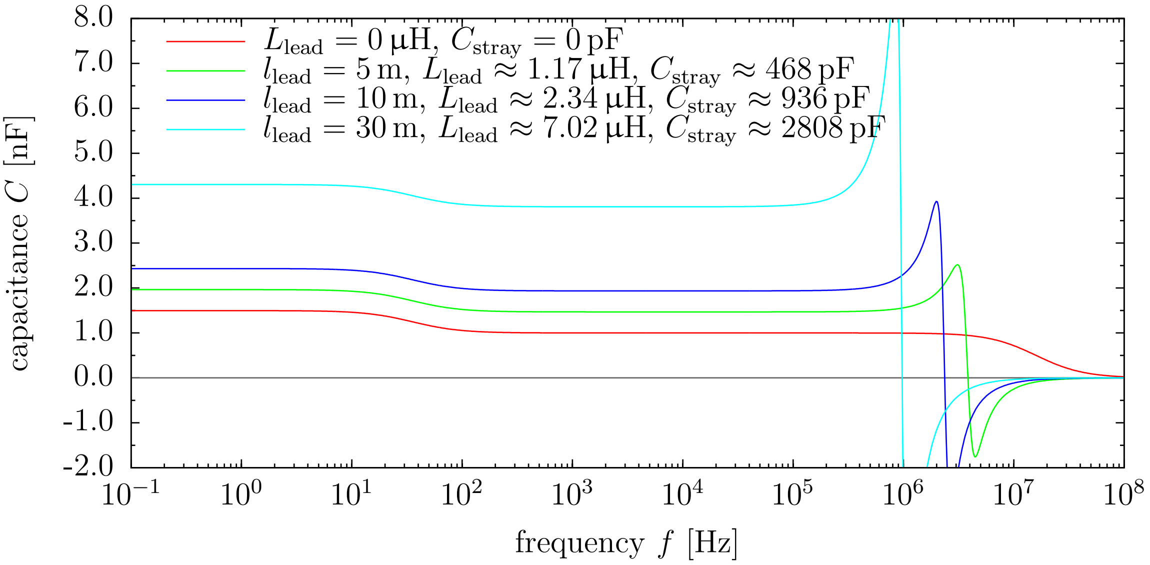

Figure 5.15.: Influence of the coaxial stray capacitance C_{stray} and lead inductance L_{lead} (cables with different lengths l_{lead}) on the measured capacitance. Equivalent circuit: see fig. 5.13. $R_{\mathrm{lead}} = 10\,\Omega$. DUT: double RC element ($R_1 = 10^6\,\Omega$, $R_2 = 10^9\,\Omega$, $C_1 = 3\,\mathrm{nF}$, $C_2 = 1.5\,\mathrm{nF}$).

In conclusion, the influence of very long measurement cables is mainly relevant for frequencies above 1 MHz due to the inductance and can be neglected for smaller frequencies. If the stray capacitance of the lead cables would not be small and could not be neglected, the measured capacitance would not represent the actual capacitance of the DUT. However, the relevant relaxation frequency f_{r} for the double RC element is not influenced by the stray capacitance and still measured accurately.

There are, however, also techniques to compensate for effects from lead cables or other contributions from, e.g., the sample holder[106]. This requires two additional measurements: one with open connections and one with short-circuited connections of the sample contacts, see fig. 5.16. In the 'short' measurement the impedance Z_{short} is defined by the lead resistance and inductance

$$Z_{\mathrm{short}} = R_{\mathrm{lead}} + \mathrm{i}\omega L_{\mathrm{lead}}\,. \tag{5.22}$$

In the 'open' measurement the impedance Z_{open} is obtained as

$$Z_{\mathrm{open}} = \frac{1}{\dfrac{1}{R_{\mathrm{stray}}} + \mathrm{i}\omega C_{\mathrm{stray}}}\,. \tag{5.23}$$

This, however, is only valid if $R_{\mathrm{lead}} + \mathrm{i}\omega L_{\mathrm{lead}} \ll \dfrac{1}{\dfrac{1}{R_{\mathrm{stray}}} + \mathrm{i}\omega C_{\mathrm{stray}}}$. Considering now the measured impedance Z_{m} of a DUT with impedance Z_{DUT} with this setup a com-

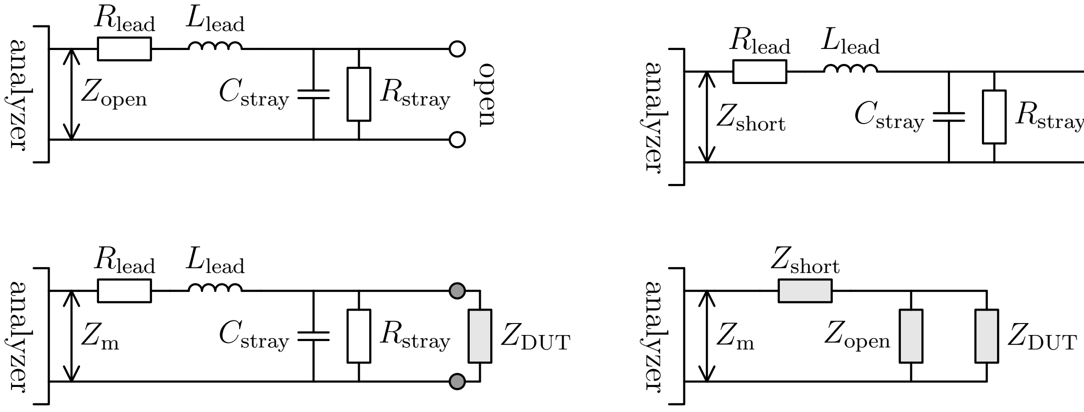

Figure 5.16.: Impedance of the device under test (DUT) Z_DUT can be calculated from the measured impedance Z_m and compensation for the measurement setup, Z_open and Z_short.

pensation formula can be derived:

$$Z_\mathrm{DUT} = \frac{Z_\mathrm{m} - Z_\mathrm{short}}{1 - \dfrac{Z_\mathrm{m} - Z_\mathrm{short}}{Z_\mathrm{open}}}\,. \tag{5.24}$$

Please note that the compensation has to be calculated for every frequency used. As has been shown earlier, the influence of the lead cables in the desired frequency range 10^{-3} to approximately 10^{6} Hz is negligible, especially when using short cables; thus, the compensation has not been applied to the samples in this thesis.

5.3. Electrical characterization of a hetero-layer OLED

As has already been indicated above, the OLEDs under investigation in this and the following chapter are derived from the reference OLED design (fig. 5.3), consisting of two undoped organic semiconductor materials, the hole-conducting TPD and the electron-conducting $\mathrm{Alq_3}$ as HTL and ETL, respectively. Thus, the OLED stack can be modeled with a double RC element, as each of these two layers is having a low, but non-vanishing, conductivity and a dielectric constant. According to eq. (5.10), the impedance is

$$\hat{Z} = \hat{Z}_\mathrm{HTL} + \hat{Z}_\mathrm{ETL} \tag{5.25}$$

$$= \frac{1}{\dfrac{1}{R_\mathrm{HTL}} + \mathrm{i}\omega C_\mathrm{HTL}} + \frac{1}{\dfrac{1}{R_\mathrm{ETL}} + \mathrm{i}\omega C_\mathrm{ETL}}\,. \tag{5.26}$$

All experimental data shown in this particular chapter correspond to the OLED already introduced in fig. 5.1, having a thin[†] F_4-TCNQ interlayer as HIL instead of PEDOT:PSS. However, the discussion is valid for all interlayers used. Differences due to different anode modifications are discussed in a separate chapter.

As OLEDs show a complex behavior in current density – voltage characteristics (see fig. 5.2), it is already expected that the resistances used to model the two layers are influenced by the applied bias voltage V_{DC} to satisfy charge injection/transport properties. However, the high frequency limit in $C-f$ measurements only depends on the capacitances (eq. (5.12)) and corresponds to the geometric capacitance C_{geo} of the OLED. As the relative permittivity ε_{r} is similar for all organic materials[70] the geometric capacitance can be written in the form of

$$C_{\mathrm{geo}} = \frac{\varepsilon_{\mathrm{r}}\varepsilon_0 A}{d}\,, \tag{5.27}$$

which is the capacitance of a plate capacitor with A being the area of the OLED pixel and $d = d_{\mathrm{HTL}} + d_{\mathrm{ETL}}$ the combined thickness of the HTL TPD and ETL $\mathrm{Alq_3}$. This geometric capacitance can also be observed in the reverse bias condition in $C-V$ characteristics (however, under the assumption that $R_{\mathrm{HTL}} \approx R_{\mathrm{ETL}}$ and $C_{\mathrm{HTL}} \approx C_{\mathrm{ETL}}$), shown again at a frequency of $f = 100\,\mathrm{Hz}$ in fig. 5.17 for the device with F_4-TCNQ interlayer ($C_{\mathrm{geo}} \approx 0.72\,\mathrm{nF}$, green line). If the bias becomes larger than a transition voltage V_{t} (for this device $V_{\mathrm{t}} \approx -0.9\,\mathrm{V}$), holes are injected into the device, raising the capacitance, as they accumulate at the TPD/$\mathrm{Alq_3}$ interface. Increasing the bias voltage further increases the capacitance toward the value of the $\mathrm{Alq_3}$ layer $C_{\mathrm{ETL}} \approx 1.70\,\mathrm{nF}$ (blue line). It is not obvious that this plateau is due the capacitance of $\mathrm{Alq_3}$ from a single curve; however, systematic thickness variations of the HTL and ETL lead to the conclusion[70] that for a bias V_{DC} exceeding a transition voltage V_{t} holes are injected into TPD, but no electrons are injected into $\mathrm{Alq_3}$ (if $V_{\mathrm{DC}} < V_{\mathrm{bi}}$). Therefore, the TPD layer is less resistive ("shortened"), holes accumulate at the TPD/$\mathrm{Alq_3}$ interface, which eventually only leaves $\mathrm{Alq_3}$ as capacitor. At the built-in voltage V_{bi}, indicated by the peak in $C-V$ at 2.2 V, electron injection from the cathode side into the device starts[‡]. As now electrons and holes recombine to generate light, charge is annihilated, thus the differential capacitance decreases rapidly with increasing potential and even becomes negative. It has been shown by Ehrenfreund et al. that the negative contribution to the capacitance only occurs at bipolar injection and thus is related to the electron injection in OLEDs[102].

The values of $C_{\mathrm{geo}} \approx 0.72\,\mathrm{nF}$ and $C_{\mathrm{ETL}} \approx 1.70\,\mathrm{nF}$ also deserve some comment. Under the assumption of $\varepsilon_{\mathrm{r}} = 3.5$ for both layers[70] the total thickness of the organic layers is calculated to $d \approx 172\,\mathrm{nm}$ (eq. (5.27)), which is slightly more than the intended

---

[†] Determination of the thickness of F_4-TCNQ interlayers was not possible, even using different techniques (profilometer, AFM, and ellipsometry). It is assumed to be less than 1 nm.

[‡] Strictly speaking, one has to distinguish between the detected onset voltage V_{on} of the current or the luminance, the peak voltage V_{peak} observed in $C-V$ measurements and the built-in voltage V_{bi} given by the difference in work function of the anode and cathode material. As pointed out in a recent publication by van Mensfoort et al.[101] due to the contribution of diffusion currents and disorder the experimental quantities V_{on} and V_{peak} can be lower than V_{bi} by some tenths of a volt. However, for the sake of simplicity this distinction is not made here.

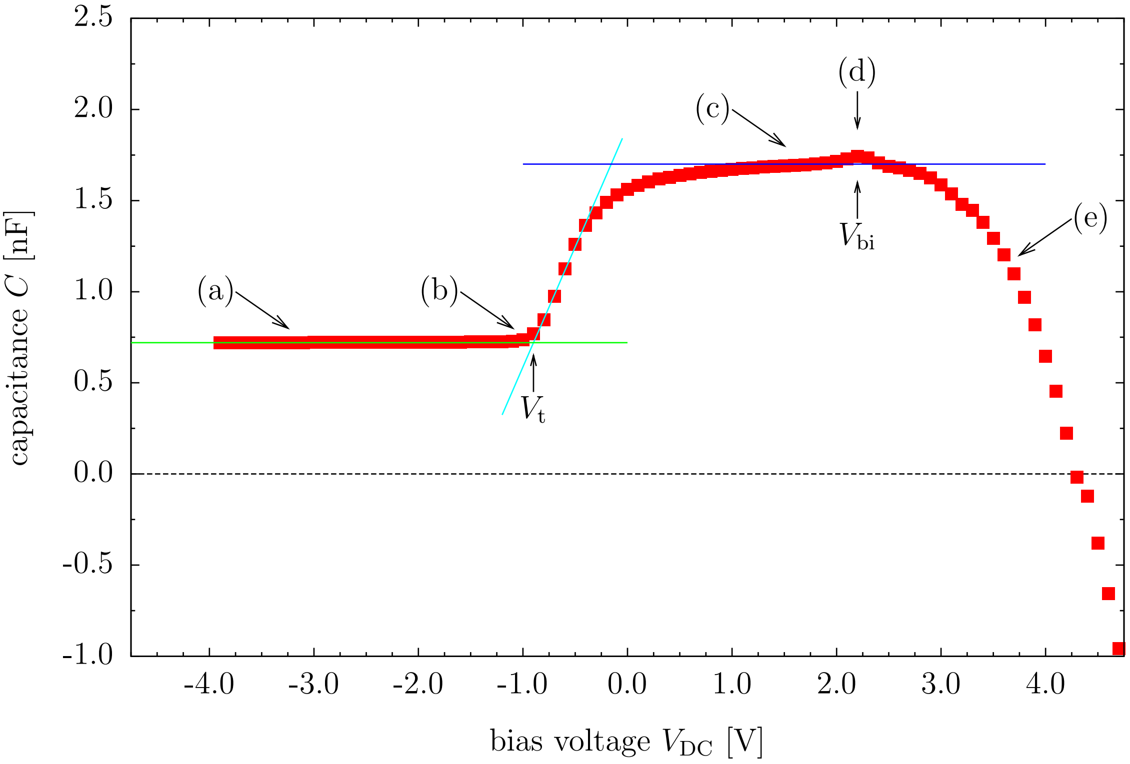

Figure 5.17.: Capacitance – voltage measurement of the device shown in fig. 5.1 at fixed frequency $f = 100\,\mathrm{Hz}$ (red squares). Green line: geometric capacitance, blue line: Alq_3 capacitance (both extracted from fits of $C - f$ measurements (fig. 5.19) yielding $C_{\mathrm{HTL}} \approx 1.25\,\mathrm{nF}$ and $C_{\mathrm{ETL}} \approx 1.70\,\mathrm{nF}$). Cyan line: linear fit of the rise in capacitance to determine the transition voltage (crossing with geometric capacitance), $V_t \approx -0.9\,\mathrm{V}$. Built-in voltage indicated by small peak, $V_{bi} \approx 2.2\,\mathrm{V}$. Letters (a) – (e) correspond to fig. 5.18.

160 nm used in the fabrication process. Three causes can be pictured: (1) the device unintentionally was grown thicker (e.g., due to not-well calibrated quartz crystal monitors), (2) the assumed value for ε_r is too high ($\varepsilon_\mathrm{r} = 3.25$ yields $d = 160\,\mathrm{nm}$), or (3) the two organic layers might have different values of ε_r. All of these three possibilities could be relevant; a clear distinction is not possible with the data available in this case. To satisfy the geometric capacitance (high frequency limit in $C - f$) one calculates $C_\mathrm{HTL} \approx 1.25\,\mathrm{nF}$ (eq. (5.11)). Using $\varepsilon_\mathrm{r} = 3.25$ for both layers, the layer thicknesses yield $d_\mathrm{HTL} \approx 92\,\mathrm{nm}$ and $d_\mathrm{ETL} \approx 68\,\mathrm{nm}$, as

$$C_\mathrm{HTL} = \frac{\varepsilon_\mathrm{r}\varepsilon_0 A}{d_\mathrm{HTL}}\,, \tag{5.28}$$

$$C_\mathrm{ETL} = \frac{\varepsilon_\mathrm{r}\varepsilon_0 A}{d_\mathrm{ETL}}\,. \tag{5.29}$$

These values are not the intended thicknesses of 80 nm. Both layers should have the same capacitance, as they should have the same thickness (however, assuming both have the same ε_r), which is clearly not the case. If the evaporated layer thicknesses would be known precisely, a determination of ε_r is possible, or vice versa. However, the exact values of the capacitances (or ε_r) is not needed for further discussion but can be used as indicators for the evaporated film thicknesses.

The overall behavior in $C - V$ requires that a negative interfacial charge Q_if is present at the TPD/Alq$_3$ interface[70,107] (as shown in the energy diagrams in fig. 5.18). At $V_\mathrm{DC} < V_\mathrm{t}$ ((a) in fig. 5.17 and 5.18) both TPD and Alq$_3$ are reverse biased and no charges can be injected. Increasing the bias voltage reduces the slope until the flat-band case for TPD is reached ($V_\mathrm{DC} = V_\mathrm{t}$, (b)) and holes are injected. However, as an effect of the negative interfacial charge the bands in Alq$_3$ are not yet in the flat-band case, meaning that no electrons can be injected at this point. More and more holes can be injected with increasing potential, raising the capacitance of the device ($V_\mathrm{t} < V_\mathrm{DC} < V_\mathrm{bi}$, (c)), while the slope of the bands in Alq$_3$ is decreasing. Finally, at $V_\mathrm{DC} = V_\mathrm{bi}$, (d), the flat-band condition for Alq$_3$ is reached and electrons can be injected into the device. For even higher voltages, $V_\mathrm{DC} > V_\mathrm{bi}$, (e), the capacitance of the OLED decreases rapidly, as holes and electrons recombine, annihilating charge. If there would be no interfacial charge, the transition voltage and the built-in voltage would be equal ($V_\mathrm{t} = V_\mathrm{bi}$), as the flat-band case would be reached simultaneously in the TPD and the Alq$_3$ layer (simultaneous hole and electron injection). As one clearly sees that $V_\mathrm{t} \neq V_\mathrm{bi}$, one comes to the conclusion that a negative interfacial charge density σ_if is present. Its value can be calculated from the following equation[70]:

$$\sigma_\mathrm{if} = \frac{Q_\mathrm{if}}{A} = \frac{\varepsilon_r\varepsilon_0}{d_\mathrm{ETL}} \cdot (V_\mathrm{t} - V_\mathrm{bi})\,. \tag{5.30}$$

With $\varepsilon_\mathrm{r} = 3.25$, $A = 4\,\mathrm{mm}^2$, and $d_\mathrm{ETL} = 68\,\mathrm{nm}$, one calculates $Q_\mathrm{if} \approx 5.25\,\mathrm{nC}$ and $\sigma_\mathrm{if} \approx 1.31\,\mathrm{mC/m}^2$, corresponding to $8.2 \cdot 10^{11}$ charges per cm^2. Similar values, also for other material combinations and obtained with other measurement techniques, have been published[70,107–109]. Recent studies show that the origin of this negative charge at the interface is due to dipole moment ordering in the Alq$_3$ layer during film preparation[109]. The polar $\mathrm{Alq_3}$ molecules grow with a preferential orientation on the HTL layer[§], so that there is a net negative charge at the HTL/ETL interface. It is thus an intrinsic property of a material consisting of polar molecules and not related to the existence of deep traps as sometimes stated in the literature[110]. Taking the dipole moment of 4.1 Debye for $\mathrm{Alq_3}$, one can estimate the degree of orientation of the dipole moments to be about 1 %. Given the fact that many molecular materials used in organic electronics are polar, similar interface charges could exist in other heterolayer devices, too.

With this microscopic explanation for the redistribution of the electric field as function of the applied bias in mind, one can now also interpret the observed relaxation frequency f_r in $C - f$ measurements, where the capacitance changes from C_ETL to the lower geometrical value C_geo. As explained above, the observation of an enhanced capacitance for a heterolayer device requires that the HTL is significantly less resistive than the ETL. This means that holes must be injected into TPD and be transported to the interface to $\mathrm{Alq_3}$. However, this process is not arbitrarily fast but limited by the mobility in the TPD layer. Thus the relaxation frequency can be taken as a measure of how good hole injection into the HTL and/or how fast hole transport to the HTL/ETL interface is.

In fig. 5.19 the $C-f$ measurement for two bias voltages, $V_\mathrm{DC} = -2\,\mathrm{V}$ and $V_\mathrm{DC} = 2\,\mathrm{V}$, is shown, along with simulation results of a double RC element. Unfortunately, very long cables have been used in these IS measurements. Therefore, a rise in capacitance occurs at high frequencies (above $\approx 0.4\,\mathrm{MHz}$) which is due to the inductance of the lead cables as has been discussed before. Using shorter cables it can be shown that the limiting case at high frequencies indeed corresponds to the geometric capacitance of the OLED.

First, the reverse bias condition $V_\mathrm{DC} = -2\,\mathrm{V}$ is analyzed: no holes and no electrons are injected into the OLED, hence the resistances corresponding to both layers are very high (in the simulation $R_\mathrm{HTL} = R_\mathrm{ETL} = 1\,\mathrm{G\Omega}$ is assumed). The capacitance in this case is almost constant over the whole frequency range. The high frequency limit corresponds to the geometric capacitance of the device (eq. (5.27)), $C_\mathrm{geo} \approx 0.72\,\mathrm{nF}$. Now, the bias is increased to $V_\mathrm{DC} = 2\,\mathrm{V} > V_\mathrm{t}$: the two typical plateaus for two RC elements connected in series with different values of resistance are visible. The experimental data at this bias voltage can be simulated assuming a considerably smaller resistance for the hole transporting layer of $R_\mathrm{HTL} = 0.7\,\mathrm{k\Omega}$ as holes are injected into the device. As no light is emitted from the device, V_DC is below V_bi, it follows that no electrons are injected, R_ETL is still assumed to be $1\,\mathrm{G\Omega}$ (The capacitances and resistances for the simulation are chosen to satisfy both experimental data curves simultaneously.). Below the relaxation frequency, $f_\mathrm{r} \approx 8 \cdot 10^4\,\mathrm{Hz}$, the experimental capacitance is almost constant. This low frequency limit (eq. (5.13)) is the capacitance of the $\mathrm{Alq_3}$ layer, $C_\mathrm{ETL} \approx 1.70\,\mathrm{nF}$. With decreasing frequency, however, the measured capacitance is not constant but rises for very low frequencies (this is also observed in the reverse bias condition), which can not be explained by the double RC element

---

[§] As discussed previously, this could affect the external quantum efficiency of the OLED due to different coupling of the oriented dipoles to the plasmonic modes.

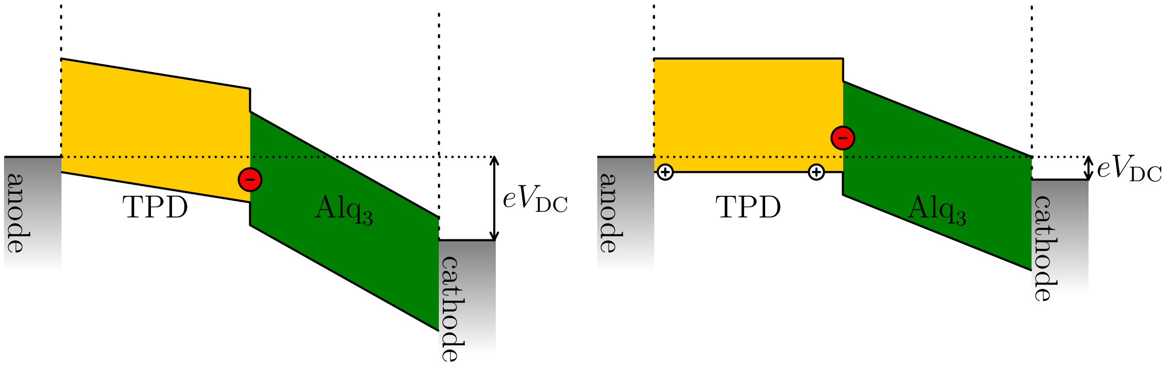

(a) $V_{\mathrm{DC}} < V_{\mathrm{t}} < V_{\mathrm{bi}},\ Q = Q_{\mathrm{if}} < 0$ ***(b)*** $V_{\mathrm{DC}} = V_{\mathrm{t}} < V_{\mathrm{bi}},\ Q_{\mathrm{if}} < Q < 0$

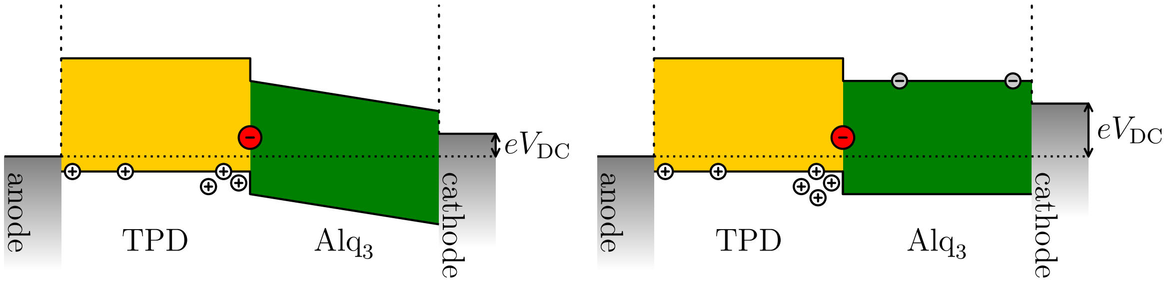

(c) $V_{\mathrm{t}} < V_{\mathrm{DC}} < V_{\mathrm{bi}},\ Q_{\mathrm{if}} < Q < 0$ ***(d)*** $V_{\mathrm{DC}} = V_{\mathrm{bi}},\ Q = 0$

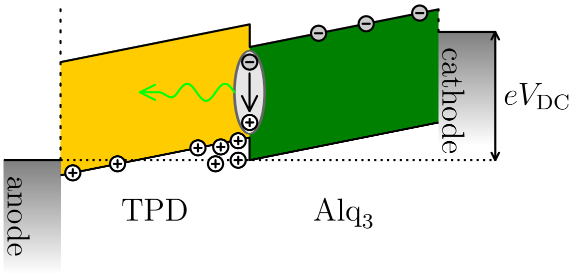

(e) $V_{\mathrm{DC}} > V_{\mathrm{bi}},\ Q > 0$

Figure 5.18.: Simplified band diagrams for different bias conditions V_{DC}. A negative interfacial charge Q_{if} is always present due to dipole moment ordering in the $\mathrm{Alq_3}$ layer. The charge Q at the interface is changing due to accumulation of holes. (a) reverse bias condition: no charge injection. (b) flat-band condition for TPD: beginning of hole injection. (c) hole injection regime: accumulation of holes at the TPD/$\mathrm{Alq_3}$ interface. (d) flat-band condition for $\mathrm{Alq_3}$: accumulated holes compensate Q_{if}; beginning of electron injection. (e) bipolar injection and recombination: the OLED emits light.

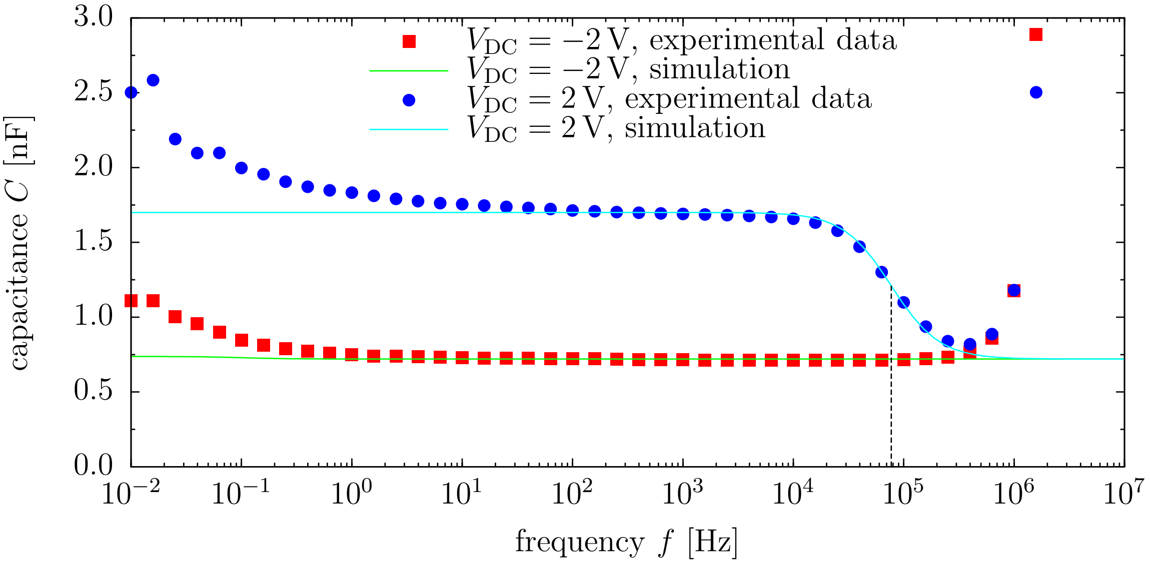

Figure 5.19.: Capacitance – frequency measurement (symbols) of the device shown in fig. 5.1 and corresponding simulations with a double RC element (lines, $C_{\mathrm{HTL}} = 1.25\,\mathrm{nF}$, $R_{\mathrm{ETL}} = 1\,\mathrm{G\Omega}$, $C_{\mathrm{ETL}} = 1.70\,\mathrm{nF}$). Reverse bias condition (red squares/green line, $R_{\mathrm{HTL}} = 1\,\mathrm{G\Omega}$): $V_{\mathrm{DC}} = -2\,\mathrm{V}$. Hole injection regime (blue circles/cyan line, $R_{\mathrm{HTL}} = 0.7\,\mathrm{k\Omega}$): $V_{\mathrm{DC}} = 2\,\mathrm{V}$. Relaxation frequency (dashed line): $f_{\mathrm{r}} \approx 8 \cdot 10^4\,\mathrm{Hz}$.

used in the simulation. However, this rise in capacitance can be attributed to leakage currents and will be discussed in the next chapter.

As has already been shown for the reverse bias ($V_{\mathrm{DC}} = -2\,\mathrm{V} < V_{\mathrm{t}}$) and hole injection regime ($V_{\mathrm{DC}} = 2\,\mathrm{V} > V_{\mathrm{t}}$), the capacitance – frequency measurement of an OLED depends on the applied bias. Fig. 5.20 additionally shows the data for $V_{\mathrm{DC}} = 0\,\mathrm{V}$ and the forward bias regime, $V_{\mathrm{DC}} = 4\,\mathrm{V} > V_{\mathrm{bi}}$, where light emission from the OLED is possible. At high frequency the behavior at 4 V is not different to the case where $V_{\mathrm{t}} < V_{\mathrm{DC}} < V_{\mathrm{bi}}$. However, for sufficiently low frequency the capacitance decreases and becomes even negative. This indicates that electrons are injected into the device, recombining with the holes under light emission. As charge is annihilated, the differential capacitance is decreasing.

5.4. Influence of different anode treatments and materials

When comparing different OLEDs, IS is capable of showing differences in hole injection and/or hole transport due to differences in the relaxation frequency f_{r}. Here, different modifications of the reference OLED design are investigated, using materials with different work function as anode: the HIL is (a) omitted, (b) PEDOT:PSS, (c) F_4-TCNQ, and (d) WO_3, see fig. 5.21. Furthermore, different treatment of the ITO prior to deposition of materials is possible: after cleaning with solvents, an argon or an oxygen plasma is used to further clean the samples. While the Ar plasma has no

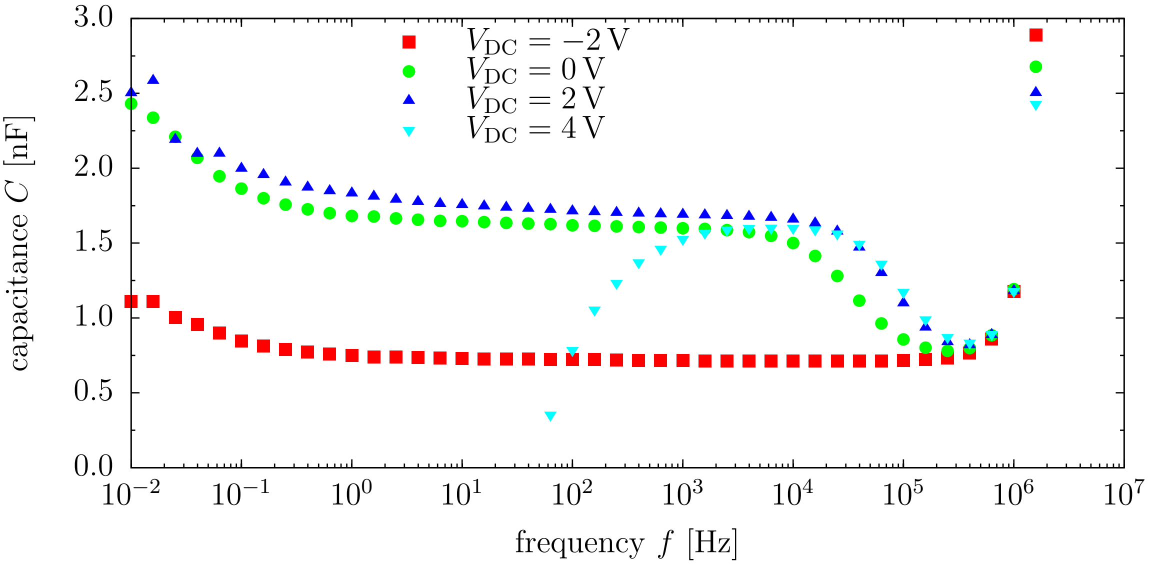

Figure 5.20.: Capacitance – frequency measurement of the device shown in fig. 5.1 at different applied bias voltage V_{DC}. Red squares: $V_{DC} = -2$ V, green circles: $V_{DC} = 0$ V, blue upward triangles: $V_{DC} = 2$ V, cyan downward triangles: $V_{DC} = 4$ V.

effect on the ITO, the oxygen plasma modifies the surface structure, hence modifying the work function of the anode and the overall efficiency of the OLED[36,37]. For all variations of anode treatment and materials only the injection properties for holes are expected to change, as all remaining OLED layers are always the same.

Determination of the work functions

The built-in voltage depends on the difference of the work functions of the electrode materials (eq. (2.12)). Additionally, the work function of the anode defines the hole injection barrier (eq. (2.10)). Therefore, determination of the work functions' values for the different anode modifications would be beneficial. A relatively simple measurement technique that can be used is 'Kelvin probe'. For a detailed introduction please see, e.g., Julia Wagner's master's thesis[111]. Kelvin probe does not evaluate the desired work function directly; it only can be used to determine differences in work functions for different materials. The anode modifications and materials have been studied intensively and with great care for Wei Ren's master's thesis[112]; unfortunately, the results are not very conclusive, as even samples prepared repeatedly in the exact same way showed different values. Therefore Kelvin probe results are not part of this thesis.

Electrical characterization

All combinations of plasma treatment and HILs have been fabricated, unfortunately not all OLEDs could be characterized, mostly due to initial shorts. This is especially a problem if no HIL is used at all. The use of PEDOT:PSS, which is a water based suspension, requires the use of oxygen plasma in order to make the ITO hydrophilic

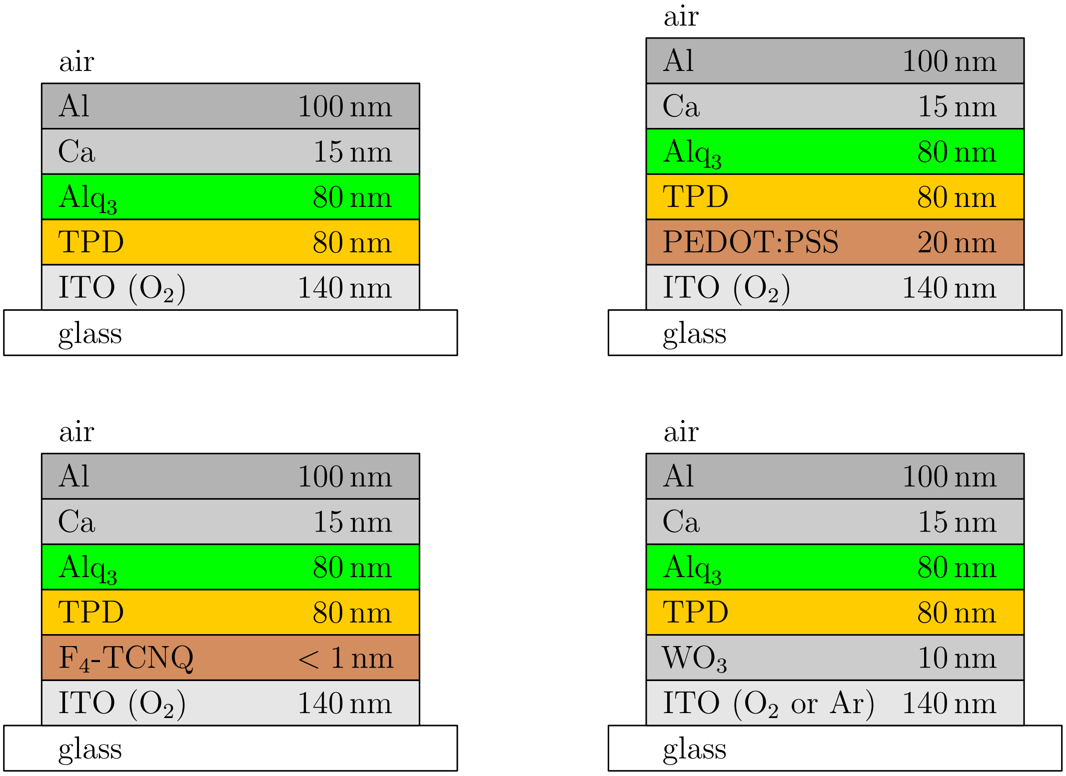

Figure 5.21.: Different anode modifications of the reference OLED design (fig. 5.1): O_2 or Ar plasma treatment of ITO and different HILs (no HIL, PEDOT:PSS, F_4-TCNQ, and WO_3).

and thus spincoating of PEDOT:PSS possible. The data shown here corresponds to four devices with oxygen plasma treatment and the four different interlayers, as well as an argon plasma treated sample with WO_3 interlayer, see fig. 5.21. Their current density – voltage – luminance characteristics are shown in fig. 5.22.

Despite huge differences in the leakage currents for $V_{\mathrm{DC}} \lesssim 2\,\mathrm{V}$, the current densities and luminance values vary by about one order of magnitude at $V_{\mathrm{DC}} = 8\,\mathrm{V}$. After subtracting the leakage currents, the onset of bipolar injection is almost the same for all devices. Due to the detection limit of the photodiode for the luminance value it is not possible to conclude which OLED starts to emit light first when increasing the applied bias. It is, however, obvious that at sufficiently high bias voltage V_{DC} the current density, as well as the corresponding luminance, is highest for the device with F_4-TCNQ, followed by the devices with PEDOT:PSS, no interlayer, WO_3 with O_2 plasma treatment, and WO_3 with Ar plasma treatment. The calculated current efficiencies for the different anode modifications are shown in fig. 5.23. Their shapes are similar and as expected (a steep increase and then almost constant), however, the devices with WO_3 show a slightly different behavior, especially with O_2 plasma treatment. This partially can be attributed to the high leakage currents in the latter two devices.

The $C - f$ measurements for the different samples are shown in fig. 5.24 for an applied bias of $V_{\mathrm{DC}} = 0\,\mathrm{V}$ which is above the transition voltage V_{t} but lower than the built-in voltage V_{bi} for all devices. Its general trends are as discussed before: at high frequency the geometric capacitances of the devices are observed[¶] (neglecting the rise due to the long cable's inductance), at the relaxation frequency the redistribution of the internal electric field takes place and thus, for lower frequencies, the capacitance of the ETL is observed. As has already been discussed before for the F_4-TCNQ-OLED, a second step at even lower frequency is visible, which can not be explained by the double RC circuit assumed for the HTL and ETL compartment. This step is especially pronounced for the samples containing PEDOT:PSS and WO_3. Its origin shall be explored in the following, as it must not be confused with the step at the relaxation frequency f_{r}.

Consider the device with PEDOT:PSS as HIL. Its $C - f$ characteristic for reverse bias, $V_{\mathrm{DC}} = -2\,\mathrm{V}$, and the hole injection regime, $V_{\mathrm{DC}} = 0\,\mathrm{V}$, is shown in fig. 5.25. Both curves show a step in capacitance in the frequency range of about 1 to 50 Hz. Also shown are corresponding simulations of a double RC circuit: for reverse bias (light green line) a constant capacitance (geometric capacitance of the device) is expected; for the hole injection regime (light blue line) one transition region and two plateaus are expected. To account for the observed second step at lower frequency other equivalent circuits have to be used. The data can be modeled when adding another RC element in series. However, this third RC circuit has no physical representation in the device structure: the HIL is assumed to be highly conductive, but not acting as capacitor. This argument is even more persuasive if the data for OLEDs with no interlayer is analyzed: even here a second step is observed, which therefore must have its origin due to a different reason. It can be found in the form of leakage paths due to the

---

[¶] The different values lead to the conclusion that the devices slightly vary in their total thickness.

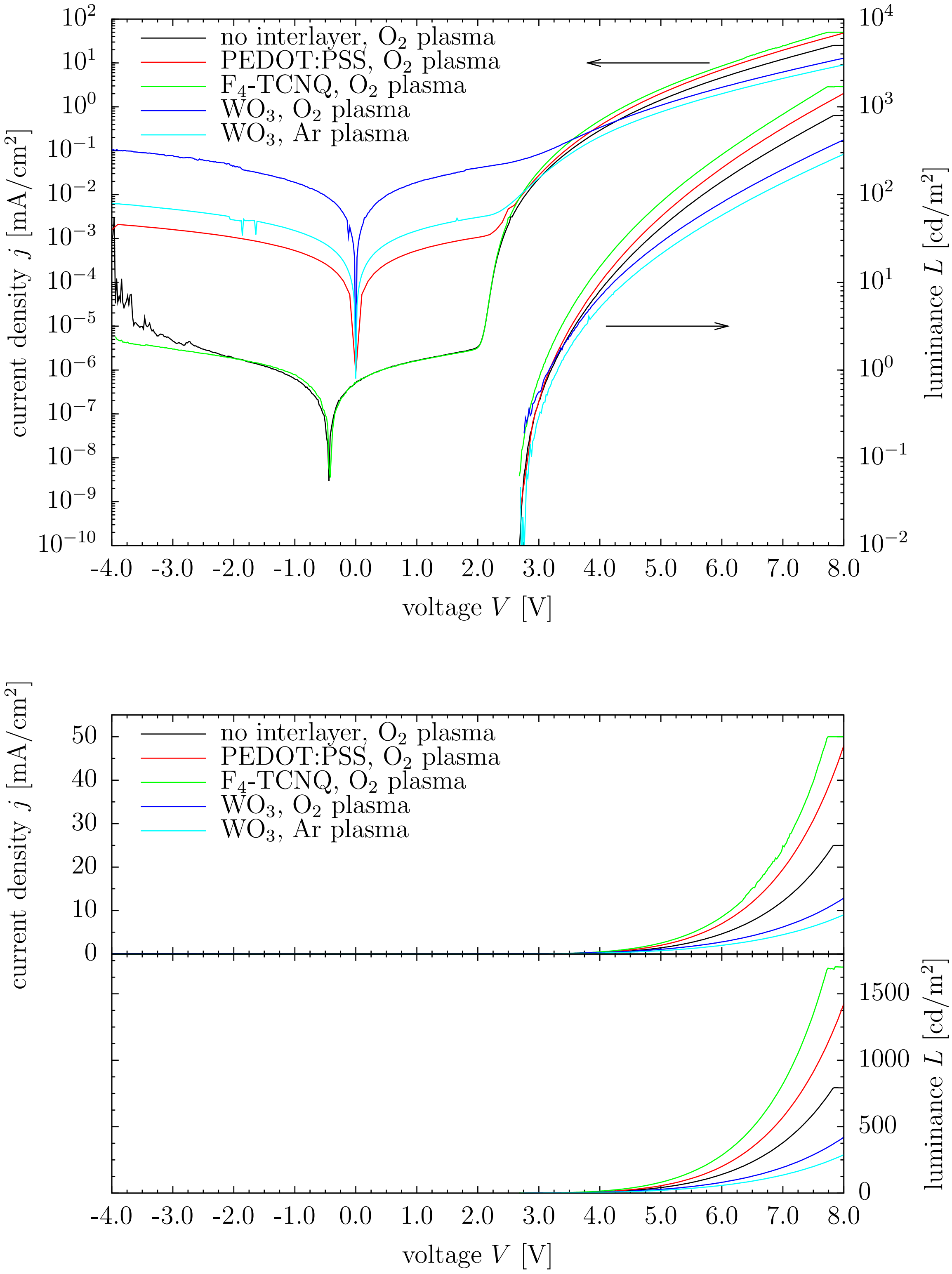

Figure 5.22.: Current density – voltage – luminance characteristics in logarithmic (top) and linear (bottom) representation for the OLEDs with different anode modifications and HILs shown in fig. 5.21. Current density limited to 25 mA/cm^2 for the device without interlayer and to 50 mA/cm^2 for the device with F_4-TCNQ.

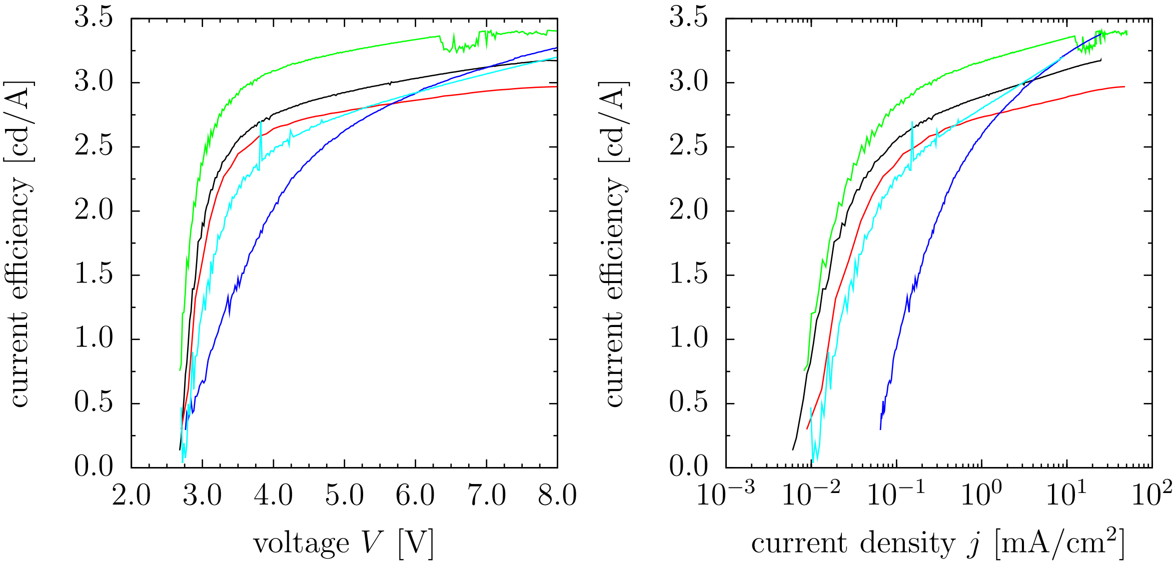

Figure 5.23.: Current efficiencies for the OLEDs with different anode modifications and HILs shown in fig. 5.21. Line colors as in fig. 5.22. Left: versus applied voltage V. Right: versus current density j.

crossbar layout of the devices, see fig. 5.26. These additional paths define a parasitic diode which has the same layer structure as the actual OLED pixel and thus can also be represented by a double RC element, with R'_{HTL}, C'_{HTL}, R'_{ETL}, and C'_{ETL}. This element is connected in parallel to the original double RC circuit together with an in-plane parasitic resistance R_{p} (corresponding to the leakage path). Please see fig. 5.27 for the corresponding equivalent circuits. The values for the additional RC elements are of the same order as the original ones, as they also correspond to the HTL and ETL, respectively; the values used for the simulation are summarized in table 5.1. The same values for the resistors of the OLED and the parasitic diode are assumed. The capacitances, however, are both scaled by a factor of about 1.9, which corresponds to a larger active area of the parasitic capacitance than the area of the OLED pixel. Fig. 5.25 shows the simulations of the double RC element (reverse bias condition: light green line, hole injection regime: light blue line) and the extended models with additional parasitic paths (reverse bias condition: dark green line, hole injection regime: dark blue line). The agreement between experimental data and simulations is very convincing and therefore confirms the validity of the models with an additional lateral current path. Please note that the second step at low frequency is related to the leakage currents observed in the $j-V$ characteristics: the higher the leakage current (smaller R_{p}) the higher the influence of the additional step in capacitance, see fig. 5.28 for simulations.

Direct evidence that the origin of the rise in capacitance is due to leakage paths could come from an OLED which has a well-defined area, e.g., a free standing stack, where all layers are on top of each other and not overlapping. Fabrication is possible using adhesive tape; then, however, securely contacting the top metal electrode with

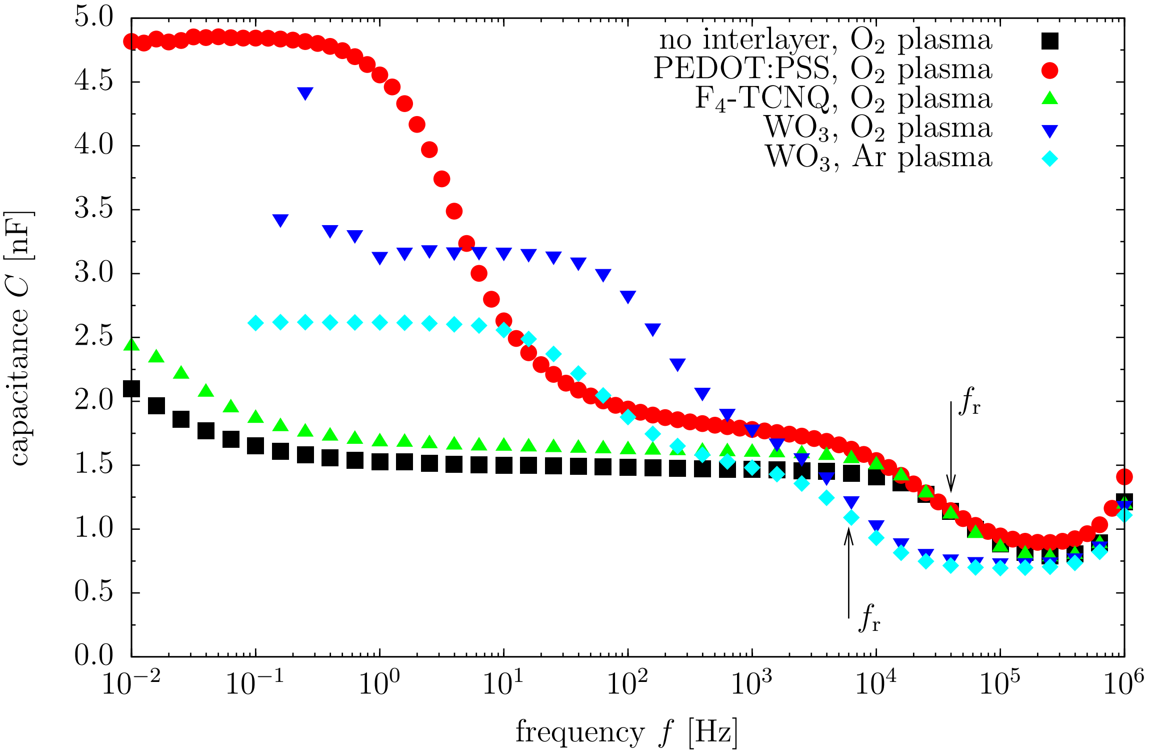

Figure 5.24.: $C-f$ characteristics for the OLEDs with different anode modifications and HILs shown in fig. 5.21 for an applied bias of $V_{DC} = 0\,V$ (hole injection regime). Relaxation frequency $f_r \approx 6 \cdot 10^3$ Hz for the devices with WO_3, and $f_r \approx 4 \cdot 10^4$ Hz for all other devices. Second step in capacitance at lower frequency due to leakage currents (see text).

circuit	R_{HTL}	C_{HTL}	R_{ETL}	C_{ETL}	
(1) + (3)	1.0 GΩ	1.7 nF	1.0 GΩ	1.7 nF	
(2) + (4)	1.8 kΩ	1.7 nF	1.0 GΩ	1.7 nF	
circuit	R'_{HTL}	C'_{HTL}	R'_{ETL}	C'_{ETL}	R_p
(3)	1.0 GΩ	3.2 nF	1.0 GΩ	3.2 nF	10 MΩ
(4)	1.8 kΩ	3.2 nF	1.0 GΩ	3.2 nF	10 MΩ

Table 5.1.: Values used for the elements in the equivalent circuits (fig. 5.27) for the simulations shown in fig. 5.25.

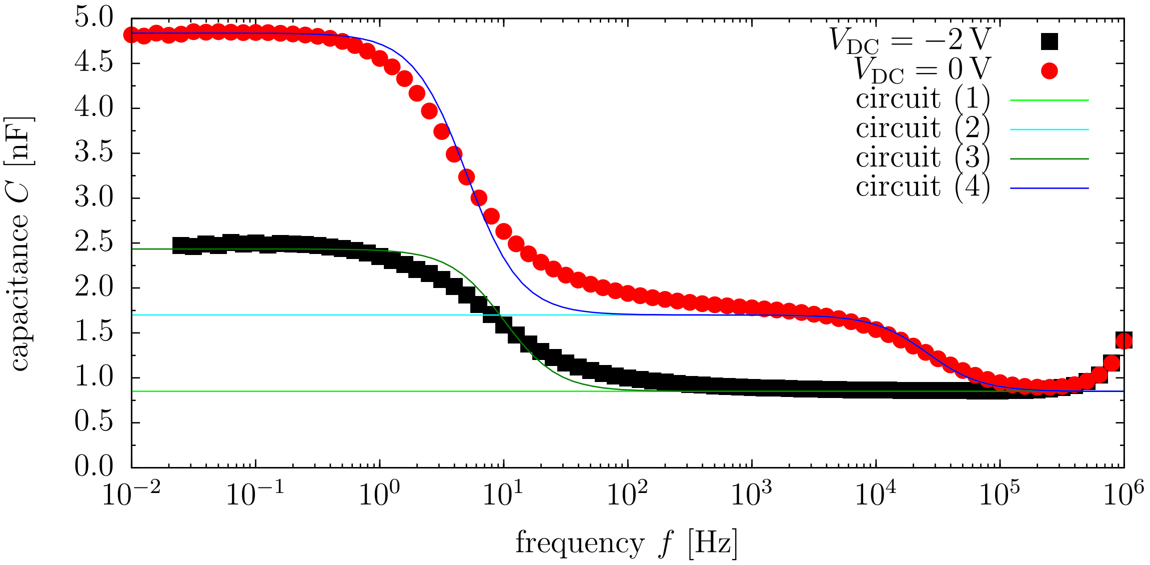

Figure 5.25.: $C - f$ characteristics for the OLED with PEDOT:PSS as HIL for applied bias $V_{DC} = -2\,V$ (black squares) and $V_{DC} = 0\,V$ (red circles). Lines: simulation results. Light green (double RC element) and dark green (including leakage path) line: reverse bias condition. Light blue (double RC element) and dark blue (including leakage path) line: hole injection regime. For the corresponding equivalent circuits and the values of their elements please see fig. 5.27 and tab. 5.1, respectively.

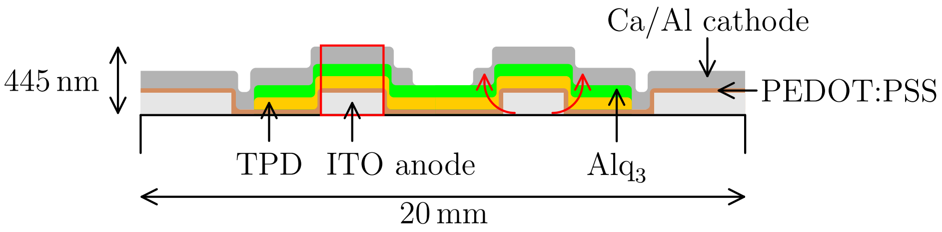

Figure 5.26.: Schematic cross section of the reference OLED devices. Ideal OLED pixel inside the red rectangle (left). Leakage paths (indicated as red arrows) due to the crossbar layout of the devices (right).

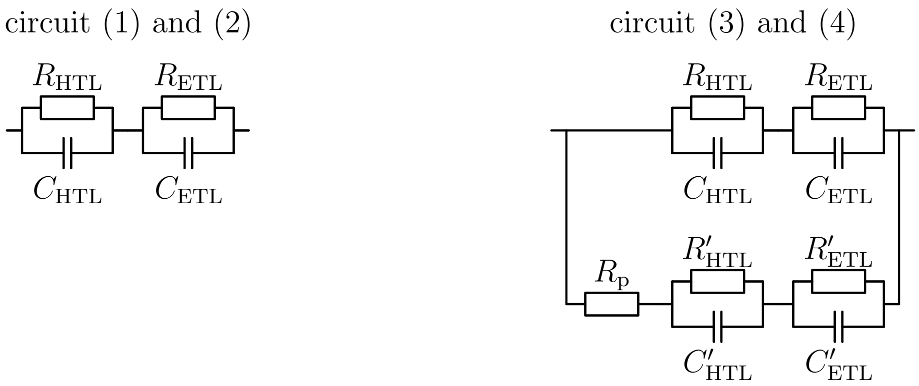

Figure 5.27.: Equivalent circuits used for the simulation of the $C-f$ measurements shown in fig. 5.25. For the values of the elements, please see tab. 5.1.

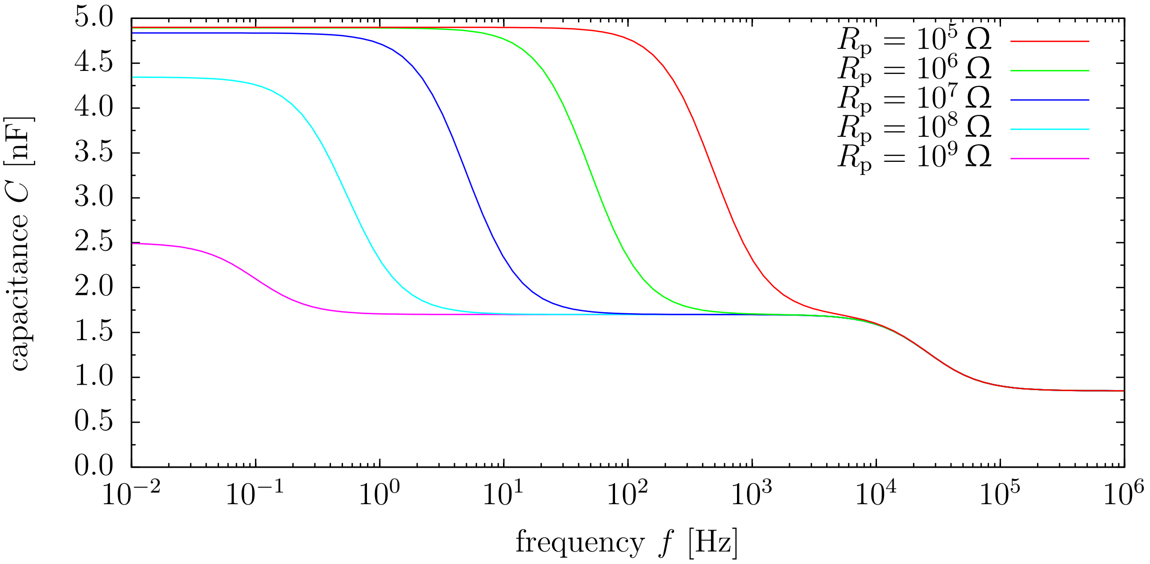

Figure 5.28.: Simulation of $C-f$ characteristics of an OLED with parasitic paths and varying in-plane parasitic resistance R_{p}. Equivalent circuit see fig. 5.27, values for the elements according to tab. 5.1 (4). Increasing R_{p} decreases the influence of the parasitic current path and thus the additional step in capacitance.

needle probes is not easy: as the organic and metal layers are very thin, the needle easily punches through all layers causing a short. Therefore, measurements can not be shown here; other approaches to a well-defined area are necessary for an experimental proof.

Nevertheless, using simulation, the nature of the increase in capacitance at low frequencies is determined to be due to the leakage currents and does not correspond to the relaxation frequency f_r. As discussed before, the latter is a measure of the quality of the hole injection and/or its transport. As can be seen in fig. 5.24, $f_\mathrm{r} \approx 6 \cdot 10^3\,\mathrm{Hz}$ for both devices with WO_3 as interlayer and $f_\mathrm{r} \approx 4 \cdot 10^4\,\mathrm{Hz}$ for all other devices. This means that hole injection in devices with WO_3 is not as good as compared to the other devices, which explains the lower current densities observed in the $j - V$ measurements. From this IS result one can come to the conclusion that a WO_3 anode is not the best choice for a good hole injecting contact, even though the current density in the OLED is not so much different compared to the other devices[‖]. From the $j - V$ data (fig. 5.22) and the current efficiencies (fig. 5.23), the device with O_2 treated ITO and F_4-TCNQ interlayer would be the best choice of the different anodes studied here: high relaxation frequency f_r (good hole injection), low leakage current, and highest luminance efficiency.

5.5. Temperature dependence

The charge transport in the amorphous organic layers of the OLED is thermally activated hopping, thus the mobility of the charge carriers depends on the temperature T, see eq. (2.15). As the relaxation frequency f_r is correlated with the charge transport in the HTL, impedance spectroscopy offers the possibility to study the temperature dependence of the mobility. This is shown for two variations of the reference design using no interlayer and F_4-TCNQ as HIL (see fig. 5.21), respectively; both with O_2 plasma treated ITO. For controlling the temperature a cryostat has been used. The temperature is recorded with a Pt-100 temperature sensor which is placed close to the sample. After changing the temperature and before starting a measurement steady temperature condition are awaited for. The total lead cable length in this setup is only about 5 m; therefore, the peaks due to the cable's inductance are not pronounced at high frequencies in the $C - f$ measurements and the geometric capacitance of the device is observed. The luminance of the samples can be recorded using a photodiode; unfortunately, this was not yet available when measuring the device without HIL[**].

Current density – voltage characteristics are shown in fig. 5.29 for the device without HIL and $j - V$ and $L - V$ characteristics in fig. 5.30 for the device with F_4-TCNQ. Both devices show, as expected, that the current densities (at constant $V_\mathrm{DC} > V_\mathrm{bi}$) are decreasing with decreasing temperature as the mobility is lower. As a result of the reduced current density also the luminance is lower.

[‖] The injection properties of WO_3 seem to depend critically on the evaporation parameters. This has also been observed by other groups using WO_3; despite good reputation in literature[113], it is not recommended as HIL, unless the critical evaporation parameters are identified and controllable.

[**] More information about these two devices can be found in Kerstin Steidle's bachelor's thesis[114].

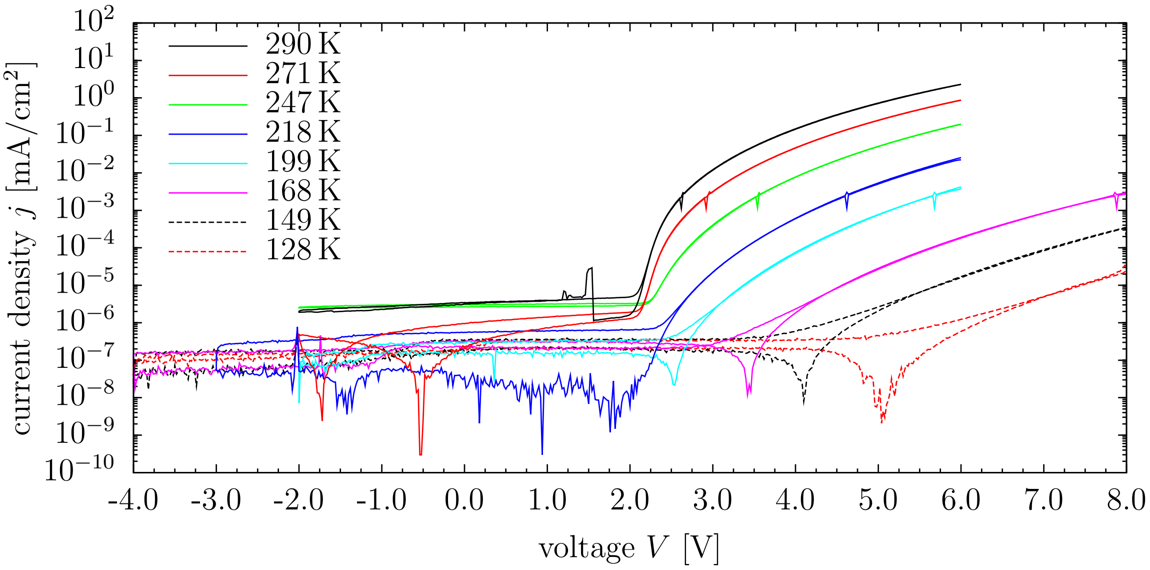

Figure 5.29.: Current density – voltage characteristics for the device without HIL (fig. 5.21) at different temperatures. Decrease of the current density with decreasing temperature due to decreasing charge carrier mobility.

For both devices the temperature dependent $C-f$ measurements for an applied bias of $V_{\mathrm{DC}} = 2\,\mathrm{V}$ are shown in fig. 5.31 and 5.32, respectively. The results show clearly the geometric capacitance at high frequency and the capacitance of the $\mathrm{Alq_3}$ layer. As expected, the transition region defined by the relaxation frequency f_{r} is shifting to lower frequencies when decreasing the temperature as a result of the decreasing mobility μ in the TPD layer. Fig. 5.33 shows the relation between relaxation frequency and temperature and a corresponding linear fit; from its slope the activation energy E_{a} for the hopping transport in TPD can be extracted, see eq. (2.15), as f_{r} is proportional to the resistance (or conductance) of the TPD layer and thus proportional to the mobility μ. It yields $E_{\mathrm{a,TPD}} \approx 0.36\,e\mathrm{V}$ which is in the range of the typical values. Berleb extracted similar values[115] for the chemically very similar hole transporting material NPB (N,N'-di(naphtalene-1-yl)-N,N'-diphenyl-benzidine, see fig. 5.34), and Ray et al. state $0.38\,e\mathrm{V}$ for TPD films doped with $\mathrm{F_4}$-TCNQ[116]. The data for both devices, expected to have different injection barriers, can be represented by the same linear fit. Intrinsically, the relaxation frequency does not allow a distinction between the injection barrier at the anode/HTL interface and bulk properties of the HTL. However, as both devices yield the same curve progression in fig. 5.33 this could be an indication that the relaxation frequency represents bulk charge carrier transport. More samples with different HILs, having different injection barriers, should be analyzed in the future to confirm this notion.

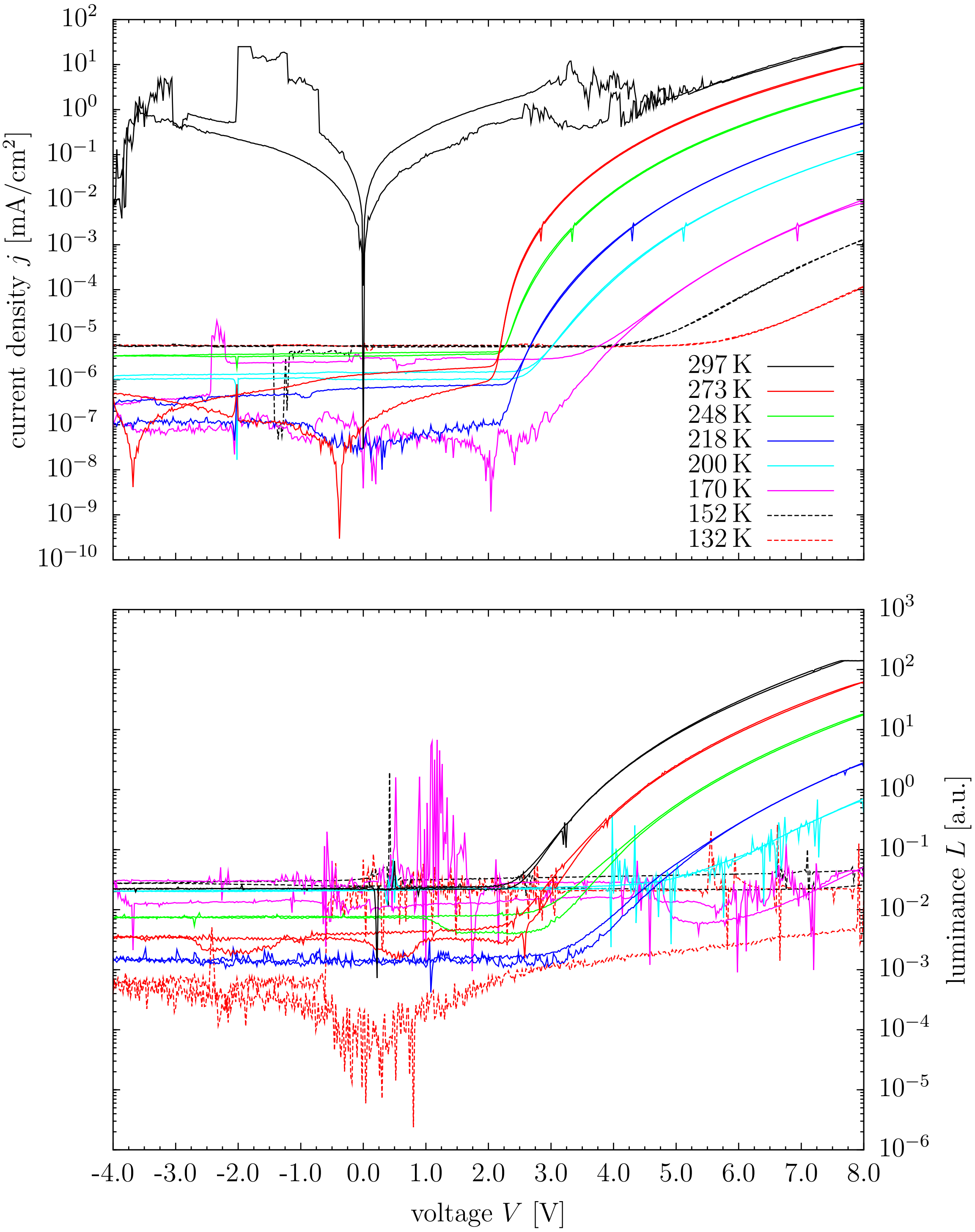

Figure 5.30.: Current density – voltage (top) and luminance – voltage (bottom) characteristics for the device with F_4-TCNQ as HIL (fig. 5.21) at different temperatures. Decrease in temperature leads to lower charge carrier mobility and thus to lower current densities and luminance.

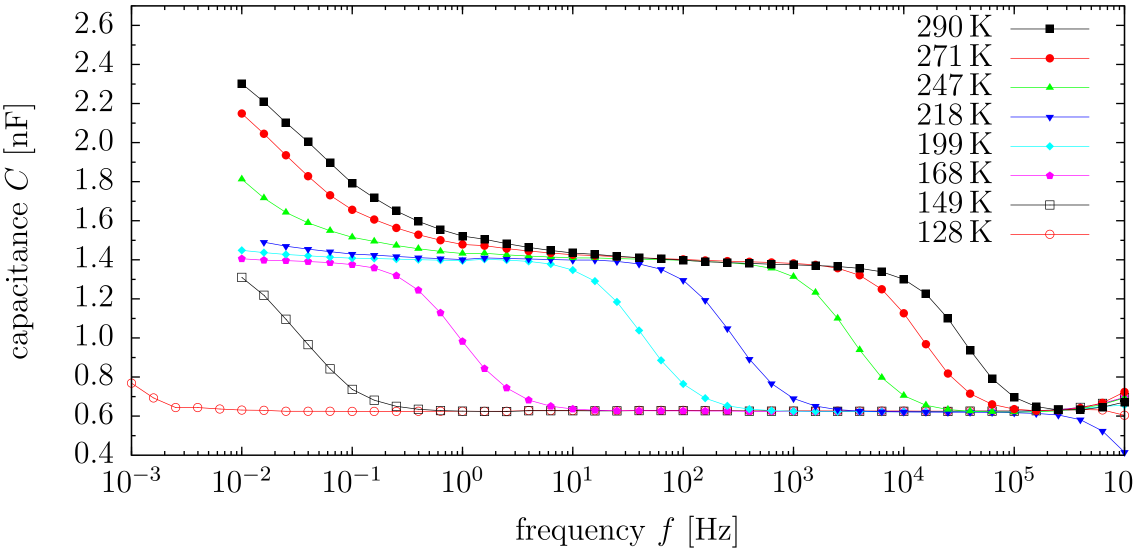

Figure 5.31.: $C - f$ characteristics of the device without HIL. $V_{\mathrm{DC}} = 2\,\mathrm{V}$. Decreasing relaxation frequency f_{r} with decreasing temperature.

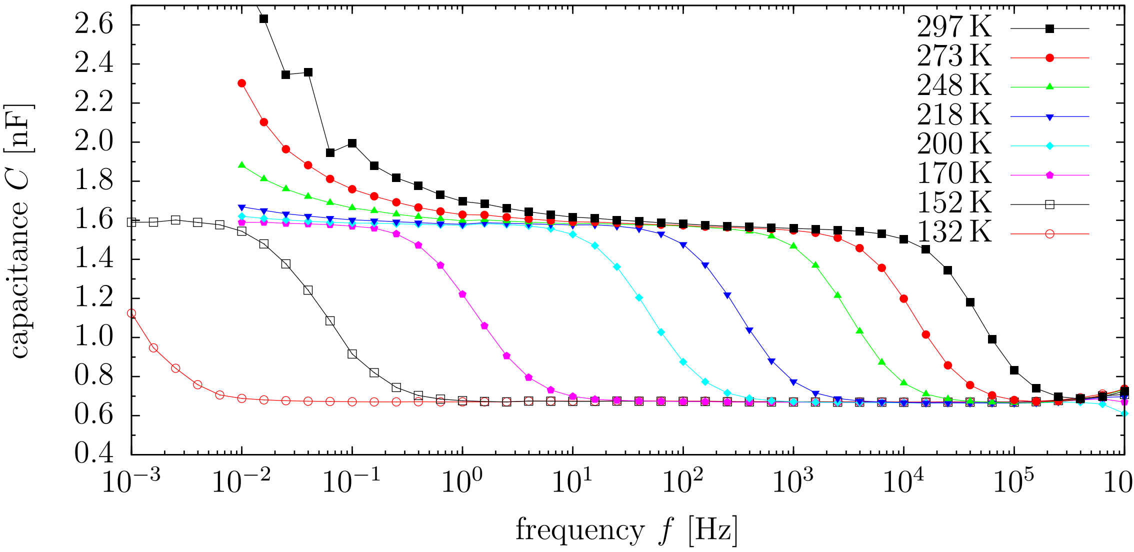

Figure 5.32.: $C - f$ characteristics of the device with F_4-TCNQ as HIL. $V_{\mathrm{DC}} = 2\,\mathrm{V}$. Decreasing relaxation frequency f_{r} with decreasing temperature.

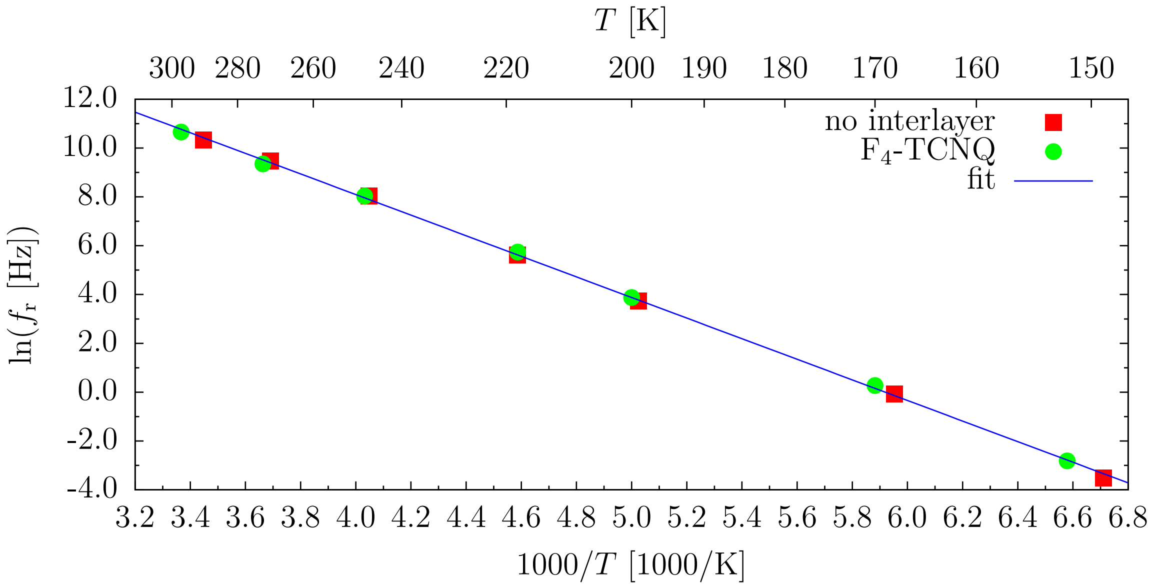

Figure 5.33.: Relation between relaxation frequency f_r and temperature T. Red squares: data from the device without HIL; green circles: data from the device with F$_4$-TCNQ. Blue line: linear fit. Its slope determines the activation energy $E_{\mathrm{a,TPD}} \approx 0.36\,e\mathrm{V}$ of the thermally activated hopping transport in TPD (eq. (2.15)).

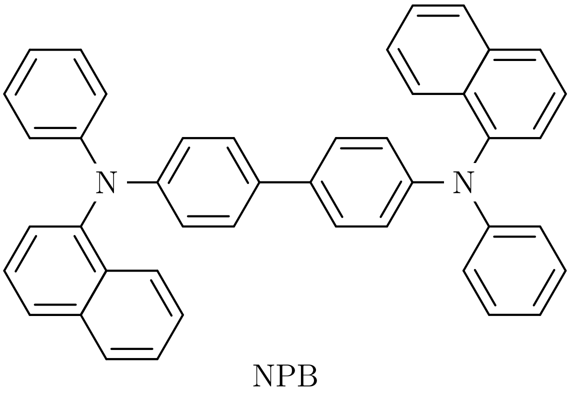

Figure 5.34.: Hole transporting material NPB (N,N'-di(naphtalene-1-yl)-N,N'-diphenyl-benzidine).

5.6. Device degradation

It is generally known that the luminance of OLEDs is decreasing with operating time, temperature and current load, hence their lifetime unfortunately is still limited. There have been various reports about possible degradation mechanisms, e.g., migration of mobile ions in the device[117–119], reorientation of molecular dipoles[120,121], chemical degradation due to oxygen[122] and/or water[123], or instability of charge-carrying species (e.g., Alq_3)[119,124,125]. However, as these reports use different materials and material combinations it might be that one or the other mechanism is more pronounced in the OLED stack of interest. Some of the observed effects, like formation of dark (non-radiative) spots or delamination of the metal electrodes, can be avoided when the OLED is protected from water and oxygen from the ambient atmosphere, e.g., by encapsulation of the device[126,127]. However, the cause of other degradation processes is not yet fully understood.

It is furthermore important to note that so far only very few experimental techniques have been employed to study OLED degradation. Among them the most direct method is the measurement of the temporal development of the voltage and the light output under electrical driving (either continuous constant current or alternating drive conditions with constant forward current for one half-cycle and constant reverse bias for the other half). This directly yields the loss of luminance and thus efficiency together with the increase in the voltage required to drive the current, which is a measure of how the current – voltage characteristics changes by electrical driving. In order to separate effects on charge transport (e.g., trapping) from effects affecting radiative recombination, photoluminescence has been studied on electrically aged devices[125]. Recently, chemical analysis of the degradation products of aged OLEDs by breaking the encapsulation and extracting the organic compounds in solvents suitable for chromatographic analysis techniques has been performed[128].

Another class of non-destructive techniques, which is well-known from inorganic semiconductor devices, makes use of the capacitive response of OLEDs under reverse bias conditions. In so-called voltammetric $j - V$ measurements the applied voltage is ramped with a high scan rate of typically $50\,\mathrm{V/s}$ and the displacement current ($C \cdot \mathrm{d}V/\mathrm{d}t$) due to charging or discharging of the sample capacitor is measured. Therefore this technique is also known as displacement current method (DCM)[129]. Kondakov et al. were the first to apply voltammetry to study OLED degradation[108]. In principle, this yields the same information as the $C - V$ measurements. Their studies confirmed the existence of negative interfacial charges in pristine NPB/Alq_3 heterolayer OLEDs as introduced before by Berleb et al.[107] and also observed in the OLEDs in this work (see, e.g., ch. 5.3) using impedance spectroscopy. Moreover, Kondakov et al. found that upon electrical aging of these devices the interfacial charge — evident through a step in the voltammetry signal in analogy to V_t in $C - V$ measurements presented here — is steadily decreasing and finally gets positive for longer operating times.

In the following, degradation studies of different OLED stacks — variations of the reference stack prepared in Augsburg and by the company H.C. Starck Clevios — are shown. First, experimental data is shown for each variation separately; the interpretation of the observed effects is then summarized for all types of devices later in a separate chapter.

5.6.1. Variation of the reference OLED stack — anode modifications

Again, variations of the reference OLED are investigated: the HILs are WO_3, PEDOT: PSS, and F_4-TCNQ (see fig. 5.21). ITO is Ar plasma treated for the device with WO_3, and oxygen plasma treated for all other devices. The device with WO_3 has been aged and measured in the nitrogen glovebox in dark and at room temperature, with slight variations over the measurement period (±1°C). To exclude effects due to temperature variations while aging or characterizing the devices, all other samples have been placed in the temperature controlled, evacuated, and dark cryostat.

Degradation of the sample with WO_3 as HIL

First, the device with WO_3 as HIL is analyzed. To degrade the device, a constant current density of $j = 10\,\mathrm{mA/cm^2}$ has been applied, while the voltage V and luminance L have been recorded, see fig. 5.35. To compare different aging times and current densities it is helpful to use the number of charges per unit area which have passed through the device:

$$N = j \cdot t\,. \tag{5.31}$$

Aging has been stopped after 10 hours and $j-V-L$, $C-f$, and $C-V$ measurements have been performed before the next aging period was started again. The measurements have not been carried out subsequently in all cases, sometimes the OLED was stored unused in the glovebox for a couple of days before intentional aging was continued; unfortunately, this leads to undesirable "regeneration" effects.

During degradation, there are reversible and irreversible effects on the OLED's electrical behavior: the driving voltage increases, however, the device seems to recover after not being operated for some time, as the voltage restarts at smaller values when the device is artificially degraded again. This effect also affects the luminance, which increases again after "regeneration", however, this is less pronounced than the recovery in voltage. Such effects have already been reported, for example, by Yahiro et al.[121]. Fig. 5.36 shows the $j-V-L$ characteristics of the sample in pristine state and after $N = 500\,\mathrm{mAh/cm^2}$ of aging (the $j-V-L$ characteristics for the intermediate aging intervals are not shown for the sake of visibility). It shows that the built-in voltage V_{bi} is unchanged. The effect of electrical aging of the device on the current density is relatively small: at 6 V only a change of about 24 %. Just from this $j-V$ curve one would expect that the device has not aged significantly. However, the variation in luminance is much more pronounced: a change of about 46 % is observed, again at 6 V. The current efficiencies for the device after the different aging steps is shown in fig. 5.37. Similar curve progressions indicate no change in the charge balance factor during aging.

Fig. 5.38 shows the capacitance – frequency behavior. A pronounced shift in the relaxation frequency f_{r} to lower frequencies is observed with aging time. Speaking in

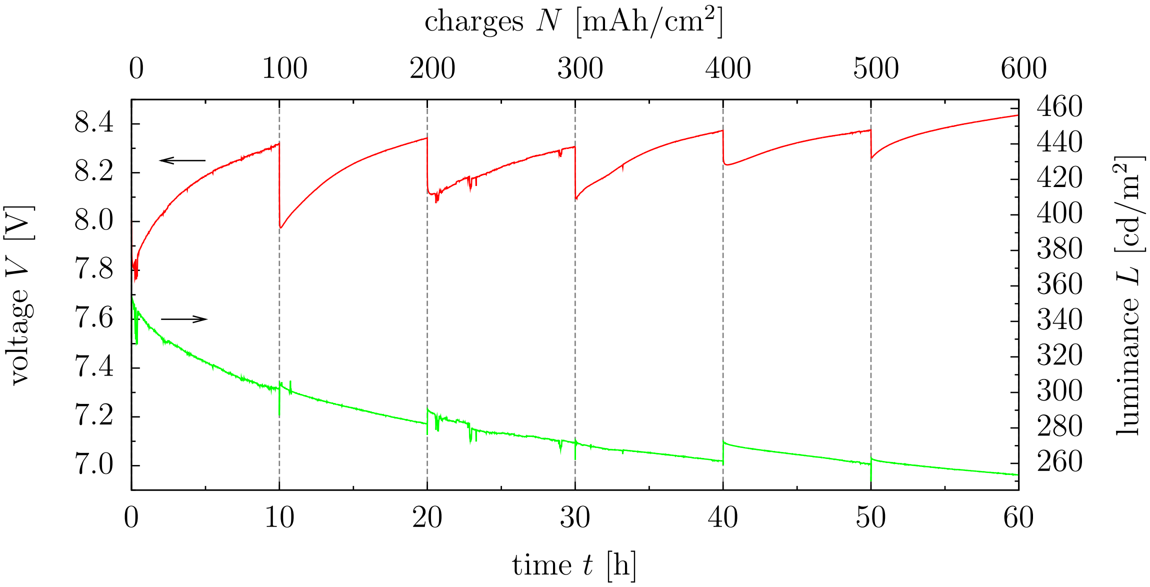

Figure 5.35.: Artificial degradation of an OLED stack with Ar treated ITO and 10 nm WO_3 interlayer (fig. 5.21). Current density $j = 10\,\mathrm{mA/cm^2}$. $L_0 \approx 354\,\mathrm{cd/m^2}$

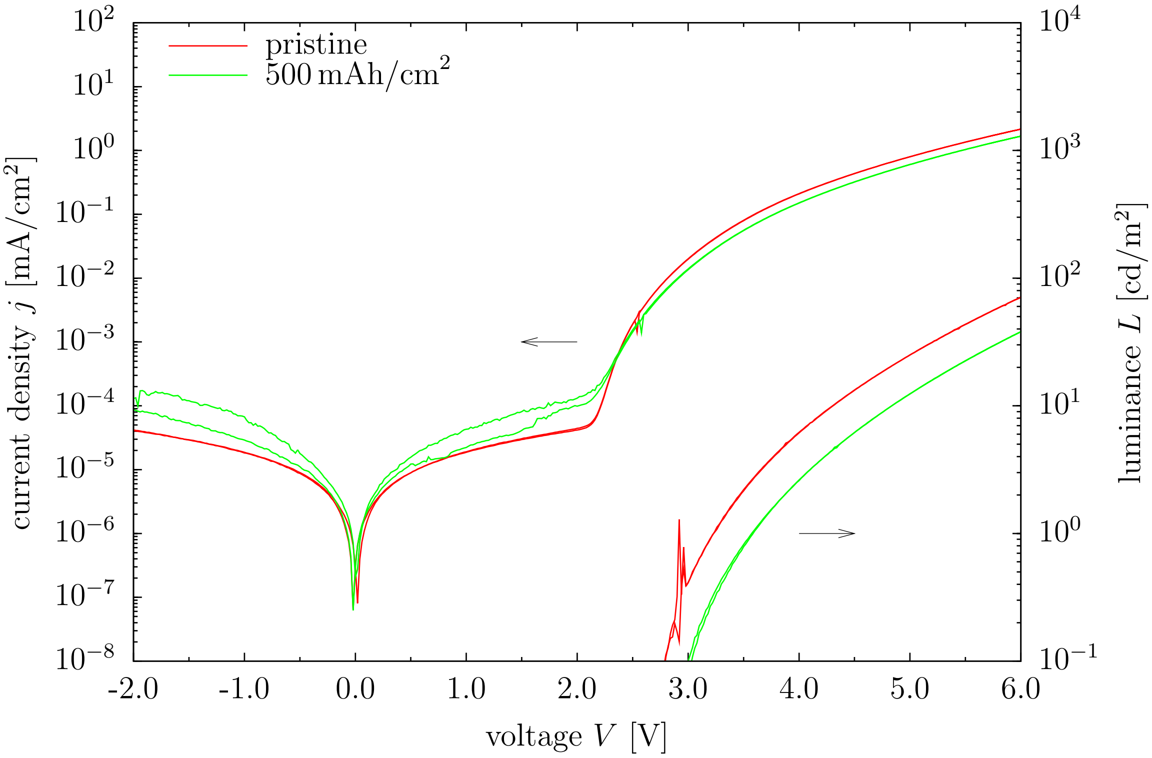

Figure 5.36.: Current density – voltage – luminance characteristic of the OLED with WO_3 in pristine state and after $N = 500\,\mathrm{mAh/cm^2}$ of aging. V_{bi} unchanged. Only small variation in current density in forward bias (24 % at 6 V); larger variation in luminance (46 % at 6 V).

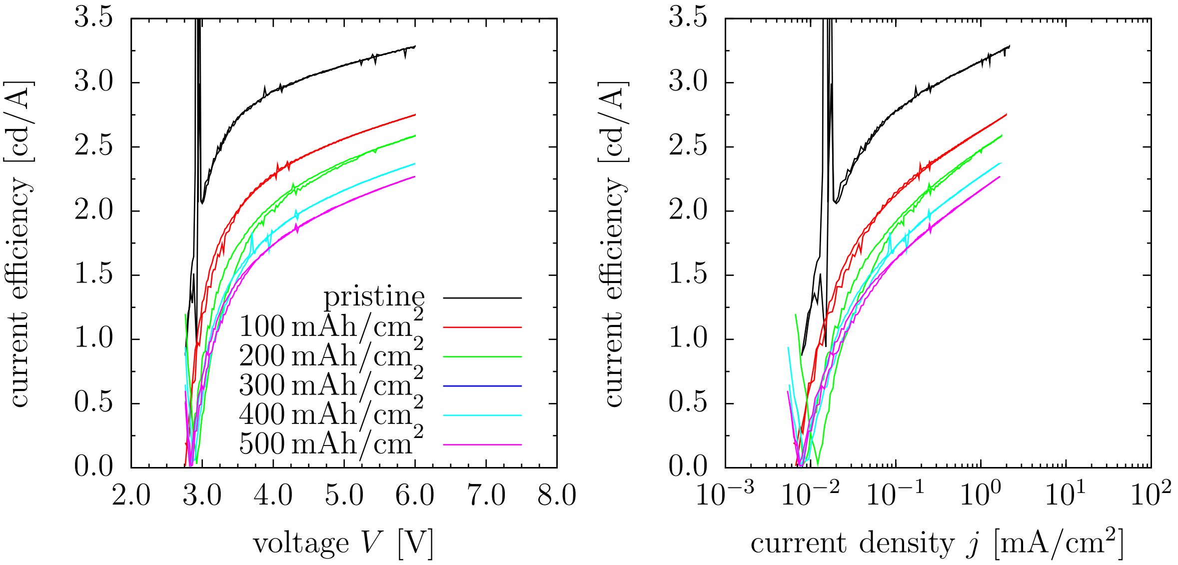

Figure 5.37.: Current efficiency of the OLED with WO_3 in pristine state and after the aging steps. The data for $N = 300\,\mathrm{mAh/cm^2}$ is not shown as it is too noisy.

terms of the equivalent circuit, the HTL resistance is increasing during aging. In the capacitance – voltage plots (fig. 5.39) one observes that the built-in voltage V_{bi} is not shifting, as is already expected from the $j - V$ measurement (fig. 5.36). However, the transition voltage V_{t} shifts to more positive potential with aging time, in agreement with the observations of Kondakov et al.[108]. This means that the absolute value of the (negative) interfacial charge density σ_{if} gets smaller (more positive), see eq. (5.30). The reduction of the interfacial charge density might be due to the generation of positive charge near the HTL/ETL interface. A detailed investigation will be given later.

Degradation of samples with PEDOT:PSS and F_4-TCNQ as HIL

Similar to the artificial degradation of the OLED with WO_3 as HIL, devices with PEDOT:PSS and F_4-TCNQ have been aged, however, using a constantly evacuated cryostat with high temperature stability. Also, a strict measurement routine has been used: aging of the device, a subsequent $j - V - L$ measurement, followed by $C - f$, $C - V$ and another $j - V - L$ measurement without waiting times between the measurements. Then the device was "resting" without applied bias until the next aging interval was started. This strict order and using the cryostat is to minimize different electrical behavior due to reversible degradation and temperature effects (which have been observed in the device with WO_3).

Again, $j = 10\,\mathrm{mA/cm^2}$ has been used as aging current density for 10 hours-intervals. However, after 70 hours of aging, the current density has been doubled to $20\,\mathrm{mA/cm^2}$ for four 20 hours-intervals and one 70 hours-interval, followed by one or two intervals with 22 hours and $60\,\mathrm{mA/cm^2}$. Please see fig. 5.40 and 5.41 for the aging of the devices with PEDOT:PSS and F_4-TCNQ, respectively, as well as the temperature T during

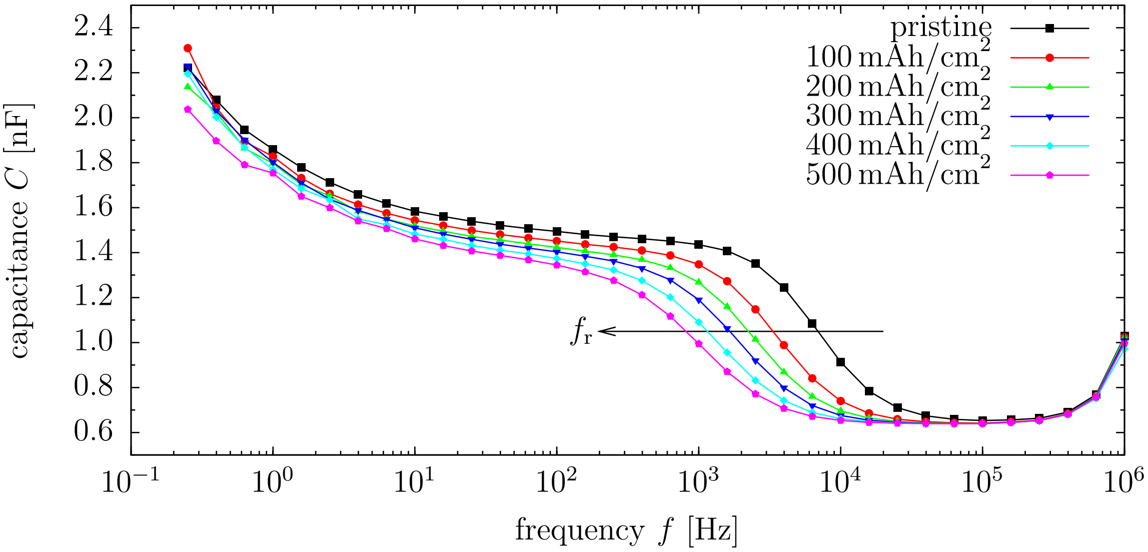

Figure 5.38.: $C - f$ characteristic after the different aging intervals of the OLED with WO_3. Shift in relaxation frequency f_r to lower values with aging time. $V_{DC} = 2$ V.

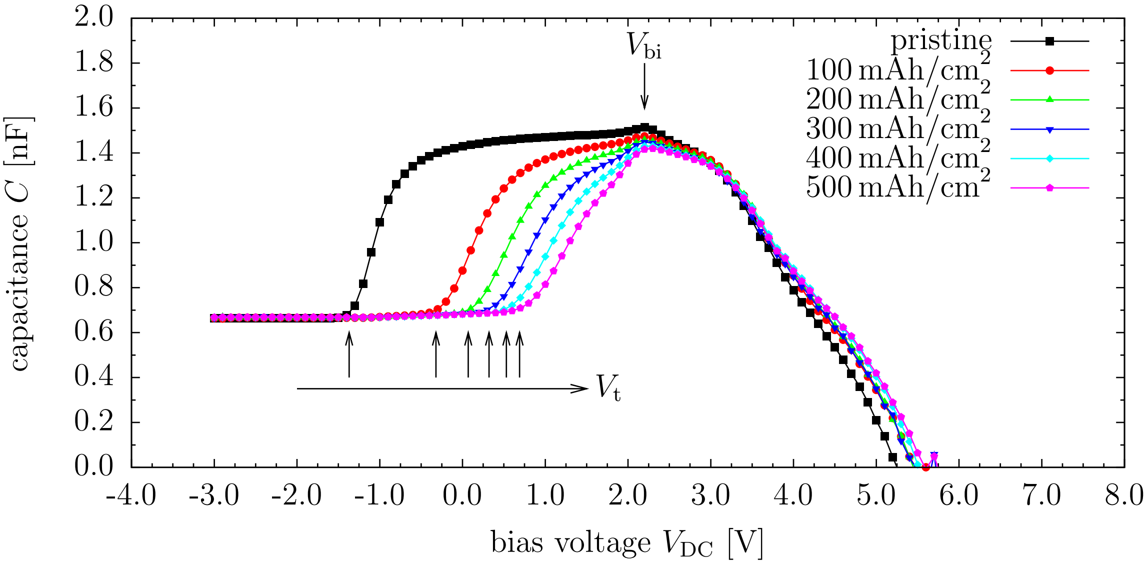

Figure 5.39.: $C - V$ characteristic after the different aging intervals of the OLED with WO_3. Shift in transition voltage V_t to more positive values with aging time. $f = 100$ Hz.

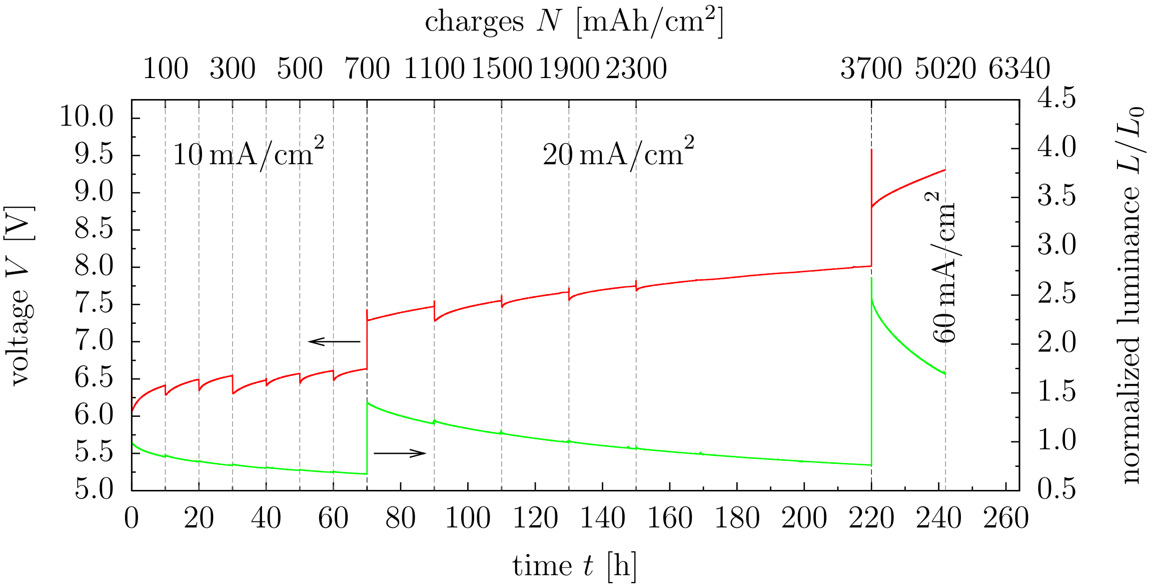

Figure 5.40.: Artificial degradation of an OLED stack with a 20 nm PEDOT:PSS interlayer (fig. 5.21). Current density $j = 10\,\mathrm{mA/cm^2}$, $20\,\mathrm{mA/cm^2}$, or $60\,\mathrm{mA/cm^2}$. $L_0 \approx 337\,\mathrm{cd/m^2}$.

degradation of these devices in fig. 5.42. Using increased current density is known as accelerated testing. The current density passing through the OLED is expected to affect the decrease in luminance linearly (half of the lifetime when doubling the current density), if the degradation process is coulombic. However, there are also reports that higher current densities decrease the half-luminance lifetime in a superlinear manner following a power law[130–132].

The decrease in current density and luminance with aging time in $j - V - L$ measurements are obvious; fig. 5.43 and 5.44 show the devices in pristine state, after $N = 500\,\mathrm{mAh/cm^2}$ and $5020\,\mathrm{mAh/cm^2}$ of aging, respectively. Current efficiencies are not shown as the detection limit of the photodiode in combination with the cryostat (light from the OLED has to pass several windows) is unfavorable. The time evolutions of $C - f$ and $C - V$ are shown in fig. 5.46 and 5.47 for the device with PEDOT:PSS and in fig. 5.48 and 5.49 for the device with F$_4$-TCNQ as HIL, respectively.

Again, the relaxation frequency f_r is shifting to lower values with the amount of charges passing through the devices, indicating an increase in the resistance of the HTL. However, the step at f_r is not distinct any more for $N \gtrsim 1500\,\mathrm{mAh/cm^2}$ at $V_\mathrm{DC} = 2\,\mathrm{V}$ as the transition voltage V_t shifts to even more positive values for both types of device with aging time (please see the corresponding $C - V$ measurements in fig. 5.47 and 5.49). It even reaches values larger than the built-in voltage of the pristine devices. The shift towards more positive values again indicates that positive charge is accumulating at or near the HTL/ETL interface.

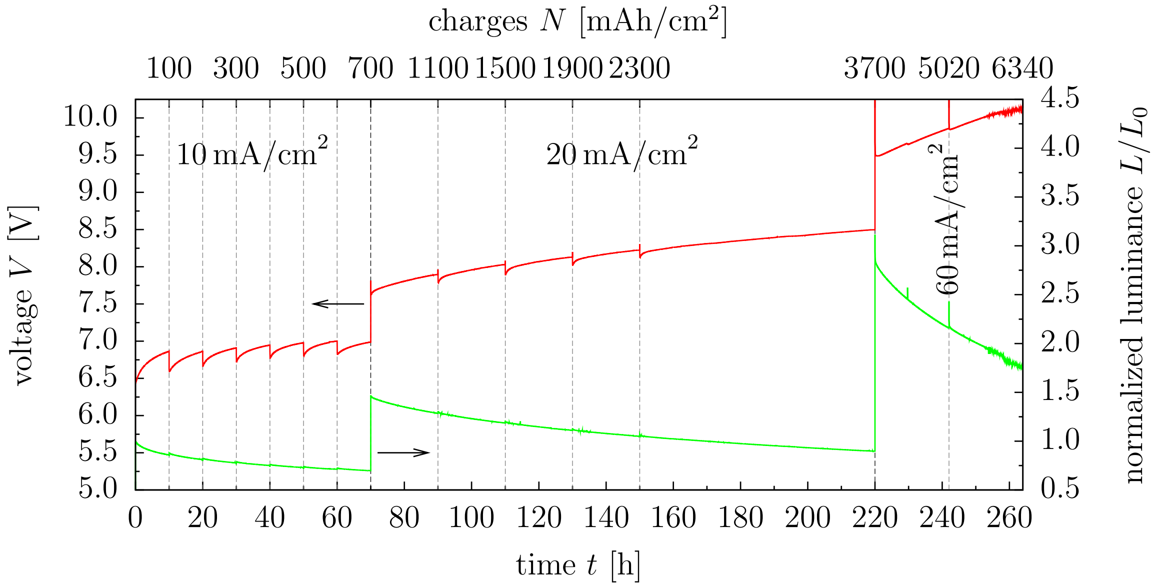

Figure 5.41.: Artificial degradation of an OLED stack with a thin F_4-TCNQ interlayer (fig. 5.21). Current density $j = 10\,\mathrm{mA/cm^2}$, $20\,\mathrm{mA/cm^2}$, or $60\,\mathrm{mA/cm^2}$. $L_0 \approx 307\,\mathrm{cd/m^2}$

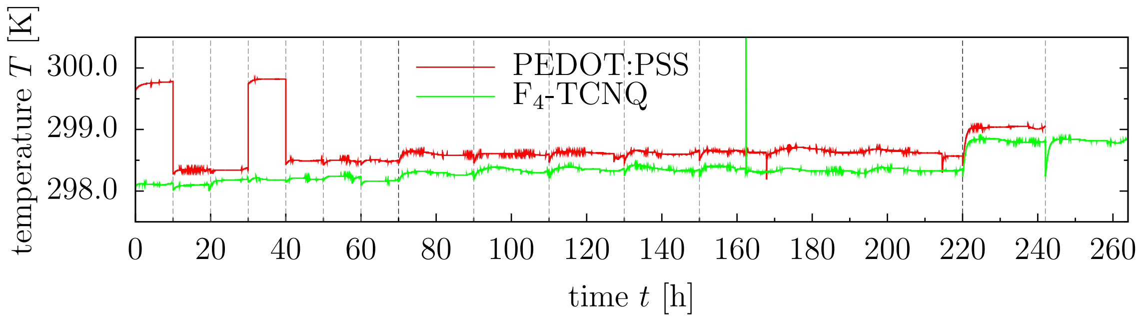

Figure 5.42.: Temperature T during artificial degradation of the OLED stacks with PEDOT:PSS (red line, fig. 5.40) and F_4-TCNQ (green line, fig. 5.41).

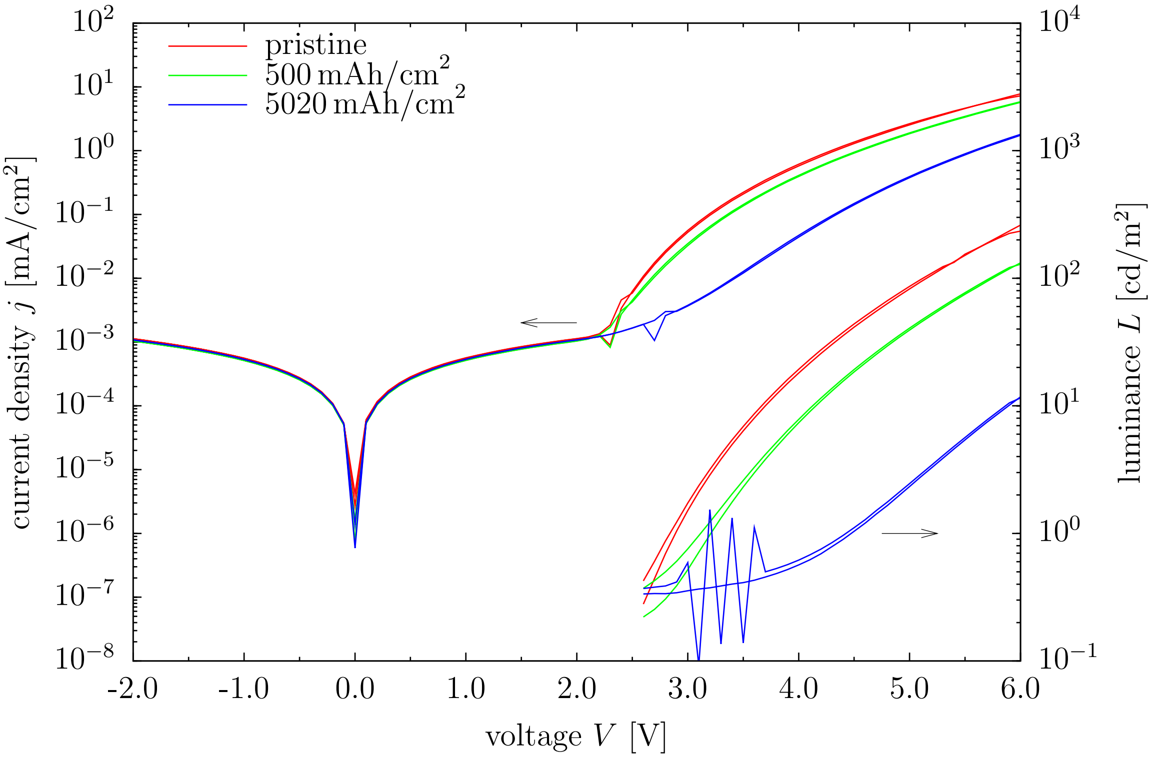

Figure 5.43.: $j - V - L$ characteristic of the OLED with PEDOT:PSS in pristine state and after $N = 500\,\mathrm{mAh/cm^2}$ and $5020\,\mathrm{mAh/cm^2}$ of aging.

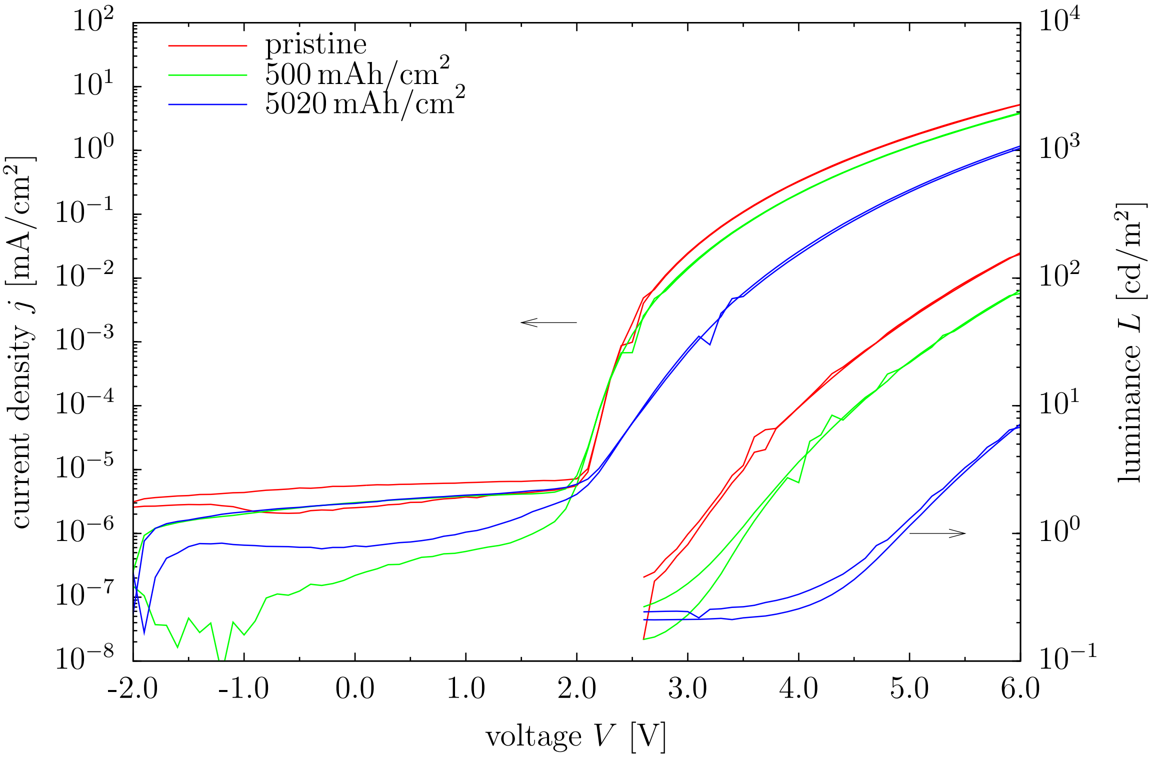

Figure 5.44.: $j - V - L$ characteristic of the OLED with F_4-TCNQ in pristine state and after $N = 500\,\mathrm{mAh/cm^2}$ and $5020\,\mathrm{mAh/cm^2}$ of aging.

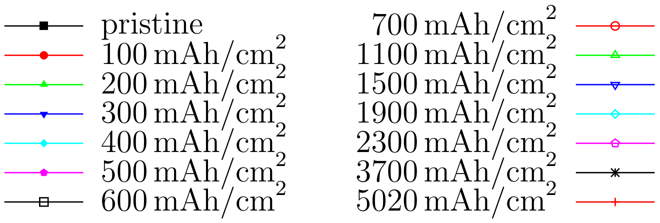

Figure 5.45.: Line colors and symbols used for the different aging times in $C - f$ and $C - V$ graphs.

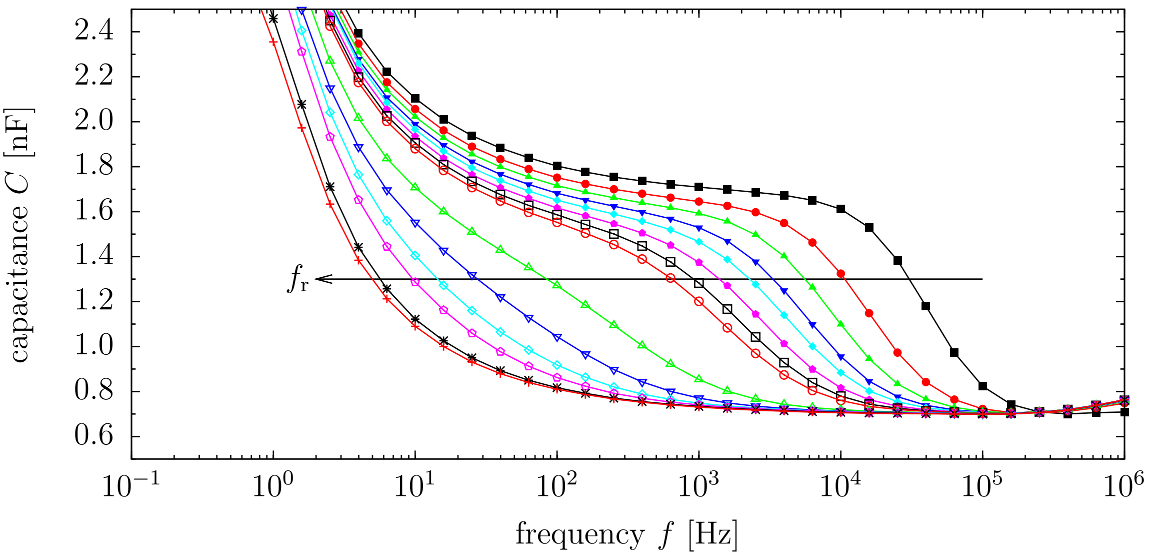

Figure 5.46.: $C - f$ characteristic after the different aging intervals of the OLED with PEDOT:PSS. $V_{\mathrm{DC}} = 2\,\mathrm{V}$. Lines and symbols as in fig. 5.45.

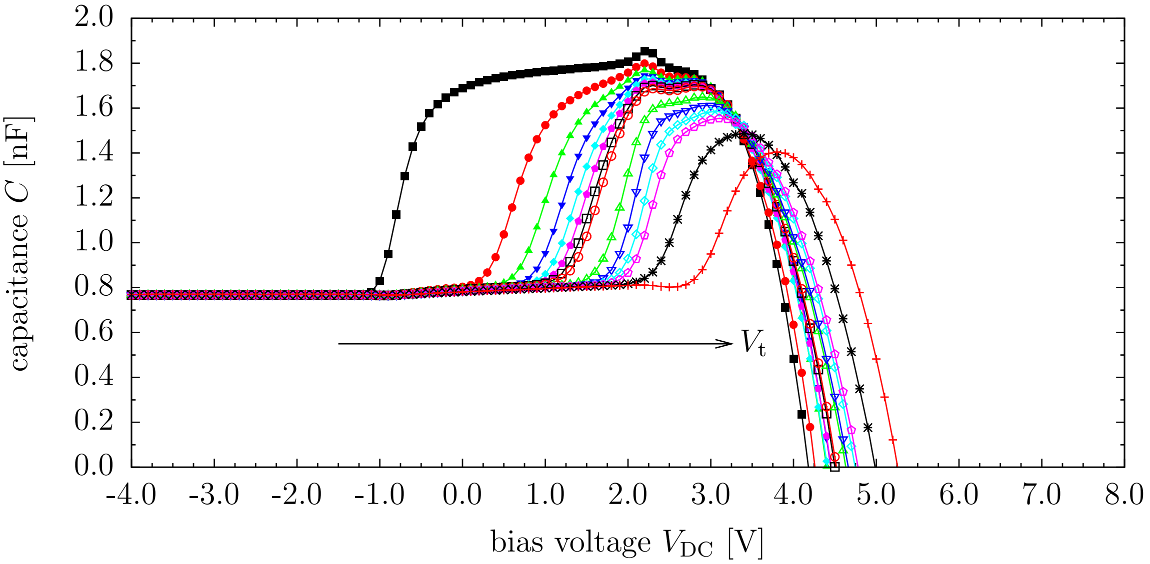

Figure 5.47.: $C - V$ characteristic after the different aging intervals of the OLED with PEDOT:PSS. $f = 100\,\mathrm{Hz}$. Lines and symbols as in fig. 5.45.

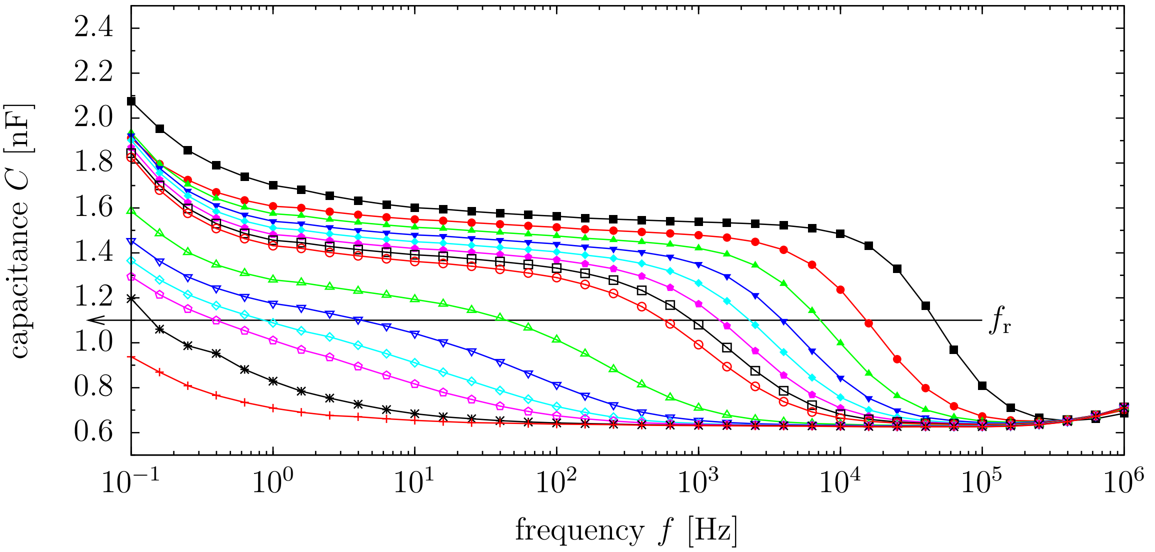

Figure 5.48.: $C - f$ characteristic after the different aging intervals of the OLED with F_4-TCNQ. $V_{DC} = 2\,V$. Lines and symbols as in fig. 5.45.

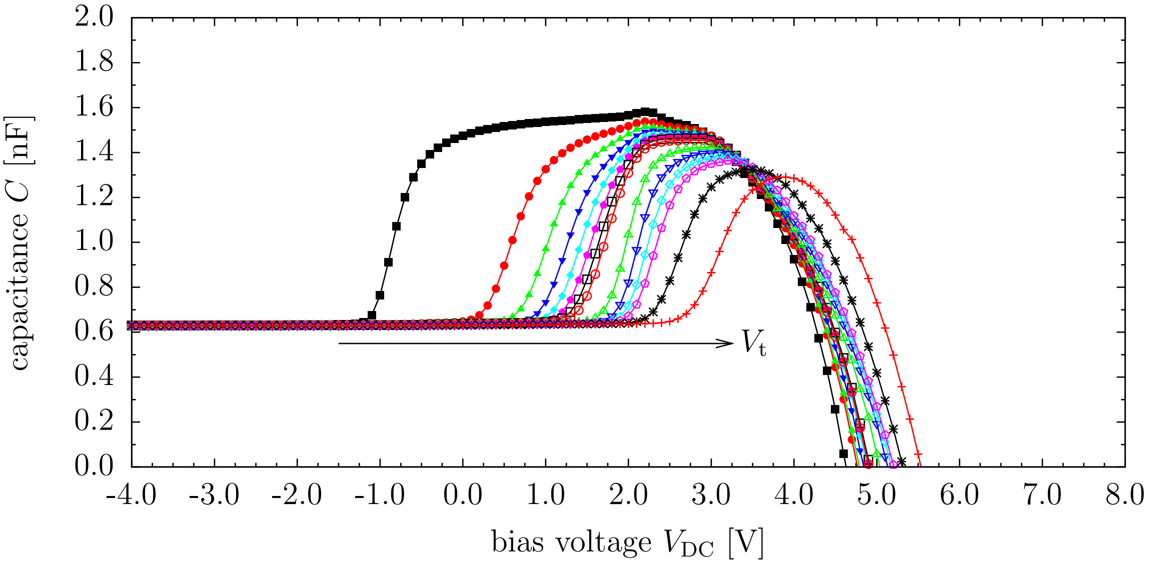

Figure 5.49.: $C - V$ characteristic after the different aging intervals of the OLED with F_4-TCNQ. $f = 100\,Hz$. Lines and symbols as in fig. 5.45.

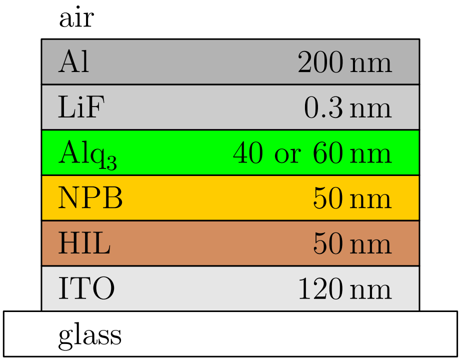

Figure 5.50.: OLED stack using different HILs (AI4083 and HIL1.3) from H.C. Starck Clevios.

5.6.2. Variation of the reference OLED stack — devices prepared by H.C. Starck Clevios

As IS allows specifically to study differences in hole injection layers and degradation effects, it is also interesting for companies developing new HIL materials. Devices shown in this section have been prepared by H.C. Starck Clevios GmbH, Leverkusen. Their OLED stack is similar to the reference stack of this thesis, however, using NPB as HTL, see fig. 5.50. However, TPD and NPB have similar properties and differ not too much (see fig. 2.4 and 5.34); therefore, a comparison of the two stack designs is possible.

The two HILs which are compared are Clevios$^{\text{TM}}$ P AI4083, an aqueous dispersion of PEDOT and PSS in a ratio of 1 : 6 by weight[††], and Clevios$^{\text{TM}}$ HIL1.3 as a new PEDOT-containing dispersion[133]. Both hole injection layers were spincast onto the cleaned substrate and dried on a hot plate at 200°C for 5 min in ambient air. The other organic materials (NPB and Alq$_3$) were deposited through shadow masks in a high vacuum chamber (base pressure $< 5 \cdot 10^7$ mbar). As cathode a 0.3 nm thin LiF layer covered by 200 nm Al was deposited by thermal evaporation in another chamber at $1 \cdot 10^6$ mbar. The area of the OLED pixel defined by a crossbar layout is also 4 mm^2. Finally, the samples were encapsulated in a nitrogen glovebox by covering them with another glass slide sealed by epoxy resin. All electrical measurements were performed under ambient conditions at room temperature. The IS measurements in this chapter have been performed using very short lead cables ($\approx$ 20 cm). Hence, $C - f$ is not showing peaks due to the cable's inductance at high frequencies but a decrease in capacitance due to a lead resistance (see fig. 5.8 for simulations).

Fig. 5.51 shows the $j - V - L$ characteristics of pristine devices with Alq$_3$ thickness $d_{\text{Alq}_3} = 40$ nm for the two different HILs. Apart from some differences in the leakage current between 0 and 2 V, which can vary from sample to sample, both OLEDs show virtually identical behavior in forward direction. In particular, the current starts to rise exponentially at about 2.3 V and at the same voltage light emission sets in.

[††] To differentiate between the PEDOT:PSS containing samples, the devices are named 'PEDOT:PSS' if prepared in Augsburg and 'AI4083' if prepared by H.C. Starck Clevios.

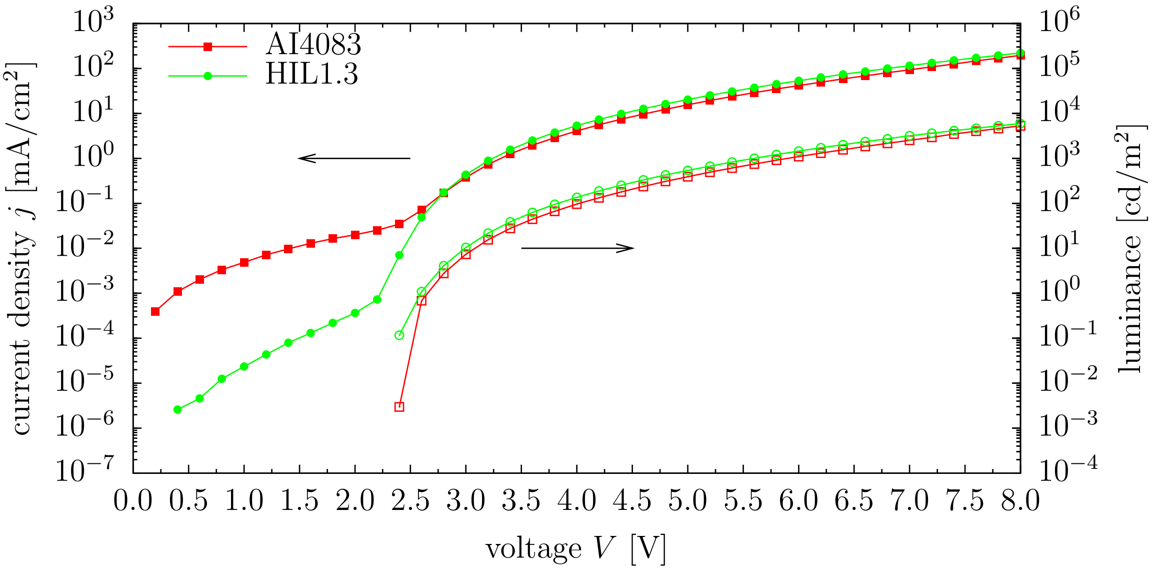

Figure 5.51.: Current density – voltage – luminance characteristics of the OLED stack shown in fig. 5.50 with an Alq_3 thickness of 40 nm using different HILs (AI4083 (red line and squares) and HIL1.3 (green line and circles)) from H.C. Starck Clevios.

These devices have been aged with a constant current density $j = 48\,\mathrm{mA/cm^2}$ for 215 h (AI4083) and 250 h (HIL1.3), respectively. The corresponding $C - f$ measurements for pristine and aged devices with different HIL are shown in fig. 5.52 for the reverse bias regime, $V_{\mathrm{DC}} = 0\,\mathrm{V}$, and the hole injection regime, $V_{\mathrm{DC}} = 2\,\mathrm{V}$. While in the case of HIL1.3 there is only very little change in the overall behavior, the curve for AI4083 as HIL changes quite significantly. Its relaxation frequency at $V_{\mathrm{DC}} = 2\,\mathrm{V}$ is almost tenfold smaller than for the pristine sample, which points toward a deterioration of hole injection and/or hole transport to the HTL/ETL interface. By contrast, the relaxation frequency for the sample with HIL1.3 is unchanged. The only changes observable in this device are less effects of stray capacitance at low frequency and a slightly smaller series resistance, leading to a roll-off beyond 1 MHz. Similarly, in $C - V$, the shift in transition voltage is much more pronounced for the sample with AI4083 (not shown here).

For a more detailed investigation, intermediate aging intervals have been chosen, also changing the Alq_3 thickness to 60 nm. As the measured pixels were partially located on different chips fabricated in different runs, there is some scattering between them, but nevertheless, one can see a clear tendency. Fig. 5.53 shows drive voltage and luminance vs. aging time for different samples of OLEDS with AI4083 and HIL1.3, respectively. Again, a constant current density of $48\,\mathrm{mA/cm^2}$ has been applied. The devices with AI4083 as HIL degrade very rapidly: the luminance drops to half of its initial value after 20 to 40 hours and after 200 hours it is less than 20 % for all samples. At the same time the drive voltage increases by about 2.5 V already after 200 hours. For samples with HIL1.3, however, the loss in luminance and the increase in drive voltage are much slower: after 200 hours the luminance is still above 70 % and the extrapolated half-luminance-lifetime would be larger than 500 hours for most

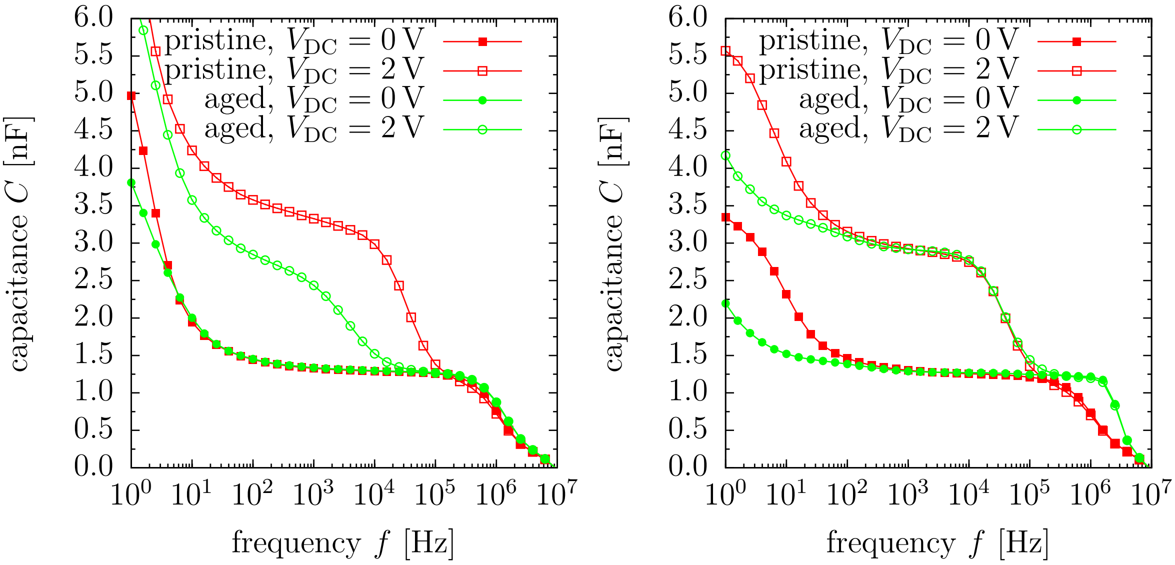

(a) *AI4083, aged for* 215 h ***(b)*** *HIL1.3, aged for* 250 h

Figure 5.52.: $C - f$ plot for pristine (red symbols and lines) and aged (green symbols and lines) samples at different applied bias $V_{\mathrm{DC}} = 0\,\mathrm{V}$ (closed symbols) and $2\,\mathrm{V}$ (open symbols). Aging performed with $j = 48\,\mathrm{mA/cm^2}$.

devices. This is a clear indication that the rapid device degradation in the former type of devices is related to the usage of AI4083 as HIL.

Comparison of the capacitance – voltage characteristics of these devices as function of operation time is shown in fig. 5.54. The behavior for both types of HILs is similar to the behavior discussed above for the variations of the reference OLED stack. Comparing both HILs, AI4083 and HIL1.3, there is a remarkable difference: OLEDs with AI4083 have a more rapid shift of the transition voltage towards more positive values. For aging times longer than 150 hours, V_{t} even exceeds the built-in voltage of the pristine sample. By contrast, devices with HIL1.3 display a much slower shift of the transition voltage and even after 450 hours of constant driving V_{t} is still well below the built-in voltage. The same is true for the peak in the capacitance close to V_{bi}, indicating that electron injection in devices with HIL1.3 is less severely degrading upon long-term device operation.

5.6.3. Discussion of degradation effects — shift in relaxation frequency and transition voltage, and loss of luminance

In all samples studied, generation of dark spots during aging has not been observed. This is attributed to the fact that ambient atmosphere (water and oxygen) has been avoided for all samples, either by using the glovebox, the evacuated cryostat, or encapsulation; this is in agreement with observations from literature[126,127]. The loss in luminance (L/L_0, where L_0 is the luminance in pristine state) with the amount of charges N having passed the device (or time t at constant current density j), shown

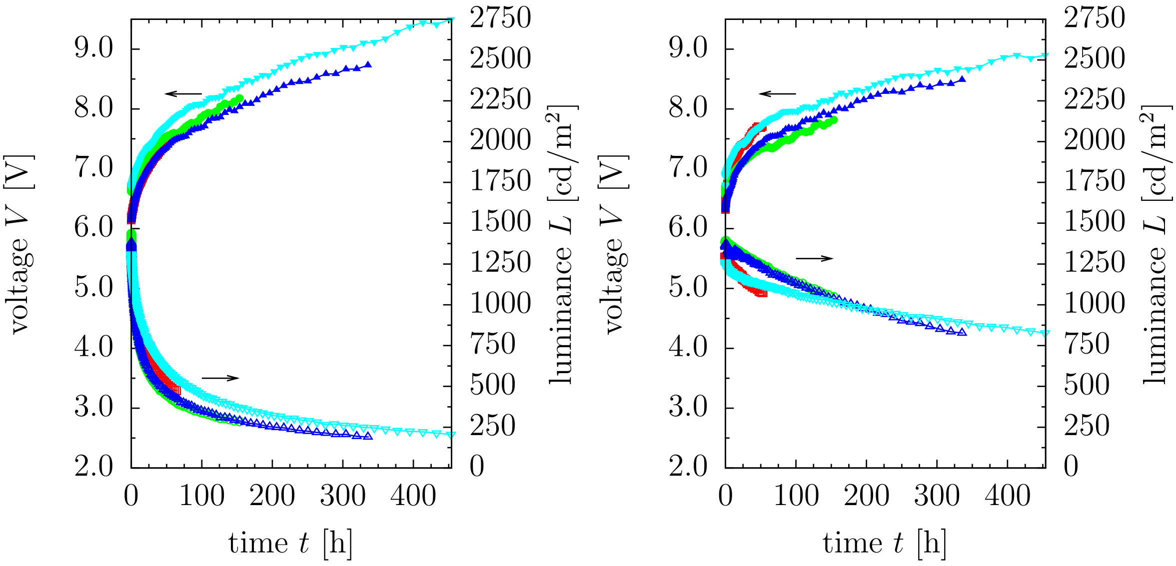

(a) AI4083 *(b) HIL1.3*

Figure 5.53.: Aging of samples with AI4083 and HIL1.3 (Alq_3 thickness 60 nm). Applied current density $j = 48\,\mathrm{mA/cm^2}$. Increase in current (closed symbols) and decrease in luminance (open symbols). Colors represent different OLED pixels and their corresponding aging times.

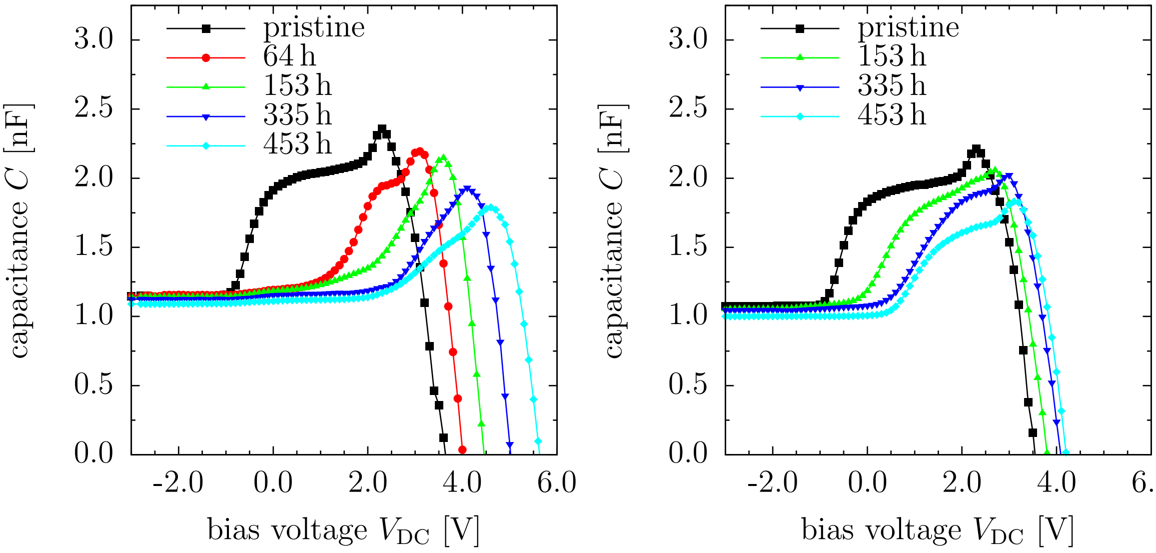

(a) AI4083 *(b) HIL1.3*

Figure 5.54.: $C-V$ plots for different aging times of samples with AI4083 and HIL1.3 (Alq_3 thickness 60 nm). $f = 100\,\mathrm{Hz}$.

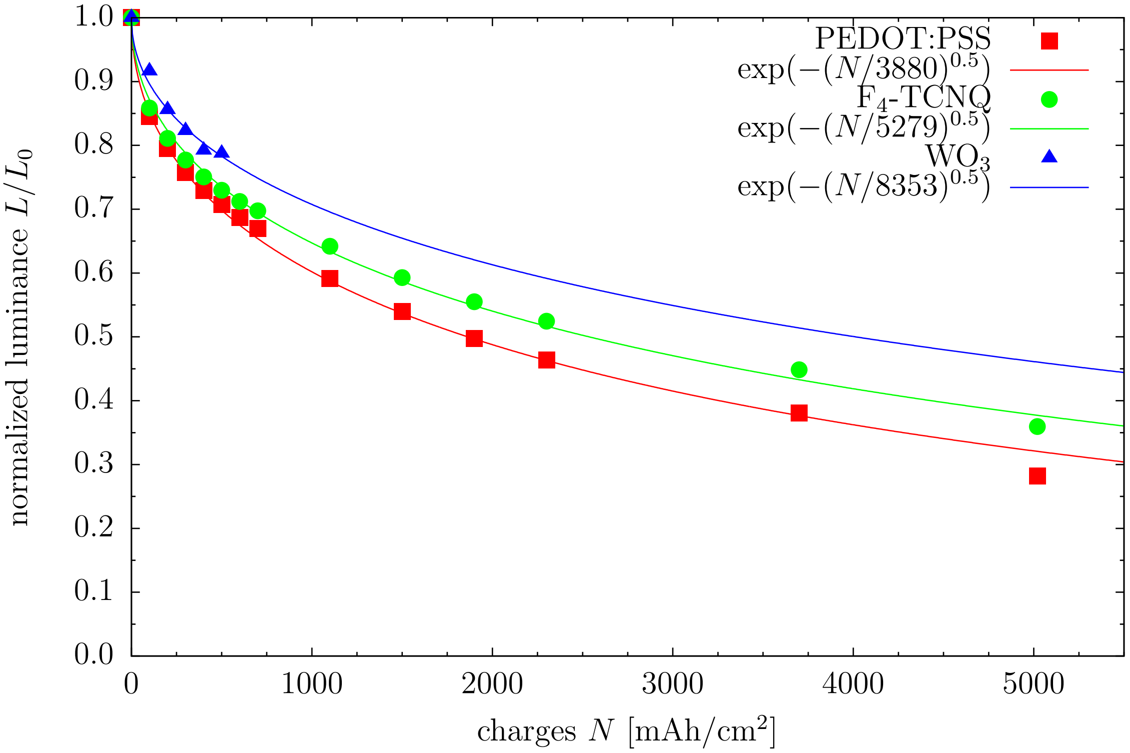

Figure 5.55.: Loss in luminance with amount of charges N having passed the device. Symbols: experimental data. Lines: Corresponding fits using a stretched exponential decay (eq. (5.33)). Luminance data weighed with current density (twice the current results in twice the luminance). PEDOT:PSS: $L_0 \approx 337\,\mathrm{cd/m^2}$, F_4-TCNQ: $L_0 \approx 307\,\mathrm{cd/m^2}$, $WO_3 : L_0 \approx 354\,\mathrm{cd/m^2}$ (all at $j = 10\,\mathrm{mA/cm^2}$).

in fig. 5.55 for the devices prepared in Augsburg and in fig. 5.56 for the devices of H.C. Starck, therefore must be caused by other mechanisms. In the beginning, the luminance decreases more rapidly than in the rest of the time. The data can be fitted by a biexponential decay

$$\frac{L}{L_0} = a \cdot \exp\left[-\left(\frac{N}{b}\right)\right] + c \cdot \exp\left[-\left(\frac{N}{d}\right)\right] . \tag{5.32}$$

As a consequence, two processes, one faster than the other, would be responsible for the loss in luminance. However, in literature, a stretched exponential decay

$$\frac{L}{L_0} = \exp\left[-\left(\frac{N}{b}\right)^{\beta}\right] \tag{5.33}$$

is often used without known physical justification[131,134]. Thereby, the fit parameter β is usually in the order of ≈ 0.5. Corresponding fits, where $\beta = 0.5$ are also shown in fig. 5.55 (which yield smaller errors than biexponential fits).

The loss in luminance is obvious and the most stable device seems to be the one with HIL1.3, but the underlying degradation mechanism is still unidentified. However,

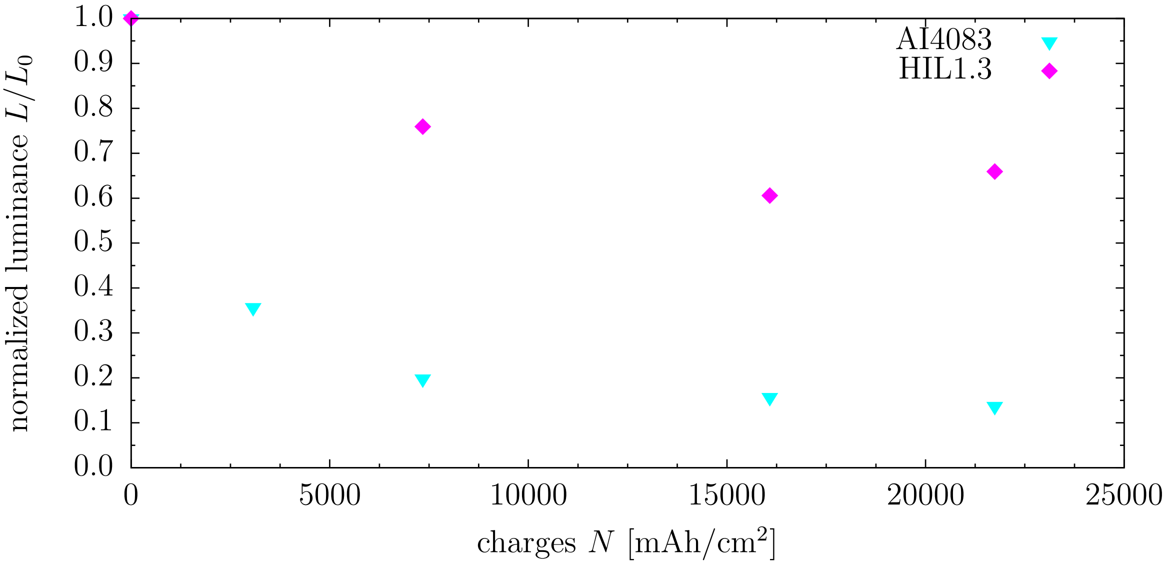

Figure 5.56.: Loss in luminance with amount of charges N having passed the four different devices per HIL. AI4083: $L_0 \approx 1385\,\mathrm{cd/m^2}$, HIL1.3: $L_0 \approx 1400\,\mathrm{cd/m^2}$ (at $j = 48\,\mathrm{mA/cm^2}$). No fit is shown due to too few data points.

the impedance spectroscopy measurements yield information about the dynamics of injected carriers via the relaxation frequency. Its shift towards lower frequencies with increasing amount of charges N having passed the device shows that the resistance of the HTL in the equivalent circuit must be increasing. A priori, this could be caused by either an increase of the injection barrier or a reduction of the hole mobility, e.g., by traps in the bulk of the HTL. It is likely that both effects may contribute. Fig. 5.57 shows the normalized (in respect to the pristine frequency $f_{\mathrm{r},0}$) relaxation frequency. After an initial phase, where f_r decreases rapidly and with different rates for the different samples, the slopes of the data in logarithmic representation are constant, hence the relaxation frequency decreases exponentially with the amount of charges N having passed the device. All three data sets can be represented by the same decay factor. This indicates, that the hole mobility in the HTL is getting lower while aging the devices. The hole injection barrier at the HIL/HTL interface only seems to affect the pristine relaxation frequency and the rate of change of f_r during the beginning of device operation.

Now the question arises if the changes in the HTL are responsible for the loss in luminance. Please note that the device with WO_3 as HIL has the lowest relaxation frequency and thus the worst hole injection and transport, but the highest luminance (tab. 5.2), which is not intuitive. It also indicates that even if devices are prepared carefully in the same way the fabrication process itself unfortunately yields devices with small variations: from the data shown before in fig. 5.22, e.g., the device with F_4-TCNQ was the one having the highest luminance. During measurements, controlling all possible disturbances, e.g., temperature, is also essential for comparable results.

Unlike fig. 5.55 the data of fig. 5.57 cannot be represented by a stretched exponential decay or biexponential decay, which leads to the assumption, that both effects, loss

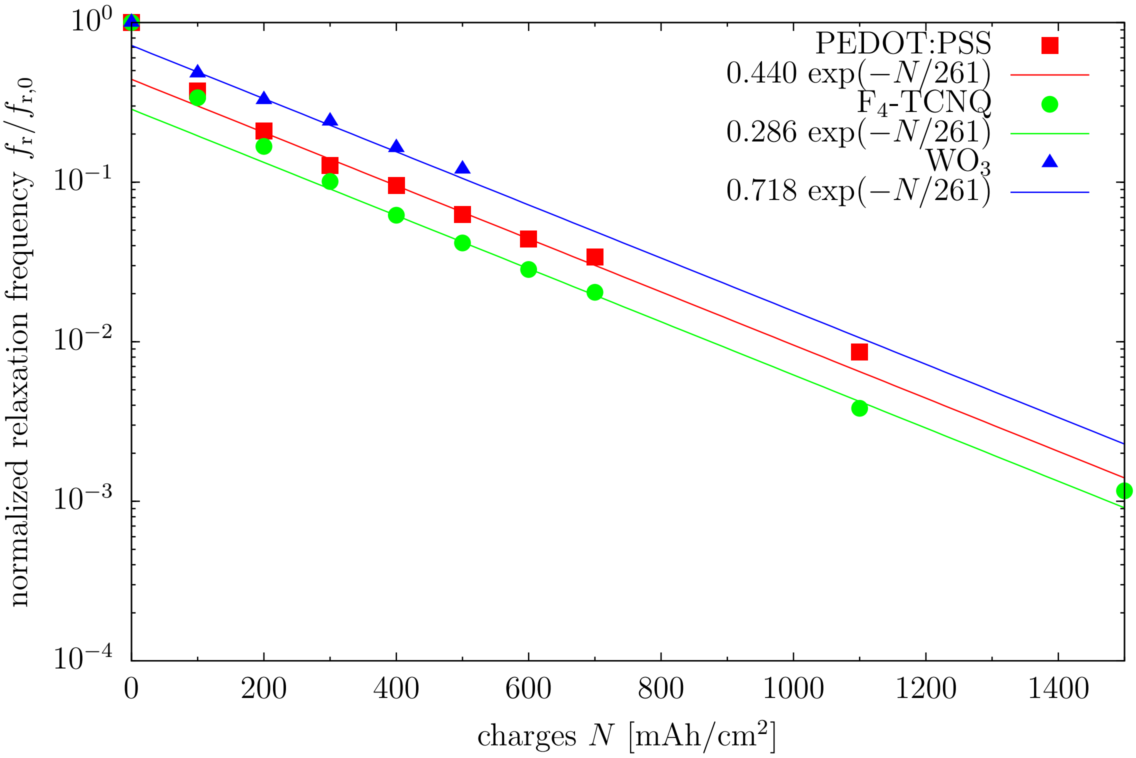

Figure 5.57.: Relaxation frequency f_r normalized with respect to the pristine frequency $f_\mathrm{r,0}$. Symbols: experimental data. Lines: corresponding exponential decay fits using the same decay constant. Decay constant extracted from a fit of the device with F_4-TCNQ; data range $N \geqslant 400\,\mathrm{mAh/cm^2}$. Constant slope indicates exponential degradation of hole injection and/or hole transport. $V_\mathrm{DC} = 2\,\mathrm{V}$. PEDOT:PSS: $f_\mathrm{r,0} \approx 37\,\mathrm{kHz}$, F_4-TCNQ: $f_\mathrm{r,0} \approx 45\,\mathrm{kHz}$, WO_3: $f_\mathrm{r,0} \approx 7\,\mathrm{kHz}$.

	$f_{r,0}$ [kHz]	L_0 [cd/m^2]
PEDOT:PSS	37	337
F_4-TCNQ	45	307
WO_3	7	354

Table 5.2.: Pristine relaxation frequency (at $V_{DC} = 2\,V$) and luminance (at $j = 10\,mA/cm^2$) for the devices used in the degradation studies.

in luminance and shift in relaxation frequency with the amount of charges having passed the device, are not correlated. Also, plotting several representations of f_r and L (not shown here) does not reveal a linear or exponential relationship. This also indicates that the two effects are not correlated directly, however, it can not be excluded completely with the available data.

However, other observations during the degradation studies are available, e.g., from $C - V$ characteristics of the devices. From the transition voltage V_t in pristine devices, it is concluded that a negative interfacial charge density must be present at the HTL/ETL interface (see eq. (5.30)). As already mentioned, the origin of this charge in pristine devices is partial dipole moment ordering (orientational polarization) of the Alq_3 molecules[109]. During degradation, a rapid shift of the transition voltage V_t toward more positive values is observed, shown in fig. 5.58 for the devices prepared in Augsburg, which even exceeds the built-in voltage $V_{bi} \approx 2.2\,V$ of the pristine samples. According to eq. (5.30), this shift translates to a shift in the interfacial charge density σ_{if}, also to more positive values. It seems that the rise in transition voltage or interfacial charge density is proportional to the logarithmic amount of charges N having passed the devices, see fig. 5.59[‡‡].

Kondakov et al. also observed negative interfacial charges in pristine devices and a shift in transition voltage during degradation[108]. From the observed linear relationship between the loss of luminance efficiency and the shift of the transition voltage (reflecting the sign and the amount of interfacial charge) they concluded that electrical aging of these OLEDs creates positive fixed charges located primarily near the HTL/ETL interface. They further suggested that these charged states act as non-radiative recombination centers. Following their approach, fig. 5.60 shows the loss in luminance and its correlation with the interfacial charge density. Linear tendencies are also visible, e.g., the devices prepared in Augsburg could share a linear fit (as they only differ in the HIL) for the data where $j = 10\,mA/cm^2$ and another one with different slope for $j = 20\,mA/cm^2$. If, after Kondakov, the loss in luminance is linearly related with the amount of accumulated positive charges, it is astonishing why there is a difference for the different aging current densities. Guided by the eye, also some curve can be construed through the data points. More experimental work is needed, e.g., aging with different current densities (yet constant for one particular OLED pixel) to see if there is a linear or other dependency.

[‡‡] For the calculations of the interfacial charge density, the thicknesses of the Alq_3 layers are determined from fits of $C - f$ measurements, using $\varepsilon_r = 3.25$.

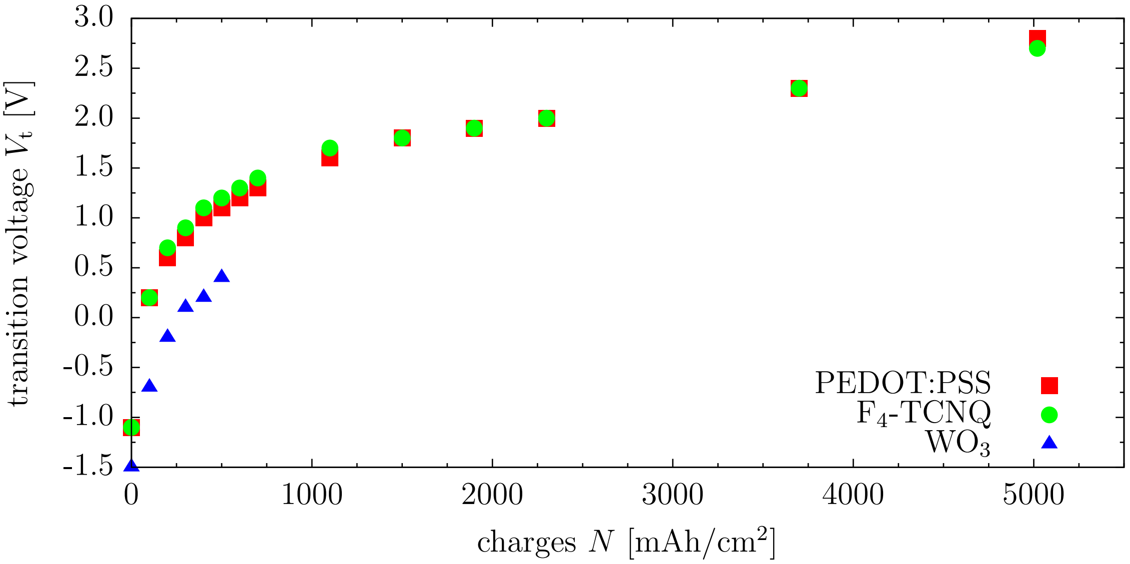

Figure 5.58.: Shift in transition voltage V_t with the amount of charges N having passed the device.

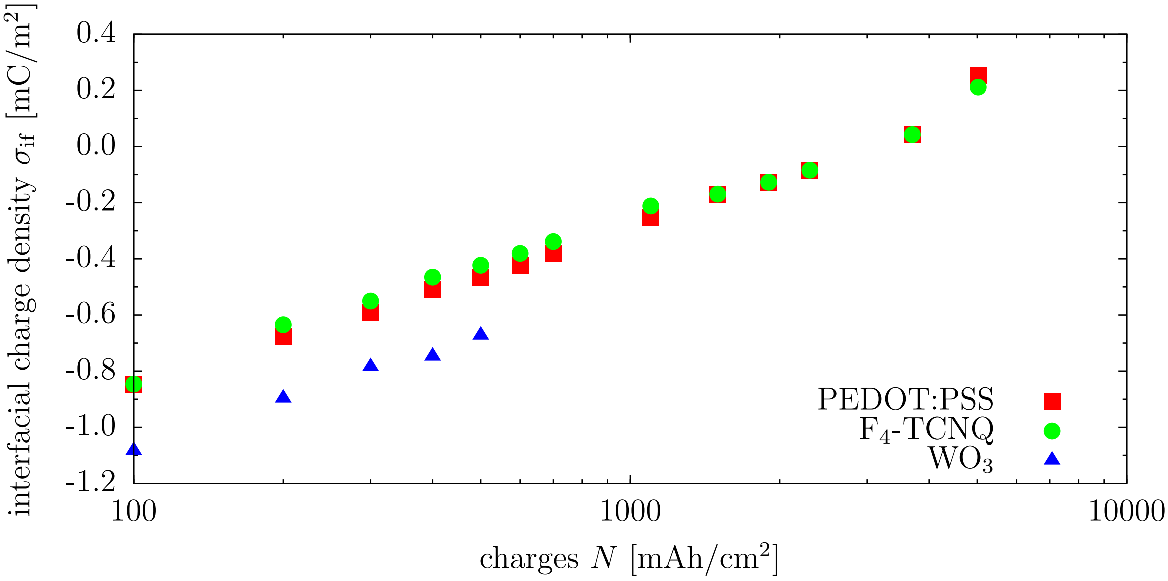

Figure 5.59.: Shift in interfacial charge density σ_{if} (or transition voltage V_t) seems to be proportional to the logarithmic amount of charges N having passed the device.

Also an analysis with the Stern-Volmer relationship could be useful. It is used to describe the fluorescence intensity F of a material in the presence of a quencher Q with different concentrations ($[Q]$):

$$\frac{F_0}{F} = 1 + K_{\mathrm{SV}} \cdot [Q]\,, \tag{5.34}$$

where F_0 is the fluorescence intensity in absence of the quencher, and K_{SV} is the Stern-Volmer constant. For a derivation see, e.g., the book of Lakowicz[18] and for an example the paper by Lüer et al., where oxygen-induced quenching in polythiophene films has been studied[135]. Two processes are possible: dynamic quenching ($K_{\mathrm{SV}} = K_{\mathrm{d}}$, deactivation of the excited fluorophore upon contact with the quencher, hence also called collisional quenching) and static quenching ($K_{\mathrm{SV}} = K_{\mathrm{s}}$, quencher and fluorophore building a non-fluorescent ground state complex[18]). In both cases, a linear relationship between the fluorescence intensity and the quencher concentration is observed, eq. (5.34). Distinguishing both processes is, however, possible due to different temperature dependencies or by using photoluminescence lifetime measurements[18]. For dynamic quenching the ratio of the fluorescence intensities is

$$\frac{F_0}{F} = 1 + K_{\mathrm{d}} \cdot [Q] = 1 + k_{\mathrm{q}} \cdot \tau_0 \cdot [Q] \tag{5.35}$$

which can also be represented by[18]

$$\frac{F_0}{F} = \frac{\tau_0}{\tau}\,, \tag{5.36}$$

where k_{q} is the bimolecular quenching constant, τ_0 is the lifetime of the fluorophore in the absence and τ the lifetime in presence of the quenchers. In the case of static quenching

$$\frac{\tau_0}{\tau} = 1\,, \tag{5.37}$$

hence a distinction is possible by photoluminescence lifetime measurements.

If both processes, dynamic and static, occur simultaneously, the Stern-Volmer equation is modified:

$$\frac{F_0}{F} = \left(1 + K_{\mathrm{d}} \cdot [Q]\right) \cdot \left(1 + K_{\mathrm{s}} \cdot [Q]\right)\,, \tag{5.38}$$

which can be linearized to

$$\frac{\frac{F_0}{F} - 1}{[Q]} = \left(K_{\mathrm{d}} + K_{\mathrm{s}}\right) + \left(K_{\mathrm{d}} \cdot K_{\mathrm{s}}\right) \cdot [Q]\,. \tag{5.39}$$

In the case of degrading OLEDs, the quencher concentration could be the amount of non-radiative recombination centers, i.e., the accumulated positive charge density σ_{acc}. Both representations of the Stern-Volmer relation are plotted in fig. 5.61 and 5.62, respectively. In both cases, the interpretation of the data is not definite, as the expected linear trend is not observed. However, for the devices prepared in Augsburg, a linear trend might be possible if only the data points with $j = 10\,\mathrm{mA/cm^2}$ are

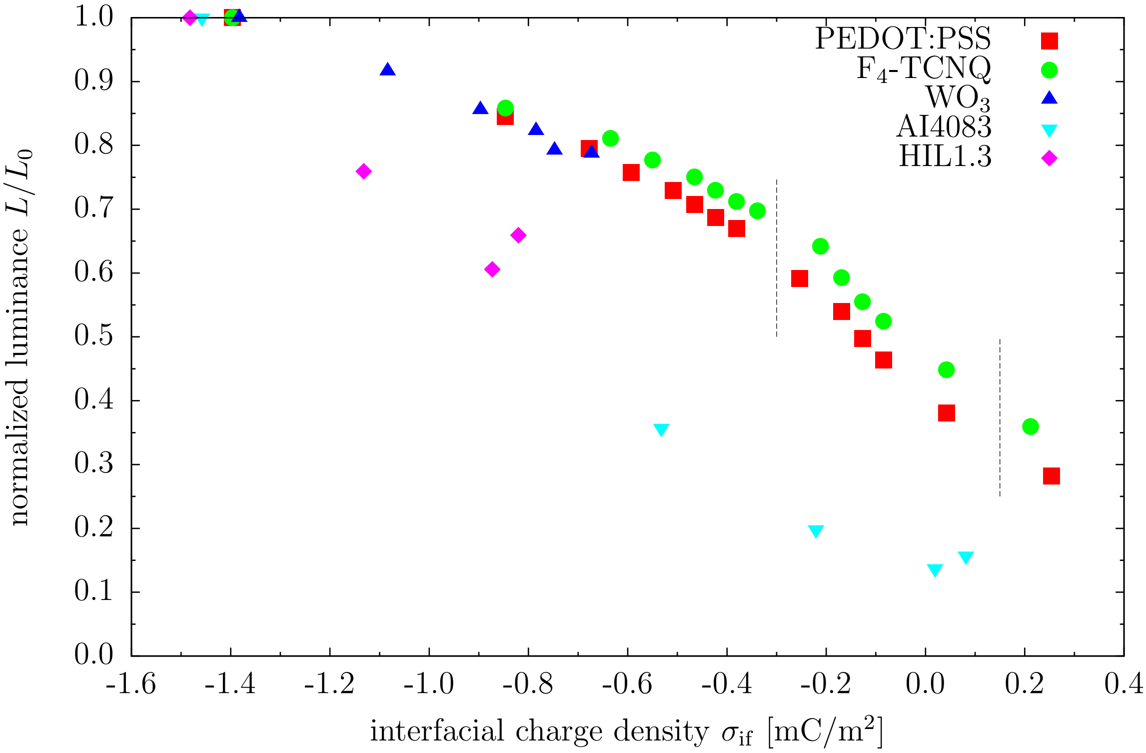

Figure 5.60.: Loss in luminance and correlation with the interfacial charge density σ_{if}. Please note that the devices prepared in Augsburg are aged with different current densities (10, 20, and 60 mA/cm^2 indicated by the dashed lines). For the devices from H.C. Starck Clevios (AI4083 and HIL1.3) 48 mA/cm^2 have been used.

analyzed. But then the question is, why there is a change when the current density is changing. Again, more data would be highly beneficial for further analysis, also supported by additional photoluminescence lifetime measurements of pristine and aged OLEDs.

Still the question remains where the accumulated positive charges originate from. A natural explanation was given in a series of papers by Aziz and Popovic[41,124,125]. They could show that degradation of NPB/Alq_3 heterolayer OLEDs is mainly caused by instability of cationic $Alq_3^{+\cdot}$, being formed by excess holes injected into the ETL. On the other hand, a recent study by Kondakov indicates that chemical degradation of the hole transporting arylamine moiety could be the cause[136]. The degradation products are considered as irreversible hole traps leading to an accumulation of positive fixed charge at the HTL/ETL interface. This could also be the cause of the observed shift in relaxation frequency during degradation.

Nevertheless, there is the question why the devices with different HIL but same HTL behave differently. Following the unstable cationic Alq_3 model suggested by Aziz and Popovic[124], one concludes that devices with good hole injection and transport would result in faster degrading OLEDs (if the holes are injected into Alq_3). However, this is not very likely, as, e.g., the $j - V$ characteristics of the devices prepared by H.C. Starck Clevios (fig. 5.51) are the same for pristine devices, but devices with HIL1.3

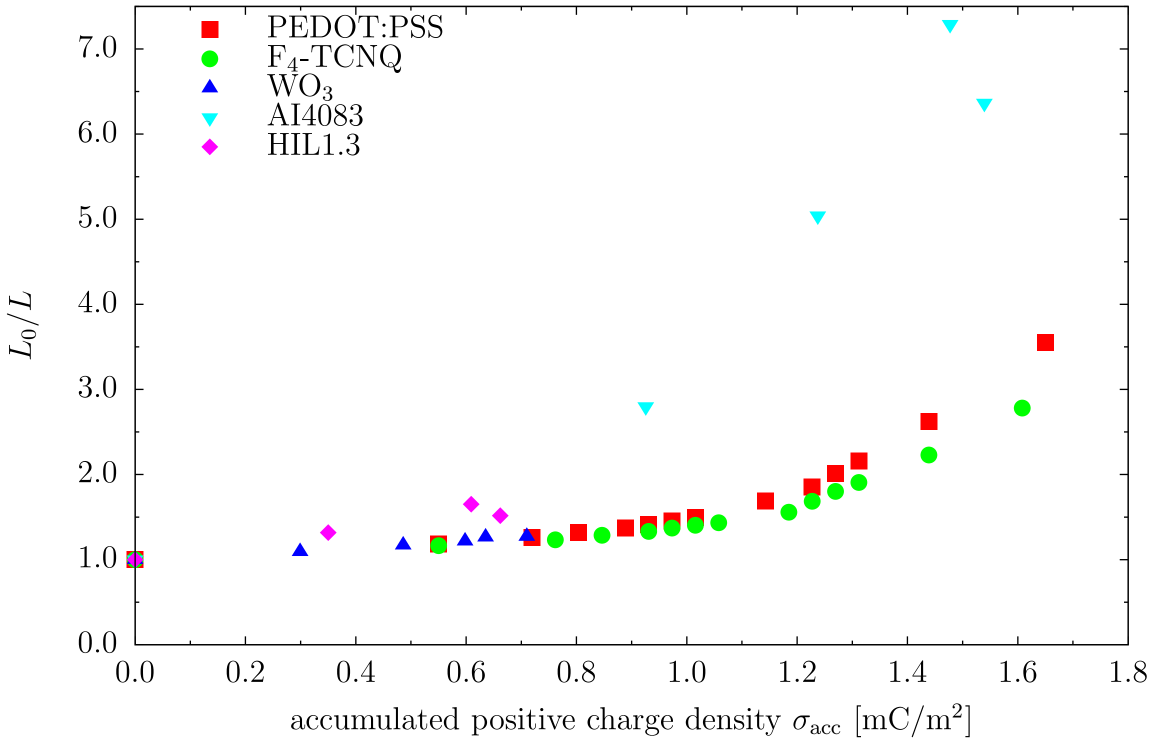

Figure 5.61.: Stern-Volmer plot for dynamic or static quenching to test eq. (5.34).

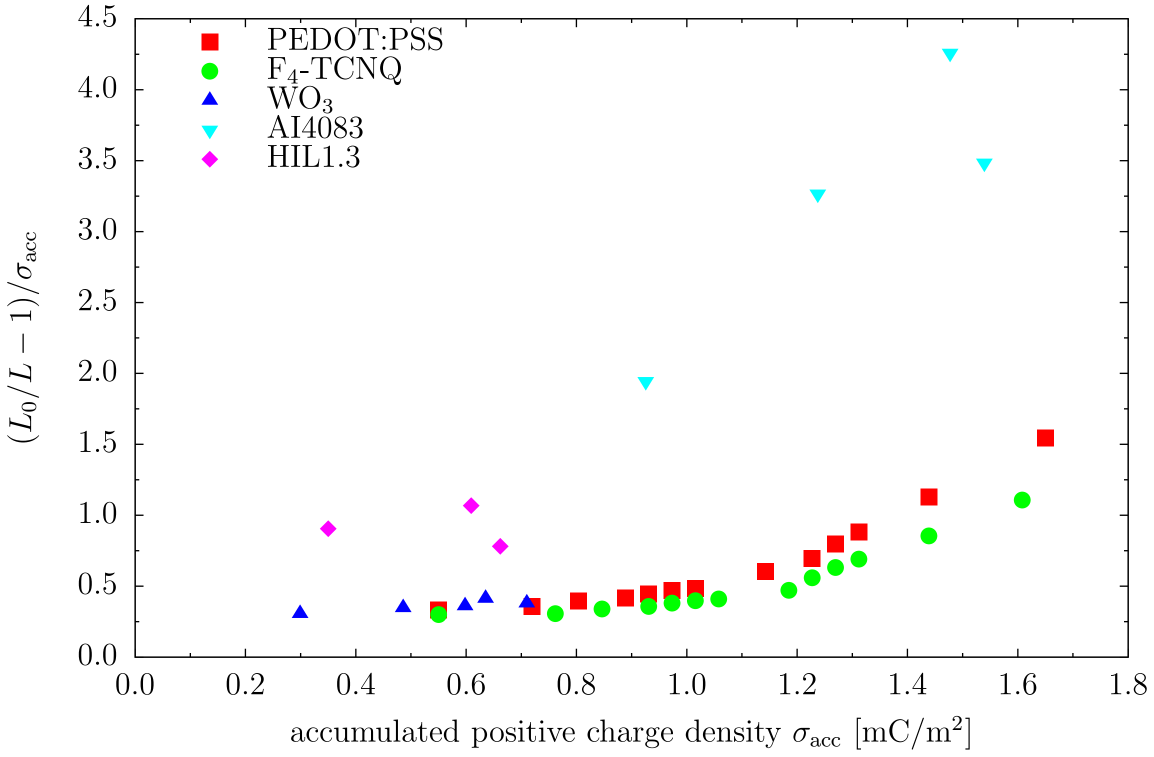

Figure 5.62.: Stern-Volmer plot for dynamic and static quenching to test eq. (5.39).

are more stable than devices with AI4083. Direct evidence comes from the $C - f$ measurements shown in fig. 5.52 where identical relaxation frequencies, i.e., identical resistance for the transport of holes to the HTL/ETL interface are observed. Moreover, upon degradation the relaxation frequency for the device with HIL1.3 decreases much slower as compared to AI4083 as HIL. From that point of view, one has to conclude that devices with HIL1.3 have better hole injection and transport over the entire range of the device's lifetime, so the amount of holes flowing through the device is obviously not the crucial point. Since both devices in the pristine state show identical hole injection properties and identical HTL/ETL interface conditions, one has to consider another possibility having its origin in the HILs themselves.

The different rate of degradation can be explained if one assumes that the HILs induce different speed for the formation of positively charged non-radiative recombination centers. Probably not by directly emitting some charged species, but by delivering some kind of degradation catalyst at a different rate or amount. As the polymeric HILs (all variants of PEDOT:PSS) are spincast from water containing dispersions a possible candidate could be water which is known to cause instability of Alq_3[123]. However, since these HILs are dried on a hot plate, they should not contain large quantities of water in their bulk. Additionally, in experiments with various drying conditions no significant differences between devices with different HILs were found[137]. Another parameter might be the acidity of the HIL being relevant for interface dipole formation and charge injection to the HTL. It does, however, not explain the difference between AI4083 and HIL1.3 as the acidity is very similar ($\mathrm{pH} = 1.6 - 1.8$) for both materials. In contrast to that, the properties of the layer surface were found to be significantly different for both HILs. Results from contact angle measurements show that HIL1.3 is less hydrophilic (contact angle with toluene 48°) as compared to AI4083, where the contact angle is almost zero[137]. Although it needs to be verified that more hydrophobic HILs will lead to more stable HIL/HTL interfaces, in general it is reasonable to explain the observed phenomenon of reduced voltage increase and luminance drop in devices with HIL1.3 in contrast to AI4083 by this mechanism. This argument could also explain improved lifetimes reported in literature for other hydrophobic HILs. Hung et al. and Tang et al. used thin CF_x films from CHF_3 plasma to enhance hole injection[138,139]. These films showed good chemical stability and lead to enhanced operational stability in NPB/Alq_3 devices. Gao et al. used an evaporable fluoro-molecule which also showed improved device performance and longer lifetimes[140]. Therefore, it seems that the hydrophobic character of the hole injection layers plays an important role in the degradation mechanism. However, one could also argue that such an interlayer impedes indium diffusion from ITO to the HTL/ETL interface. This seems very unlikely, as the films used by Hung, Tang and Gao have thicknesses of only a few nanometers and might even be porous[138–140]. Other observations also contradict the model of indium diffusion, thus it is no longer considered to play a dominant role in OLED degradation[141].

It is also worth mentioning that impedance spectroscopy also gives a hint towards changes of electron injection during degradation by a shift of the peak voltage in the $C - V$ curves. Devices with AI4083 show a shift of both V_t and V_peak already in the early stage of degradation, whereas those with HIL1.3 have V_peak remaining unaffected in the beginning. The devices prepared in Augsburg confirm this notion: the use of different HILs also affects the electron injection under electrical aging of the devices. There is currently very little quantitative work[102], but, in the future, IS could also prove to be a very useful technique to study recombination dynamics in OLEDs and how this is affected by device degradation. Some preliminary data is shown in the theses of Wei Ren[112] and Kerstin Steidle[114], respectively; however, more systematic work is necessary to draw conclusions.

6. Summary

From a physicist's point of view, two major topics, the external quantum efficiency and the device lifetime, need improvement before OLEDs are being competitive with established and new lighting techniques (e.g., fluorescent tubes and LEDs, respectively) and, thus, widely being featured in lighting applications. Both topics have been investigated in this thesis using optical device simulation and impedance spectroscopy for electrical characterization, respectively.

It has been shown that the dipole model, where the emission of light originates from electrical dipoles embedded in the OLED stack, and its implementation in the MAPLE program "PDCalc", originally written by Nils Reinke during his PhD thesis[68], is suited for optical simulations of OLEDs by comparing its results to experimental data and other calculations from different authors.

Systematic variation of layer thicknesses of a reference OLED has provided insight to the distribution of light emitted into different channels, i.e., light emitted directly from the OLED, light trapped inside the substrate, light waveguided in the OLED stack, excitation of surface plasmon polaritons at metallic interfaces, and intrinsic, non-radiative loss. As a result, some generalized design rules for high external quantum efficiencies can be established. Due to the reflected electric field and its influence on the decay rate of the radiative dipoles, the position of the dipole layer, i.e., the emission zone, is crucial for the external quantum efficiency: e.g., the dipoles should not be placed too close to metallic interfaces, as then plasmons are excited, which do not contribute to emitted light. Moreover, it has been shown that the optimal layer thicknesses also depend on the quantum efficiency q of the emitter material. As a consequence, it has been realized that for high-q materials it can be beneficial to move the emission layer very far away from metallic electrodes, e.g., several 100 nm, into a second, even higher, maximum for the external quantum efficiency. This, however, requires electrically doped transporting layers, in order to ensure the electrical operability of the device. Due to the influence of the quantum efficiency on the optimal layer thicknesses, q has to be taken into account in the simulation of the device. It can not be applied afterward by simply multiplying q with the simulation results for $q = 1$, which usually is assumed in literature.

In the case that q is undetermined, two methods have been presented (using external quantum efficiency measurements, or photoluminescence or pulsed electroluminescence lifetime measurements) to extract the value from actual OLED stacks. As a result of this analysis, it has been concluded that phosphorescent emitter materials do not necessarily have a quantum efficiency of $q = 1$, which usually is assumed in literature. Another conclusion one unfortunately must draw from the simulation results is that even under optimal prerequisites, i.e., singlet/triplet ratio $\eta_{s/t}$, charge balance factor γ, and quantum efficiency q all equal to 1, only about 40 % of the generated light can be coupled out of ordinary glass substrates. Hence, improved light outcoupling techniques (e.g., substrates with high refractive index or emission layers with adjusted dipole orientation) have to be investigated and considered in the future to achieve even higher external quantum efficiencies.

Impedance spectroscopy has turned out to be a useful tool for electrical characterization of OLEDs as it also yields information under reverse bias condition, which usually is not accessible, e.g., in current density – voltage characteristics. Two kinds of impedance spectroscopy measurements and data representations have been used in this thesis, capacitance – frequency ($C - f$) at different applied bias voltages and capacitance – voltage ($C - V$) at different applied frequencies.

The hole injection and hole transport properties can be investigated using $C - f$ measurements. For example, temperature dependent measurements presented in this thesis of devices using different hole injection layers (HILs) yield the bulk transport properties of the hole transporting layer (HTL), however, more experimental data (i.e., using several other HILs and HTLs) is needed to confirm this notion. When the devices have been aged, changes in the $C - f$ curves show a deterioration of hole injection and/or hole transport. As these changes occur on different timescales, a critical influence of the HIL has been found. This is probably due to the HIL providing some degradation catalyst, e.g., water or other contaminants.

In heterolayer devices using TPD or NPB as HTL and Alq_3 as electron transporting layer, the existence of a negative interfacial charge density has been confirmed using $C - V$ measurements. Its origin is partial dipole moment ordering of Alq_3 during evaporation. Upon degradation of the OLEDs, it has been shown that this charge gets more positive. Simultaneously, the luminance is decreasing with aging time and current flow. The loss in luminance can be correlated to the accumulated positive charges, which are proposed to act as non-radiative quenching centers. However, further investigation is necessary as the observed behavior and its origin (e.g., differences due to different applied current densities during artificial aging) is not yet fully explainable. Understanding the involved degradation processes will eventually lead to longer-living OLEDs for lighting applications and a bright future.

A. Appendix

A.1. Abbreviations

A.1.1. Chemicals

abbreviation	**chemical name**
α-NPD	α-naphthylphenylbiphenyl
Alq_3	tris-(8-hydroxyquinoline) aluminum
BPhen	4,7-diphenyl-1,10-phenanthroline
C545T	10-(2-benzothiazolyl)-2,3,6,7-tetrahydro-1,1,7,7-tetramethyl-1H,5H,11H-(1)-benzopyropyrano(6,7-8-i,j)quinolizin-11-one
F_4-TCNQ	tetrafluorotetracyano-quinodimethane
HMTPD	4,4'-bis[N,N'-(3-tolyl)amino]-3,3'-dimethyl biphenyl
$Ir(ppy)_3$	tris(2-phenylpyridine) iridium
ITO	indium tin oxide
m-MTDATA	4,4',4"-tris(3-methylphenylphenylamino)triphenylamine
NPB	N,N'-di(naphtalene-1-yl)-N,N'-diphenyl-benzidine
PEDOT	poly(3,4)-ethylendioxythiophene
PMMA	poly(methyl methacrylate)
PPV	poly(*p*-phenylene vinylene)
$(ppy)_2Ir(acac)$	bis(2-phenylpyridine) iridium(III) acetylacetonate
PSS	poly(styrene sulfonate)
R6G	rhodamine 6G
TAZ	3-phenyl-4-(1'-naphthyl)-5-phenyl-1,2,4-triazole
TCTA	4,4',4"-tris(N-carbazolyl)-triphenylamine
TPBi	1,3,5-tris(phenyl-2-benzimidazolyl)-benzene
TPD	N,N'-diphenyl-N,N'-bis(3-methylphenyl)-1,1'-biphenyl-4,4-diamine

A.1.2. Miscellaneous

abbreviation	meaning
DCM	displacement current method
DUT	device under test
EBL	electron blocking layer
EIL	electron injection layer
EL	electroluminescence
EML	emission layer
ETL	electron transporting layer
EQE	external quantum efficiency
HBL	hole blocking layer
HIL	hole injection layer
HTL	hole transporting layer
IS	impedance spectroscopy
OFET	organic field effect transitor
OLED	organic light emitting diode
OPVC	organic photovoltaic cell
PL	photoluminescence
QE	quantum efficiency
SPP	surface plasmon polariton
TE	transverse electric or s-polarized
TM	transverse magnetic or p-polarized

A.2. Excitation of surface plasmon polaritons using the Kretschmann configuration

It is possible to excite surface plasmon polaritons by using the Kretschmann configuration where light incises from a medium with refractive index $n_{\mathrm{i}} > 1$, e.g., glass, onto a thin metal film, see fig. A.1. An evanescent wave penetrates this thin metal film and excites plasmons on the outer side of the film facing air. As a result the light line is shifted to higher k_{x} values as its dispersion relation is now

$$\omega = \frac{c}{n_{\mathrm{i}}} \cdot \frac{k}{\sin\theta_{\mathrm{i}}} = \frac{c}{n_{\mathrm{i}}} \cdot k_{\mathrm{x}} \,. \tag{A.1}$$

At the intersection with the dispersion relation of the plasmonic mode energy and impulse conservation is now fulfilled (fig. A.2): the excitation of the surface plasmon is possible. For light with a given frequency ω (wavelength λ) incident from a medium with refractive index n_{i} there exists one angle of incidence θ_{i} where energy and impulse conservation can be fulfilled, see fig. A.2 and fig. A.3, respectively.

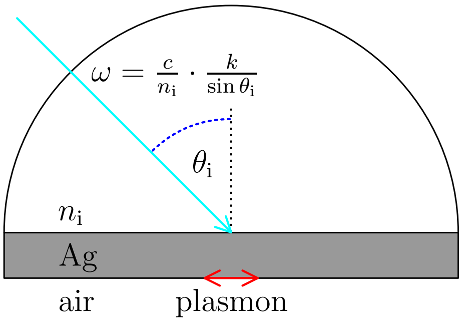

Figure A.1.: Kretschmann configuration for excitation of surface plasmons.

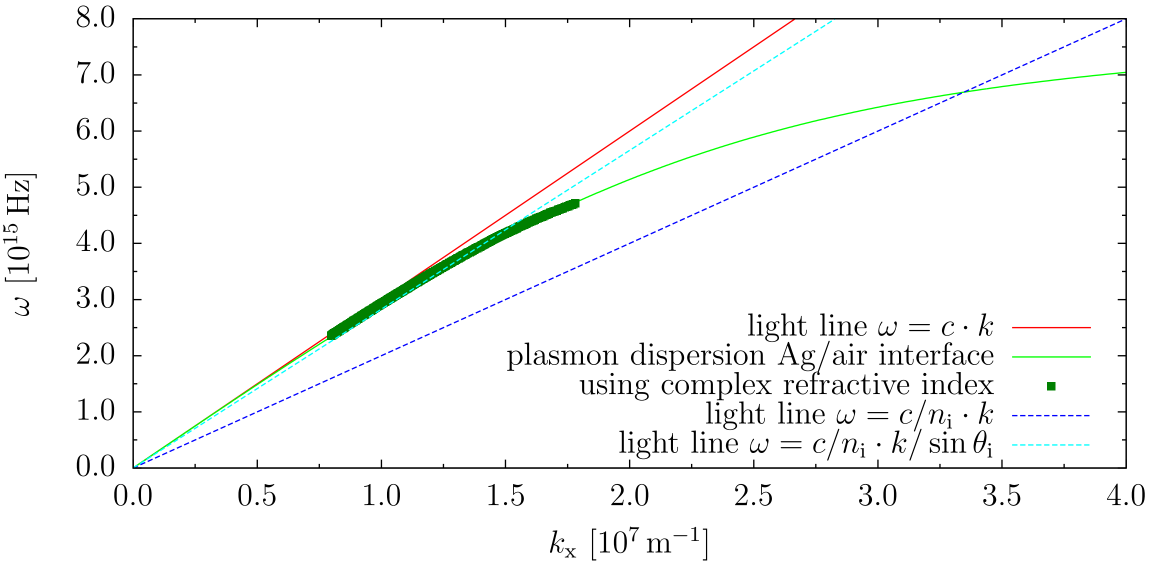

Figure A.2.: Dispersion relations for the Kretschmann configuration of a plasmon at a Ag/air interface and the shifted light lines due to the refractive index $n_i = 1.5$ of the incident material. Calculation for an angle of incidence $\theta_i = 90°$ (blue dashed line) and $\theta_i = 45°$ (cyan dashed line).

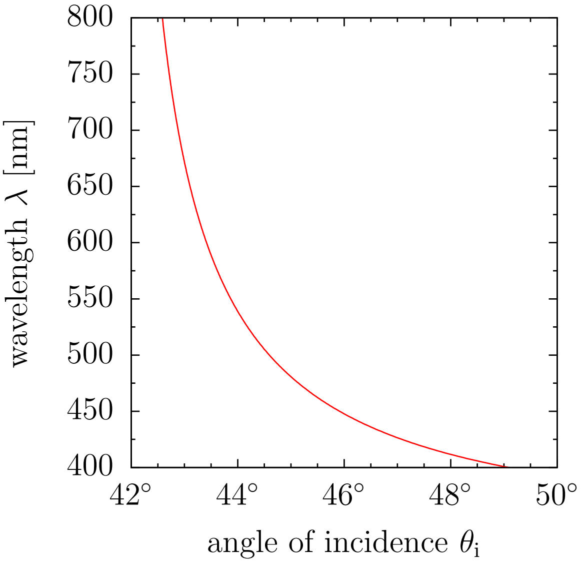

Figure A.3.: Plasmon excitation at a Ag/air interface through glass (Kretschmann configuration, fig. A.1) as incident medium, $n_i = 1.5$, requires a specific wavelength λ for a given angle of incidence θ_i or vice versa.

A.3. Refractive indices

Refractive indices used for the reference OLED and other work from Augsburg

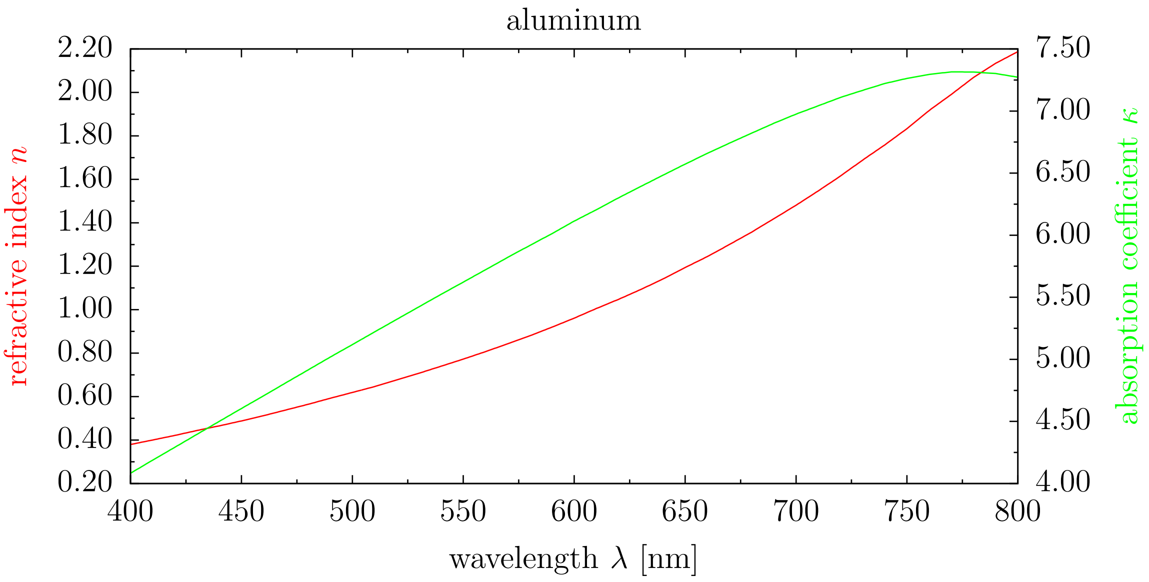

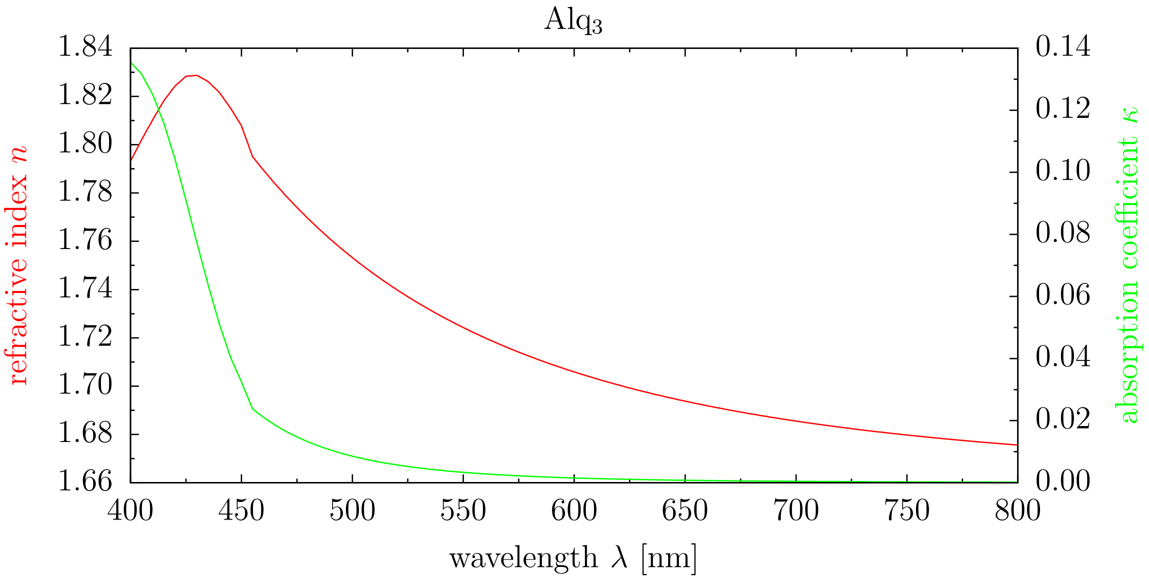

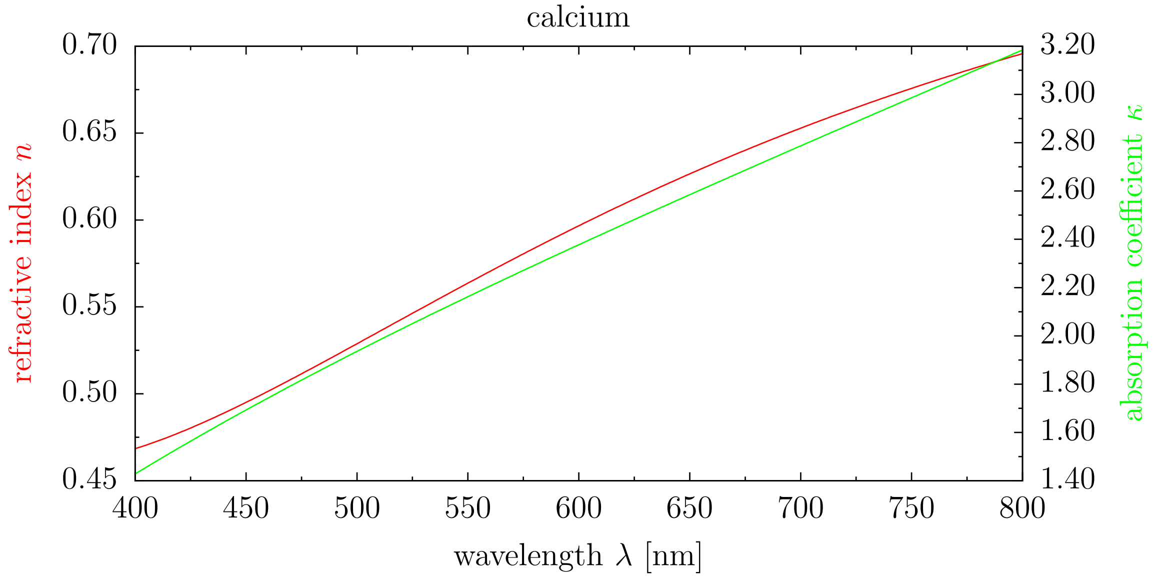
calcium
refractive index n
absorption coefficient κ
0.70
0.65
0.60
0.55
0.50
0.45
3.20
3.00
2.80
2.60
2.40
2.20
2.00
1.80
1.60
1.40
400
450
500
550
600
650
700
750
800
wavelength λ [nm]

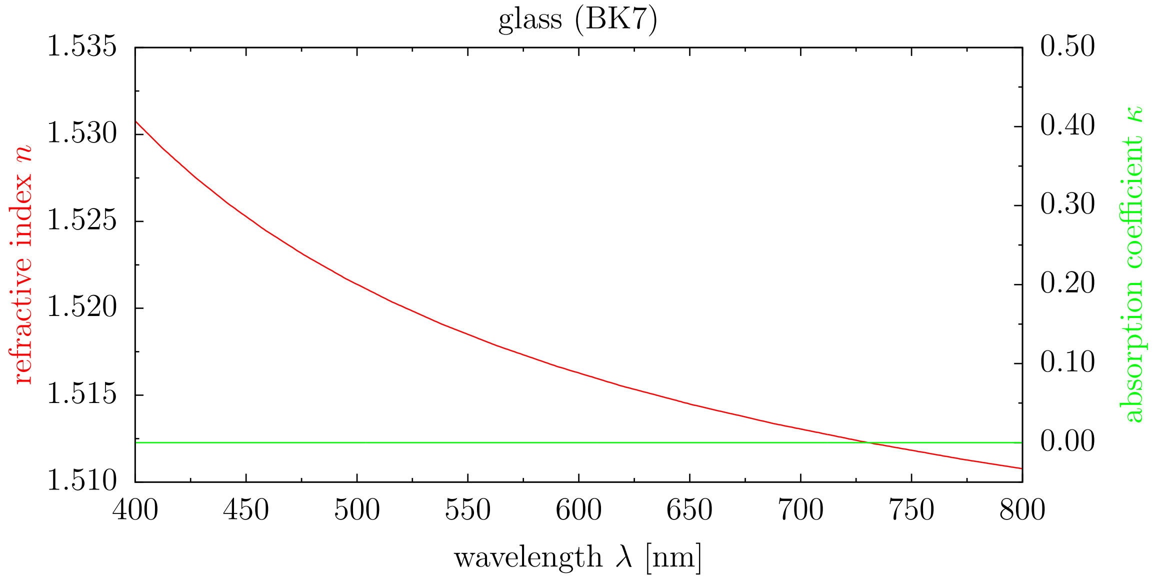
glass (BK7)
refractive index n
absorption coefficient κ
1.535
1.530
1.525
1.520
1.515
1.510
0.50
0.40
0.30
0.20
0.10
0.00
400
450
500
550
600
650
700
750
800
wavelength λ [nm]

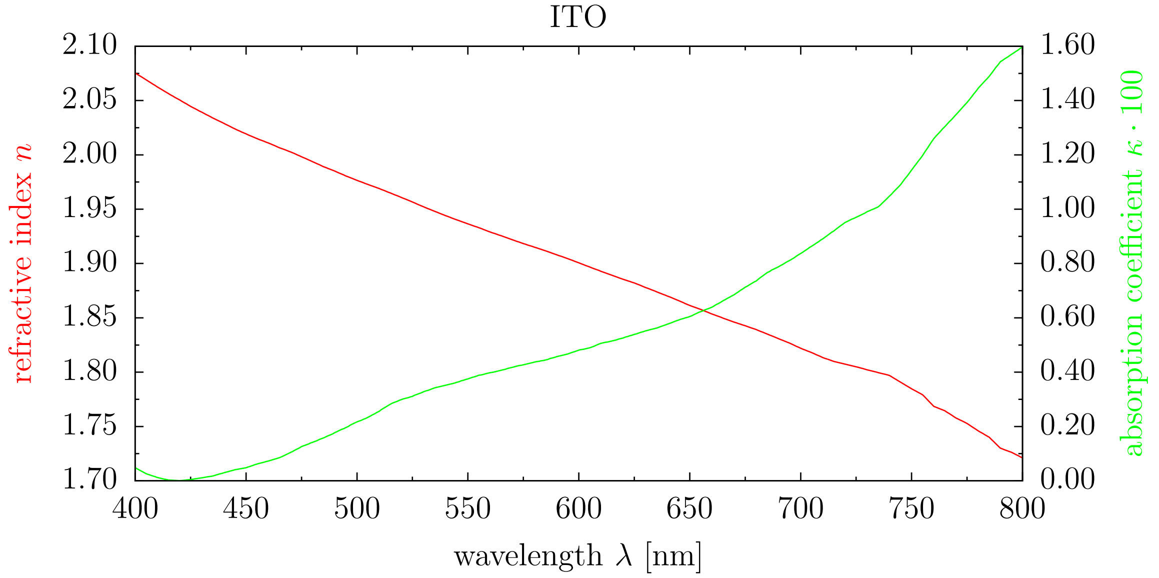
ITO
refractive index n
absorption coefficient $\kappa \cdot 100$
2.10
2.05
2.00
1.95
1.90
1.85
1.80
1.75
1.70
1.60
1.40
1.20
1.00
0.80
0.60
0.40
0.20
0.00
400
450
500
550
600
650
700
750
800
wavelength λ [nm]

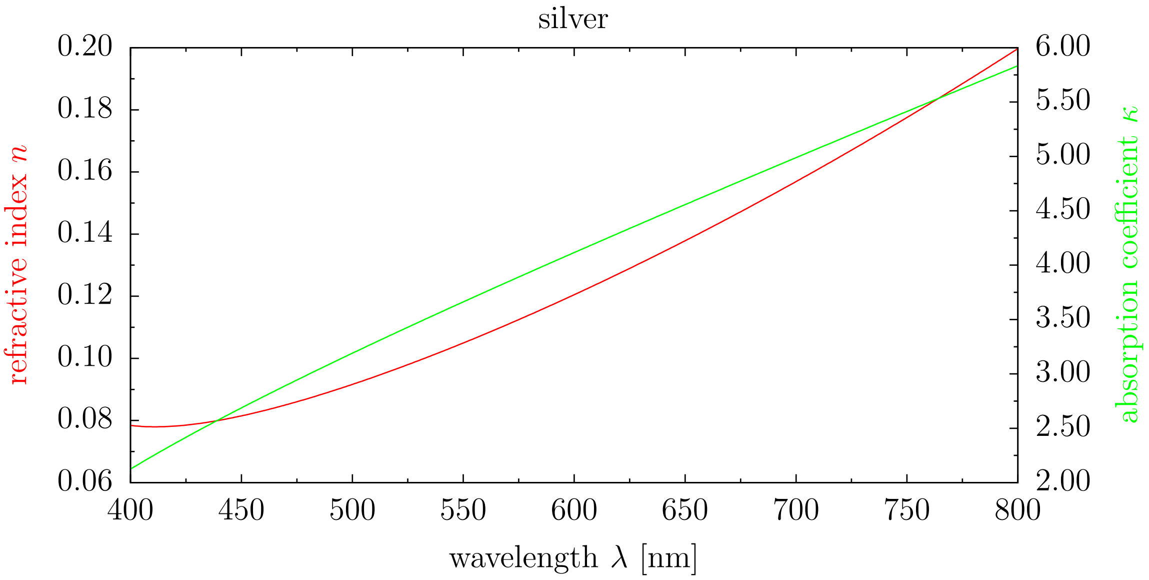
silver
refractive index n
absorption coefficient κ
0.20
0.18
0.16
0.14
0.12
0.10
0.08
0.06
6.00
5.50
5.00
4.50
4.00
3.50
3.00
2.50
2.00
400
450
500
550
600
650
700
750
800
wavelength λ [nm]

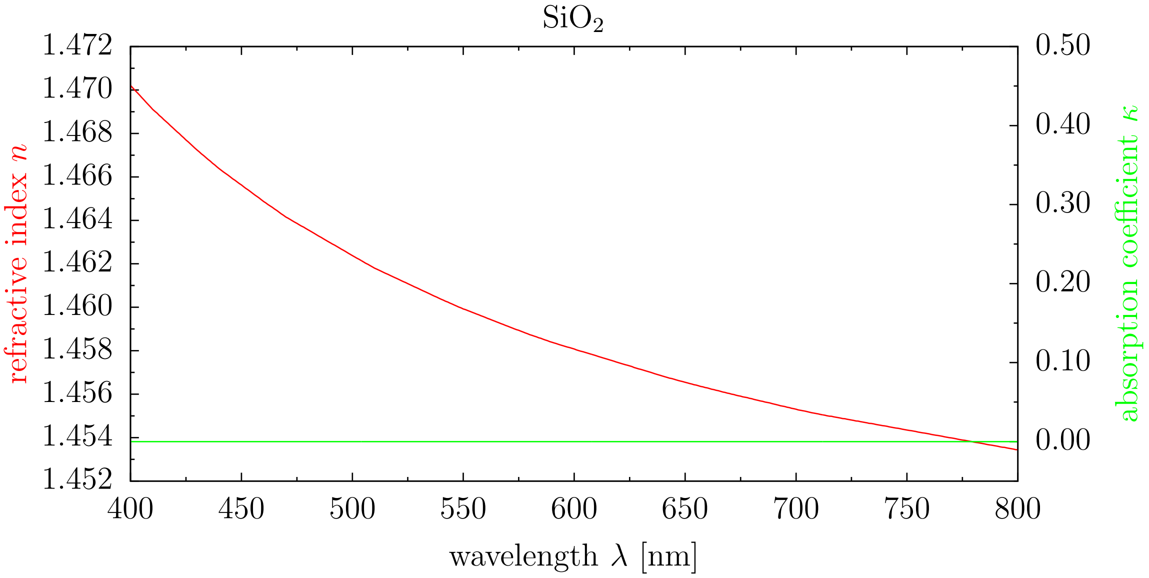
SiO$_2$
refractive index n
absorption coefficient κ
1.472
1.470
1.468
1.466
1.464
1.462
1.460
1.458
1.456
1.454
1.452
0.50
0.40
0.30
0.20
0.10
0.00
400
450
500
550
600
650
700
750
800
wavelength λ [nm]

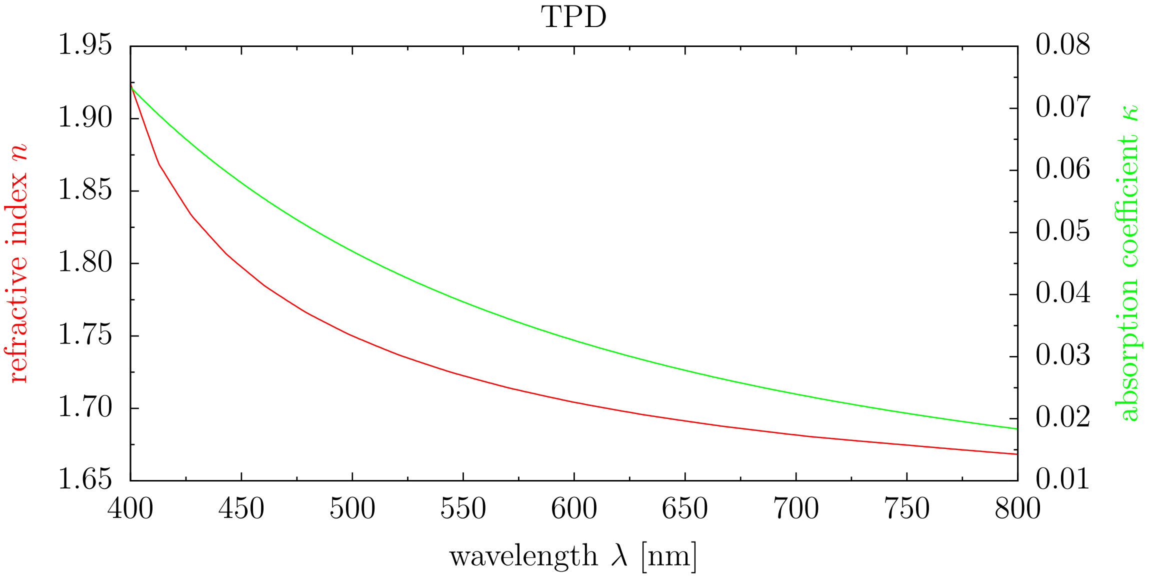
TPD
refractive index n
absorption coefficient κ
1.95
1.90
1.85
1.80
1.75
1.70
1.65
0.08
0.07
0.06
0.05
0.04
0.03
0.02
0.01
400
450
500
550
600
650
700
750
800
wavelength λ [nm]

Refractive indices used for the stack of Lin et al.[72]

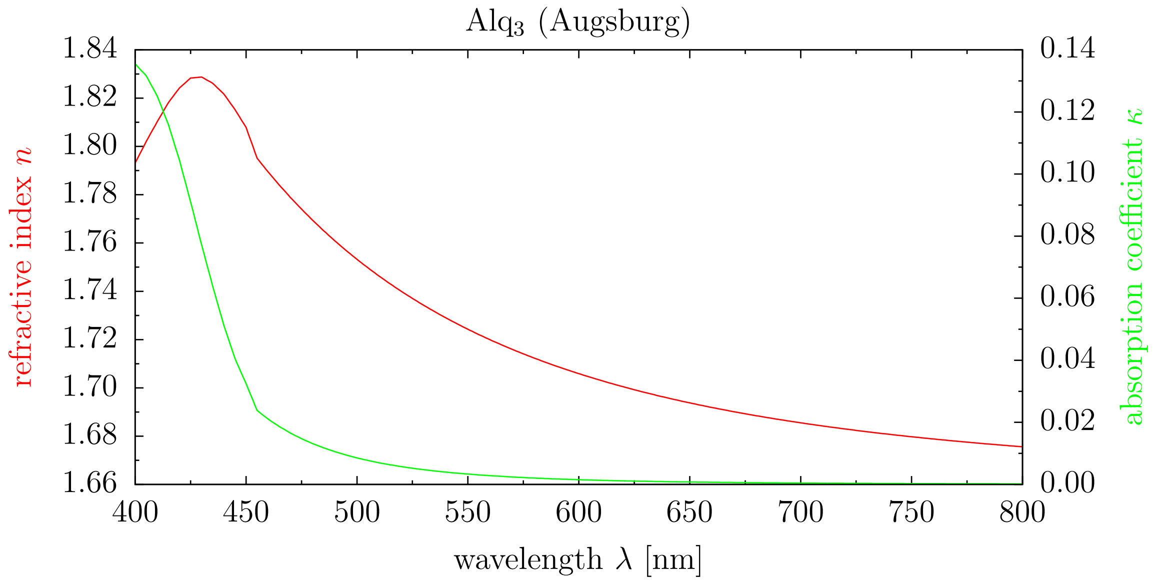

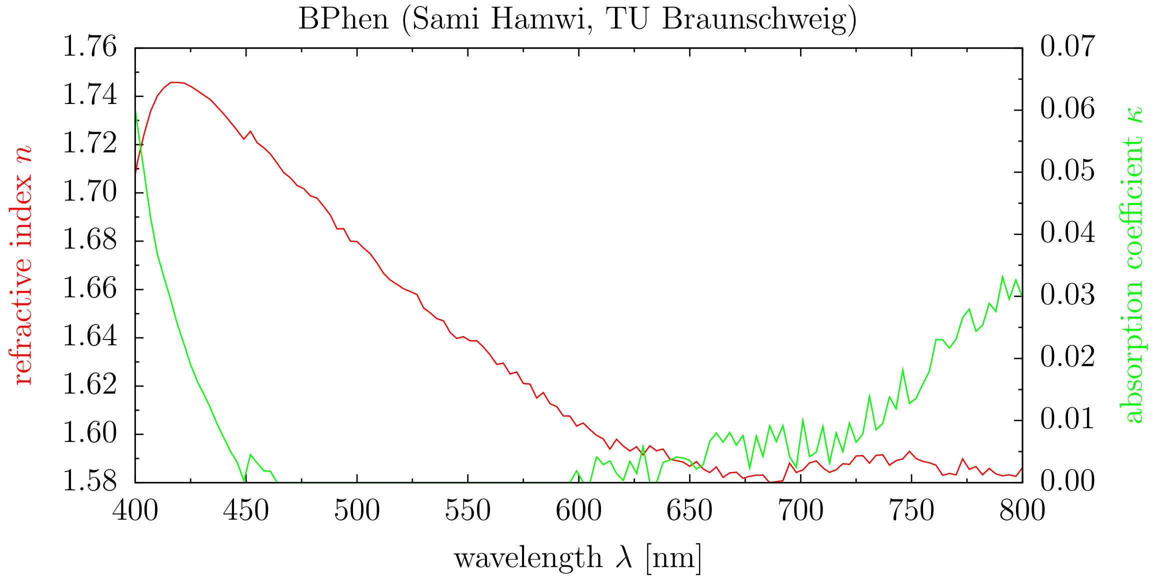

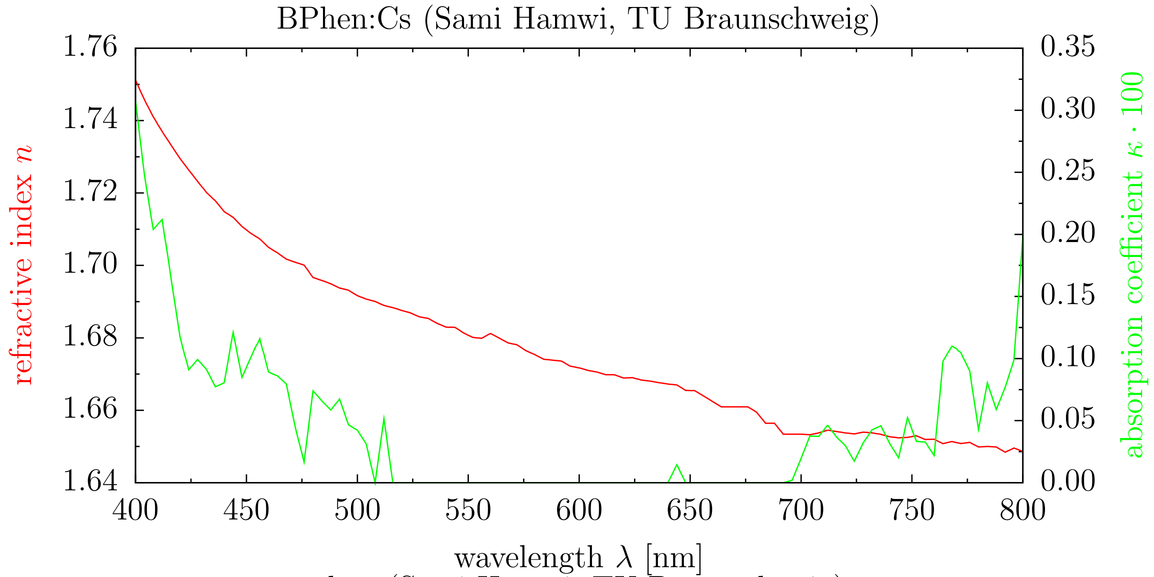
BPhen:Cs (Sami Hamwi, TU Braunschweig)
refractive index n
1.76
1.74
1.72
1.70
1.68
1.66
1.64
absorption coefficient $\kappa \cdot 100$
0.35
0.30
0.25
0.20
0.15
0.10
0.05
0.00
400
450
500
550
600
650
700
750
800
wavelength λ [nm]

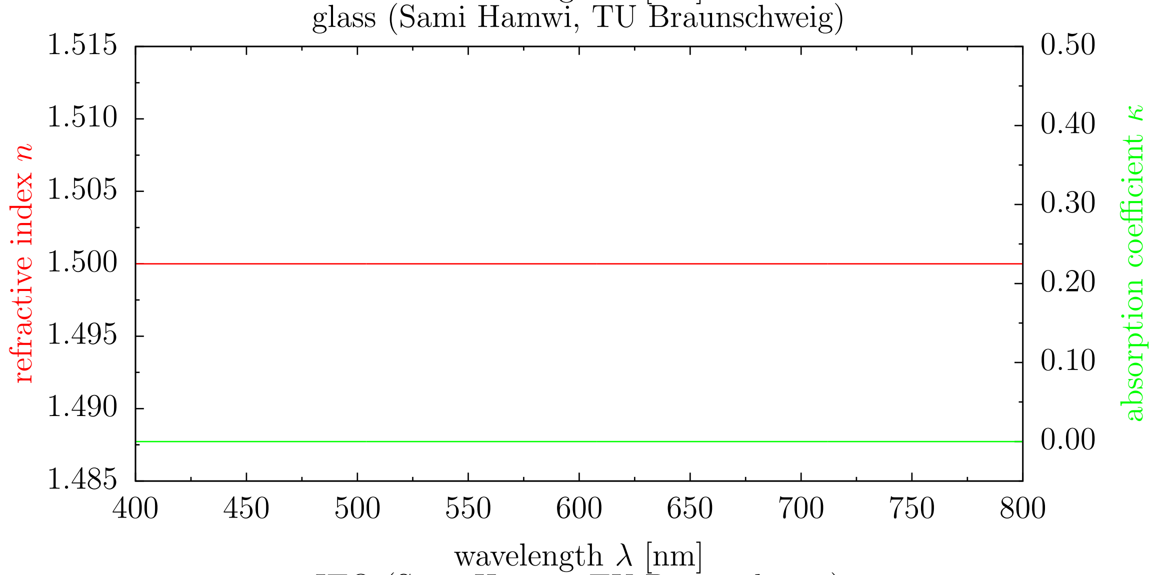
glass (Sami Hamwi, TU Braunschweig)
refractive index n
1.515
1.510
1.505
1.500
1.495
1.490
1.485
absorption coefficient κ
0.50
0.40
0.30
0.20
0.10
0.00
400
450
500
550
600
650
700
750
800
wavelength λ [nm]

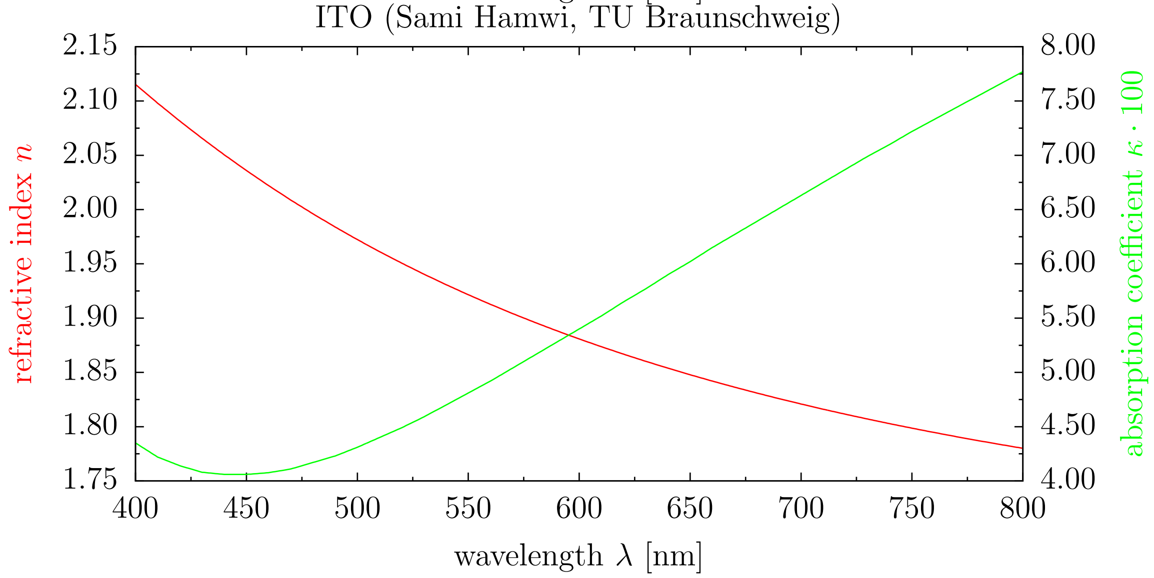
ITO (Sami Hamwi, TU Braunschweig)
refractive index n
2.15
2.10
2.05
2.00
1.95
1.90
1.85
1.80
1.75
absorption coefficient $\kappa \cdot 100$
8.00
7.50
7.00
6.50
6.00
5.50
5.00
4.50
4.00
400
450
500
550
600
650
700
750
800
wavelength λ [nm]

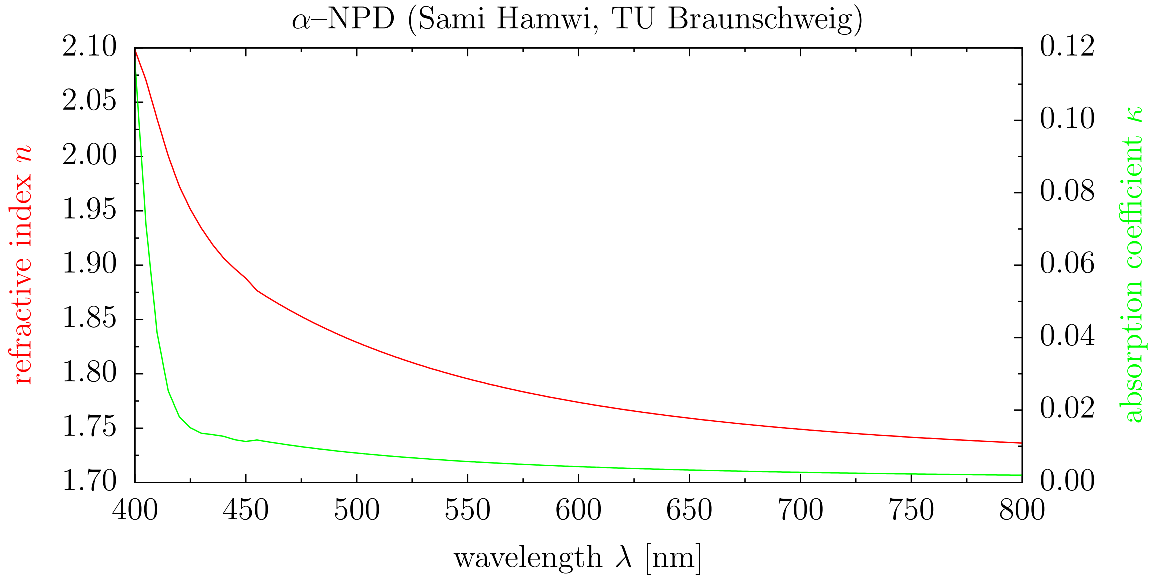
α–NPD (Sami Hamwi, TU Braunschweig)
refractive index n
absorption coefficient κ
wavelength λ [nm]
2.10
2.05
2.00
1.95
1.90
1.85
1.80
1.75
1.70
0.12
0.10
0.08
0.06
0.04
0.02
0.00
400
450
500
550
600
650
700
750
800

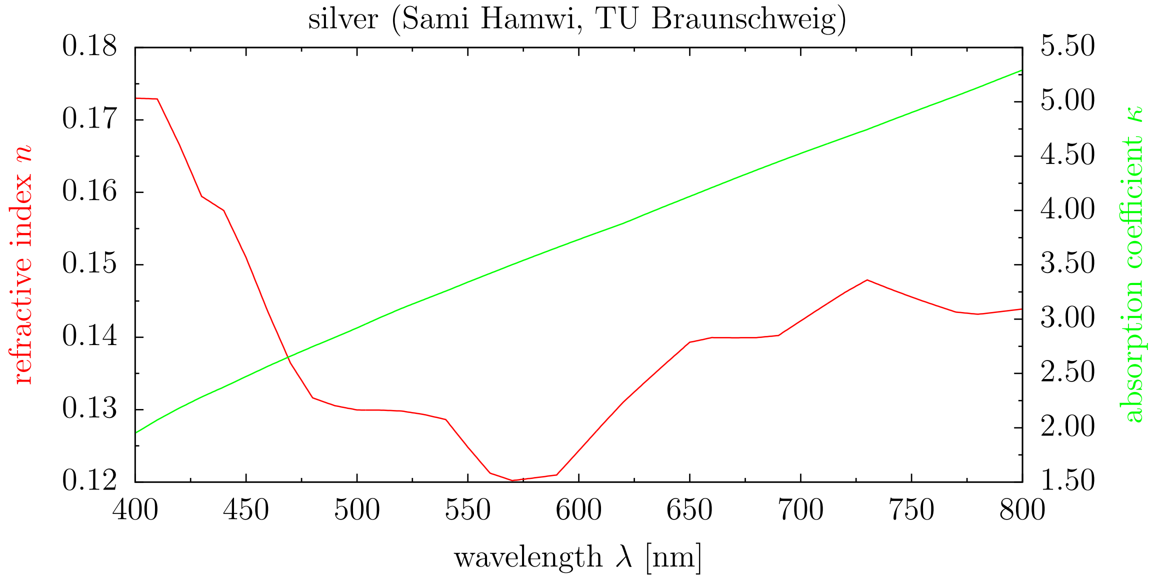
silver (Sami Hamwi, TU Braunschweig)
refractive index n
absorption coefficient κ
wavelength λ [nm]
0.18
0.17
0.16
0.15
0.14
0.13
0.12
5.50
5.00
4.50
4.00
3.50
3.00
2.50
2.00
1.50
400
450
500
550
600
650
700
750
800

Refractive indices used for the stack of Meyer et al.[89]

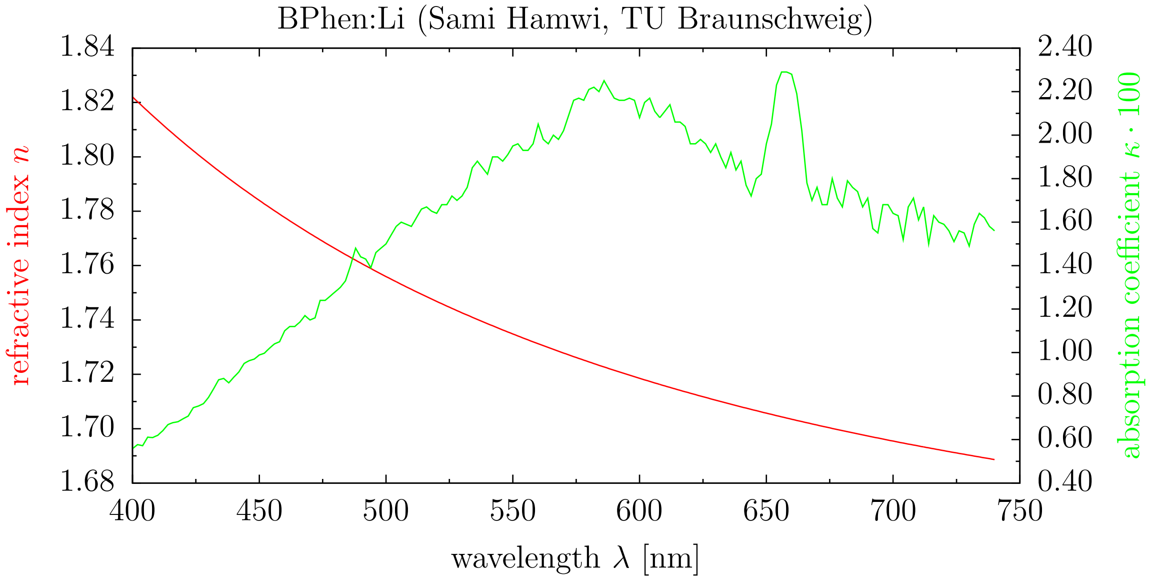

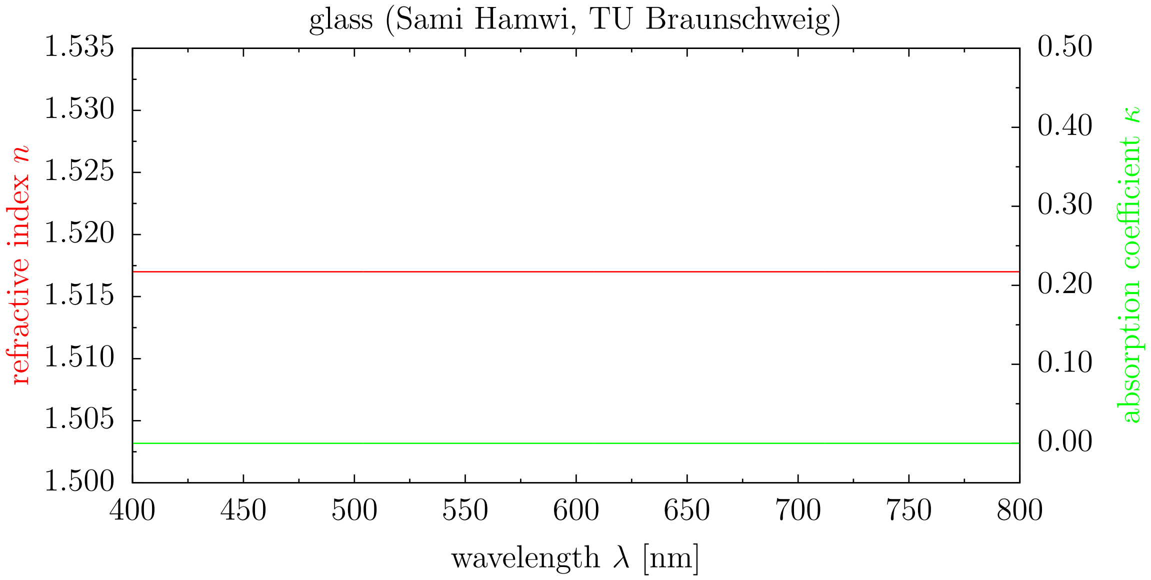

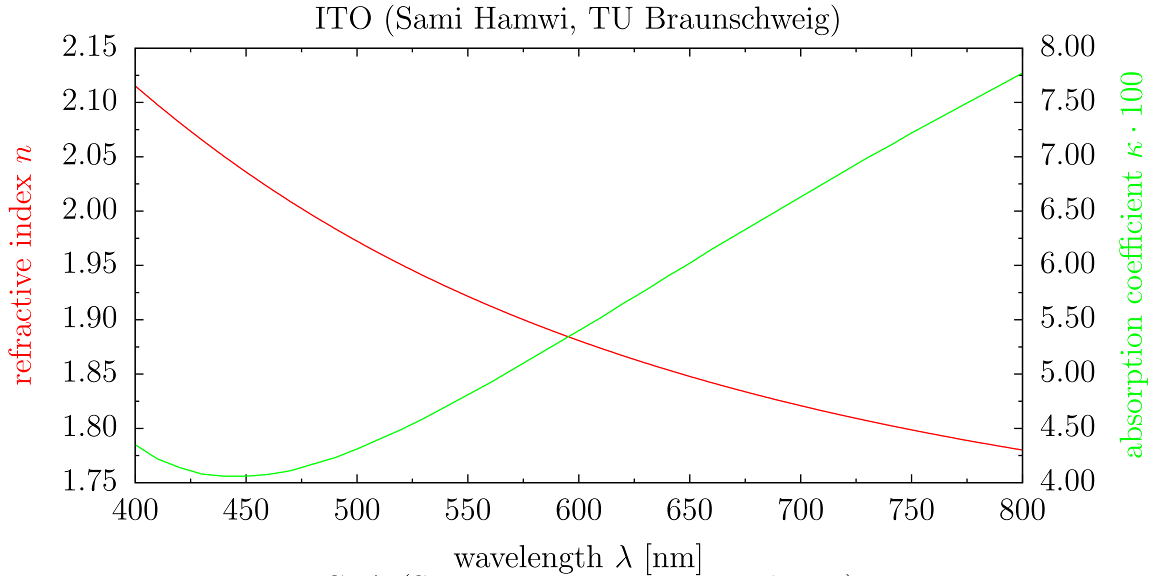
ITO (Sami Hamwi, TU Braunschweig)

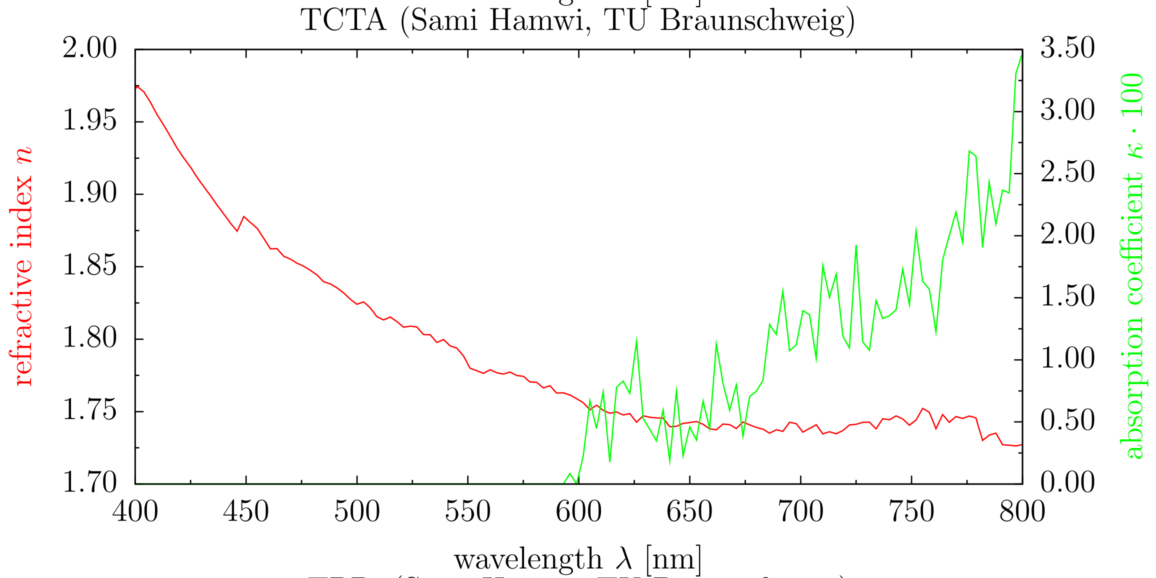
TCTA (Sami Hamwi, TU Braunschweig)

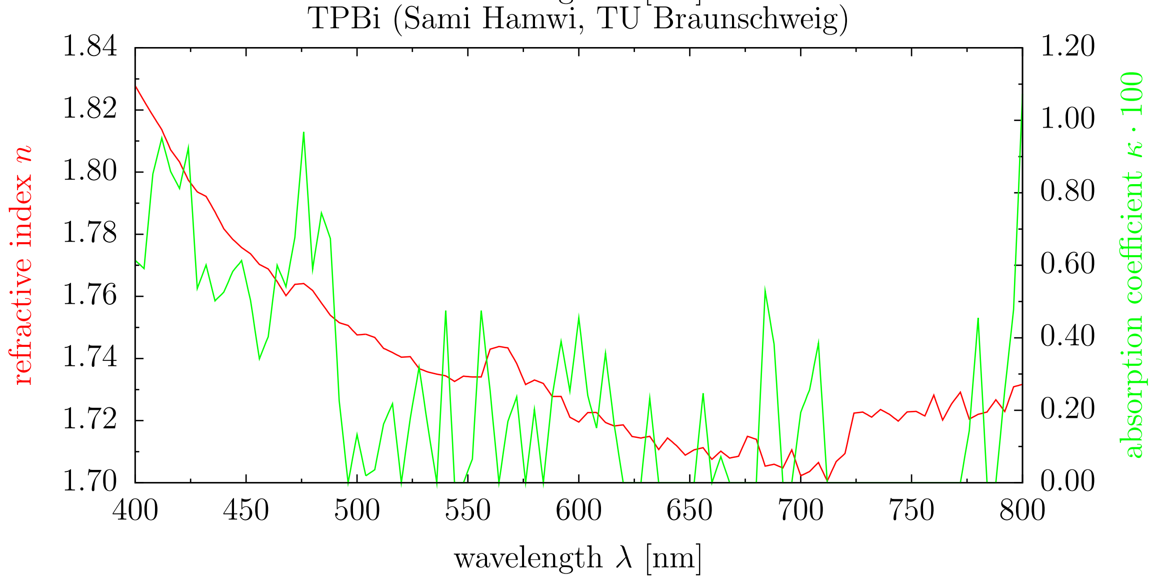
TPBi (Sami Hamwi, TU Braunschweig)

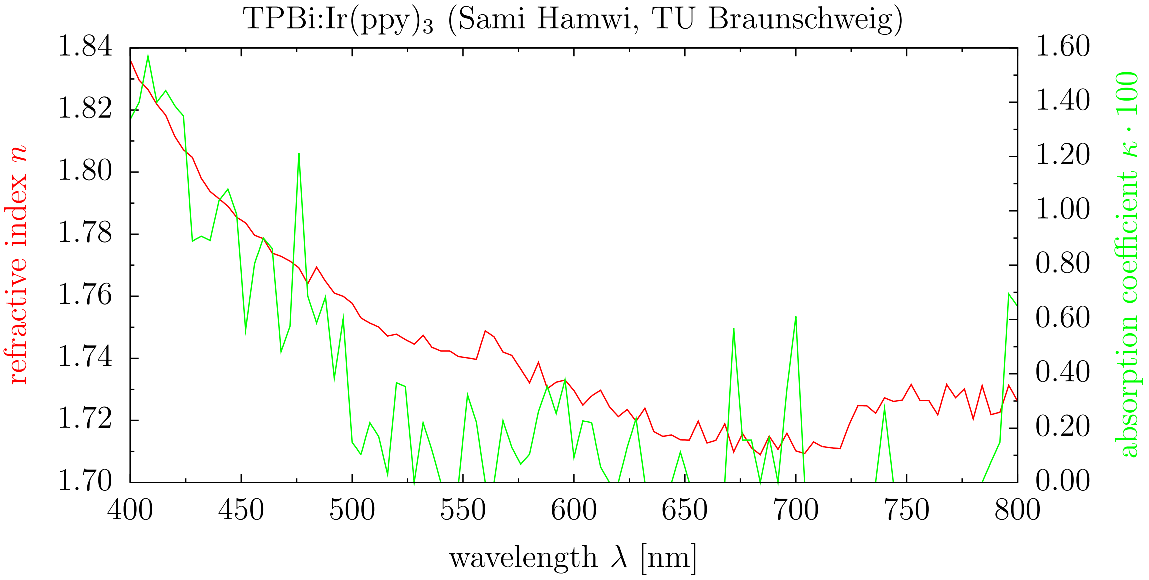
TPBi:Ir(ppy)$_3$ (Sami Hamwi, TU Braunschweig)
refractive index n
1.84
1.82
1.80
1.78
1.76
1.74
1.72
1.70
absorption coefficient $\kappa \cdot 100$
1.60
1.40
1.20
1.00
0.80
0.60
0.40
0.20
0.00
400
450
500
550
600
650
700
750
800
wavelength λ [nm]

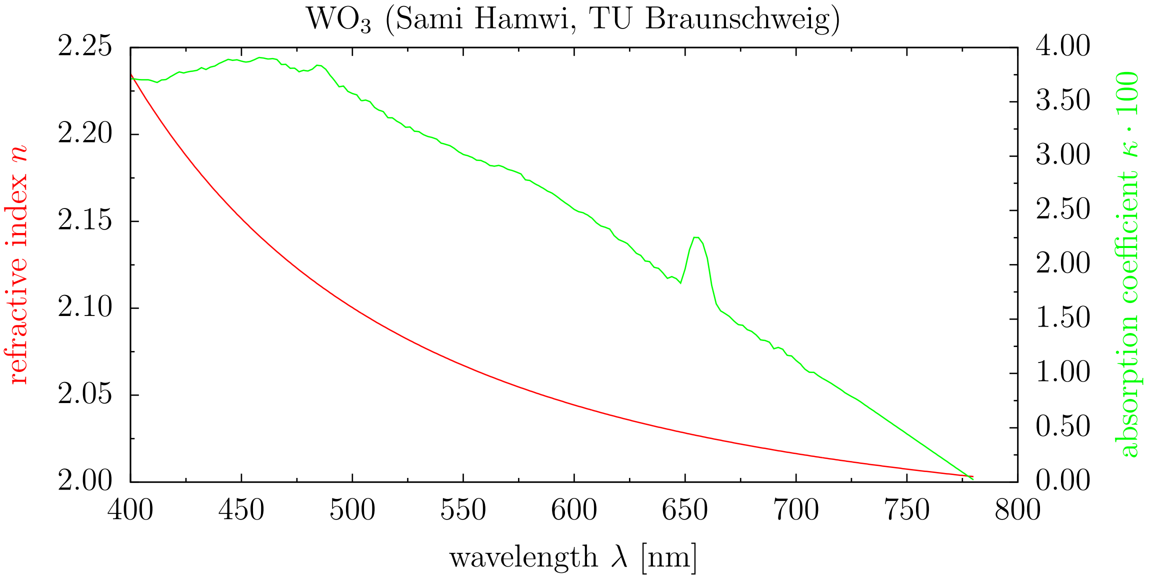
WO$_3$ (Sami Hamwi, TU Braunschweig)
refractive index n
2.25
2.20
2.15
2.10
2.05
2.00
absorption coefficient $\kappa \cdot 100$
4.00
3.50
3.00
2.50
2.00
1.50
1.00
0.50
0.00
400
450
500
550
600
650
700
750
800
wavelength λ [nm]

A.4. PDCalc

This section addresses the technical and physical difficulties encountered while using the simulation routine “PDCalc” originally written by Nils Reinke near the end of his PhD thesis[68]. The tasks of the author of the present thesis was to test the simulation routine intensively, remove the bugs, and reduce the time needed for one simulation. The encountered problems and their solutions will be discussed in the following.

Simulation runtime

One of the main concerns in the beginning of “PDCalc” was the time it took for one simulation to be finished. For the reference OLED (fig. 4.3), it took the MAPLE program about 12 hours on a, at that time, reasonable Pentium IV, 3.4 GHz, with 1 GB of RAM, WinXP, and Maple 9.5 ($k_\mathrm{x} \leqslant 4 \cdot 10^7\,\mathrm{m}^{-1}$, $\Delta k_\mathrm{x} = 2 \cdot 10^5\,\mathrm{m}^{-1}$, $400\,\mathrm{nm} \leqslant \lambda \leqslant 800\,\mathrm{nm}$). One possibility to reduce the runtime is to use fewer layers in the OLED stack. In the case of the reference OLED, the Al cathode can be calculated as semi-infinite, as it is thick enough to be non-transparent. However, coupling to plasmons might be affected by the missing air layer on top. Calculations have shown that the difference, Al as thin layer with air on top or Al as semi-infinite, are considerably small and can be neglected, if desired. Concerning the reduced runtime, this unfortunately does not chop off some hours, merely minutes. Reducing the amount of layers and taking some mean value, e.g., for the refractive indices of the organic layers, like in Adachi et al.[71], was not an option. Just before leaving Augsburg, Nils Reinke managed to make the Maple code more efficient: the reference OLED now took about 10 hours of runtime. This, however, was still a lot of time for just one simulation: imagine a layer thickness variation with 20 different thicknesses. Eventually, using Maple 11 this issue has been solved drastically, as the runtime of the reference OLED was reduced to about 1.5 hours just by using this different program version and variations of the OLED stack could finally be performed in a reasonable time. The next step in optimizing the time needed for simulations was to use a Core2Quad Q6600 processor with four cores, running at 2.4 GHz, 4 GB of RAM, and WinXP (64-bit version). The runtime for one simulation of the reference OLED with the above described parameters was reduced to almost exactly 1 hour. As Maple natively does not use multithreading, the simulations only can make use of one core. However, one can run three simulations at the same time, reducing the overall simulation time to very reasonable values. Using all four cores of the processor does not benefit: the simulation time for one simulation increases drastically, so one core should be reserved for Windows running in the background. Maple 12 (64-bit version) does not improve speed, it even seems to be slightly slower than the previous version (runtime for the reference stack about 1.2 hours). However, on a Corei7-860, 2.8 GHz, 4 GB of DDR3 RAM, running a 64-bit Linux (highly optimized Gentoo) and Maple 13 (64-bit version) the reference OLED simulation is calculated in 23.5 minutes. This shows that there is still room for improvement concerning runtime. In the author’s opinion there are two more possibilities to improve speed on the software level: 1) rewriting the maple code in such a way that it uses multithreading, and 2) completely rewriting the program, also using multithreaded programming, in a real programming language like C/C++, maybe even running on recent GPUs (graphics processing units, which are able to massively compute parallel data). “PDCalc” is perfectly suited for multithreaded programming as the calculation for one wavelength does not influence the calculation for another. However, option 1) requires to rewrite the maple code in some parts, and option 2) requires writing “PDCalc” from scratch. It is also not known if option 2) has advantages over option 1) concerning runtime, as Maple usually uses very efficient math algorithms. In the authors opinion, using a multithreaded version of “PDCalc” could decrease the runtime of one simulation drastically.

Choosing an appropriate value for Δk_{x}

As “PDCalc” uses the in-plane wave vector k_{x} as variable, the chosen step size Δk_{x} is of physical importance. The parameters chosen at first, $2 \cdot 10^5\,\mathrm{m}^{-1} \leqslant k_{\mathrm{x}} \leqslant 4 \cdot 10^7\,\mathrm{m}^{-1}$ and $\Delta k_{\mathrm{x}} = 2 \cdot 10^5\,\mathrm{m}^{-1}$, result in 200 points in k_{x} for each wavelength. This number of sample points is essential especially for sharp modes, i.e., the waveguided modes: if Δk_{x} is too wide, they simply are passed over, as one can imagine from the cross section of the power dissipation spectrum shown in fig. 4.6. Therefore their contribution to the fraction of power would not be honored, leading to false simulation results. However, for the reference OLED the chosen values are usable, calculations with more sample points, e.g., 400 ($\Delta k_{\mathrm{x}} = 1 \cdot 10^5\,\mathrm{m}^{-1}$) or 800 ($\Delta k_{\mathrm{x}} = 5 \cdot 10^4\,\mathrm{m}^{-1}$) do not alter the simulation results significantly. Using more sample points leads to more precise results and should be favored, however, simulation runtime certainly increases.

For the “simple” stacks, e.g., dipoles facing a silver mirror in a distance d maintained by a spacer (e.g., fig. 4.32) the choice of Δk_{x} and therefore the number of sample points is utterly crucial. In these structures waveguided modes are excited, in increasing numbers with increasing thickness d of the spacer. As an example for simulation results with different Δk_{x} values, the radiative lifetime of Alq_3 facing a silver mirror is discussed. The spacer used is SiO_2, see fig. 4.34. Δk_{x} was first set to $2 \cdot 10^5\,\mathrm{m}^{-1}$ and then further reduced, to the lowest usable level of $2 \cdot 10^4\,\mathrm{m}^{-1}$ (corresponding to 2000 sample points), see fig. A.4. If the number of sample points is too small, the calculated photoluminescence lifetime is very noisy, however, a trend is still visible. Increasing the number of sample points (decreasing Δk_{x}) yields smoother curves. But even for $\Delta k_{\mathrm{x}} = 2 \cdot 10^4\,\mathrm{m}^{-1}$ the curves are not entirely smooth especially at large spacer thicknesses where many waveguided modes are excited and have to be considered for the calculation. Unfortunately, Δk_{x} could not be lowered even more: the current setup with the Core2Quad processor lacks enough memory. It should be noted at this point that Maple 11 is only able to address 2 GB of RAM (for one instance) and simply stops the calculation when more RAM would be needed (swapping out memory to the harddisk is not possible). The use of the 64-bit version of Maple 12 is necessary, as these limitations do not apply any more. After upgrading the RAM to 8 GB (which is the limit of the mainboard) the above described calculations were possible. One (!) of these 251 simulations took about 6 to 7 hours and fully loaded the available RAM. Here again the use of multithreaded calculations would be highly beneficial: the amount of RAM needed is almost the same, however, more cores could be used for the calculation

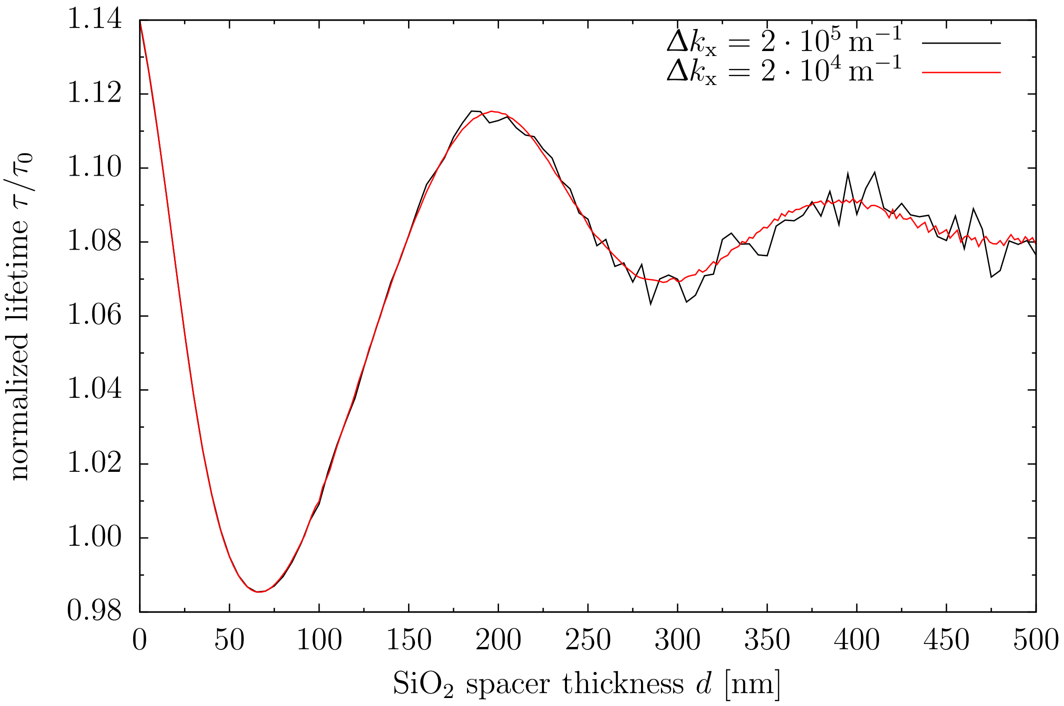

Figure A.4.: Normalized lifetime of Alq$_3$ calculated for different SiO$_2$ spacer thickness d (fig. 4.34) and different Δk_x values. Black line: $\Delta k_\mathrm{x} = 2 \cdot 10^5\,\mathrm{m}^{-1}$, $\Delta d = 5\,\mathrm{nm}$. Red line: $\Delta k_\mathrm{x} = 2 \cdot 10^4\,\mathrm{m}^{-1}$, $\Delta d = 2\,\mathrm{nm}$. Smaller values of Δk_x yield better results as the sharp waveguided modes are better accounted for. ($q = 0.2$)

itself. In principle, decreasing the step size further is possible, however, the simulation runtime is unbearable, as swapping memory out to the harddisk is necessary, being much slower then RAM. However, as swapping is possible in Maple 12, two instances of the above mentioned stack have been calculated at once, taking about 9 hours each.

Media having no absorption coefficient

Using “PDCalc”, one has to be careful if media without absorption are used, especially, when used in waveguide structures. For example, if no absorption in a symmetric three-layer waveguide, like device 2 in fig. 4.27 (an Alq$_3$ film surrounded by air), is considered, the simulation yields no waveguided modes, which obviously is wrong. The underlying problem is that the resonances (the waveguided modes) are extremely sharp (becoming δ-distribution if the absorption coefficient is lowered successively). Therefore, the step size Δk_x used in the numerical calculations is always too broad. To circumvent such behavior, one has to consider media with some small absorption coefficient and small step size Δk_x. Nevertheless, questioning the simulation results, especially, when waveguided modes are expected, is also of importance.

The maximum value of k_x used for simulation

Choosing an appropriate maximum value for k_x for the simulations is not straightforward. Using the dipole model, k_x should in principle be run until infinity[54,57]. However, as the integrals are not calculated analytically but numerically, this is not possible. Setting $k_{\mathrm{x,max}} = 4 \cdot 10^7\,\mathrm{m}^{-1}$ for the reference OLED seemed a reasonable choice as the plasmon is fully visible (fig. 4.6) and therefore has been established as standard value. From the cross section, also shown in fig. 4.6, however, one can see that there is still a contribution at $k_{\mathrm{x,max}} = 4 \cdot 10^7\,\mathrm{m}^{-1}$. Evidently the question arises if one has to choose a higher value for $k_{\mathrm{x,max}}$. Especially, as the plasmon dispersion for a metal/organic interface in fig. 3.10 yields also higher k_x values than $4 \cdot 10^7\,\mathrm{m}^{-1}$ in the visible wavelength range. Therefore the simulation of the reference OLED has been repeated until $k_{\mathrm{x,max}} = 16 \cdot 10^7\,\mathrm{m}^{-1}$ with $\Delta k_\mathrm{x} = 2 \cdot 10^5\,\mathrm{m}^{-1}$, see fig. A.5. As one can see, there is a minimum at about $k_\mathrm{x} = 4 \cdot 10^7\,\mathrm{m}^{-1}$ and then a huge increase for higher k_x again. This increase should have a maximum and then decrease again at large k_x and are so called 'lossy surface waves'[142]. This has also been realized by Barnes in a calculation where the emitting dipoles are residing in free space with distance d to a silver mirror[54]. For comparability, his values ($\hat{\varepsilon}_{\mathrm{Ag}} = -16 + \mathrm{i} \cdot 0.6$, and $d = 3\,\mathrm{nm}$, $10\,\mathrm{nm}$, $30\,\mathrm{nm}$, $100\,\mathrm{nm}$) are used for the monochromatic calculation ($\lambda = 614\,\mathrm{nm}$) shown in fig. A.6. If the dipoles are moved further away from the mirror, the coupling to the lossy surface waves is decreasing. Hence, they are especially important when the emitting dipoles are very close to a reflecting surface as then Förster transfer of energy to the surface and subsequent quenching sets in. All possible quenching mechanisms involve the formation of an electron-hole pair (an exciton) in the reflecting material (for details see Ford and Weber[142], and Barnes[54]). However, this distinction is not considered in the simulation program "PDCalc", which also is the reason for the differences at very small distances of the dipoles to reflecting materials in other simulations from literature or experiments (e.g., fig. 4.33). Nevertheless, in this kind of stack there is no increase in the intensity at large k_x, in contrast to the behavior of the reference OLED (fig. A.5). The question arises why this is happening, especially as the increase in fig. A.5 seems to be proportional to k_x^2 (fig. A.7): is it due to the model itself or the implementation of "PDCalc"?

Further investigation shows that the proportionality to k_x^2 only appears if two prerequisites are fulfilled simultaneously: (1) the dipole layer is placed exactly between two materials, which (2) have different values for the absorption constants (extinction coefficients κ). If one places the dipoles, e.g., one nanometer away from the interface, a roll off (but still a rather large contribution) and not a steadily increasing intensity is obtained, although the simulation results should be nearly the same. For a simple stack, a Ag substrate supporting a film of 160 nm of $\mathrm{Alq_3}$ in air (fig. A.8), this is shown in fig. A.9. This, along with the behavior seen for the stack of Barnes, indicates that the observed behavior is not just a bug in "PDCalc", but related to the model*. This notion is endorsed after a discussion with Horst Greiner, Philips Research, Aachen, who is using a similar simulation routine based on the work of Neyts[60,143], where simi-

---

*However, the two constant plateaus at $k_\mathrm{x} > 4 \cdot 10^9\,\mathrm{m}^{-1}$ for $d = 1\,\mathrm{nm}$ and $159\,\mathrm{nm}$ seem to be a limitation of the simulation routine.

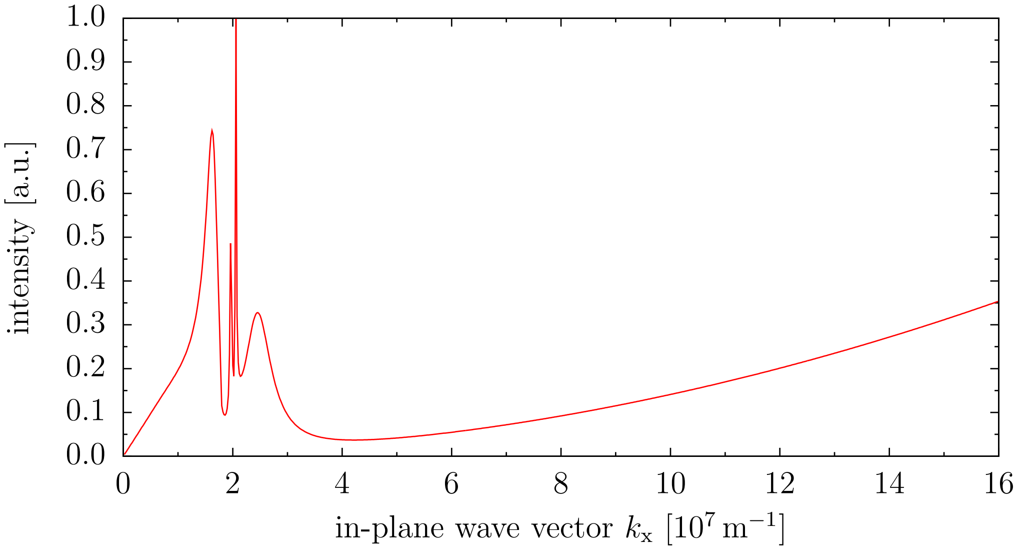

Figure A.5.: Cross section of the power dissipation spectrum at $\lambda = 525\,\mathrm{nm}$ for the reference OLED (fig. 4.3) calculated until $k_{\mathrm{x,max}} = 16 \cdot 10^7\,\mathrm{m}^{-1}$. $\Delta k_{\mathrm{x}} = 2 \cdot 10^5\,\mathrm{m}^{-1}$.

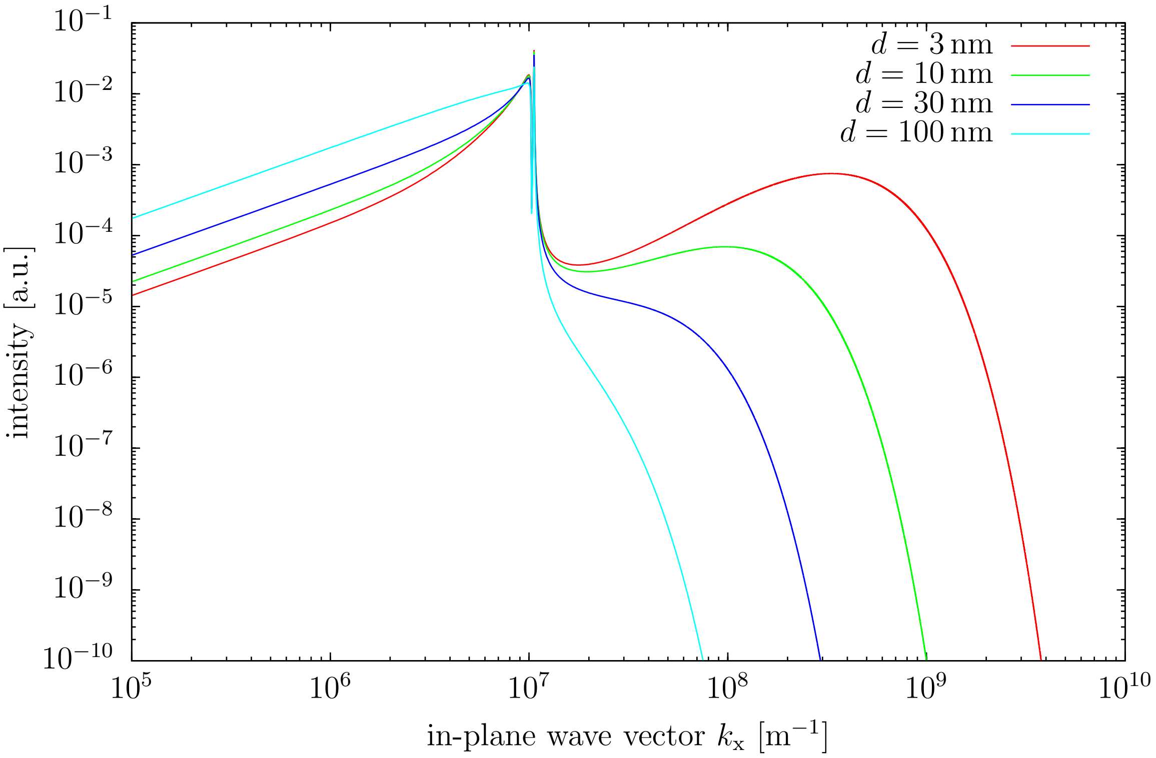

Figure A.6.: Power dissipation spectrum at $\lambda = 614\,\mathrm{nm}$ for dipoles residing in free space with distance d to a silver mirror after Barnes ($\hat{\varepsilon}_{\mathrm{Ag}} = -16 + \mathrm{i} \cdot 0.6$, equivalent to $n_{\mathrm{Ag}} \approx 0.0075$ and $\kappa_{\mathrm{Ag}} \approx 4.0$)^{54}. $\Delta k_{\mathrm{x}} = 1 \cdot 10^5\,\mathrm{m}^{-1}$, $k_{\mathrm{x,max}} = 1 \cdot 10^{10}\,\mathrm{m}^{-1}$.

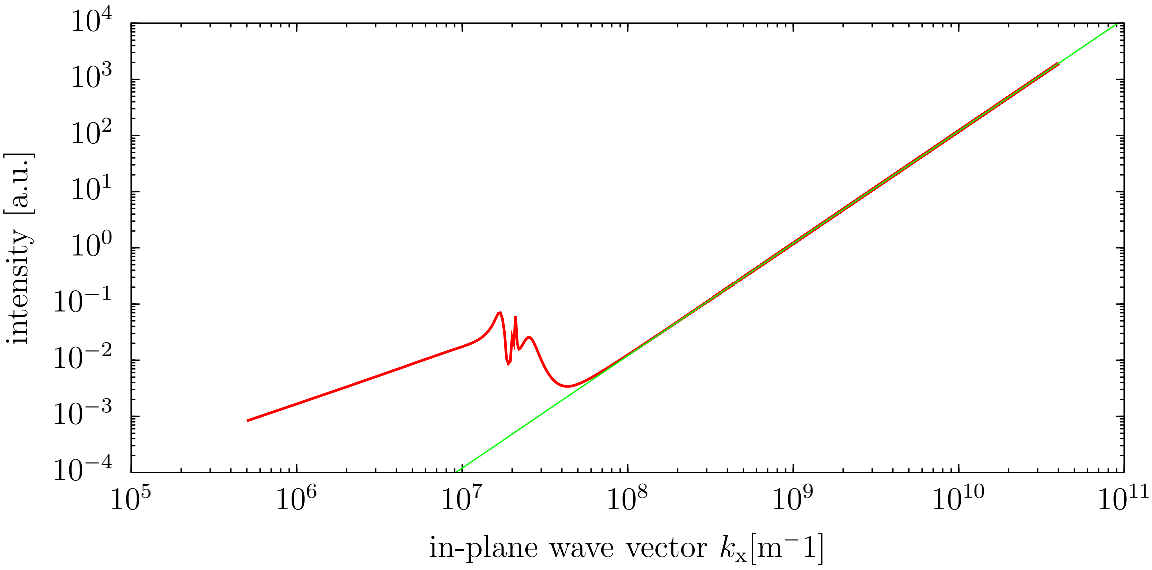

Figure A.7.: Cross section of the power dissipation spectrum at $\lambda = 525\,\mathrm{nm}$ (red line) for the reference OLED (fig. 4.3) and fit proportional to k_x^2 (green line). $\Delta k_\mathrm{x} = 5 \cdot 10^5\,\mathrm{m}^{-1}$, $k_{\mathrm{x,max}} = 4 \cdot 10^{10}\,\mathrm{m}^{-1}$.

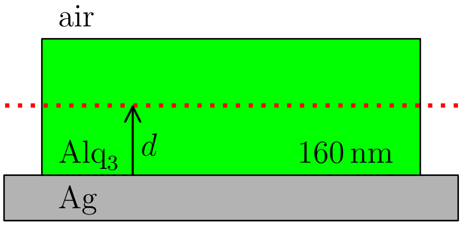

Figure A.8.: Simple test stack: a film of Alq_3 (thickness: 160 nm) on a Ag substrate. Dipole layer embedded in Alq_3 with distance d to the Ag mirror.

lar effects are observed. Therefore, to circumvent such problems, the dipole layer itself is placed in an additional thin layer having no absorption coefficient in his simulations.

The causes of the observed behavior should be investigated furthermore in the future, as it is yet also unknown if the curves' progressions have a physical meaning ("what corresponds to a wave vector $k_\mathrm{x} = 10^{10}\,\mathrm{m}^{-1}$?") or just are an artifact of the model. However, in conclusion, the chosen maximum value of $k_\mathrm{x} = 4 \cdot 10^7\,\mathrm{m}^{-1}$ seems to be a reasonable trade-off, as the plasmon is mainly considered and overall allows quite accurate descriptions of experimental values of OLEDs.

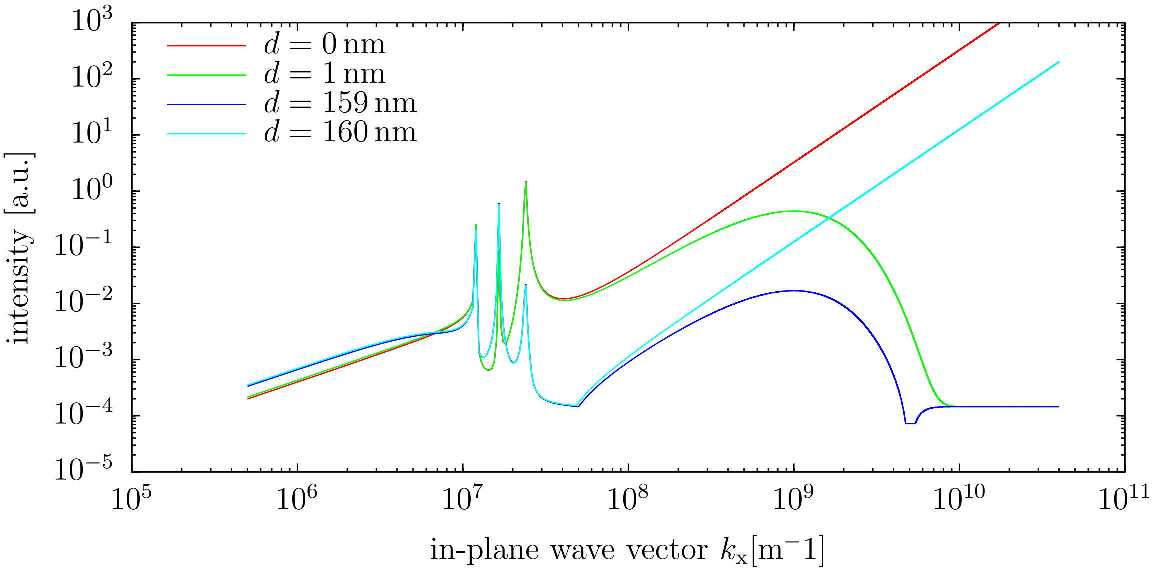

Figure A.9.: Power dissipation spectrum at $\lambda = 525\,\mathrm{nm}$ for the stack shown in fig. A.8) for different distance d of the dipoles to the Ag mirror. If the dipoles are exactly placed at an interface ($d = 0\,\mathrm{nm}$: at the Ag interface; $d = 160\,\mathrm{nm}$: at the air interface), an increase proportional to k_x^2 appears. $\Delta k_\mathrm{x} = 5 \cdot 10^5\,\mathrm{m}^{-1}$, $k_\mathrm{x,max} = 1 \cdot 10^{10}\,\mathrm{m}^{-1}$.

Bibliography

[1] T. A. Edison. “Electric Lamp”. *Patent* **US 223898**.

[2] *Verordnung (EG) Nr. 244/2009 der Kommission vom 18. März 2009* (Amtsblatt der Europäischen Union).

[3] European Commission – Joint Research Centre. http://ec.europa.eu/dgs/jrc/downloads/jrc_091130_newsrelease_electricity_de.pdf.

[4] http://www.diehl-aerospace.de/index.php?id=1402&L=1.

[5] http://www.osram-os.com/osram_os/EN/Press/Press_Releases/Organic_LED/ORBEOS-OLED-light-source.jsp.

[6] http://www.osram-os.com/osram_os/EN/Press/Press_Releases/Organic_LED/OLED-lighting-project-Ingo-Maurer.jsp.

[7] D. F. Williams and M. Schadt. “A simple organic electroluminescent diode”. *Proceedings of the IEEE* **58**(3) (1970) 476.

[8] C. W. Tang and S. A. VanSlyke. “Organic electroluminescent diodes”. *Applied Physics Letters* **51**(12) (1987) 913–915.

[9] H. Shirakawa, E. J. Louis, A. G. MacDiarmid, C. K. Chiang, and A. J. Heeger. “Synthesis of electrically conducting organic polymers - halogen derivates of polyacetylene, $(CH)_x$”. *Journal of the Chemical Society - Chemical Communications* **16** (1977) 578–580.

[10] C. K. Chiang, C. R. Fincher, Y. W. Park, A. J. Heeger, H. Shirakawa, E. J. Louis, S. C. Gau, and A. G. MacDiarmid. “Electrical-conductivity in doped polyacetylene”. *Physical Review Letters* **39**(17) (1977) 1098–1101.

[11] C. K. Chiang, M. A. Druy, S. C. Gau, A. J. Heeger, E. J. Louis, A. G. MacDiarmid, Y. W. Park, and H. Shirakawa. “Synthesis of highly conducting films of derivates of polyacetylene, $(CH)_x$”. *Journal of the American Chemical Society* **100**(3) (1978) 1013–1015.

[12] http://nobelprize.org/nobel_prizes/chemistry/laureates/2000.

[13] http://nobelprize.org/nobel_prizes/physics/laureates/2000.

[14] J. H. Burroughes, D. D. C. Bradley, A. R. Brown, R. N. Marks, K. Mackay, R. H. Friend, P. L. Burns, and A. B. Holmes. “Light-emitting diodes based on conjugated polymers”. *Nature* **347** (1990) 539–541.

[15] C. W. Tang. “Two-layer organic photovoltaic cell”. *Applied Physics Letters* **48** (1986) 183–185.

[16] M. Schwoerer and H. C. Wolf. *Organische Molekulare Festkörper* (Wiley-VCH, 2005).

[17] B. Mills. ben@benjamin-mills.com.

[18] J. R. Lakowicz. *Principles of Fluorescence Spectroscopy* (Springer, 2006), third ed.

[19] E. F. Schubert. *Light-Emitting Diodes* (Cambridge University Press, 2006), second ed.

[20] M. A. Baldo, D. F. O’Brien, Y. You, A. Shoustikov, S. Sibley, M. E. Thompson, and S. R. Forrest. “Highly efficient phosphorescent emission from organic electroluminescent devices”. *Nature* **395** (1998) 151–154.

[21] M. Cölle, J. Gmeiner, W. Milius, H. Hillebrecht, and W. Brütting. “Preparation and Characterization of Blue-Luminescent Tris(8-hydroxyquinoline)aluminum (Alq_3)”. *Advanced Functional Materials* **13**(2) (2003) 108–112.

[22] M. Cölle and W. Brütting. “Thermal, structural and photophysical properties of the organic semiconductor Alq_3”. *Physica Status Solidi A* **201**(6) (2004) 1095–1115.

[23] M. Pfeiffer, K. Leo, X. Zhou, J. S. Huang, M. Hofmann, A. Werner, and J. Blochwitz-Nimoth. “Doped organic semiconductors: physics and application in light emitting diodes”. *Organic Electronics* **4** (2003) 89–103.

[24] H. Ishii, K. Sugiyama, E. Ito, and K. Seki. “Energy Level Alignment and Interfacial Electronic Structures at Organic/Metal and Organic/Organic Interfaces”. *Advanced Materials* **11**(8) (1999) 605–625.

[25] I. G. Hill, D. Milliron, J. Schwartz, and A. Kahn. “Organic semiconductor interfaces: electronic structure and transport properties”. *Applied Surface Science* **166** (2000) 354–362.

[26] K. Seki, N. Hayashi, H. Oji, E. Ito, Y. Ouchi, and H. Ishii. “Electronic structure of organic/metal interfaces”. *Thin Solid Films* **393** (2001) 298–303.

[27] N. Karl. In O. Madelung, M. Schulz, and H. Weiss (eds.), “Landolt-Börnstein (New Series)”, vol. 17 of *Group III*, pp. 106–218 (Springer, 1985).

[28] M. E. Gershenson, V. Podzorov, and A. F. Morpugo. “Colloquium: Electronic transport in single-crystal organic transistors”. *Reviews of Modern Physics* **78**(3) (2006) 973–989.

[29] H. Bässler. “Charge transport in disordered organic photoconductors”. *Physica Status Solidi B* **175** (1993) 15–56.

[30] C. Tanase, E. J. Meijer, P. W. M. Blom, and D. M. de Leeuw. “Unification of the Hole Transport in Polymeric Field-Effect Transistors and Light-Emitting Diodes”. *Physical Review Letters* **91** (2003) 216601.

[31] R. Coehoorn, W. F. Pasveer, P. A. Bobbert, and M. A. J. Michels. “Charge-carrier concentration dependence of the hopping mobility in organic materials with Gaussian disorder”. *Physical Review B* **72** (2005) 155206.

[32] D. Hertel and H. Bässler. “Photoleitung in Polymeren”. *Physik Journal* **5**(11) (2006) 39–45.

[33] W. Brütting and W. Rieß. “Grundlagen der organischen Halbleiter”. *Physik Journal* **7**(5) (2008) 33–38.

[34] H. Kanno, Y. Hamada, K. Nishimura, K. Okumoto, N. Saito, H. Ishida, H. Takahasi, K. Shibata, and K. Mameno. “High Efficiency Stacked Organic Light-Emitting Diodes Employing Li_2O as a Connecting Layer”. *Japanese Journal of Applied Physics* **45**(12) (2006) 9219–9223.

[35] S. Reineke, F. Lindner, G. Schwartz, N. Seidler, K. Walzer, B. Lüssern, and K. Leo. “White organic light-emitting diodes with fluorescent tube efficiency”. *Nature* **459** (2009) 234–239.

[36] C. C. Wu, C. I. Wu, J. C. Sturm, and A. Kahn. “Surface modification of indium tin oxide by plasma treatment: An effective method to improve the efficiency, brightness, and reliability of organic light emitting devices”. *Applied Physics Letters* **70** (1997) 1348–1350.

[37] K. Sugiyama, H. Ishii, Y. Ouchi, and K. Seki. “Dependence of indiumtinoxide work function on surface cleaning method as studied by ultraviolet and x-ray photoemission spectroscopies”. *Journal of Applied Physics* **87** (2000) 295–298.

[38] G. Wyszecki and W. S. Stiles. *Color Science: Concepts and Methods, Quantitative Data and Formulae* (John Wiley & Sons, 2000), second ed.

[39] http://cvrl.ioo.ucl.ac.uk.

[40] D. Pascale. “A review of RGB color spaces”. http://www.babelcolor.com/download/A%20review%20of%20RGB%20color%20spaces.pdf.

[41] Y. Luo, H. Aziz, G. Xu, and Z. D. Popovic. “Improving the stability of organic light-emitting devices by using a hole-injection-tunable-anode-buffer-layer”. *Journal of Applied Physics* **101** (2007) 054512.

[42] “OLLA White Paper on the Necessity of Luminous efficacy Measurement Standardisation of OLED Light Sources” (2007). http://www.hitech-projects.com/euprojects/olla/news/press_release_4_september_2007/OLLA-project_White_Paper.pdf.

[43] J. C. de Mello, H. F. Wittman, and R. H. Friend. “An Improved Experimental Determination of External Photoluminescence Quantum Efficiency”. *Advanced Materials* **9**(3) (1997) 230–232.

[44] T. Fließbach. *Elektrodynamik* (Elsevier - Spektrum Akademischer Verlag, 2005).

[45] P. Yeh. *Optical Waves in Layered Media* (John Wiley & Sons, 1988).

[46] I. N. Bronstein, K. A. Semendjajew, G. Musiol, and H. Mühlig. *Taschenbuch der Mathematik* (Verlag Harri Deutsch, 2000), fifth ed.

[47] H. Fouckhardt. *Photonik* (Teubner, 1994).

[48] H. Kogelnik. “Theory of Optical Waveguides”. In T. Tamir (ed.), “Guided-Wave Optoelectronics”, (Springer, 1990).

[49] H. Raether. *Surface Plasmons on smooth and rough surfaces and on gratings* (Springer, 1988).

[50] J. A. Dionne, L. A. Sweatlock, H. A. Atwater, and A. Polman. “Planar metal plasmon waveguides: frequency-dependent dispersion, propagation, localization, and loss beyond the free electron model”. *Physical Review B* **72** (2005) 075405.

[51] T. Tsutsui, E. Aminaka, C. P. Lin, and D.-U. Kim. “Extended molecular design concept of molecular materials for electroluminescence: sublimed-dye films, molecularly doped polymers and polymers with chromophores”. *Philosophical Transactions of the Royal Society of London A* **355** (1997) 801–814.

[52] N. C. Greenham, R. H. Friend, and D. D. C. Bradley. “Angular Dependence of the Emission from a Conjugated Polymer Light-Emitting Diode: Implications for Efficiency Calculations”. *Advanced Materials* **6**(6) (1994) 491–494.

[53] L. Novotny. “Allowed and forbidden light in near-field optics. I. A single dipolar light source”. *Journal of the Optical Society of America A* **14**(1) (1997) 91–104.

[54] W. L. Barnes. “Fluorescence near interfaces: the role of photonic mode density”. *Journal of Modern Optics* **45**(4) (1998) 661–699.

[55] H. Kuhn. “Classical Aspects of Energy Transfer in Molecular Systems”. *The Journal of Chemical Physics* **53**(1) (1970) 101–108.

[56] R. R. Chance, A. Prock, and R. Silbey. “Lifetime of an emitting molecule near a partially reflecting surface”. *The Journal of Chemical Physics* **60**(7) (1974) 2744–2748.

[57] R. R. Chance, A. Prock, and R. Silbey. “Molecular Fluorescence and Energy Transfer near Interfaces”. *Advances in Chemical Physics* **37** (1978) 1–65.

[58] T. Tsutsui, C. Adachi, S. Saito, M. Watanabe, and M. Koishi. "Effect of confined radiation field on spontaneous-emission lifetime in vacuum-deposited fluorescent dye films". *Chemical Physics Letters* **182**(2) (1991) 143–146.

[59] H. Becker, S. E. Burns, and R. H. Friend. "Effect of metal films on the photoluminescence and electroluminescence of conjugated polymers". *Physical Review B* **56**(4) (1997) 1893–1905.

[60] K. A. Neyts. "Simulation of light emission from thin-film microcavities". *Journal of the Optical Society of America A* **15**(4) (1998) 962–971.

[61] B. Ruhstaller, T. Beierlein, H. Riel, S. Karg, J. C. Scott, and W. Riess. "Simulating Electron and Optical Processes in Multilayer Organic Light-Emitting Devices". *IEEE Journal on Selected Topics in Quantum Electronics* **9**(3) (2003) 723–731.

[62] N. A. Reinke, C. Ackermann, and W. Brütting. "Light extraction via leaky modes in organic light emitting devices". *Optics Communications* **266** (2006) 191–197.

[63] A. Sommerfeld. "Über die Ausbreitung der Wellen in der drahtlosen Telegraphie". *Annalen der Physik* **28**(4) (1909) 665–736.

[64] J. A. E. Wasey and W. L. Barnes. "Efficiency of spontaneous emission from planar microcavities". *Journal of Modern Optics* **47**(4) (2000) 725–741.

[65] L. H. Smith, J. A. E. Wasey, I. D. W. Samuel, and W. L. Barnes. "Light Out-Coupling Efficiencies of Organic Light-Emitting Diode Structures and the Effect of Photoluminescence Quantum Yield". *Advanced Functional Materials* **15**(11) (2005) 1839–1844.

[66] K. Celebi, T. D. Heidel, and M. A. Baldo. "Simplified calculation of dipole energy transport in a multilayer stack using dyadic Green's functions". *Optics Express* **15**(4) (2007) 1762–1772.

[67] W. Lukosz and R. E. Kunz. "Light emission by magnetic and electric dipoles close to a plane interface. I. Total radiated power". *Journal of the Optical Society of America* **67**(12) (1977) 1607–1615.

[68] N. A. Reinke. *Photophysikalische Prozesse und Lichtextraktion in organischen Leuchtdioden.* PhD thesis, Universität Augsburg, Germany (2008).

[69] K. Meerholz and D. C. Müller. "Outsmarting Waveguide Losses in Thin-Film Light-Emitting Diodes". *Advanced Functional Materials* **11**(4) (2001) 251–253.

[70] W. Brütting, S. Berleb, and A. G. Mückl. "Device Physics of organic light-emitting diodes based on molecular materials". *Organic Electronics* **2** (2001) 1–36.

[71] C. Adachi, M. A. Baldo, M. E. Thompson, and S. R. Forrest. “Nearly 100% internal phosphorescence efficiency in an organic light emitting device”. *Journal of Applied Physics* **90**(10) (2001) 5048–5051.

[72] C.-L. Lin, T.-Y. Cho, C.-H. Chang, and C.-C. Wu. “Enhancing light outcoupling of organic light-emitting devices by locating emitters around the second antinode of the reflective metal electrode”. *Applied Physics Letters* **88** (2006) 081114.

[73] D. Z. Garbuzov, V. Bulović, P. E. Burrows, and S. R. Forrest. “Photoluminescence efficiency and absorption of aluminum-tris-quinolate (Alq_3) thin films”. *Chemical Physics Letters* **249** (1996) 433–437.

[74] H. Mattoussi, H. Murata, C. D. Merritt, Y. Iizumi, J. Kido, and Z. H. Kafafi. “Photoluminescence quantum yield of pure and molecularly doped organic solid films”. *Journal of Applied Physics* **86**(5) (1999) 2642–2650.

[75] K. H. Drexhage. “Influence of a dielectric interface on fluorescence decay times”. *Journal of Luminescence* **1-2** (1970) 693–701.

[76] B. Lebsanft. Diplomarbeit, Universität Augsburg, Germany (to be published).

[77] http://www.basf.com/additives/bcadditiveslumogen.html.

[78] J. A. Martin. *Charakterisierung von Dünnschichtkonvertern zur externen Lichtumwandlung in Verbindung mit einer organischen Leuchtdiode*. Diplomarbeit, Universität Augsburg, Germany (2008).

[79] S. K. So, W. K. Choi, L. M. Leung, and K. Neyts. “Interference effects in bilayer organic light-emitting diodes”. *Applied Physics Letters* **74**(14) (1999) 1939–1941.

[80] C. Schmitz, M. Thelakkat, and H.-W. Schmidt. “A Combinatorial Study of the Dependence of Organic LED Characteristics on Layer Thickness”. *Advanced Materials* **11**(10) (1999) 821–826.

[81] T. A. Beierlein. *Combinatorial Methods for Organic Light-Emitting Materials and Devices*. PhD thesis, University of Bayreuth, Germany (2003).

[82] T. Schmidt. PhD thesis, Universität Augsburg, Germany (to be published).

[83] P. Andrew and W. L. Barnes. “Energy transfer across a metal film mediated by surface plasmon polaritons”. *Science* **306** (2004) 1002–1005.

[84] B. J. Arndt. *Lichtauskopplung aus organischen Leuchtdioden: Reduktion von Oberflächenplasmonenverlusten*. Bachelor’s thesis, Universität Augsburg, Germany (2009).

[85] B. C. Krummacher, F. Schindler, N. A. Reinke, W. Brütting, J. Frischeisen, and S. Nowy. “Strahlungsemittierendes Bauelement”. *Patent* **DE 10 2008 022 830 A1**.

[86] J. Frischeisen. PhD thesis, Universität Augsburg, Germany (to be published).

[87] B. Scholz. Diplomarbeit, Universität Augsburg, Germany (to be published).

[88] S. Mladenovski, K. Neyts, D. Pavicic, A. Werner, and C. Rothe. “Exceptionally efficient organic light emitting devices using high refractive index substrates”. *Optics Express* **17**(9) (2009) 7562–7570.

[89] J. Meyer, T. Winkler, S. Hamwi, S. Schmale, H.-H. Johannes, T. Weimann, P. Hinze, W. Kowalsky, and T. Riedl. “Transparent Inverted Organic Light-Emitting Diodes with a Tungsten Oxide Buffer Layer”. *Advanced Materials* **20** (2008) 3839–3843.

[90] H.-W. Lin, C.-L. Lin, H.-H. Chang, Y.-T. Lin, C.-C. Wu, Y.-M. Chen, R.-T. Chen, Y.-Y. Chien, and K.-T. Wong. “Anisotropic optical properties and molecular orientation in vacuum-deposited ter(9,9-diarylfluorene)s thin films using spectroscopic ellipsometry”. *Journal of Applied Physics* **95**(3) (2004) 881–886.

[91] H.-W. Lin, C.-L. Lin, C.-C. Wu, T.-C. Chao, and K.-T. Wong. “Influences of molecular orientations on stimulated emission characteristics of oligofluorene films”. *Organic Electronics* **8** (2007) 189–197.

[92] D. Yokoyama, A. Sakaguchi, M. Suzuki, and C. Adachi. “Horizontal orientation of linear-shaped organic molecules having bulky substituents in neat and doped vacuum-deposited amorphous films”. *Organic Electronics* **10** (2009) 127–137.

[93] J. Frischeisen, D. Yokoyama, C. Adachi, and W. Brütting. “Determination of molecular dipole orientation in doped fluorescent organic thin films by photoluminescence measurements”. *Applied Physics Letters* **96** (2010) 073302.

[94] J. R. Macdonald (ed.). *Impedance Spectroscopy* (John Wiley & Sons, 1987).

[95] J. A. Garrido, S. Nowy, A. Härtl, and M. Stutzmann. “The Diamond/Aqueous Electrolyte Interface: an Impedance Investigation”. *Langmuir* **24**(8) (2008) 3897–3904.

[96] M. Meier, S. Karg, and W. Riess. “Light-emitting diodes based on poly-p-phenylene-vinylene: II. Impedance spectroscopy”. *Journal of Applied Physics* **82**(4) (1997) 1961–1966.

[97] J. Scherbel, P. H. Nguyen, G. Paasch, W. Brütting, and M. Schwoerer. “Temperature dependent broadband impedance spectroscopy on poly-(p-phenylene-vinylene) light-emitting diodes”. *Journal of Applied Physics* **83**(10) (1998) 5045–5055.

[98] A. J. Campbell, D. D. C. Bradley, E. Werner, and W. Brütting. “Deep level transient spectroscopy (DLTS) of a poly(p-phenylene vinylene) Schottky diode”. *Synthetic Metals* **111-112** (2000) 273–276.

[99] H. C. F. Martens, H. B. Brom, and P. W. M. Blom. “Frequency-dependent electrical response of holes in poly(p-phenylene vinylene)”. *Physical Review B* **60**(12) (1999) R8489–R8492.

[100] S. Berleb and W. Brütting. “Dispersive Electron Transport in tris(8-hydroxyquinoline) Aluminum (Alq$_3$) Probed by Impedance Spectroscopy”. *Physical Review Letters* **89**(28) (2002) 286601.

[101] S. L. M. van Mensfoort and R. Coehoorn. “Determination of Injection Barriers in Organic Semiconductor Devices from Capacitance Measurements”. *Physical Review Letters* **100** (2008) 086802.

[102] E. Ehrenfreund, C. Lungenschmied, G. Dennler, H. Neugebauer, and N. S. Sariciftci. “Negative capacitance in organic semiconductor devices: Bipolar injection and charge recombination mechanism”. *Applied Physics Letters* **91** (2007) 012112.

[103] D. M. Taylor and H. L. Gomes. “Electrical characterization of the rectifying contact between aluminium and electrodeposited poly(3-methylthiophene)”. *Journal of Physics D - Applied Physics* **28** (1995) 2554–2568.

[104] P. R. Karmel, G. D. Colef, and R. L. Camisa. *Introduction to Electromagnetic and Microwave Engineering* (John Wiley & Sons, 1998).

[105] P. A. Tipler. *Physik* (Spektrum Akademischer Verlag, 1994).

[106] M. Honda. *The Impedance Measurement Handbook* (Yokogawa - Hewlett Packard, 1989).

[107] S. Berleb, W. Brütting, and G. Paasch. “Interfacial charges and electric field distribution in organic hetero-layer light-emitting devices”. *Organic Electronics* **1** (2000) 41–47.

[108] D. Y. Kondakov, J. R. Sandifer, C. W. Tang, and R. H. Young. “Nonradiative recombination centers and electrical aging of organic light-emitting diodes: Direct connection between accumulation of trapped charge and luminance loss”. *Journal of Applied Physics* **93**(2) (2003) 1108–1119.

[109] Y. Noguchi, N. Sato, Y. Tanaka, Y. Nakayama, and H. Ishii. “Threshold voltage shift and formation of charge traps induced by light irradiation during the fabrication of organic light-emitting diodes”. *Applied Physics Letters* **92** (2008) 203306.

[110] V. V. Jarikov and D. Y. Kondakov. “Studies of the degradation mechanism of organic light-emitting diodes based on *tris*(8-quinolinolate)aluminum Alq and 2-*tert*-butyl-9,10-di(2-naphthyl)anthracene TBADN”. *Journal of Applied Physics* **105** (2009) 034905.

[111] J. Wagner. *Electronic properties of interfaces in organic devices studied by Kelvin probe and impedance spectroscopy.* Master's thesis, Universität Augsburg, Germany (2008).

[112] W. Ren. *Impedance spectroscopy of hetero-layer organic light-emitting diodes.* Master's thesis, Universität Augsburg, Germany (2009).

[113] J. Meyer, S. Hamwi, T. Bülow, H.-H. Johannes, T. Riedl, and W. Kowalsky. "Highly efficient simplified organic light emitting diodes". *Applied Physics Letters* **91** (2007) 113506.

[114] K. Steidle. *Impedanzspektroskopie an organischen Leuchtdioden.* Bachelor's thesis, Universität Augsburg, Germany (2009).

[115] S. Berleb. *Raumladungsbegrenzte Ströme und Hoppingtransport in organischen Leuchtdioden aus Tris-(8-hydroxyquinolin)-Aluminium (Alq$_3$).* PhD thesis, Universität Bayreuth, Germany (2001).

[116] D. Ray and K. L. Narasimhan. "Measurement of deep states in hole doped organic semiconductors". *Journal of Applied Physics* **103** (2008) 093711.

[117] S. T. Lee, Z. Q. Gao, and L. S. Hung. "Metal diffusion from electrodes in organic light-emitting diodes". *Applied Physics Letters* **75**(10) (1999) 1404–1406.

[118] J. Shen, D. Wang, E. Langlois, W. A. Barrow, P. J. Green, C. W. Tang, and J. Shi. "Degradation mechanisms in organic light emitting diodes". *Synthetic Metals* **111-112** (2000) 233–236.

[119] Y. Luo, H. Aziz, Z. D. Popovic, and G. Xu. "Degradation mechanisms in organic light-emitting devices: Metal migration model versus unstable tris(8-hydroxyquinoline) aluminum cationic model". *Journal of Applied Physics* **101** (2007) 034510.

[120] T. Yamada, D. Zou, H. Jeong, Y. Akaki, and T. Tsutsui. "Recoverable degradation and internal field forming process accompanied by the orientation of dipoles in organic light emitting diodes". *Synthetic Metals* **111-112** (2000) 237–240.

[121] M. Yahiro, D. Zou, and T. Tsutsui. "Recoverable degradation phenomena of quantum efficiency in organic EL devices". *Synthetic Metals* **111-112** (2000) 245–247.

[122] J. C. Scott, J. H. Kaufman, P. J. Brock, R. DiPetro, J. Salem, and J. A. Goitia. "Degradation and failure of MEH-PPV light-emitting diodes". *Journal of Applied Physics* **79**(5) (1996) 2745–2751.

[123] F. Papadimitrakopoulos, X.-M. Zhang, D. L. Thomsen, and K. A. Higginson. "A Chemical Failure Mechanism for Aluminum(III) 8-Hydroxyquinoline Light-Emitting Devices". *Chemistry of Materials* **8** (1996) 1363–1365.

[124] H. Aziz, Z. D. Popovic, N.-X. Hu, A.-M. Hor, and G. Xu. "Degradation Mechanism of Small Molecule-Based Organic Light-Emitting Devices". *Science* **283** (1999) 1900–1902.

[125] Z. D. Popovic, H. Aziz, N.-X. Hu, A. Ioannidis, and P. N. M. dos Anjos. "Simultaneous electroluminescence and photoluminescence aging studies of tris(8-hydroxyquinoline) aluminum-based organic light-emitting devices". *Journal of Applied Physics* **89**(8) (2001) 4673–4675.

[126] P. E. Burrows, V. Bulovic, S. R. Forrest, L. S. Sapochak, D. M. McCarty, and M. E. Thompson. "Reliability and degradation of organic light emitting devices". *Applied Physics Letters* **65**(23) (1994) 2922–2924.

[127] H. Aziz, Z. Popovic, C. P. Tripp, N.-X. Hu, A.-M. Hor, and G. Xu. "Degradation processes at the cathode/organic interface in organic light emitting devices with Mg:Ag cathodes". *Applied Physics Letters* **72**(21) (1998) 2642–2644.

[128] D. Y. Kondakov, W. C. Lenhart, and W. F. Nichols. "Operational degradation of organic light-emitting diodes: Mechanism and identification of chemical products". *Journal of Applied Physics* **101** (2007) 024512.

[129] S. Egusa, A. Miura, N. Gemma, and M. Azuma. "Carrier injection characteristics of organic electroluminescent devices". *Japanese Journal of Applied Physics* **33** (1994) 2741–2745.

[130] M. C. Gather, S. Köber, S. Heun, and K. Meerholz. "Improving lifetime of white polymeric organic light-emitting diodes". *Journal of Applied Physics* **106** (2009) 024506.

[131] C. Féry, B. Racine, D. Vaufrey, H. Doyeux, and S. Cinà. "Physical mechanism responsible for the stretched exponential decay behavior of aging organic light-emitting diodes". *Applied Physics Letters* **87** (2005) 213502.

[132] R. Meerheim, K. Walzer, M. Pfeiffer, and K. Leo. "Ultrastable and efficient red organic light emitting diodes with doped transport layers". *Applied Physics Letters* **89** (2006) 061111.

[133] http://www.clevios.com.

[134] W. E. Howard and O. F. Prache. "Microdisplays based upon organic light-emitting diodes". *IBM Journal of Research and Development* **45**(1) (2001) 115–127.

[135] L. Lüer, H.-J. Egelhaaf, D. Oelkrug, G. Cerullo, G. Lanzani, B.-H. Huisman, and D. de Leeuw. "Oxygen-induced quenching of photoexcited states in polythiophene films". *Organic Electronics* **5** (2004) 83–89.

[136] D. Y. Kondakov. “Role of chemical reactions of arylamine hole transport materials in operational degradation of organic light-emitting diodes”. *Journal of Applied Physics* **104** (2008) 084520.

[137] A. Elschner. *private communication* (2009).

[138] L. S. Hung, L. R. Zheng, and M. G. Mason. “Anode modification in organic light-emitting diodes by low-frequency plasma polymerization of CHF_3”. *Applied Physics Letters* **78**(5) (2001) 673–675.

[139] J. X. Tang, Y. Q. Li, L. R. Zheng, and L. S. Hung. “Anode/organic interface modification by plasma polymerized fluorocarbon films”. *Journal of Applied Physics* **95**(8) (2004) 4397–4403.

[140] D. Q. Gao, M. Y. Chan, S. W. Tong, F. L. Wong, S. L. Lai, C. S. Lee, and S. T. Lee. “Application of an evaporable fluoro-molecule as an anode buffer layer in organic electroluminescent devices”. *Chemical Physics Letters* **399** (2004) 337–341.

[141] H. Aziz and Z. D. Popovic. “Degradation Phenomena in Small-Molecule Organic Light-Emitting Devices”. *Chemistry of Materials* **16** (2004) 4522–4532.

[142] G. W. Ford and W. H. Weber. “Electromagnetic interactions of molecules with metal surfaces”. *Physics Reports (Review Section of Physics Letters)* **113**(4) (1984) 195–287.

[143] H. Greiner. *private communication* (2010).

Danksagungen

Ich danke...

- Prof. Dr. Wolfgang Brütting für die Aufnahme in seine Arbeitsgruppe, das entgegengebrachte Vertrauen in allen Belangen, die stets offene Tür, die zahlreichen Diskussionen und die sorgfältige Korrektur meiner Manuskripte bei allen Veröffentlichungen.

- Prof. Dr. Achim Wixforth für seine Bereitschaft, das Zweitgutachten dieser Arbeit zu erstellen.

- dem Lehrstuhlinhaber Prof. Dr. Bernd Stritzker.

- meinen Kollegen aus der Organik-Gruppe, Andreas Opitz, Silviu Grecu, Markus Bronner, Nils Reinke, Michael Kraus, Thomas Wehlus und Ulrich Hörmann für die äußerst gute Zusammenarbeit. Besonders hervorheben möchte ich die Arbeit mit Jörg Frischeisen bezüglich der optischen Simulationen, wodurch unsere beiden Dissertationen eng miteinander verknüpft sind. Einen besonderen Dank möchte ich Tobias Schmidt und Julia Wagner für die sorgfältige Korrektur des Manuskriptes aussprechen.

- "meinen" Studenten, Jasmin Martin, Wei Ren, Kerstin Steidle, Josef Weber und Benjamin Lebsanft für ihren Arbeitseinsatz.

- allen anderen Mitgliedern des Lehrstuhls, besonders unserer langjährigen Sekretärin Cornelia Ludescher, sowie den Technikern Wolfgang Reiber, Sybille Heidemeyer und Birgit Knoblich.

- der Elektronikwerkstatt und der Mechanikwerkstatt, die meine zahlreichen Anliegen stets kompetent und zügig bearbeitet haben.

- dem Bundesministerium für Bildung und Forschung für die Finanzierung durch die Projekte OPAL2008 (FKZ 13N8995) und TOPAS2012 (FKZ 13N10474).

- unseren Ansprechpartnern bei OSRAM OS, Regensburg, Karsten Heuser, Florian Schindler, Benjamin Krummacher, Thomas Dobbertin und Arndt Jaeger für die hervorragende Zusammenarbeit in den Projekten OPAL und TOPAS und die daraus resultierenden Veröffentlichungen.

- den Kollegen aus dem OPAL Projekt, Sami Hamwi, TU Braunschweig, und Andrea Gassmann, TU Darmstadt, für den Datenaustausch.

- Andreas Elschner, H.C. Starck Clevios, Leverkusen, für die gute Zusammenarbeit für das gemeinsame Paper.

Publikationsliste

Publikationen in wissenschaftlichen Zeitschriften

1. A. Härtl, S. Nowy, J. Hernando, J. A. Garrido, M. Stutzmann
   "Bio-Interfacing of Diamond Films for Sensor Applications"
   IEEE Sensors (2005)

2. A. Härtl, J. A. Garrido, S. Nowy, R. Zimmermann, C. Werner, D. Horinek, R. Netz, M. Stutzmann
   "The Ion Sensitivity of Surface Conductive Single Crystalline Diamond"
   Journal of the American Chemical Society **129** (2007) 1287–1292

3. J. A. Garrido, S. Nowy, A. Härtl, M. Stutzmann
   "The diamond/aqueous electrolyte interface: an impedance investigation"
   Langmuir **24**(8) (2008) 3897–3904

4. S. Nowy, N. A. Reinke, J. Frischeisen, W. Brütting
   "Light extraction and optical loss mechanisms in organic light-emitting diodes"
   Proceedings of SPIE **6999** (2008) 69992V

5. J. Frischeisen, N. A. Reinke, C. Ostermayr, J. Neumann, S. Nowy, W. Brütting
   "Surface plasmon resonance sensor based on a planar polychromatic OLED light source"
   Proceedings of SPIE **7003A** (2008) 70031B

6. J. Frischeisen, C. Mayr, N. A. Reinke, S. Nowy, W. Brütting
   "Surface plasmon resonance sensor utilizing an integrated organic light emitting diode"
   Optics Express **16** (2008) 18426–18436

7. S. Nowy, B. C. Krummacher, J. Frischeisen, N. A. Reinke, W. Brütting
   "Light extraction and optical loss mechanisms in organic light-emitting diodes: influence of the emitter quantum efficiency"
   Journal of Applied Physics **104** (2008) 123109

8. B. C. Krummacher, S. Nowy, J. Frischeisen, M. Klein, W. Brütting
   "Efficiency Analysis of Organic Light-Emitting Diodes based on Optical Simulation"
   Organic Electronics **10** (2009) 478–485
9. S. Nowy, W. Ren, J. Wagner, J. A. Weber, W. Brütting
   "Impedance spectroscopy of organic hetero-layer OLEDs as a probe for charge carrier injection and device degradation"
   Proceedings of SPIE **7415** (2009) 74150G
10. S. Nowy, J. Frischeisen, W. Brütting
    "Simulation based optimization of light-outcoupling in organic light-emitting diodes"
    Proceedings of SPIE **7415** (2009) 74151C
11. S. Nowy, W. Ren, A. Elschner, W. Lövenich, W. Brütting
    "Impedance spectroscopy as a probe for the degradation of organic light-emitting diodes"
    Journal of Applied Physics **107** (2010) 054501
12. T. Wehlus, T. Körner, S. Nowy, J. Frischeisen, H. Karl, B. Stritzker, W. Brütting
    "Hybrid organic–inorganic materials for integrated optoelectronic devices"
    physica status solidi a, in press
13. D. S. Setz, T. D. Schmidt, M. Flämmich, S. Nowy, J. Frischeisen, B. C. Krummacher, T. Dobbertin, K. Heuser, D. Miachaelis, N. Danz, W. Brütting, A. Winnacker
    "Comprehensive Efficiency Analysis of Organic Light-Emitting Devices"
    Journal of Photonics for Energy, accepted
14. T. D. Schmidt, A. Buchschuster, M. Holm, S. Nowy, J. A. Weber, W. Brütting
    "Degradation effect on the magnetoresistance in organic light emitting diodes"
    Synthetic Metals, accepted

Patente

- B. C. Krummacher, F. Schindler, N. A. Reinke, W. Brütting, J. Frischeisen, S. Nowy
  "Strahlungsemittierendes Bauelement"
  DE 10 2008 022 830 A1
- J. Frischeisen, S. Nowy, W. Brütting
  "Organische Leuchtdiode"
  DE 10 2009 037 185 A1 / WO 2010/136537 A1

Curriculum vitae

Stefan Nowy

geboren am 30. April 1981 in Karlsruhe

seit 08/2010	**Wissenschaftlicher Mitarbeiter** Physikalisch-Technische Bundesanstalt, Braunschweig
06/2006 – 06/2010	**Wissenschaftlicher Mitarbeiter / Doktorand** Lehrstuhl für Experimentalphysik IV Universität Augsburg
01/2006 – 05/2006	**Wissenschaftlicher Mitarbeiter** Weiterführung von Experimenten zum Diplomarbeitsthema Walter Schottky Institut, Zentralinstitut für physikalische Grundlagen der Halbleiterelektronik der Technischen Universität München
10/2000 – 12/2005	**Studium: Physik, Technische Universität München** Abschluss: Diplom-Physiker **Studienrichtung:** Technische Physik **Experimentelle Diplomarbeit:** **„Diamond based Ion Sensitive Field Effect Transistors“** Walter Schottky Institut, Zentralinstitut für physikalische Grundlagen der Halbleiterelektronik der Technischen Universität München Betreuung: Dr. J. A. Garrido und Prof. Dr. M. Stutzmann
09/1991 – 06/2000	**Leonhard - Wagner - Gymnasium, Schwabmünchen** Abschluss: Allgemeine Hochschulreife
09/1987 – 07/1991	**Grundschule St. Ulrich, Schwabmünchen**

Braunschweig, im Dezember 2010